

**GMR Limits for Interlayer Coupled
and Pinned Trilayers
and
New Concepts for GMR-Sensors**

Experimental Investigations
and Computer Simulation

Dissertation zur Erlangung des Grades eines
Doktors der Naturwissenschaften der
Fakultät für Physik der Universität Bielefeld

vorgelegt von **Tobias Hempel**

14. Oktober 2005

Erklärung

Hiermit versichere ich an Eides statt, dass ich die vorliegende Arbeit selbständig verfasst und keine anderen als die angegebenen Quellen und Hilfsmittel verwendet habe.

Muntelier, 9. Oktober 2005

(Tobias Hempel)

Gutachter:

Prof. Dr. G. Reiss

Prof. Dr. D. Anselmetti

Datum des Einreichens der Arbeit: 14. Oktober 2005

Contents

1	Preface	1
2	Theory	5
2.1	Magnetic Parameters and their Units	6
2.2	GMR-Effect	7
2.2.1	Electron Transport in Magnetic Systems	7
2.2.2	Resistor Network Model	8
2.2.3	Amplitudes of the GMR-Effect	10
2.3	Magnetic Anisotropy	14
2.3.1	Shape Anisotropy	15
2.3.2	Induced Anisotropy	17
2.4	Interlayer Exchange Coupling	18
2.4.1	Phenomenological Description	19
2.4.2	Applying the RKKY-Theory on IEC	20
2.4.3	Quantum Confinement Model	21
2.4.4	Survey of the Models to IEC	27
2.4.5	Application as Fitting Equation	28
2.5	Exchange Biasing	28
2.6	Orange Peel Coupling	29
2.7	Calculation of GMR(H) and M(H)	30
2.7.1	Standard Model for GMR-Calculation	31
2.7.2	Enhanced Model for GMR-Calculation	31
2.7.3	Calculation of Magnetization Loop	35
2.8	Phenomenological Law for M(H)	35

3 Experiments and Discussion on Interlayer Coupled and Pinned Magnetic Trilayers	37
3.1 Introduction	37
3.2 Definition of Measurable Quantities	40
3.3 Review on Unpinned Trilayers	41
3.4 Sample Preparation and Characterization	42
3.5 Typical Characteristic	45
3.6 Ideal Thickness of the Magnetic Layers	46
3.7 Variation of Spacer Layer Thickness	51
3.8 Structural Analysis	56
3.8.1 Investigation on Layer Roughness	56
3.8.2 Investigation on Grain Size and Layer Quality	58
3.9 Magnetic Measurements	59
3.10 Comparison of Pinned and Unpinned Trilayers	66
3.11 Conclusion	68
4 Simulation of the GMR-Characteristics	71
4.1 Model for Magnetization Reversal	72
4.1.1 Requirements and Assumptions of the Model	72
4.1.2 Model for Coupled and Pinned Trilayers	74
4.1.3 GMR and Magnetization Characteristics	77
4.1.4 Model for Other Stacking Sequences	78
4.1.5 Simplifications for Vanishing Anisotropy	78
4.2 Simulation Program GMRSim	80
4.2.1 Procedure of Simulation	80
4.2.2 Determination of Parameters	83
4.3 Comparison to Lattice Calculations	83
4.4 Application of the Simulation	88
4.4.1 Determination of Input Parameters	88

4.4.2	Characteristics and Evaluated Parameters	88
4.4.3	Interpretation of the Results	89
4.4.4	Comparison to RKKY-like Interaction	96
4.5	Conclusion	97
5	New Sensor Concepts	99
5.1	Introduction	99
5.2	Answer of a Wheatstone Bridge	101
5.3	Exploitation of Shape Anisotropy	102
5.3.1	Initial Considerations	102
5.3.2	Test Structures	102
5.3.3	Measurement of Resistance	105
5.3.4	Measurement of GMR Characteristics	105
5.3.5	Results	106
5.3.6	Enhancement of Sputter Anisotropy	111
5.4	Optimized Test Structures	114
5.4.1	Processes	114
5.5	Interdiffusion by Local Heat-Treatment	116
5.5.1	Realization	116
5.5.2	Results on Cu/Co-Multilayers	117
5.5.3	Results on Cu/NiFe-Multilayers	118
5.5.4	Perspective for Local Annealing	118
5.6	Demonstrator Device for GMR Sensors	121
6	Summary	123
	<u>Appendix</u>	127

A	Enhanced Stoner-Wohlfarth's Model for Various Systems	127
A.1	Model for Trilayers	127
A.1.1	GMR and Magnetization for Trilayers	130
A.2	Model for Doubled Trilayers	131
A.2.1	GMR and Magnetization for Doubled Trilayers	133
A.3	Model for Bottom Spin Valves	133
A.3.1	GMR and Magnetization for Bottom Spin Valves	135
A.4	Model for Multilayers	135
A.4.1	GMR and Magnetization for Multilayers	137
A.5	Enhanced Model for Multilayers	137
A.5.1	GMR and Magnetization for Multilayers in the En- hanced Model	139
B	Overview to Parameters for the Simulations	141
C	Starting Parameters for Simulations	146
D	Source Code of Simulation Kernel	147
	References	175
	Publications and Conferences	183
	List of Figures	187
	List of Tables	191
	Acknowledgment	193

Chapter 1

Preface

About two decades ago the discovery of antiferromagnetic interlayer coupling in metallic *Fe/Cr*-multilayers [Grü86] triggered an enormous research activity in the area of magnetic thin films. It has been experimentally found [Bai88] [Par90] that depending on the thickness of the non-ferromagnetic layers, e.g. *Cr*, *Cu*, *Ag* or *Ru*, the magnetic moments of adjacent ferromagnetic layers are spontaneously aligned antiferro- or ferromagnetically. The underlying oscillatory exchange interaction between the magnetic layers mediated by the nonmagnetic spacer layers has subsequently been identified as a Ruderman-Kittel-Kasuya-Yosida (RKKY)-like interaction between two thin magnetic sheets embedded in a free electron gas (e.g. [Coe91]).

The alignment of the magnetization in the ferromagnetic layers of the multilayer stack strongly influences the resistance of the system. Usually the resistance in the antiferromagnetic state is much higher than in the parallel state at magnetic saturation. This effect, called **giant magneto resistance** (GMR), is caused by spin-dependent scattering of the conduction electrons in the magnetic layer and a change in the relative band structure during the magnetization process.

The GMR multilayers have already found their way into automotive sensor technology and into leading-edge hard disk drive products, as they can be engineered to be more sensitive to very small magnetic fields than all conventional ferromagnetic metals known. In addition GMR based sensors show an outstanding signal-to-noise ratio.

This thesis will address two different aspects of today's research on GMR, one related to basics, the other to the application of GMR as a sensor device. Chapter 3 reports on investigations on interlayer coupled and pinned magnetic trilayers. This is one of the simplest stacking sequences combining oscillatory interlayer exchange coupling and exchange bias. Here the results

will definitely prove wrong the general statement that there is a lower limit of about 2 nm below which no antiferromagnetic alignment can be realized in spin valve structures. In chapter 5 the transfer of laboratory results to a production line for **micro system technology** (MST), especially the cost saving realization of a Wheatstone bridge, is presented.

A special feature of this thesis is the introduction of a new simulation tool for GMR characteristics (chapter 4). Its applicability to understand experimental results will be demonstrated as well as its capability to predict characteristics of newly designed stacking sequences and to address other application related questions.

Overview

Chapter 2 will provide the reader with the fundamental theory for GMR and related topics in magnetism as far as this information is referred to in the ongoing chapters. Starting with a section on magnetic parameters and their units (section 2.1), GMR-effect (section 2.2), magnetic anisotropy (section 2.3), interlayer exchange coupling (section 2.4), and exchange bias (section 2.5) important basics for the model implemented in the simulation tool will be extracted. Especially the relevant contributions of anisotropy and fitting equations for the interlayer coupling will be assorted and explained.

In section 2.2.3 it will be pointed out why the stacking sequence $NiFe - Co/Cu/Co/IrMn$ is an ideal test system for investigating the limits of the GMR effect with regard to its amplitude and minimal spacer layer thickness.

Furthermore existing models for orange peel coupling (section 2.6) and for the calculations of $GMR(H)$ and $M(H)$ (section 2.7) will be extracted from literature and adjusted to meet the needs of the simulation and the discussion of results. Finally a phenomenological law for $M(H)$ -characteristics based on results of Stearns will be developed (section 2.8).

Chapter 3 will then report on the experiments on interlayer coupled and pinned magnetic trilayers. The stacking sequence $NiFe - Co/Cu/Co/IrMn$ is one of the simplest layered system showing the GMR effect, and ideal for exploiting interlayer coupling and exchange bias. These very sensitive structures were realized by forming simple sandwiches of two ferromagnetic layers which are separated by a thin nonmagnetic but well conducting copper layer (spacer) [Die91a]. Due to the exchange bias to the adjacent layer of antiferromagnetic material ($IrMn$) the magnetic moment of the top ferromagnetic layer is fixed to one direction, while the moment of the bottom ferromagnetic layer ($Co - NiFe$) can – more or less freely – follow external magnetic field changes, depending on amplitude and phase of the interlayer exchange coupling.

The spacer thickness of typical spin valve structures is about 2 nm to 3 nm where the intrinsic interlayer exchange coupling is fairly weak. This is in contrast to multilayers, where the GMR effect is accompanied by a large magnitude of the interlayer exchange coupling at first or second maximum. In biased spin-valves it is generally observed that there is a critical spacer thickness of about 2 nm for *Cu* and *Au* used as spacer materials below which the GMR effect rapidly drops to zero. As the underlying reason it is argued that the competition between the interlayer exchange interaction and the exchange bias or the presence of pin holes result in insufficient antiparallel aligned magnetic moments and hence to a loss in the GMR effect amplitude.

Hence it is the objective of this study to demonstrate for the first time that in well grown trilayers of the type *NiFe-Co/Cu/Co/IrMn* the RKKY-like antiferromagnetic coupling is dominating the ferromagnetic coupling down to a spacer layer thickness of about 1 nm .

After a more detailed introduction to the objective (3.1) and the definition of measurable quantities (section 3.2) a review on unpinned trilayers will be given (section 3.3), followed by a section on sample preparation (section 3.4) and the explanation of a typical characteristic (section 3.5).

After determining the ideal thickness of the ferromagnetic layers (section 3.6) it will be reported on the decisive series, the *Cu* spacer layer variation from 0.8 nm to 9.7 nm (3.7).

Structural analysis (section 3.8) will show that the samples under investigation feature an extraordinary smoothness at their interfaces. This causes the RKKY-like interlayer coupling to dominate the ferromagnetic orange peel coupling and/or pin holes. Furthermore the average grain size will be determined.

Magnetic measurements (section 3.9) and its analysis by means of a phenomenological law as presented in section 2.8 provide the reader with an insight in the magnetization process and its implications for the $\Delta R/R$ -characteristic.

The comparison of the former series of unpinned trilayers [Hem00] with the new measurements of pinned trilayers (section 3.10) will show coherent results.

To get a deeper understanding and allow for a quantitative analysis of the interlayer coupling, anisotropy and exchange bias based on the existing experimental results a new simulation tool was developed. The first section of chapter 4 will provide the underlying model for magnetization reversal based on a model introduced by E. C. Stoner and E. P. Wohlfarth [Sto48] and for the first time applied to magnetic devices by H. Holloway and D. J. Kubinski [Hol98].

The implementation of this model in the program package `GMRSim`¹ will be explained in section 4.2. In the consecutive section 4.3 the applicability and outstanding features of the new simulation tool will be compared to existing micromagnetic calculation programs.

For the last two sections 4.4 and 4.5 we will return to interlayer coupled and pinned magnetic trilayers and apply our simulation, in order to get a deeper understanding of the influence of crystalline and induced anisotropy, exchange bias, and interlayer coupling on the GMR characteristic.

The final chapter 5 will report on the cooperation with HL Planartechnik, Dortmund, Germany. Within the framework of the *Robert Bosch GmbH Leitprojekt Magneto-Elektronik*² the aim of the subproject *GMR Sensors for Automation* was the development of a prototype for a contact free switch. This thesis and the underlying investigations will help in the transfer of fundamental knowledge to ready to use sensor concepts.

To yield a cost-saving and easy to handle realization of a Wheatstone bridge the exploitation of shape anisotropy was suggested based on simulation results and test structures processed and analyzed (section 5.3). As an alternative approach a bridge circuit based on interdiffusion by local heat treatment was investigated (section 5.5). Finally a demonstrator device for GMR sensors will be presented in section 5.6.

¹The program package `GMRSim` is available on the author's homepage

²Supported by the German Ministry for Education and Research, BMBF, under grant #13N73797/4

Chapter 2

Theory

Magnetoresistance (MR) describes the effect of changing the resistance of a system by an external magnetic field. In 1988 M. N. Baibich *et al.* [Bai88] and G. Binasch *et al.* [Bin89] discovered that this effect is extraordinary high in multilayer structures of ferromagnetic and non magnetic (paramagnetic) films. In layered magnetic materials and other microstructured devices the polarization of the electrons leads to high magnetoresistance effects for small magnetic fields.

At the beginning of this chapter magnetic parameters and their units will be introduced (Section 2.1). Section 2.2 then addresses the GMR-effect itself in some detail.

The appearance of the GMR-effect is strongly correlated to the relative alignment of the magnetization of adjacent magnetic layers which of course is altered, when an external magnetic field is applied. Therefore we have to consider the magnetization processes in these structures in some detail.

Section 2.3 deals with the anisotropy, which is more or less present in all ferromagnetic materials but of special interest in thin films. In multilayer structures the coupling of the magnetization between the different layers becomes a major aspect. The discovery of the interlayer exchange coupling (IEC) in 1986 by P. Grünberg *et al.* [Grü86] and its oscillatory behavior [Par90] triggered the investigation of thin magnetic fields. A survey of the most important aspects is given in section 2.4. Furthermore the effects of exchange biasing (section 2.5) and orange peel coupling (section 2.6) will be introduced.

The GMR can be understood as a transition of a disordered state to an ordered state where all magnetic moments are oriented parallel to each other and the external field. In section 2.7 of this chapter it will be explained how to calculate the GMR(H)-characteristic and the magnetization loop when the

angles of magnetization as a function of the external field for each single layer is known. Here the AF-order-parameter will be used which was introduced to GMR multilayer stacks by H. Holloway and D. J. Kubinski [Hol98].

In the final section 2.8 a phenomenological law to fit the magnetization of trilayers will be introduced.

2.1 Magnetic Parameters and their Units

The introduction of magnetism in literature differs with regard to the fundamental parameters and their units. SI units are prescribed, but the old cgs-system is still quite common. In table 2.1 an overview of the most important parameters for magnetism and their units in both systems is given.

The units of the field strength H , the flux density B , the magnetization M , and the magnetic moment m are directly derived from the technical units of the electric current (Ampère) and Voltage (Volt). The three parameters H , B , and m basically have the same unit considering cgs units, but it is common to use ‘Oersted’, ‘Gauss’, and ‘emu’, respectively.

	SI system	cgs system
permeability of the vacuum μ_0	$\mathbf{B} = \mu_0(\mathbf{H} + \mathbf{M})$ $\mu_0 = 4\pi \cdot 10^{-7} Tm/A$	$\mathbf{B} = \mathbf{H} + 4\pi\mathbf{M}$ $\mu_0 = 1$
field strength H	$[A/m]$	$[Oe] = \text{Oersted}$ $79.577 A/m = 1 Oe$
flux density B	$[T]=[Vs/m^2] = \text{Tesla}$	$[G] = \text{Gauss}$ $1 T = 10^4 G$
magnetization M	$[A/m]$	$[G]$
magnetic moment m	$[Am^2]$ $1 Am^2 = 10^3 emu$	$[emu]$
anisotropy coupling constant K	$[J/m^3]$ $1 J/m^3 = 10 erg/cm^3$	$[erg/cm^3]$
interlayer coupling constant J	$[J/m^2]$ $1 mJ/m^2 = 1 erg/cm^2$	$[erg/cm]$

Table 2.1: Comparison of SI and cgs system.

2.2 GMR-Effect

In this thesis the Giant Magneto Resistance is defined as the change in resistance between the parallel and antiparallel alignment divided by the resistance of the parallel alignment:

$$\frac{\Delta R}{R} = \frac{R_{\uparrow\downarrow} - R_{\uparrow\uparrow}}{R_{\uparrow\uparrow}} \quad (2.1)$$

R. E. Camley and J. Barnaś developed a theory of the GMR based on a simple Free-Electron-Model in the Fuchs-Sondheimer-approximation, which was extended to layered systems later [Cam89]. Over the last few years several models have been proposed, which describe the different aspects more or less realistic. An overview is for example given by [Lev95], [Lev96], [Tsy99], [Tsy01] and the enclosed sources.

Before introducing how the GMR(H)-characteristic and the magnetization can be calculated (see section 2.7) as part of a simulation routine we will try to get some insight on how the GMR effect arises. But I will abstain from giving a full review of one of the models mentioned above.

2.2.1 Electron Transport in Magnetic Systems

The electric resistance of metals is due to scattering processes of the free electrons. In bulk material phonons and structural defects contribute to the scattering. Taking the model of a free electron gas the resistivity ρ is given by the Drude-Sommerfeld-Equation:

$$\rho = \frac{m^* \nu_F}{ne^2 l_\infty} = \frac{m^*}{ne^2 \tau} \quad (2.2)$$

Here m^* is the effective mass of the electrons, ν_F the Fermi velocity, n the electron density, l_∞ the mean free path, and $\tau = l_\infty/\nu_F$ the relaxation time.

In a system of thin films the influence of surfaces and interfaces cannot be neglected as the film thickness is in the order of the mean free path. Fuchs calculated in 1938 for the resistivity versus film thickness d .

$$\frac{\rho_\infty}{\rho(d)} = 1 - \frac{3}{2} \cdot \int_1^\infty \left(\frac{1}{t^3} - \frac{1}{t^5} \right) \frac{1 - \exp\left(-\frac{d}{l_\infty} t\right)}{1 - p \exp\left(-\frac{d}{l_\infty} t\right)} dt \quad (2.3)$$

The phenomenological parameter p describes the probability that an electron is reflected specularly at the surface, $t = 1/\cos \theta$ is the integration variable, and θ is the angle between the z-axis (perpendicular to the plane of the film) and the charge carriers velocity direction. A detailed discussion of this model and its application to layers systems is given in [Rei99].

Mostly scattering processes are elastic, so there is no or only very little energy transfer. Due to Pauli's Rule electrons are only allowed to scatter in free states. Therefore they can only scatter in states in the vicinity of the Fermi energy.

The larger the number of free states in the attainable band the higher is the probability of scattering and thus the resistivity:

$$\rho = \frac{1}{\sigma} \propto D(E_F) \quad (2.4)$$

Here σ is the conductivity and $D(E_F)$ the density of states (DOS) at the Fermi level.

To account for the GMR-effect there are two more crucial observations: The probability for spin flip scattering is much less than for spin conserving scattering. Therefore I. A. Campbell and A. Fert proposed to treat the spin channels for \uparrow - and \downarrow -electrons separately and add their conductivities [Cam82]. Furthermore the density of states for the two electron channels in a ferromagnet differs. Eq. (2.4) therefore has to be altered as follows.

$$\rho_\sigma \propto D_\sigma(E_F) \quad (2.5)$$

The index $\sigma = \uparrow, \downarrow$ gives the spin direction of the electrons. The resistivity of \uparrow - and \downarrow -electrons can differ widely, especially for transition metals [Mat91].

2.2.2 Resistor Network Model

In 1991 J. Mathon introduced a simple two channel model [Mat91]. We will in short describe the concepts and results.

As given above the resistivity for a given spin channel depends on the direction of the magnetization of the magnetic layer. For parallel alignment the majority electrons see a low resistivity in all layers, whereas the minority electrons always see a high resistivity. For an antiparallel alignment both channels have a low resistivity in one and a high resistivity in the other layer (see Fig. 2.1).

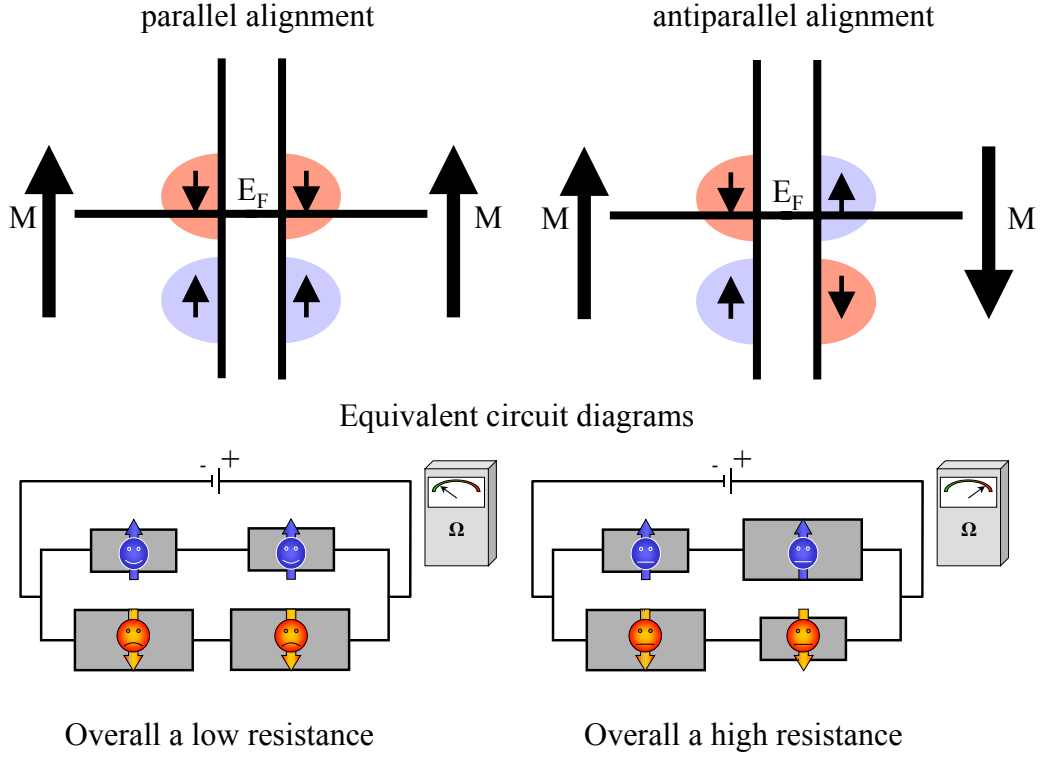


Figure 2.1: Illustration of the resistor network model.

The network model assumes a mean free path in the regime of the layer thickness or greater. Then we can in a first approach calculate the resistivity for one channel as average independently of the geometry of the measurement.

Introducing the parameters α and β

$$\alpha = \frac{\rho^H}{\rho^N}, \quad \beta = \frac{\rho^L}{\rho^N} \quad (2.6)$$

and the spin asymmetry

$$\gamma = \frac{\alpha}{\beta} = \frac{\rho^H}{\rho^L} \quad (2.7)$$

Eq. (2.1) becomes:

$$\frac{\Delta R}{R} = \frac{(\alpha - \beta)^2}{4 \left(\alpha + \frac{N}{M}\right) \left(\beta + \frac{N}{M}\right)} = \frac{(\gamma - 1)^2}{4 \left(\gamma + \frac{1}{\beta} \cdot \frac{N}{M}\right) \left(1 + \frac{1}{\beta} \cdot \frac{N}{M}\right)} \quad (2.8)$$

Here M and N are the layer thickness of the magnetic and non magnetic film, respectively. ρ^N is the resistivity of the non magnetic layer, ρ^L (Low) the resistivity for the majority and ρ^H (High) for the minority spin channel in the magnetic layer.

Although this model gives a basic understanding of GMR it has several limitations. In many cases this assumption of a comparatively long free mean path is not correct as we have to consider the realistic mean free path in a thin film structure and not in bulk material (e.g. [Gur93], [Rei99]). This model also yields identical results for current in plane (CIP) and current perpendicular to plane (CIP) measurements which is in contrast to experiments.

2.2.3 Amplitudes of the GMR-Effect

Research in the last couple of years has shown the dependence of the achievable GMR-effect on various physical parameters. The choice of magnetic and nonmagnetic materials and their combination is thereby a major aspect. In the rather simple model presented above the band structure and the density of states for the magnetic layer has been taken into consideration. But when the band structures for magnetic and nonmagnetic material differs the interface acts as a potential barrier for the electrons and the transmissions becomes smaller than 1. Also the quality of the atomic structure of the borders and the surfaces enhances the GMR.

Further aspects are the thickness of magnetic and non magnetics layers, the method of pinning, the buffer and capping layers, the defect concentration within the layer, the crystalline structure and many more. These are more or less included in the different models.

In the review article [Tsy01] E. Y. Tsybmal and D. G. Pettifor present the most important results. In the following synopsis of their argumentation we will concentrate on results which explain why the immiscible system Cu/Co is particularly suitable for the investigations accomplished in chapter 3.

Spin-dependent Conductivity

As described above in Eq. (2.2) the resistivity depends on the relaxation time which can be estimated from the Fermi golden rule:

$$\tau^{-1} = \frac{2\pi}{\hbar} \langle V_{scat}^2 \rangle n(E_F) \quad (2.9)$$

Here $\langle V_{scat}^2 \rangle$ is an average value of the scattering potential and $n(E_F)$ it the density of electronic states at the Fermi energy E_F for the appropriate

spin. All relevant quantities are in general spin dependent, but the origin is different.

The effective mass m^* and the Fermi velocity v_F are intrinsic properties of the metal and entirely determined by the electronic band structure of the metal. In ferromagnetic metals these quantities are different for the up- and down-spin electrons. The density of states at the Fermi energy $n(E_F)$ is also determined by the spin-polarized band structure.

However the scattering potential is generated by the scatterers such as lattice vibrations (phonons), impurities and defects and is not an intrinsic property of the metal. It can be either spin-dependent or spin-independent.

In real magnetic multilayers the interfaces are not ideal. Interfacial roughness and/or substitutional disorder, i.g. mixing of the adjacent metal atoms at the interface, are always present. Randomness of the atomic potentials at the interface results in enhanced interfacial scattering, which might be strongly spin-dependent.

But apart from the non-ideal interfaces various types of defects, such as grain boundaries, stacking faults, and misfit dislocations, are always present. Because the relaxation time is determined by the configurationally averaged value of the scattering potential squared, various types of scattering centers can make the average value spin-independent, and the relative importance of spin-dependent scattering potentials can be diminished. The spin-polarized band structure of the multilayer becomes the dominant contribution to the conductivity.

Role of Band Structure

The most important property that determines the spin-dependent conductivity and consequently is responsible for the GMR is the electronic band structure of the multilayer. The electronic band structure of the ferromagnetic metals *Co*, *Fe*, *Ni*, and their alloys and the nonmagnetic metals *Cu*, *Cr*, *Ag*, and *Au* is characterized by a number of similar features. As an example the electronic band structures and the density of states of *Cu* (a) and fcc *Co* is given in Fig. 2.2.

The conductivity is determined by the position of the Fermi energy with respect to the d-bands. In the case of *Cu*, the d-bands are fully occupied and the Fermi level lies within the sp-band. Due to the high velocity of the electrons within the sp-band and the low density of states with resultant low probability of scattering, the mean free path is long and *Cu* is a very good conductor. On the other hand, in the case of a ferromagnetic metal like *Co*, as a result of the exchange splitting, the majority d-band is fully occupied,

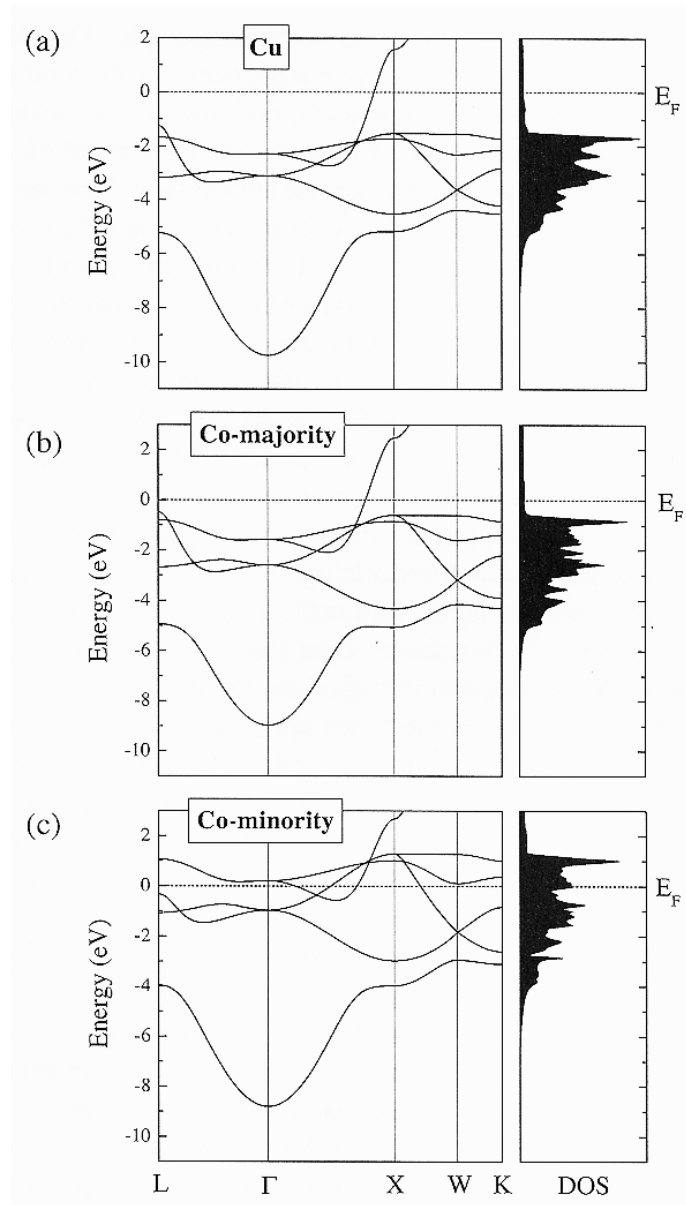


Figure 2.2: Electronic band structures (left panels) and the density of states (right panels) of *Cu* (a) and fcc *Co* for the majority-spin (b) and minority-spin (c) electrons. The Fermi level lies within the sp-band for the majority-spin electrons in *Co*, which leads to high conductivity of the majority-spin channel. The Fermi level lies, however, within the d-band for the minority-spin electrons, resulting in low conductivity of the minority-spin channel. [Tsy01]

whereas the minority d-band is only partly occupied. The Fermi level lies therefore, within the sp-band for the majority spins but within the d-band of the minority spins. The exchange splitting of the spin bands leads to a crucial difference in the conductivity between the two spin channels.

Based on the spin-polarized band structure the strong spin asymmetry in the conductivity of bulk *Co* can be explained.

Multilayers of thin metallic films add a further important feature. Two adjacent metals creating the interface have different band structures, which leads to potential steps at the interface and results in the transmission probability across the interface being less than 1 and being spin-dependent if one of the metals is ferromagnetic. A good band matching as for *Cu* and the majority-spin electrons of *Co* results in a high transmission, whereas a large band mismatch as for *Cu* and the minority spin in *Co* implies a poor transmission. Therefore, the interfaces of the *Co/Cu*-stack act as a spin filter.

When the filters, i.e. the magnetizations of the *Co*-layers, are aligned, the majority spin electrons can pass through relatively easily. When the filters are antialigned, the electrons in both spin channels are reflected at one of the interfaces.

In addition, roughness and intermixing near the interfaces results in spin-dependent scattering as a consequence of the lateral randomness in the atomic potentials. Large spin dependence in scattering arises if the atomic potentials of the types of atoms are similar (matched) for one spin orientations but strongly dissimilar (mismatches) for the other spin orientations. But experimental results show that the systems with highest GMR, such as *Fe/Cr*, *Co/Cu*, *Co/Ag*, *Ni₈₀Fe₂₀/Au*, and *Ni₈₀Fe₂₀/Ag* are all immiscible. This fact indicates that intermixing at the interfaces is not favorable to GMR.

Lattice Matching

When experimental results are analyzed it appears that the spin asymmetry in the band structure is a necessary but not sufficient condition for high GMR values: There are two factors crucial for obtaining high values of GMR. These are the band matching and the lattice matching between the ferromagnetic and nonmagnetic metals. Lattice mismatch leads to the formation of misfit dislocations and other structural defects at the interfaces. Scattering by these defects in the nonmagnetic spacer layer is spin independent, resulting in a reduction of GMR. Although the scattering by defects in a ferromagnetic layer could be spin-dependent in principal, the spin asymmetry in the scattering potentials will vary depending on structural details. The presence

of various types of defects will make the average of the scattering potential only weakly dependent on the spin.

In *Cu/Co*-multilayers these two conditions are almost perfectly satisfied. There is an excellent band matching between the majority-spin electrons of *Co* and a strong band mismatch between the minority spin electrons in *Co* and *Cu*. Thin films of *Co* grow in the fcc structure with the lattice parameter of about 0.356nm , which is only 2% less than the lattice parameter of 0.361 nm in fcc *Cu*.

At this point we should also note that the lattice parameter of fcc-permalloy ($\text{Ni}_{80}\text{Fe}_{20}$) which will be used as a buffer layer in our experimental realization of a interlayer coupled and pinned trilayers (chapter 3) is close to that in *Co* and *Cu*.

2.3 Magnetic Anisotropy

In the investigation of the magnetization reversal in thin magnetic layers anisotropy plays a major role. This is due to the huge difference in the dimensions parallel and perpendicular to the layer. When dealing with structured samples the system is restrained to another dimension. The following mechanisms are important for the anisotropy to take place [Zor99]:

Shape anisotropy: Because of the high anisotropy of the demagnetization factor the measured magnetic properties parallel or perpendicular to the layer are different. Additionally, structured samples show an anisotropy in the layer plane.

Crystalline anisotropy: If the local crystal field seen by an atom is of low symmetry and if the bonding electrons of that atom have an asymmetric charge distribution ($L_z \neq 0$), then the atomic orbits interact anisotropically with the crystal field. In other words, certain orientation for the bonding electron charge distribution are energetically preferred. The coupling of the spin part of the magnetic moment to the electronic orbital shape and orientation (spin-orbit coupling) on a given atom generates the crystalline anisotropy.

Induced anisotropy: When the sample is grown or annealed in a magnetic field an additional anisotropy is induced. This effect is of special importance for ferromagnetic layers pinned to an antiferromagnet.

Surface anisotropy: The atoms of the outer atomic layers have less nearest neighbors of the same element. In other words we have a break of the

symmetry at the surface or interface. The influence of the surface increases by decreasing layer thickness.

Magnetoelastic anisotropy: A mechanical stress or strain applied to a magnetic thin film will result in an additional anisotropy. For example this can be done by growing the layer on a buffer with a different lattice parameter.

Here we will concentrate on shape, crystalline and induced anisotropy.

2.3.1 Shape Anisotropy

When the magnetization loop $M(H)$ is measured one has to note that the external field H_0 usually is not identical to the field in the sample. The external field H_0 generates in a spherical sample a magnetization M . This again generates outside the sample an additional field H_{add} , which is identical to a magnetic dipole $m = V \cdot M$, where $V = 4\pi R^3/3$ denotes the volume of the sphere. The overall field outside the sample becomes

$$\vec{H}_a = \vec{H}_0 + \frac{3(\vec{m} \cdot \vec{r})\vec{r} - r^2\vec{m}}{4\pi r^5} \quad (2.10)$$

In a large distance r the field keeps unchanged equal to H_0 . Near the sphere the magnetic flux lines are pulled into the sample for paramagnetic and ferromagnetic materials.

Inside the sphere the additional field is homogeneous and has a value of $-\vec{M}/3$. For ferromagnetic materials it points in the opposite direction of the external field. The inner field reduces to

$$\vec{H}_i = \vec{H}_0 - \frac{\vec{M}}{3} \quad (2.11)$$

$-M/3$ is called demagnetizing field and the factor $\mathcal{N} = 1/3$ demagnetizing factor. The problem of demagnetizing is analytically solvable for ellipsoids with rotational symmetry. In general there are different demagnetizing factors \mathcal{N}_a , \mathcal{N}_b , and \mathcal{N}_c in the direction of the principal axis of length a , b , and c with $a = b$ for an ellipsoide with rotational symmetry. Thus, the demagnetization is not isotropic.

$$\begin{aligned} H_{i,x} &= H_{0,x} - \mathcal{N}_a M_x \\ H_{i,y} &= H_{0,y} - \mathcal{N}_b M_y \\ H_{i,z} &= H_{0,z} - \mathcal{N}_c M_z \end{aligned} \quad (2.12)$$

	c/a	\mathcal{N}_c	$\mathcal{N}_a = \mathcal{N}_b$
thin film	0	1	0
sphere	1	1/3	1/3
long needle	∞	0	1/2

Table 2.2: Demagnetizing factors for three special geometries.

The sum of the three demagnetizing factors always is equal to one. Results for the special cases of a thin film, a sphere and a pin are given in table 2.2.

The difference of the energy per unit volume between parallel (E_{\parallel}) and perpendicular (E_{\perp}) saturation magnetization has to be considered to calculate the shape anisotropy:

$$K = \frac{E_{\perp} - E_{\parallel}}{V} \quad (2.13)$$

Layered structures showing the GMR-effect consist of layers in the range of several nm . Usually it is highly favorable to have the direction of the magnetization in the layer plane, K is positive.

This can easily be checked for the contribution of the shape anisotropy: As given in table 2.2 we have $\mathcal{N}_a = \mathcal{N}_b = 0$. Therefore demagnetization is only relevant for the component $M_z = M_s \cos \theta$. Its energy is given by:

$$E_{shape, thin film} = \frac{1}{2} \mu_0 M_{sat}^2 \sin^2 \theta \quad (2.14)$$

Setting $\theta = 0$ (perpendicular) and $\theta = \pi/2$ (parallel) we yield for $K_{shape, thin film}$:

$$K_{shape, thin film} = \frac{1}{2} \mu_0 M_{sat}^2 \quad (2.15)$$

Therefore we assume an easy axis in the layer plane for the consecutive calculations.

When the lateral structure of the magnetic system approaches a size of some μm or smaller, shape anisotropy *in* the layer plane becomes important, too. Usually this can be expressed in form of the angle dependence given in Eq. (2.14) as this is the simplest form for uniaxial geometry.

$$\frac{E_{shape}}{A} = K_{shape} t \sin^2(\xi - \theta) \quad (2.16)$$

Here A is a unit area, ξ denotes the angle of the long axis of the structure, and θ the angle of the magnetization with reference to the x-axis.

For a given rectangular structure with thickness t , length l , and width b the associated anisotropy constant can be estimated as [O'H00]:

$$\begin{aligned} K_{shape} &= \frac{1}{2} \mu_0 M_{sat}^2 \left(\frac{2t}{\pi b} \sqrt{\frac{2l}{b}} - \frac{2t}{\pi l} \sqrt{\frac{2b}{l}} \right) \\ &= \mu_0 M_{sat}^2 t \frac{1}{\pi} \left(\sqrt{\frac{2l}{b^3}} - \sqrt{\frac{2b}{l^3}} \right) \end{aligned} \quad (2.17)$$

2.3.2 Induced Anisotropy

When the sample is grown or annealed in a magnetic field a uniaxial anisotropy is induced. We will account for it by the following energy term:

$$\frac{E_{K,ind}}{A} = K_{ind} t \sin^2(\theta - \varphi_{ind}), \quad (2.18)$$

where $(\theta - \varphi_{ind})$ denotes the angle between the (fixed) easy axis and the magnetization.

Additionally we will allow for a biaxial induced anisotropy. It may be due to the alignment of a material with high crystalline biaxial anisotropy:

$$\frac{E_{K,bi}}{A} = \frac{1}{4} K_{ind,bi} t \sin^2(2(\theta - \varphi_{ind})) = K_{ind,bi} t \sin^2(\theta - \varphi_{ind}) \cos^2(\theta - \varphi_{ind}) \quad (2.19)$$

Effective Anisotropy

The contributions of $K_{crystal}$, $K_{surface}$ and $K_{magnetoelastic}$ are summarized to the 'effective' anisotropy K_{eff} .

The energy contribution for the intrinsic anisotropy can be expanded in a series. Taking into account the uniaxial and biaxial term only it results into:

$$\frac{E_{K,uni}}{A} = K_{uni} t \sin^2(\theta - \varphi), \quad (2.20)$$

and

$$\frac{E_{K,bi}}{A} = \frac{1}{4} K_{bi} t \sin^2(2(\theta - \varphi)) = K_{bi} t \sin^2(\theta - \varphi) \cos^2(\theta - \varphi) \quad (2.21)$$

where $(\theta - \varphi)$ denotes the angle between the easy axis and the magnetization. The effect of shape and induced anisotropy is accessible by angle resolved measurements of the magnetization or GMR-effect. The contributions of $K_{crystal}$, $K_{surface}$ and $K_{magneto\ elastic}$ can not be resolved easily in polycrystalline samples as prepared by sputtering techniques. Therefore in our calculations the energy contributions of crystalline, surface and magneto elastic anisotropy are summarized in the intrinsic anisotropy. As the nature of the anisotropy, being uniaxial or biaxial, is not known a priori, both terms are included. Shape and induced anisotropy are added separately.

2.4 Interlayer Exchange Coupling

The discovery of antiferromagnetic coupling of adjacent ferromagnetic layers through a nonmagnetic spacer layer by P. Grünberg *et al.* [Grü86] triggered the investigation on interlayer exchange coupling (IEC) and from there to giant and tunnel magneto resistance and related phenomena.

The next step in understanding Grünbergs results was the discovery of the oscillating behavior of the interlayer exchange coupling for various multilayer systems by Parkin, More, and Roche in 1990 [Par90]. This so called bilinear coupling can be parallel or antiparallel.

In special cases, where the bilinear coupling is vanishing, a 90° -coupling of the magnetization of the ferromagnetic layers is observed. J. C. Slonczewski showed [Slo91] that this phenomenon can be based likewise on the conventional exchange coupling. Spatial fluctuation of the order of one atomic layer induce static waves of magnetization whose energy has the observed biquadratic form. Other theories suggest that this coupling is intrinsic (e.g. [Eri93]) or based on localized-electron states [Slo93].

If there is no static magnetic order in the spacer layer the interlayer exchange coupling has to be of indirect nature transmitted by the electrons of the nonmagnetic material [Grü99].

To predict the period and amplitude of this coupling, various theoretical models have been investigated.

- Application of the model by Ruderman, Kittel, Kasuya, and Yosida to layered systems (e.g. [Yaf87b], [Bru91], [Coe91]), see section 2.4.2 for details.

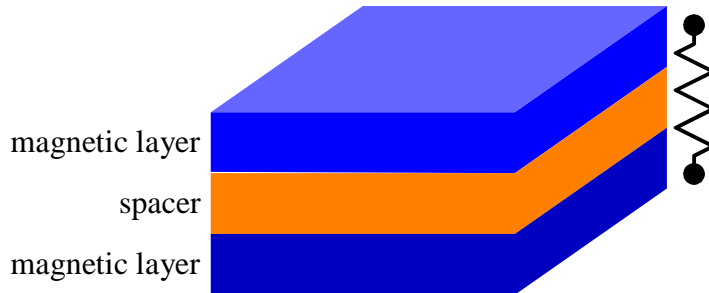


Figure 2.3: Illustration of the interlayer exchange coupling.

- Model of free electrons (e.g. [Bar92], [Eri93])
- Anderson model (e.g. [Edw91])
- *ab-initio* calculation (quantum confinement models), see section 2.4.3 for details.

2.4.1 Phenomenological Description

The interlayer exchange coupling can be described by determining its energy E_i :

$$\begin{aligned} \frac{E_i}{A} &= -J_L \frac{\vec{M}_1 \cdot \vec{M}_2}{|\vec{M}_1| \cdot |\vec{M}_2|} - J_Q \left(\frac{\vec{M}_1 \cdot \vec{M}_2}{|\vec{M}_1| \cdot |\vec{M}_2|} \right)^2 \\ &= -J_L \cos(\theta_2 - \theta_1) - J_Q \cos^2(\theta_2 - \theta_1) \end{aligned} \quad (2.22)$$

Here $(\theta_2 - \theta_1)$ is the angle between the magnetization direction \vec{M}_1 and \vec{M}_2 of the two adjacent ferromagnetic layers on both sides of the spacer layer. A is a unit area. Type and strength of the coupling are stated by the parameters J_L and J_Q .

If J_L is greater than J_Q the coupling is called bilinear. If J_L is positive, the coupling is ferromagnetic, otherwise the coupling is antiferromagnetic, as the system always takes the configuration of lowest energy. If the second term dominates and J_Q is negative it results in a 90°-coupling, the so called biquadratic coupling.

With regard to the energies for ferromagnetic (index F) ($\Delta\theta = 0$) and anti-ferromagnetic (index AF) ($\Delta\theta = \pi$) configuration, J_L can be defined as the energy difference per lateral unit cell at the two interfaces [Grü99].

$$J_L = -\frac{E_F - E_{AF}}{2A} \quad (2.23)$$

2.4.2 Applying the RKKY-Theory on IEC

Following the already mentioned discovery of Parkin, More, and Roche in 1990 [Par90] the periodic oscillation of the interlayer exchange coupling was shown for various systems by measuring the magneto resistance or more direct measurements as SPLEED³ and MOKE⁴. The measured period Λ varied from 0.29 nm for the $Fe/Cr/Fe(100)$ -system [Pur91] to 1.75 nm in the $Fe/Au/Fe(100)$ -system [Ung91].

Various authors proposed a connection to the period λ of the spin-density oscillation caused by a layer of magnetic atoms in a matrix of a nonmagnetic metal. Within the framework of the RKKY-theory⁵ and considering large spacer layer thicknesses a period $\lambda = \pi/k_F$ is determined in the case of a spherical Fermi surface with a Fermi wavevector k_F . E.g. for copper we yield $\lambda = \pi/k_F = 0.231 \text{ nm}$, very much in a disagreement with the measured period Λ . Furthermore the periodicity often depends on the growth direction and on the crystalline structure of the nonmagnetic layer which is not yet taken into consideration.

Yafet succeeded for the first time to apply this coupling model to layered systems ([Yaf87a] and [Yaf87b]). Within in RKKY-theory the space between the magnetic layers is continuous. The interlayer exchange of two uniformly magnetized, infinitely thin parallel planes oscillates with $\sin(k_F L)/L^2$ with $L \gg \lambda$. This period is identical to the period calculated for the coupling of two magnetic impurities embedded in a metal with free electrons. But whereas the coupling strength for impurities vanishes with $1/L^3$, in the planar (pseudo one-dimensional) case the decay is only $1/L^2$.

The continuous line in Fig. 2.4 plots the calculated coupling $J(L)$ and reflects the oscillation of the spin density induced in a free electron gas by one of the magnetic layers.

The dashed line demonstrates the fact that the agreement to experimental data is much better when the atomic structure of the interlayer is correctly build into the model. Here the coupling only for distances of $L = Nd$ is taken into consideration where d is the lattice parameter in a given crystalline direction and N an integer. The resulting oscillation period Λ is much bigger than the period λ for the original RKKY-theory [Coe91]. To yield the correct

³SPLEED: Spin-Polarized Low-Energy Electron Diffraction

⁴MOKE: Magneto Optic Kerr Effect

⁵RKKY-Theory named after Ruderman, Kittel, Kasuya, and Yosida

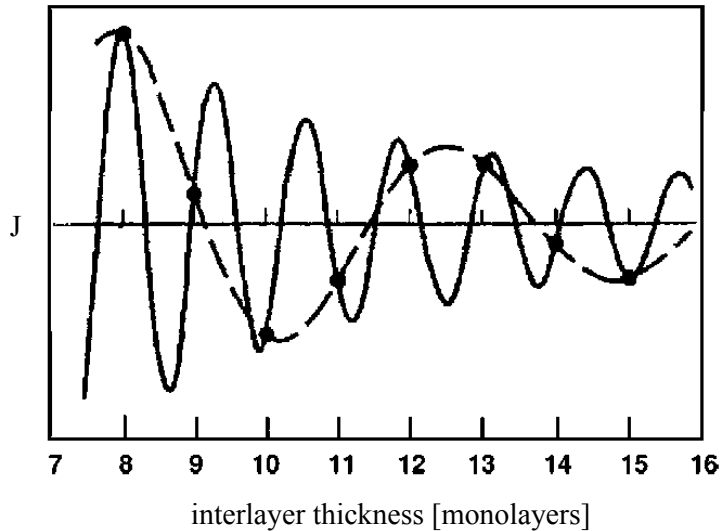


Figure 2.4: Continuous line: The coupling $J(L)$ for a monovalent fcc (100) material (arbitrary units) calculated with the continuous RKKY model. Dashed line: The true coupling function for $L = nd$. In the case of partially filled atomic layers at the interfaces $J(L)$ is as well defined for fractional values of L/d and might be understood as a weighted sum of $J(Nd)$. (from [Coe91])

periodicity Λ the wavenumber π/λ has to be reduced to the first Brillouin zone of the one dimensional lattice with a lattice parameter d . This is a projection to an axis parallel to the growth direction of the three dimensional lattice. Λ then follows to:

$$\Lambda = \frac{1}{|1/\lambda - n/d|} \quad (2.24)$$

Here the integer n has to be chosen so that Λ is greater or equal to $2d$. Λ goes to infinity if λ becomes equal to d/n [Coe91].

2.4.3 Quantum Confinement Model

The mechanism which is now widely accepted for the interlayer exchange coupling is based upon quantum interference in the spacer layer due to spin-dependent confinement. In this subsection the most important results for the analysis of the experimental results will be presented. We follow the model in the form presented by P. Bruno and C. Chappert ([Bru91], [Bru95], [Bru99]).

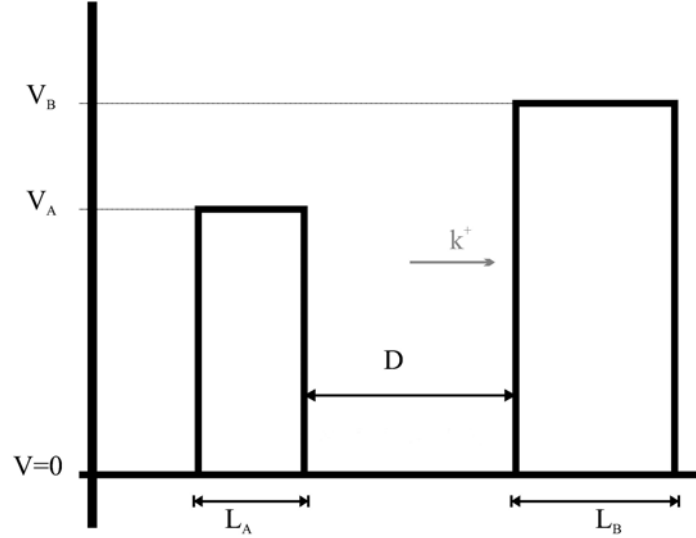


Figure 2.5: This sketch shows the introduced variables.

Elementary Discussion on Quantum Confinement

We will start with a one-dimensional quantum well as presented in Fig. 2.5. The quantum well represents the spacer layer with potential $V = 0$ and thickness D , sandwiched between two barriers A and B of width L_A and L_B and potentials V_A and V_B , respectively. V_A and V_B might be positive or negative, the barriers can be of infinite widths.

An electron reflected on both barriers with wave vector k^+ to the right and k^- to the left has a phase shift after one full cycle including a reflection on barrier A and barrier B of

$$\Delta\phi = qD + \phi_A + \phi_B . \quad (2.25)$$

Here q presents the difference of the wavevectors $k^+ - k^-$ and ϕ_A and ϕ_B the phase shift when reflected on barrier A and B, respectively. Of course, in the one-dimensional case we have $k^- = -k^+$.

To yield constructive interference the following condition has to be fulfilled:

$$\Delta\phi = 2m\pi \quad (2.26)$$

Here m is an integer.

Thus the modification of the density of states in the spacer layer, $\Delta n(\epsilon)$, varies with D like

$$\cos(qD + \phi_A + \phi_B) . \quad (2.27)$$

The variation in the density of states $\Delta n(\epsilon)$ will be proportional to the amplitude of the reflections on the barriers A and B, i.e., to $|r_A r_B|$, to the width D of the spacer and to the density of states per unit energy and unit width, including a factor of 2 for spin degeneracy.

$$\frac{2}{\pi} \frac{dq}{d\epsilon} \quad (2.28)$$

Considering an infinite number of round trips and gathering all the terms, we get:

$$\begin{aligned} \Delta n(\epsilon) &\approx \frac{2D}{\pi} \frac{dq}{d\epsilon} \sum_{m=1}^{\infty} |r_A r_B|^m \cos m(qD + \phi_A + \phi_B) \\ &= \frac{2}{\pi} \Im \left(i \frac{dq}{d\epsilon} \frac{r_A r_B e^{iqD}}{1 - r_A r_B e^{iqD}} \right) \end{aligned} \quad (2.29)$$

It is more convenient to consider the integrated density of states:

$$N(\epsilon) \equiv \int_{-\infty}^{\epsilon} n(\epsilon') d\epsilon' \quad (2.30)$$

The modification $\Delta N(\epsilon)$ of the integrated density of states due to electron confinement is

$$\Delta N(\epsilon) = -\frac{2}{\pi} \Im (\ln (1 - r_A r_B e^{iqD})) . \quad (2.31)$$

We have to state that the period of the oscillation does not depend on the confinement strengths $|r_A r_B|$, but only on the wave vector $q \equiv k^+ - k^-$, namely $\Lambda = 2\pi/q$.

With this confinement an energy difference ΔE is associated. In order to conserve the total number of electrons, it is convenient to consider the thermodynamic grand-potential, which is given by:

$$\begin{aligned}
\Phi &\equiv -k_B T \int_{-\infty}^{+\infty} \ln \left[1 + \exp \left(\frac{\epsilon_F - \epsilon}{k_B T} \right) \right] n(\epsilon) d\epsilon \\
&= - \int_{-\infty}^{+\infty} N(\epsilon) f(\epsilon) d\epsilon
\end{aligned} \tag{2.32}$$

The energy ΔE associated with the interferences is the contribution to Φ corresponding to $\Delta N(\epsilon)$.

$$\Delta E = \frac{2}{\pi} \Im \left(\int_{-\infty}^{+\infty} \ln (1 - r_A r_B e^{iqD}) f(\epsilon) d\epsilon \right) \tag{2.33}$$

For the three-dimensional case we yield

$$\Delta N(\epsilon) = -\frac{1}{2\pi^3} \Im \left(\int d^2 \mathbf{k}_{\parallel} \ln (1 - r_A r_B e^{iq_{\perp} D}) \right) \tag{2.34}$$

and

$$\Delta E = \frac{1}{2\pi^3} \Im \left(\int d^2 \mathbf{k}_{\parallel} \int_{-\infty}^{+\infty} \ln (1 - r_A r_B e^{iq_{\perp} D}) f(\epsilon) d\epsilon \right). \tag{2.35}$$

Interlayer Exchange Coupling Due to Quantum Interference

For a paramagnetic layer sandwiched between two ferromagnetic layers A and B the coefficients of reflection on both sides of the paramagnetic layer are spin dependent. *A priori*, the angle $\Delta\theta$ between the magnetization of the two ferromagnetic layers can take any value. Here we will concentrate on the case of parallel ($\Delta\theta = 0$) and antiparallel ($\Delta\theta = \pi$) alignment of the magnetization.

Let us define the spin asymmetry as follows:

$$\Delta r \equiv \frac{r^{\uparrow} - r^{\downarrow}}{2} \tag{2.36}$$

For the ferromagnetic configuration, the energy per unit area due to quantum interference is obtained from Eq. (2.35).

$$\begin{aligned} \Delta E_F &= \frac{1}{4\pi^3} \Im \left(\int d^2 k_{\parallel} \int_{-\infty}^{+\infty} \left[\ln \left(1 - r_A^{\uparrow} r_B^{\uparrow} e^{iq_{\perp} D} \right) \right. \right. \\ &\quad \left. \left. + \ln \left(1 - r_A^{\downarrow} r_B^{\downarrow} e^{iq_{\perp} D} \right) \right] f(\epsilon) d\epsilon \right) \end{aligned} \quad (2.37)$$

For the antiferromagnetic configuration the energy difference becomes:

$$\begin{aligned} \Delta E_{AF} &= \frac{1}{4\pi^3} \Im \left(\int d^2 k_{\parallel} \int_{-\infty}^{+\infty} \left[\ln \left(1 - r_A^{\uparrow} r_B^{\downarrow} e^{iq_{\perp} D} \right) \right. \right. \\ &\quad \left. \left. + \ln \left(1 - r_A^{\downarrow} r_B^{\uparrow} e^{iq_{\perp} D} \right) \right] f(\epsilon) d\epsilon \right) \end{aligned} \quad (2.38)$$

Then the energy difference for parallel and antiparallel alignment can be simplified in the limit of weak confinement to:

$$E_F - E_{AF} \approx -\frac{1}{\pi^3} \Im \left(\int d^2 \mathbf{k}_{\parallel} \int_{-\infty}^{+\infty} f(\epsilon) \Delta r_A \Delta r_B e^{iq_{\perp} D} d\epsilon \right) \quad (2.39)$$

The physical interpretation of this expression for the interlayer exchange coupling can be understood quite easily. The integration over the first two-dimensional Brillouin zone and over all energies up to the Fermi level shows that the coupling is summed up over all occupied energy states. The contributions of single states of energy ϵ and wave vector \mathbf{k}_{\parallel} in the layer plane consist of a product with three factors: The two factors Δr_A and Δr_B depict the spin asymmetry of the confinement due to the magnetic layers A and B. The exponential factor $e^{iq_{\perp} D}$ describes the propagation through the spacer and is responsible for the interference effect. This approach confirms the direct link of interlayer exchange coupling and quantum size effects as observed in photoemission.

In the limit of large spacer thickness D , the exponential factor oscillates rapidly, which leads to some cancelation of the contributions to the interlayer exchange coupling due to the different electronic states. However, because the integration over energy is abruptly stopped at the Fermi energy, states located at the Fermi level give predominant contributions. Furthermore only wave vectors neighboring critical vectors $\mathbf{k}_{\parallel}^{\alpha}$ where q_{\perp}^{α} is stationary contribute to the coupling.

Considering this when calculating the integrals the coupling constant J can be expressed as

$$J(D) = \Im \left(\sum_{\alpha} \frac{\hbar v_{\perp}^{\alpha} \kappa_{\alpha}}{4\pi^2 D^2} \Delta r_A^{\alpha} \Delta r_B^{\alpha} e^{iq_{\perp}^{\alpha} D} \cdot F \left(\frac{2\pi k_B T D}{\hbar v_{\perp}^{\alpha}} \right) \right), \quad (2.40)$$

where

$$F(x) \equiv \frac{x}{\sinh x} \quad (2.41)$$

and

$$\kappa_{\alpha} \equiv (\kappa_x^{\alpha})^{1/2} (\kappa_y^{\alpha})^{1/2}. \quad (2.42)$$

Here q_{\perp}^{α} , v_{\perp}^{α} , Δr_A^{α} and Δr_B^{α} refer to the critical vectors $\mathbf{k}_{\parallel}^{\alpha}$. κ_x^{α} and κ_y^{α} are combinations of the curvature radii of the Fermi surface at $(k_{\parallel}^{\alpha}, k_{\perp}^{+\alpha})$ and $(k_{\parallel}^{\alpha}, k_{\perp}^{-\alpha})$. The velocity v_{\perp}^{α} is a combination of the group velocities at the extremities $k_{\perp Fermi}^{+}$ and $k_{\perp Fermi}^{-}$.

This analysis shows that the only remaining terms in the limit of large spacer thicknesses D arise from the neighborhood of states having in-plane wavevectors $\mathbf{k}_{\parallel}^{\alpha}$ such that the spanning vector of the Fermi surface $q_{\perp Fermi} = k_{\perp Fermi}^{+} - k_{\perp Fermi}^{-}$ is stationary with respect to \mathbf{k}_{\parallel} for $\mathbf{k}_{\parallel} = \mathbf{k}_{\parallel}^{\alpha}$. The corresponding contribution oscillates with a wavevector equal to $q_{\perp Fermi}^{\alpha}$.

This selection rule was first derived in the context of the RKKY model [Bru91]. Depending on the crystallographic direction there might be more than one such stationary vector at the Fermi surface.

The above selection rule allows to predict the oscillation period of the inter-layer exchange coupling versus spacer thickness by just inspecting the bulk Fermi surface of the spacer material. Fig. 2.6 demonstrates this for the Fermi surface of copper. For the (111) direction a long period, for the (001) direction a long and a short and for the (110) direction four different periods are predicted.

For copper (111) in the system $Co/Cu/Co$ this results in a period of 4.5 monolayers. For a distance of 0.208 nm for neighboring lattice planes this gives a period of 0.936 nm. For copper (001) in the same system $Co/Cu/Co$ we yield a period of 2.6 and 5.9 atomic layers or 0.468 nm and 1.062 nm.

Within the framework of this model it can also be shown that the inter-layer exchange coupling oscillates as a function of the thickness of the ferromagnetic layers and furthermore depends on consecutive layers [Bru99].

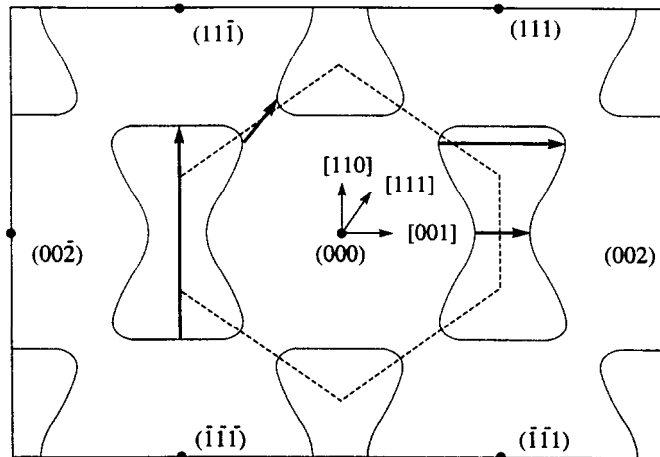


Figure 2.6: Cross section of the Fermi surface of Cu along the $(1\bar{1}0)$ plane. The solid dots indicate the reciprocal lattice vectors, the dashed lines indicate the boundary of the first Brillouin zone. The solid arrows indicate the vectors q_{\perp}^{α} giving the oscillation period(s). The selected cross section shows for the (100) -direction only one of the three critical vectors [Bru99].

2.4.4 Survey of the Models to IEC

All models predict basically the same relationship of the coupling constant J and the interlayer thickness t for thick spacer layers [Sti99]:

$$J(t) = \sum_{\alpha} \frac{J^{\alpha}}{t^2} \sin(q_{\perp}^{\alpha} t + \phi^{\alpha}) \quad (2.43)$$

There are several critical values indexed by α : The *spanning*-vector q_{\perp}^{α} , the coupling strength J^{α} and the phase ϕ^{α} , which all contribute to the coupling.

The period of the oscillation can be calculated by the given critical *spanning*-vectors in the Fermi surface belonging to the spacer layer:

$$\Lambda^{\alpha} = \frac{2\pi}{q_{\perp}^{\alpha}} \quad (2.44)$$

Notice that the calculated coupling strength depends on the model.

M. D. Stiles points out the difficulties in comparing experimental data to the given models [Sti99]. On the one hand it is not possible for experimentally realized samples to satisfy the idealized assumptions of the models, on the other hand it is hard to build up models which take into account all

experimental restrictions. For example the layer borders are not sufficiently perfect for modeling. Other disorders might be theoretically treatable but the experimental data are not available.

Another problem is the determination of the coupling strength from experimental data, as it cannot be measured directly. Usually some kind of model is used to simulate a measured characteristic of the system. Then the parameters, including the coupling strength, are varied to fit the experimental data. Unless all energy contributions of an appropriate model are considered correctly this method will not lead to meaningful results.

If magnetization reversal is included in the model, magnetic moments have to be determined. For a first approximation the saturation magnetization of the bulk material and the full thickness of the magnetic layers are used although there might exist magnetically dead atomic layers due to roughness and interdiffusion at the interfaces.

2.4.5 Application as Fitting Equation

When equation (2.43) is used to fit experimental results it is quite useful to reduce it to one spanning vector as far as there is no obvious sign for more than one coupling period.

As the spacer layer will not be perfect in experiments spin independent scattering also has to be considered when measured data are fitted [Spe93]. Therefore a factor of exponential decay is added with the spacer layer thickness t and a phenomenological decay length λ_0 .

$$J(t) = \frac{J_0}{t^2} \sin(q_{\perp}t + \phi) \cdot e^{-\frac{t}{\lambda_0}} = \frac{J_0}{t^2} \sin\left(\frac{2\pi}{\Lambda}t + \phi\right) \cdot e^{-\frac{t}{\lambda_0}} \quad (2.45)$$

2.5 Exchange Biasing

To get one-valued answers of a sensor it is desirable to pin the magnetic moment of one of the ferromagnetic layers to a fixed direction. This is commonly done by an (artificial) antiferromagnet, exploiting the phenomenon of exchange biasing. For γ defined as the angle between the pinning direction and θ being the direction of the magnetization with reference to the x-axis, the associated energy contribution is given by:

$$\frac{E_{pinning}}{A} = -J_{af} \cos(\gamma - \theta), \quad (2.46)$$

Here J_{af} is assumed to be positive for ferromagnetic and negative for anti-ferromagnetic coupling.

Essentially the exchange bias shows a spacial fluctuation due to interface roughness between antiferromagnet and adjacent ferromagnet. This results additionally to the pinning in a significant increase in the anisotropy of the ferromagnetic layer. For details see e.g. [Bay99].

2.6 Orange Peel Coupling

The roughness of the interface between two layers induces a so called “orange peel coupling” which leads to another energy contribution [Née62]:

$$\frac{E_{OP}}{A} = -J_{op} \cos(\theta_2 - \theta_1) \quad (2.47)$$

Here we will use a model introduced by J. C. S. Kools and W. Kula [Koo99] for stacks with columnar structure. They extended the original Néel Model also considering the finite thickness of the magnetic layers. Following their reasoning two cases have to be distinguished as illustrated in Fig. 2.7.

Model A

When the stack starts with the ferromagnetic layer the lower surface of this layer can be regarded as being flat so that no magnetic poles occur (Fig. 2.7A). If the waviness of the consecutive spacer (S) and ferromagnetic (FM2) layer does not increase, J_{op} is given by Eq. (2.48).

$$J_{op} = \mu_0 M_{sat,1} \cdot M_{sat,2} \cdot \pi^2 \frac{H_{OP}^2}{\sqrt{2}L_{OP}} \cdot \left(1 - e^{\frac{-2\pi\sqrt{2}t_2}{L_{OP}}}\right) \cdot e^{\frac{-2\pi\sqrt{2}t_s}{L_{OP}}} \quad (2.48)$$

Here the amplitude of the waviness is determined by H_{OP} , its wavelength by L_{OP} .

Model B

On the other hand, if the stack starts with an antiferromagnet or any other nonmagnetic buffer (Fig. 2.7B) the waviness on the lower surface of the first ferromagnetic layer (FM1) has to be included in the calculation of J_{op} , resulting in equation 2.49.

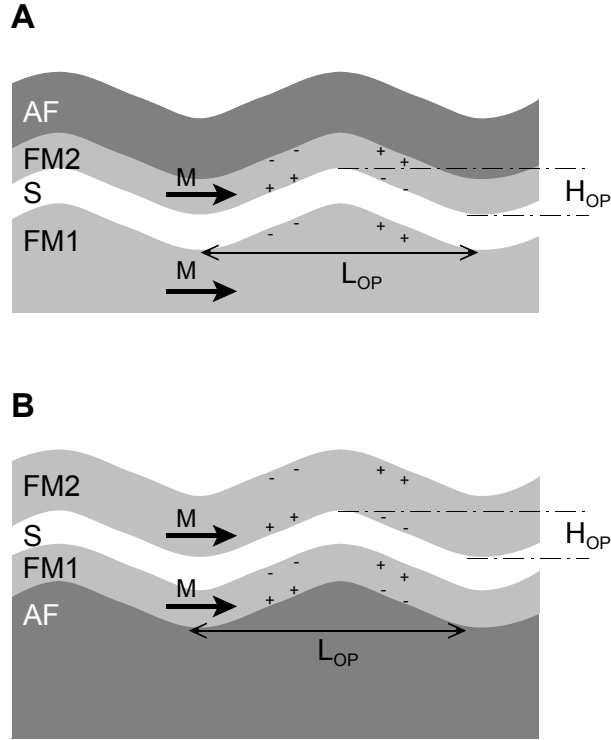


Figure 2.7: Schematic of the magnetostatic interaction. In A the stack starts with a ferromagnetic layer, in B an antiferromagnetic or nonmagnetic buffer layer is included.

$$J_{op} = \mu_0 M_{sat,1} \cdot M_{sat,2} \cdot \pi^2 \frac{H_{OP}^2}{\sqrt{2}L_{OP}} \cdot \left(1 - e^{-\frac{-2\pi\sqrt{2}t_1}{L_{OP}}}\right) \cdot \left(1 - e^{-\frac{-2\pi\sqrt{2}t_2}{L_{OP}}}\right) \cdot e^{-\frac{-2\pi\sqrt{2}t_s}{L_{OP}}} \quad (2.49)$$

2.7 Calculation of GMR(H) and M(H)

In the preceding sections we saw what the GMR-effect is and which are the most important factors for the magnetization process in multilayer stacks. In this section it will be shown how to calculate the GMR(H)-characteristic and the magnetization loop when the angles of magnetization as a function of the external field $\theta_i(H)$ for each single layer and the GMR-amplitude g is already known. This is to prepare the simulation routine given in chapter 4.

2.7.1 Standard Model for GMR-Calculation

H. Holloway and D. J. Kubinski introduced an AF-order-parameter $AF(H)$ to GMR multilayer stacks[Hol98].

$$AF(H) = \frac{1}{2} [1 - \cos(\theta_{II}(H) - \theta_I(H))] \quad (2.50)$$

Here $\theta_I(H)$ and $\theta_{II}(H)$ are the angles of magnetization for the two adjacent ferromagnetic layers on both sides of the spacer layer with reference to a fixed axis.

When the GMR effect amplitude is denoted as g the characteristic follows to ([Hol98] and [Sch00b]):

$$\frac{\Delta R(H)}{R_{\uparrow\uparrow}} = g \cdot AF(H) = g \cdot \frac{1}{2} [1 - \cos(\theta_{II}(H) - \theta_I(H))] \quad (2.51)$$

2.7.2 Enhanced Model for GMR-Calculation

An enhanced model to calculate the GMR effect is presented by W. Schepper [Sch00b]. In this model the conductivity of the magnetic layer is divided in a fixed contribution and a second contribution depending on the magnetization of the adjacent ferromagnetic layer. Every pair of coupled magnetic layers is dealt with separately. Furthermore this model explicitly accounts for the conductivity of the nonmagnetic layers. See Fig. 2.8 for a graphical representation.

Given a stack of width w and length l , the resistance of the nonmagnetic layers R_n of conductivity σ_n and (not necessarily identical) thickness t_i can be calculated to:

$$\frac{1}{R_n} = \frac{w}{l} \sigma_n \sum_{i=1}^{N-1} t_i \quad (2.52)$$

The conductivity σ_i of the magnetic sheets contains two parts: a constant one σ_m and another depending on the differences of the magnetization directions of adjacent layers $\Delta\alpha_i = \alpha_{i+1} - \alpha_i$. The angle dependence $\cos^2(\Delta\alpha_i/2)$ corresponds to the AF-order parameter of Eq. (2.50).

$$\sigma_i = \sigma_m \left(1 + g_i \cos^2 \frac{\Delta\alpha_i}{2} \right) \quad (2.53)$$

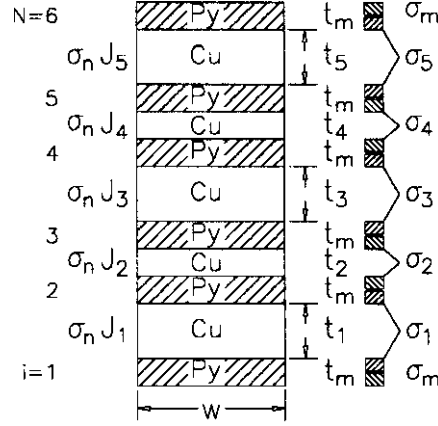


Figure 2.8: The simplest mixed multilayer, layer thickness t , and conductivity σ , (t_i , σ_n) in the nonmagnetic and (t_m , σ_i) in the magnetic layers (from [Sch00b]).

The factor g_i accounts for the amplitude of the conductivity variation as a function of the magnetization directions.

When calculating the resistance of the magnetic layers R_m we have to account for the lower part of the first ferromagnetic layer and the upper part of the last ferromagnetic layer, which are not influenced by adjacent layers, separately.

$$\begin{aligned}
 \frac{1}{R_m} &= \frac{w}{l} \left[2 \frac{t_m}{2} \sigma_m + t_m \sum_{i=1}^{N-1} \sigma_i \right] \\
 &= \frac{w t_m}{l} \left[\sigma_m + \sum_{i=1}^{N-1} \sigma_i \right] \\
 &= \frac{w t_m}{l} \left[\sigma_m + \sum_{i=1}^{N-1} \sigma_m \left(1 + g_i \cos^2 \frac{\Delta \alpha_i}{2} \right) \right]
 \end{aligned} \tag{2.54}$$

Adding Eq. (2.52) and Eq. (2.54) we get for the resistance as function of the relative angles of magnetization $\Delta \alpha_i$:

$$\frac{1}{R}(\Delta \alpha_i) = \frac{w}{l} \left[\sigma_n \sum_{i=1}^{N-1} t_i + t_m \sigma_m + t_m \sum_{i=1}^{N-1} \sigma_m \left(1 + g_i \cos^2 \frac{\Delta \alpha_i}{2} \right) \right] \tag{2.55}$$

For saturation magnetization H_{sat} $\Delta \alpha_i$ becomes 0 for all i . From Eq. (2.55) we can deduce:

$$\frac{1}{R_0} \equiv \frac{1}{R}(\Delta\alpha_i = 0) = \frac{w}{l} \left[\sigma_n \sum_{i=1}^{N-1} t_i + t_m \sigma_m + t_m \sum_{i=1}^{N-1} \sigma_m (1 + g_i) \right] \quad (2.56)$$

The GMR effect amplitude for a given configuration $\Delta\alpha_i$ can be calculated from (2.55) and (2.56) to:

$$\begin{aligned} \frac{\Delta R(H)}{R_0} &= \frac{R(H) - R_0}{R_0} = \frac{R(\Delta\alpha_i) - R_0}{R_0} = \frac{R(\Delta\alpha_i)}{R_0} - 1 \\ &= \frac{\sigma_n \sum_{i=1}^{N-1} t_i + t_m \sigma_m + t_m \sum_{i=1}^{N-1} \sigma_m (1 + g_i)}{\sigma_n \sum_{i=1}^{N-1} t_i + t_m \sigma_m + t_m \sum_{i=1}^{N-1} \sigma_m (1 + g_i \cos^2 \frac{\Delta\alpha_i}{2})} - 1 \end{aligned} \quad (2.57)$$

Let us now apply this model to a top spin valve with a bottom magnetic layer with a thickness t_I , conductivity σ_I , and angle of magnetization θ_I , a top magnetic layer of thickness t_{II} , conductivity σ_{II} , and angle of magnetization θ_{II} . The quantities t_s , σ_s and t_p , σ_p refer to the thickness and conductivity of the spacer and pinning layer, respectively.

The factor g_1 accounts for the amplitude of the conductivity variation as a function of the magnetization directions for the two ferromagnetic layers.

Eq. 2.52 has to be reduced to one spacer layer and the pinning layer has to be added.

$$\frac{1}{R_n} = \frac{w}{l} [\sigma_s t_s + \sigma_p t_p] \quad (2.58)$$

For Eq. 2.54 we get

$$\frac{1}{R_m} = \frac{w}{l} \left[(t_I \sigma_I + t_{II} \sigma_{II}) \left(1 + g_i \cos^2 \frac{\Delta\alpha_i}{2} \right) \right] \quad (2.59)$$

With these two equations $\Delta R(H)/R_0$ becomes:

$$\frac{\Delta R(H)}{R_0} = \frac{t_s \sigma_s + t_p \sigma_p + (t_I \sigma_I + t_{II} \sigma_{II})(1 + g_1)}{t_s \sigma_s + t_p \sigma_p + (t_I \sigma_I + t_{II} \sigma_{II}) (1 + g_1 \cos^2 \frac{\Delta\alpha_i}{2})} - 1 \quad (2.60)$$

Defining g as

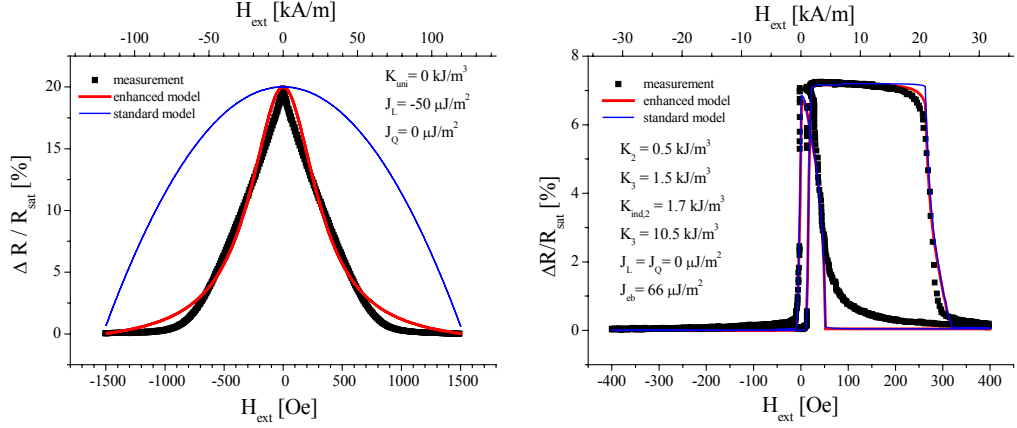


Figure 2.9: Comparison of the two models to calculate the GMR characteristics. Simulation of different systems multilayer (left) and unpinned trilayer (right) with identical sets of parameters.

$$g = \frac{t_I \sigma_I + t_{II} \sigma_{II}}{t_s \sigma_s + t_p \sigma_p + t_I \sigma_I + t_{II} \sigma_{II}} \cdot g_1 \quad (2.61)$$

we yield for the GMR characteristic

$$\frac{\Delta R(H)}{R_{\uparrow\uparrow}} = \frac{1 + g}{1 + g \cdot \cos^2 \frac{\theta_{II}(H) - \theta_I(H)}{2}} - 1 = \frac{g}{2} \cdot \frac{1 - \cos(\theta_{II}(H) - \theta_I(H))}{1 + g \cdot \cos^2 \frac{\theta_{II}(H) - \theta_I(H)}{2}}. \quad (2.62)$$

The standard model chooses a global approach for the correlation of magnetization and GMR, whereas the presented enhanced model describes this correlation as a phenomenon depending only on the magnetization of two adjacent layers (“local approach”).

The experiment has to decide, which model is more suitable to describe measured characteristics. In principal both models can be used to fit experimental data but the resulting set of parameter might differ considerably. This is demonstrated in Fig. 2.9, where the resulting parameter set for the enhanced model is directly fed into the standard model.

The advantages of the enhanced model become more obvious when a whole series of characteristics is calculated systematically and compared to measurements. See chapter 4 for details.

2.7.3 Calculation of Magnetization Loop

The magnetization loop is given by [Sch00a]:

$$M(H) = \frac{1}{t_I + t_{II}} (M_{sat,I} \cdot t_I \cdot \cos \theta_I(H) + M_{sat,II} \cdot t_{II} \cdot \cos \theta_{II}(H)) \quad (2.63)$$

The equations (2.51), (2.62) and (2.63) have to be adjusted to the layer system in question. See section 4.1 for details.

2.8 Phenomenological Law for Magnetization Loops of Trilayers

In 1994 M. B. Stearns and Y. Cheng applied an phenomenological law to fit magnetization curves of granular GMR systems [Ste94]. Here I will confine myself on the ferromagnetic part of their equation.

$$M(H) = \frac{2 M_{sat}}{\pi} \operatorname{atan} \left[\frac{H \pm H_C}{H_C} \left(\frac{\pi S}{2} \right) \right] \quad (2.64)$$

M_{sat} is the saturation magnetization, H_C the coercivity field, and S the squareness of the magnetization loop, i.e., the ratio of the remanent magnetization, M_r , to M_{sat} . For decreasing fields the magnetization switches after zero field, thus for H being negative. In this case the '+'-sign has to be used. For increasing fields the '-'-sign is relevant.

For simplicity I will restrict myself on normalized data ($M_{sat} \equiv 1$) and introduce a parameter P .

$$P = \frac{H_C}{\tan \left(\frac{\pi S}{2} \right)}. \quad (2.65)$$

Now Eq. (2.64) becomes

$$M(H)_{norm} = \frac{2}{\pi} \operatorname{atan} \left[\frac{H \pm H_C}{P} \right]. \quad (2.66)$$

To apply this law to the case of magnetic trilayers further extensions are necessary. In the magnetization loop we have to allow for the contribution

of the free and pinned layer (bottom and top layer for unpinned system) separately. Their relative magnetization may be denoted as A_{free} and A_{pinned}

The switching points of the pinned layer are not only shifted by $H_{C,pinned}$ due to its anisotropy, but also by $H_{e.b.}$ due to the exchange bias. Therefore we have to introduce a general shifting field $H_{shift,pinned} = H_{e.b.} \pm H_{C,pinned}$. The two parameters can be separated when the data for increasing and decreasing field are fitted.

A similar reasoning holds for the free layer. Here the switching point is not only shifted by $H_{C,free}$ due to its anisotropy, but also by $H_{i.e.c.}$ due to the interlayer exchange coupling. Here we have to introduce a general shifting field $H_{shift,free} = H_{i.e.c.} \pm H_{C,free}$. The sign of $H_{i.e.c.}$ will change according to the interlayer exchange coupling being ferromagnetic or antiferromagnetic.

Doing so I assume the interlayer exchange coupling being of negligible influence on the magnetization behavior of the pinned layer due to an effective exchange bias and a high coercivity.

Including this in Eq. (2.66) we yield:

$$\begin{aligned}
 M(H)_{norm} &= \frac{2 A_{free}}{\pi} \operatorname{atan} \left(\frac{H - H_{shift,free}}{P_{free}} \right) \\
 &+ \frac{2 A_{pinned}}{\pi} \operatorname{atan} \left(\frac{H - H_{shift,pinned}}{P_{pinned}} \right)
 \end{aligned} \tag{2.67}$$

The two addends allow for separating the contribution of free and pinned layer. The obtained parameters can be used to calculate the GMR characteristic by means of the standard GMR model as presented in section 2.7.

$$\begin{aligned}
 \frac{R(H)}{R_{\uparrow\uparrow}} &= g \cdot \frac{1}{2} \left[1 + \cos \left(\operatorname{atan} \left(\frac{H - H_{shift,free}}{P_{free}} \right) \right. \right. \\
 &\left. \left. + \operatorname{atan} \left(\frac{H - H_{shift,pinned}}{P_{pinned}} \right) \right) \right]
 \end{aligned} \tag{2.68}$$

Here g denotes the amplitude which is taken directly from the measurement.

Chapter 3

Experiments and Discussion on Interlayer Coupled and Pinned Magnetic Trilayers

3.1 Introduction

The GMR amplitude of a given spin valve structure strongly depends on the thickness t_{NM} of the nonmagnetic spacer layer. The GMR amplitude can be expressed phenomenologically as [Die94]:

$$\frac{\Delta R}{R}(t_{NM}) = \left(\frac{\Delta R}{R}\right)_0 \cdot \frac{\exp\left(-\frac{t_{NM}}{l_{NM}}\right)}{1 + \frac{t_{NM}}{t_0}} \quad (3.1)$$

Here, l_{NM} is related to the mean-free path of the conduction electrons in the spacer layer, t_0 is an effective thickness representing the shunting of the current in the remaining structure, and $(\Delta R/R)_0$ is a normalization coefficient that depends on the combination of the materials. Consequently, the largest MR amplitudes are obtained for spacer layers as thin as possible.

Since the pioneering work of Th. G. S. Rijks *et al.* [Rij94] and B. Dieny *et al.* [Die91b] it is generally believed that there is a critical interlayer thickness about 2 nm, below which no perfect antiparallel alignment of the magnetization of a exchange biased spin valve can be realized. High ferromagnetic coupling, possibly caused by pinholes or orange peel coupling [Koo99], results in a parallel alignment of the pinned and free layer regardless of the external field.

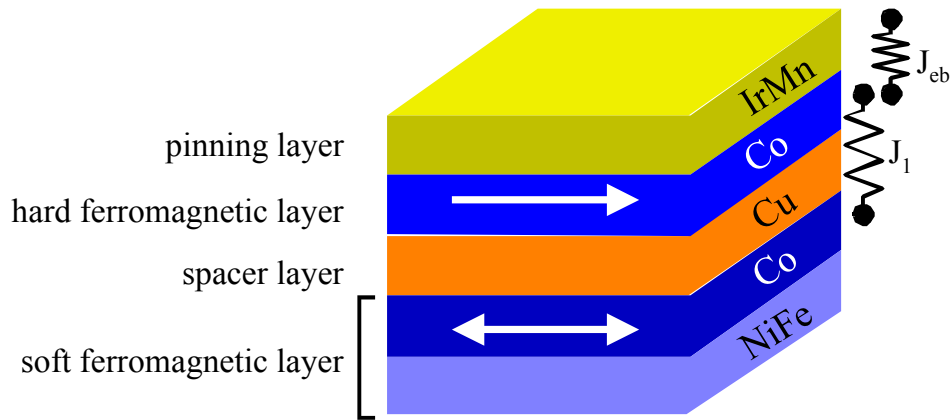


Figure 3.1: Coupled and pinned trilayer. All relevant aspects are displayed: Hard and soft magnetic layer, exchange biasing (J_{eb}) and interlayer coupling (J_l).

For the first time S. Jo and M. Seigler [Jo02] demonstrated antiferromagnetically coupled spin valves which showed GMR for a sophisticated system of the type *underlayer/NiFe/CoFe/Cu/CoFe/Ru/CoFe/MnIr/overlayer*.

It is the objective of this study to demonstrate that in well grown trilayers of the type *NiFe–Co/Cu/Co/IrMn* the RKKY-like antiferromagnetic coupling is dominating the ferromagnetic coupling down to a spacer layer thickness of about 1 nm . For spacer layer thicknesses below 3.5 nm the MR amplitude shows the oscillatory behavior known from multilayers. This is related to the oscillating interlayer coupling, being ferromagnetic or antiferromagnetic depending on the value of t_{NM} . In section 3.7 these results will be presented in detail.

As already mentioned in chapter 2 the appearance of GMR requires a transition of an unordered state of magnetization to an ordered state when an external magnetic field is applied. These two different states for the magnetization can be achieved in the following ways:

Antiferromagnetic coupling: Using the correct thickness of the nonmagnetic spacer the adjacent magnetic layers are aligned antiparallel without an external field because of the interlayer exchange coupling. When an external field is applied, the magnetization starts rotating until a magnetization parallel to the external field is reached at the saturation magnetization H_{sat} . This is the main mechanism for multilayer GMR stacks. See section 2.4 in the previous chapter.

Pinning: Using an (artificial) antiferromagnet one of the magnetic layers is pinned. The free layer follows the external field and is therefore parallel or antiparallel oriented to the pinned layer. This is the basic idea of true spin valves. See section 2.5.

Materials of different coercivity: When the magnetic system consists of materials with different coercivities, one of the layers switches in the direction of the external field before the others will follow. The antiparallel alignment will not be reached at zero field but at the external field value, which belongs to the coercivity field of the soft magnetic material.

In a given stack usually a combination of those effects occurs with varying importance. The presented coupled and pinned trilayer system is one of the simplest thin film combination possible in which all of the mentioned aspects are significant. Therefore it is an ideal model system to examine the interaction of interlayer coupling and exchange biasing.

The selected combination of the immiscible material combination *Co* and *Cu* on a *Ni₈₀Fe₂₀*-buffer is highly favorable for this investigation as explained in section 2.2.3.

This chapter will start with the definition of the used parameters (section 3.2 and a short review on unpinned trilayer systems (section 3.3). Details of the latter have been reported in [Hem00].

Following the section 3.4 on sample preparation and characterization techniques the GMR and magnetization measurements will be presented and discussed: Before starting with the main subject of investigation, the variation of the spacer layer thickness (section 3.7) the ideal thickness of the magnetic layers has to be determined (section 3.6).

To get a deeper understanding of our extraordinary GMR-amplitudes and the oscillatory behavior of the interlayer coupling in the studied system the investigations continue with a structural analysis (section 3.8) and magnetic measurements (section 3.9) and their analysis.

This chapter will close with a comparison of pinned and unpinned trilayers (section 3.10) and a conclusion (section 3.11).

To get a further insight into the relevant physical parameters for the shape of the GMR-characteristics a specially developed simulation tool will be introduced and applied to the systems under investigation in the following chapter 4.

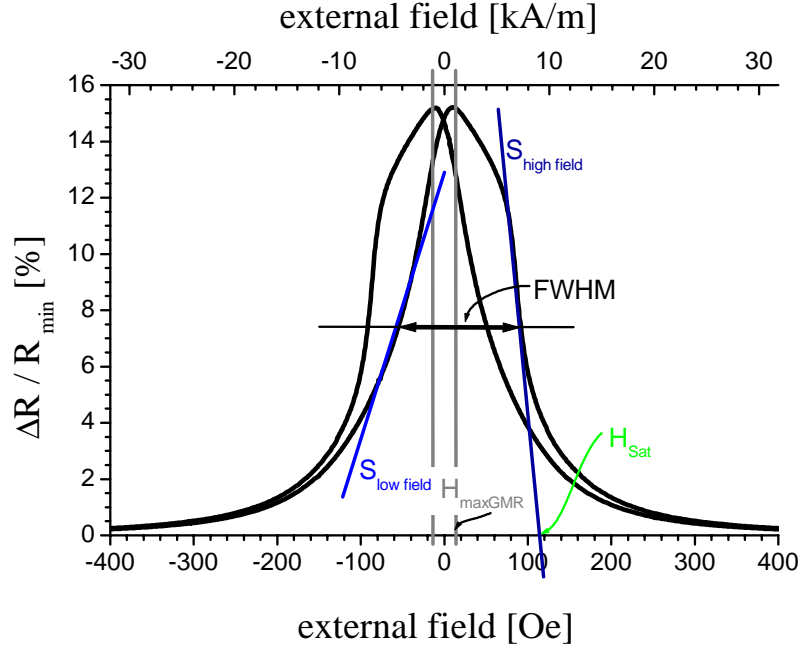


Figure 3.2: The figure shows the parameters as explained in the text. The plotted characteristic refers to a magnetic trilayer in the first antiferromagnetic coupling maximum.

3.2 Definition of Measurable Quantities

To give a meaningful interpretation of the measured data, suitable parameters have to be selected. Because of ambiguous parameter definition in literature, this section summarizes the parameters and their definition in the form they are used within this document.

The MR-characteristic is plotted according to the definition of $\frac{\Delta R(H)}{R_{\uparrow\uparrow}}$ in equation (2.1). It starts with the external field at high negative values, reaches the maximum field and returns to maximal negative field. When the virgin loop is included the field loop starts at zero.

The following parameters can be determined (see also Fig. 3.2):

GMR-effect g : The GMR-effect (or simply GMR) is defined as the maximum of the $R(H)$ -plot, divided by the minimal resistance measured. It is common practice to give this number as percentage.

Field at maximum H_{maxGMR} : As parameter for the hysteresis the value H_{maxGMR} is determined. It is half the difference of the field values

for which the $\frac{\Delta R(H)}{R_{\uparrow\uparrow}}$ -plot reaches its maximum during increasing and decreasing field.

Full width at half maximum FWHM: Here the widths of the GMR characteristic at half of the maximum GMR value is determined. For pinned layers this might be considerably different for increasing or decreasing magnetic field.

Crossover: The crossover marks the $\frac{R(H)}{R_{\uparrow\uparrow}}$ -value for which the graphs of back and forward loop cross each other.

Saturation field H_{sat} : The saturation field is the field value, at which all magnetic moments are aligned parallel to the external field and therefore the resistance keeps constant. From a technical point of view the long slowly decreasing tails due to the size distribution are of no interest. Therefore the saturation field is defined as follows: At half maximum the slope is plotted. The field value at which this slope meets the field-axis (x-axis) is defined as H_{sat} .

Sensitivity S : As sensitivity the slope at half maximum is defined. This value differs for inner and outer edge.

3.3 Review on Unpinned Trilayers

Before reporting on pinned trilayers I will give a short review of unpinned trilayers which have been prepared under comparable conditions. For details see [Hem00]. Here I will concentrate on the Cu layer dependence in the system $(Ni_{80}Fe_{20})_{2.8\text{ nm}} - Co_{2.6\text{ nm}}/Cu_t/Co_{2.9\text{ nm}}$ as presented in Fig. 3.3.

The first antiferromagnetic coupling maximum (AFCM) shows an effect of 15% at a spacer layer thickness of 1.3 nm, the second and third AFCM with 11% and 7% were found at a spacer layer thickness of 2.0 nm and 2.7 nm, respectively. The oscillation wavelength Λ is determined to 0.7 nm.

For a comparison of this system and the pinned and interlayer coupled systems see section 3.10.

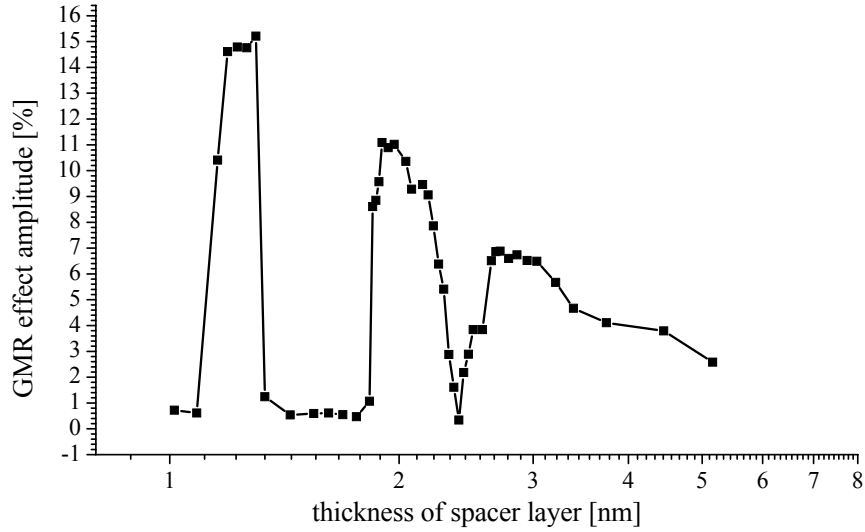


Figure 3.3: GMR amplitude as a function of the Cu layer thickness in the system $(Ni_{80}Fe_{20})_{2.8\text{ nm}} - Co_{2.6\text{ nm}} / Cu_t / Co_{2.9\text{ nm}}$.

3.4 Sample Preparation and Characterization Techniques

DC Magnetron Sputtering

All samples under investigation were prepared by DC magnetron sputtering in high vacuum computer automated Leybold sputter deposition system, Leybold L560 (Fig. 3.4). The targets had a distance of 110 mm to the substrate and could be closed by a rotating shutter during the presputtering time. The base pressure was hold below $7.0 \cdot 10^{-7} \text{ mbar}$, the argon pressure during the sputtering process was kept to $1.5 \cdot 10^{-3} \text{ mbar}$ for the metals and to $2.1 \cdot 10^{-3} \text{ mbar}$ for $IrMn$. The standard sputtering powers were set to 91W, 102W, 93W, and 105W for Cu , $Ni_{80}Fe_{20}$, Co , and $IrMn$, respectively, the temperature during deposition was about $30^\circ C$.

Series of spin valves $(Ni_{80}Fe_{20})_{t1} - Co_{t2} / Cu_x / Co_{t3} / IrMn_{t4}$ (target material $Ir_{83}Mn_{17}$) have been deposited onto thermally oxidized Si(100)-substrates. During the process an external magnetic field of 9.5 kA/m was applied to determine the in-plane direction of the exchange anisotropy of the biased Co layer by a magnetic mask (Fig. 3.5).

The role of the $NiFe$ layer is to provide a flat buffer to obtain smooth interfaces. The $NiFe$ layer combined with the next ferromagnetic layer forms an overall single soft magnetic layer. The second ferromagnetic layer on top of the structure is magnetically hard and pinned to the antiferromagnet.



Figure 3.4: Sputter device lab 560 from Leybold.

GMR prober

The magnetoresistance was measured at room temperature in a four-point probe geometry. The probe current, usually 1mA , was applied in the film plane along the DC magnetic field of up to 0.3T (CIP-geometry). Samples, which have been exposed to an external magnetic field during deposition, were aligned so that the probe current was parallel to the direction of this field. For further details see [Mro98].

The magnetoresistance values $\frac{\Delta R}{R_{sat}}$ are relative to the high-field resistance R_{sat} .

XRD

X-ray diffraction has been measured on a *Philips X'Pert PRO MPD* diffractometer of Type PW3050/60, having a vertical θ/θ configuration in Bragg-Bentano parafocusing geometry. For details see [Hei04]. The individual layer thickness has been determined on corresponding samples by S. Heitmann and S. Kämmerer.

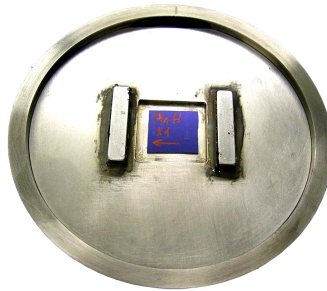


Figure 3.5: Magnetic mask to align the ferromagnet next to the antiferromagnetic IrMn-layer.

AFM

The roughness of selected samples has been analyzed by an atomic force microscopy (*digital instruments Nanoscope IIIa*). Measurements have been carried out by D. Meyners.

AGM

The magnetization characteristics have been measured by I. Ennen with a *MicroMag 2900* AGM. For details see [Sud00].

TEM

D. Sudfeld carried out the transmission electron microscopy of one sample of the trilayer series with a (HR)-TEM by *Philips CM 200 SuperTWIN* to analyze the grain size of the samples.

REM

E-beam lithography and examination of the structure were done with a *LEO* scanning electron microscope.

3.5 Typical Characteristic

The GMR characteristic of an interlayer coupled and pinned trilayer can be generally understood when looking at the switching points as marked in Fig. 3.6.

For high negative magnetic fields the magnetization of all layers is aligned parallel to each other and to the external field as depicted at point 1. Then at point 2 the free layer switches to the opposite direction. Due to hysteresis of the bottom layer this occurs for small positive fields when the interlayer coupling is neglected. This configuration keeps unchanged until point 3 is reached. Here the Zeeman energy becomes dominant and the magnetization of the pinned layer aligns parallel to the external field although this is not favorable with regard to exchange bias. At 4 the magnetization of all layers is aligned parallel to the positive external field. For decreasing field the magnetization keeps unchanged due to a high anisotropy of the top magnetic layer until point 5 where the upper layer switches because of the exchange bias.

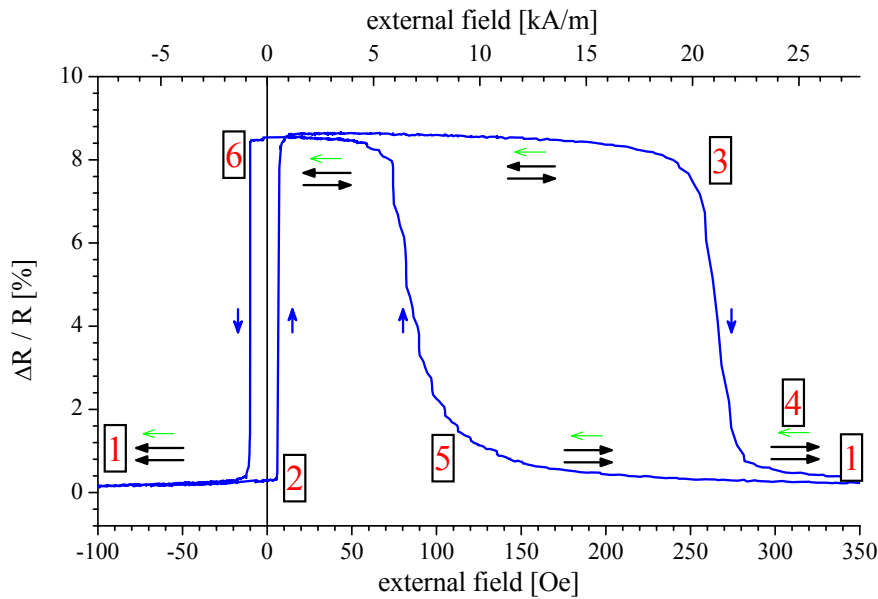


Figure 3.6: Plot for general understanding of the GMR characteristics. For the selected sample $(Ni_{80}Fe_{20})_{3.9\text{ nm}} - Co_{2.7\text{ nm}}/Cu_{2.0\text{ nm}}/Co_{2.7\text{ nm}}/IrMn_{9.0\text{ nm}}$ the switching points are well separated. The dark arrows give the direction of magnetization for the free (bottom) and pinned (top) layer, the small green arrow indicates the preferred direction of magnetization for the pinned layer due to the exchange bias.

At 6 the soft layer follows and the magnetization of all layers is again parallel to each other and to the negative external field.

The switching points 2 and 6 will be shifted to negative field values for antiferromagnetically coupled systems and to positive field values for ferromagnetically coupled systems. The switching points 3 and 5 are not symmetrically situated to zero field due to the exchange bias.

A deeper understanding of the magnetization process is provided by the magnetization measurements and their interpretation within a phenomenological model. See section 3.9.

3.6 Ideal Thickness of the Magnetic Layers

Before dealing with the main objective of this study, the variation of the spacer layer thickness, the ideal thickness for the magnetic layers has to be determined. Here “ideal” stands for an optimal GMR-amplitude and characteristics which could be measured with our GMR-prober with regard to resolution and necessary magnetic fields to yield saturation. Starting points for the experimental realization could be taken from the former studies on unpinned trilayers (see section 3.3).

Pinned Co-Layer

Fig. 3.7 and 3.8 show the GMR characteristics for different thicknesses $t_{Co,2}$ of the top *Co*-layer in the first and second antiferromagnetic coupling maximum (AFCM), respectively.

In the first AFCM there is a minimum thickness of more than 2.3 nm before the pinning of the top *Co*-layer has the desired effect on the magnetization process. For thicknesses above 3.5 nm the GMR effect vanishes due to the increasing shunting effect. Furthermore the Zeeman-energy becomes more and more relevant and the shift due to the pinning is reduced.

In Fig. 3.8 for the second AFCM we see that for layer thicknesses up to 1.5 nm the chosen field of 300 Oe at the measuring device was too small to switch the upper cobalt layer. But for this regime of layer thickness the quality of the film was not sufficient to yield high GMR values in agreement to former results [Hem00]. For *Co* layer thicknesses of more than 3 nm the increasing shunting reduces the GMR amplitude.

For both maxima the optimal thickness of the pinned *Co*-layer was chosen to about 2.8 nm .

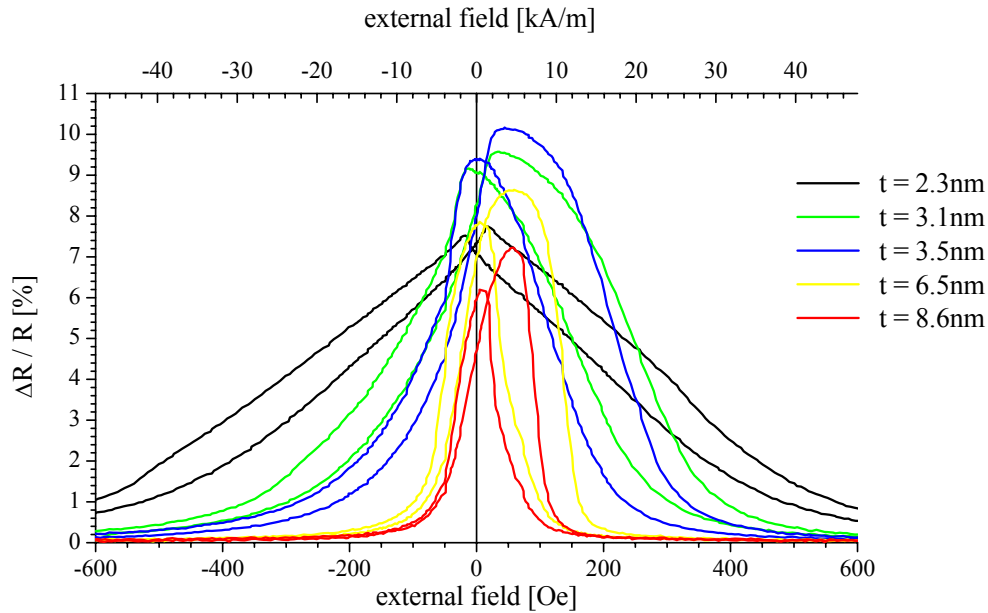


Figure 3.7: Variation of pinned Co -layer thickness for the system $(Ni_{80}Fe_{20})_{3.4\text{ nm}} - Co_{2.8\text{ nm}}/Cu_{1.0\text{ nm}}/Co_t/IrMn_{14\text{ nm}}$ in the first AFCM.

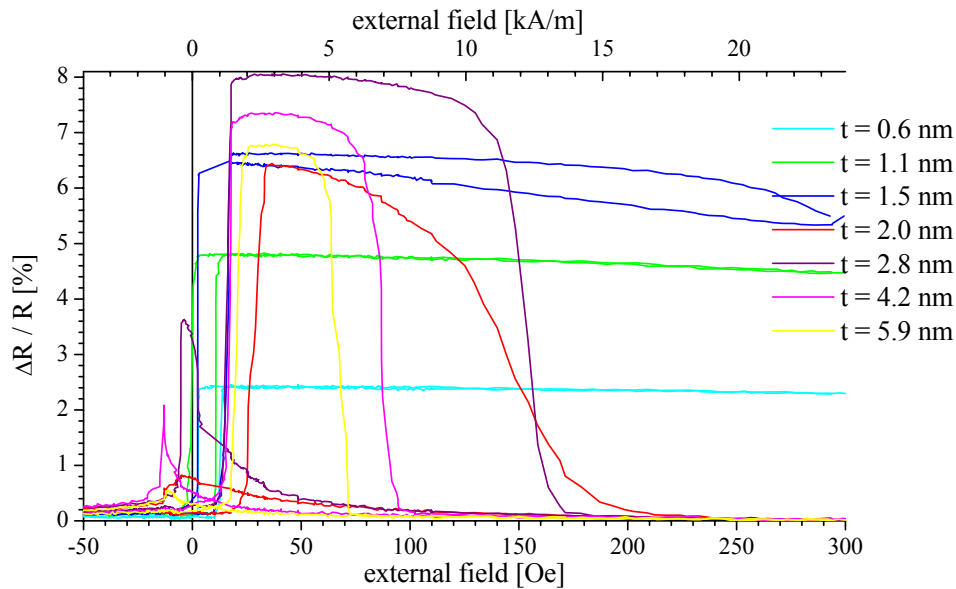


Figure 3.8: Variation of pinned Co -layer thickness for the system $(Ni_{80}Fe_{20})_{3.4\text{ nm}} - Co_{2.8\text{ nm}}/Cu_{2.2\text{ nm}}/Co_t/IrMn_{14\text{ nm}}$ in the second AFCM.

Free Co-Layer

An identical series as above was carried out for the free *Co*-layer for the first (Fig. 3.9) and second (Fig. 3.10) AFCM. In the first AFCM it is obvious that a minimum layer thickness of about 2.3 nm is necessary for the coupling to come along well. Of course, there might be a pronounced coupling maximum for smaller thicknesses of the *Co*-layer when the spacer layer thickness is adjusted correspondingly.

For the second AFCM there is an optimum layer thickness for the *Co*-layer with respect to the GMR amplitude as well.

Buffer Layer

The $Ni_{80}Fe_{20}$ buffer layer has two different functions in this stacking sequence. On the one hand $Ni_{80}Fe_{20}$ is known to care for smooth interfaces at the succeeding layers, on the other hand it is part of the free layer consisting of $Ni_{80}Fe_{20}$ and *Co* and making it magnetically softer than a pure *Co*-layer. $Ni_{80}Fe_{20}$ needs a thickness of about 3.4 nm to fulfill these functions as can be seen in Fig. 3.11. For too thick layers the GMR-amplitude decreases again because of the shunting effect.

Pinning Layer

As the interlayer coupling as the antagonist of the exchange bias is much stronger in the first AFCM the variation of the *IrMn*-layer thickness was done for a *Cu*-layer thickness of 1.0 nm . An optimum of GMR effect-amplitude and pinning was obtained for a thickness of about 9.0 nm . See Fig. 3.12 for details.

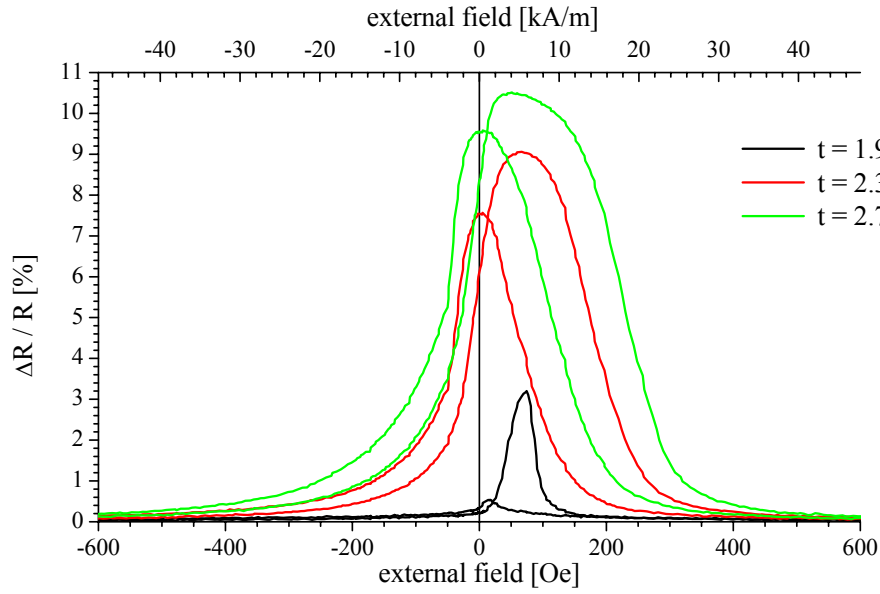


Figure 3.9: Variation of free *Co*-layer thickness for the system $(Ni_{80}Fe_{20})_{3.4\text{ nm}} - Co_t/Cu_{1.0\text{ nm}}/Co_{2.8\text{ nm}}/IrMn_{14\text{ nm}}$ in the first AFCM.

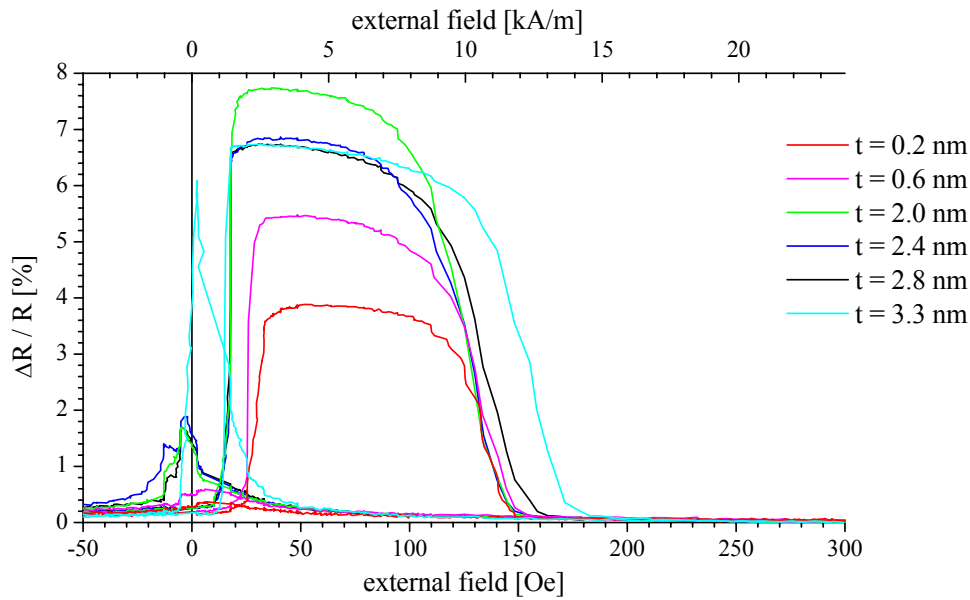


Figure 3.10: Variation of free *Co*-layer thickness for the system $(Ni_{80}Fe_{20})_{3.4\text{ nm}} - Co_t/Cu_{2.2\text{ nm}}/Co_{2.8\text{ nm}}/IrMn_{14\text{ nm}}$ in the second AFCM.

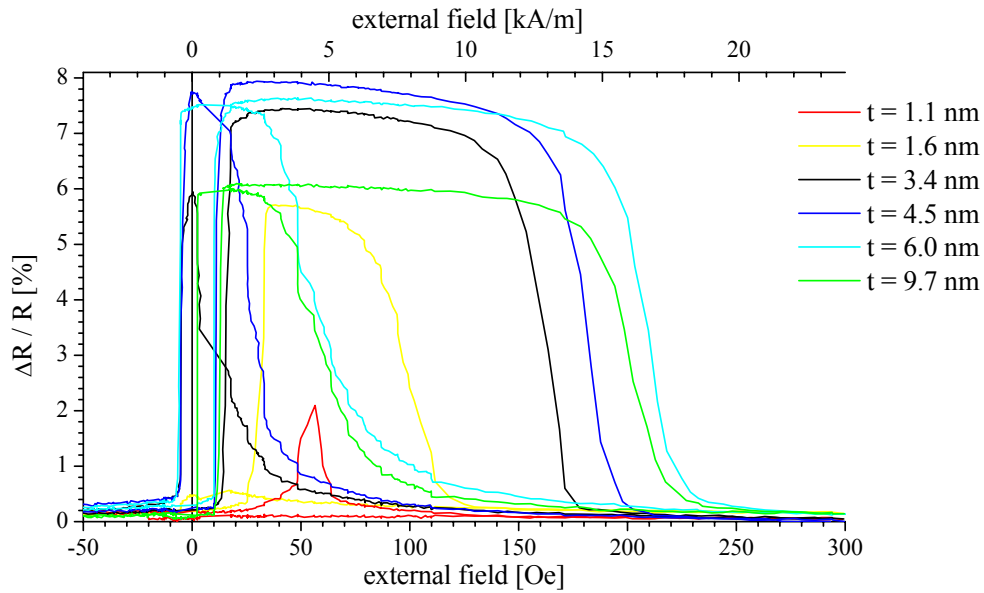


Figure 3.11: Variation of buffer layer thickness for the system $(Ni_{80}Fe_{20})_t - Co_{2.8\text{ nm}}/Cu_{2.2\text{ nm}}/Co_{2.8\text{ nm}}/IrMn_{14\text{ nm}}$ in the second AFCM.

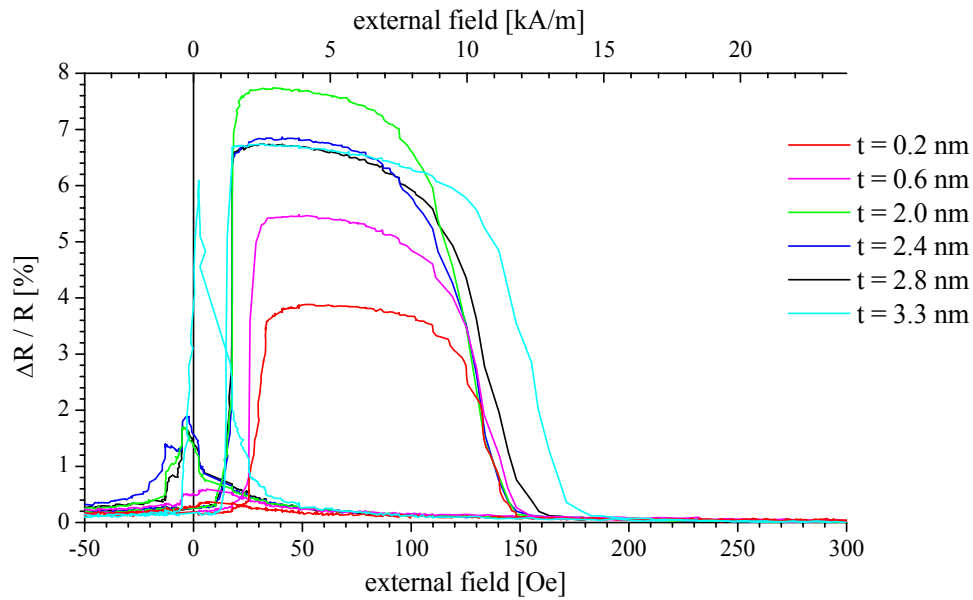


Figure 3.12: Variation of pinning layer thickness for the system $(Ni_{80}Fe_{20})_{3.4\text{ nm}} - Co_{2.8\text{ nm}}/Cu_{1.0\text{ nm}}/Co_{2.8\text{ nm}}/IrMn_t$ in the first AFCM.

3.7 Variation of Spacer Layer Thickness

The variation of the spacer layer thickness is one of the major aspects of this thesis. Based on the investigations on the layer thickness of the ferromagnetic layers and the pinning layer, reported in section 3.6, this series of experiments was done as $(Ni_{80}Fe_{20})_{3.9\text{ nm}} - Co_{2.7\text{ nm}}/Cu_t/Co_{2.7\text{ nm}}/IrMn_{9.0\text{ nm}}$. Here t was varied from 0.8 nm up to 9.7 nm . All measurements have been deduced in four point geometry at room temperature.

Before having a look on single GMR characteristics Fig. 3.13 presents an overview of the GMR amplitude as a function of the spacer layer thickness. At a spacer layer thickness of 1.8 nm the GMR amplitude is equal to 10.6% . This Cu layer thickness corresponds to the spacer layer thickness for the second antiferromagnetic coupling maximum in a comparable system of unpinned trilayers (see section 3.3).

For further decreasing layer thickness the GMR-effect amplitude falls off and is finally completely suppressed with the increasing contribution of the ferromagnetic RKKY coupling for t_{NM} from 1.6 nm to 1.3 nm . Close to the first AFCM the GMR amplitude recovers and reaches 11.5% at a spacer layer thickness of 1.1 nm .

For $t_{Cu} = 0.9\text{ nm}$ still a GMR amplitude of 7.5% was measured. Then the GMR amplitude drops rapidly to less than 1% for spacer layer thicknesses being less than 0.9 nm .

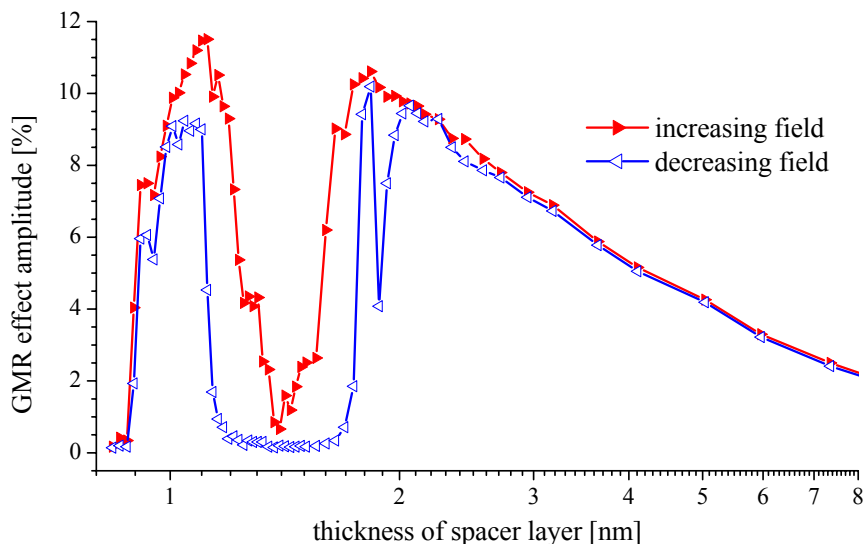


Figure 3.13: GMR as function of the spacer layer thickness in the series $(Ni_{80}Fe_{20})_{3.9\text{ nm}} - Co_{2.7\text{ nm}}/Cu_t/Co_{2.7\text{ nm}}/IrMn_{9.0\text{ nm}}$.

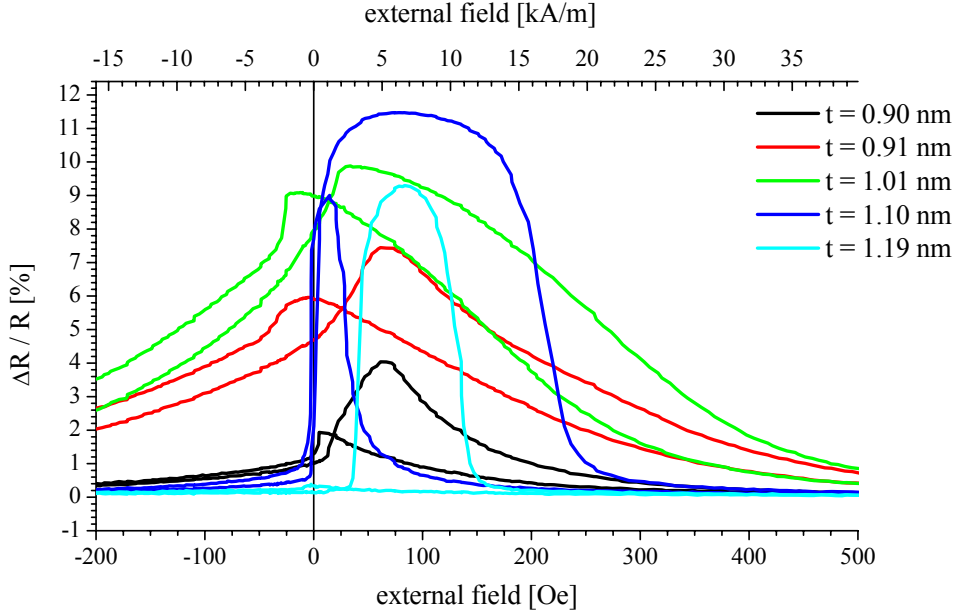


Figure 3.14: GMR characteristics near the 1st AFCM of selected samples in the series $(Ni_{80}Fe_{20})_{3.9\text{ nm}} - Co_{2.7\text{ nm}}/Cu_t/Co_{2.7\text{ nm}}/IrMn_{9.0\text{ nm}}$.

Considering the GMR amplitudes for spacer layer thicknesses of more than 1.8 nm it is quite striking that there is no meaningful slump corresponding to a ferromagnetic coupling between the second and third AFCM. Only the GMR amplitude measured for decreasing fields drops down to 4.1% for $t_{Cu} = 1.9\text{ nm}$. Here we have the typical spin valve behavior as thoroughly described by B. Dieny *et al.* [Die94] and many others.

Now let us have a detailed look on the characteristics around the first AFCM presented in Fig. 3.14. The GMR effect in this experiment can be seen for a spacer layer thickness of about 0.9 nm. The high saturation field of about 375 Oe (average for all four edges, which were determined in accordance to section 3.2) for the GMR characteristic at nominal 0.91 nm is an unambiguous indication for a high interlayer coupling. It can be estimated to about $200\ \mu\text{J}/\text{m}^2$ according to Eq. 4.20.

Compared to this interlayer coupling the exchange bias is small and only shifts the characteristic to positive fields. For higher spacer layer thicknesses the GMR amplitude rises although the interlayer coupling obviously decreases already. The switching point for the free layer become symmetric to zero field and the exchange bias is the dominant factor for the shape of the characteristic. The zero field sensitivity of 9 %/mT for $t_{Cu} = 1.10\text{ nm}$ is remarkable high.

The characteristic at $t_{Cu} = 1.19 \text{ nm}$ needs some explication. For high negative fields the alignment of the ferromagnetic layers is parallel to each other and to the external field. But only when a positive field of about 35 Oe is reached the “free” bottom layer switches and the relative alignment becomes antiparallel, resulting in an increase of the resistance. This can only be due to a ferromagnetic coupling. Although the exchange bias favors this antiparallel alignment the pinned layer switches soon after, the value for $\Delta R/R$ falls to zero.

For decreasing field no antiparallel alignment of the magnetic layers is obtained at all. When the pinned layer switches, which of course happens for smaller fields as for increasing fields due to anisotropy, the free bottom layer follows immediately. This again is a consequence of the ferromagnetic interlayer coupling.

Near the second AFCM the GMR effect starts again at a spacer layer thickness of about 1.56 nm , see Fig. 3.15.

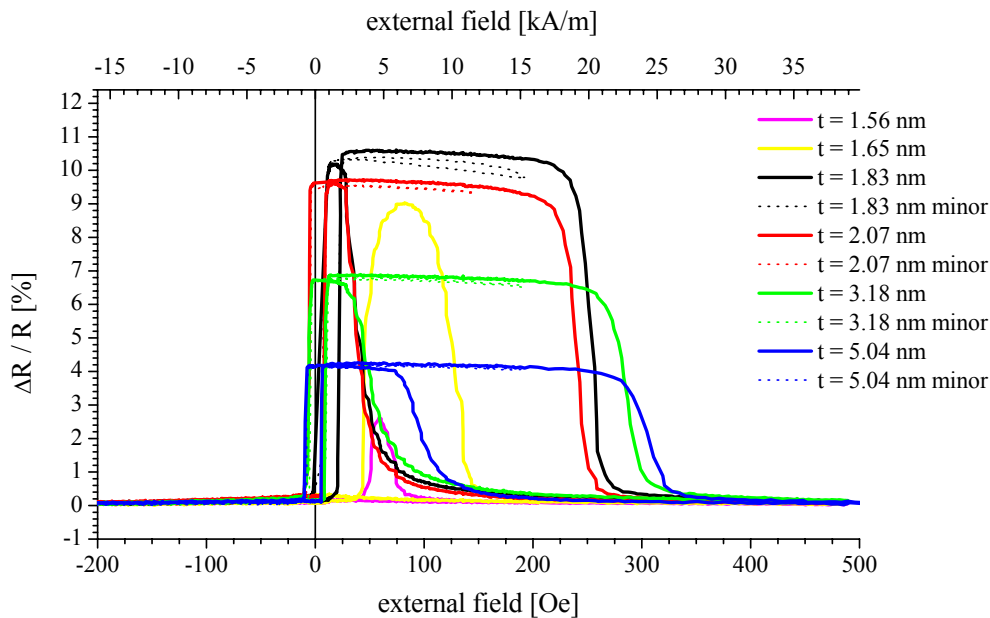


Figure 3.15: GMR characteristics near and above the 2^{nd} AFCM of selected samples in the series $(Ni_{80}Fe_{20})_{3.9 \text{ nm}} - Co_{2.7 \text{ nm}}/Cu_t/Co_{2.7 \text{ nm}}/IrMn_{9.0 \text{ nm}}$. For samples with a layer thickness of more than 1.8 nm minor loops are included.

For $t_{Cu} = 1.65\text{ nm}$ the characteristic equals very much that at $t_{Cu} = 1.19\text{ nm}$. Again there is a change in the resistance for increasing fields but not for decreasing as described above. For copper thickness of 1.83 nm the GMR amplitude reaches its maximum at the second AFCM with 10.6%. Still the interlayer coupling is slightly ferromagnetic as can be seen from the shift of the switching points for the bottom layer to positive fields.

For further increasing spacer layer thickness we see more and more a typical spin valve behavior. The switching points of the free layer are only slightly shifted around zero field due to decreasing interlayer coupling. The zero field sensitivity reaches values up to $33\%/mT$ for $t_{Cu} = 1.86\text{ nm}$.

The minor loops which are also plotted in Fig. 3.15 show that for spacer layer thicknesses greater than 1.9 nm the layers switch separately. A plateau of about 200 Oe is clearly developed.

Finally Fig. 3.16 gives an overview on the measurements.

Our experimental results prove that pinned trilayers definitely show an alternating interlayer exchange coupling and that meaningful GMR amplitudes can be reached for spacer layer thicknesses down to 0.9 nm . The data are described above and explained qualitatively. A further analysis of this data will be carried out by simulating the GMR characteristics based on an extended Stoner-Wohlfarth's model. This simulation program and its application is the second main topic of this thesis and is presented in chapter 4.

Before I will continue with some further experimental results and their analysis.

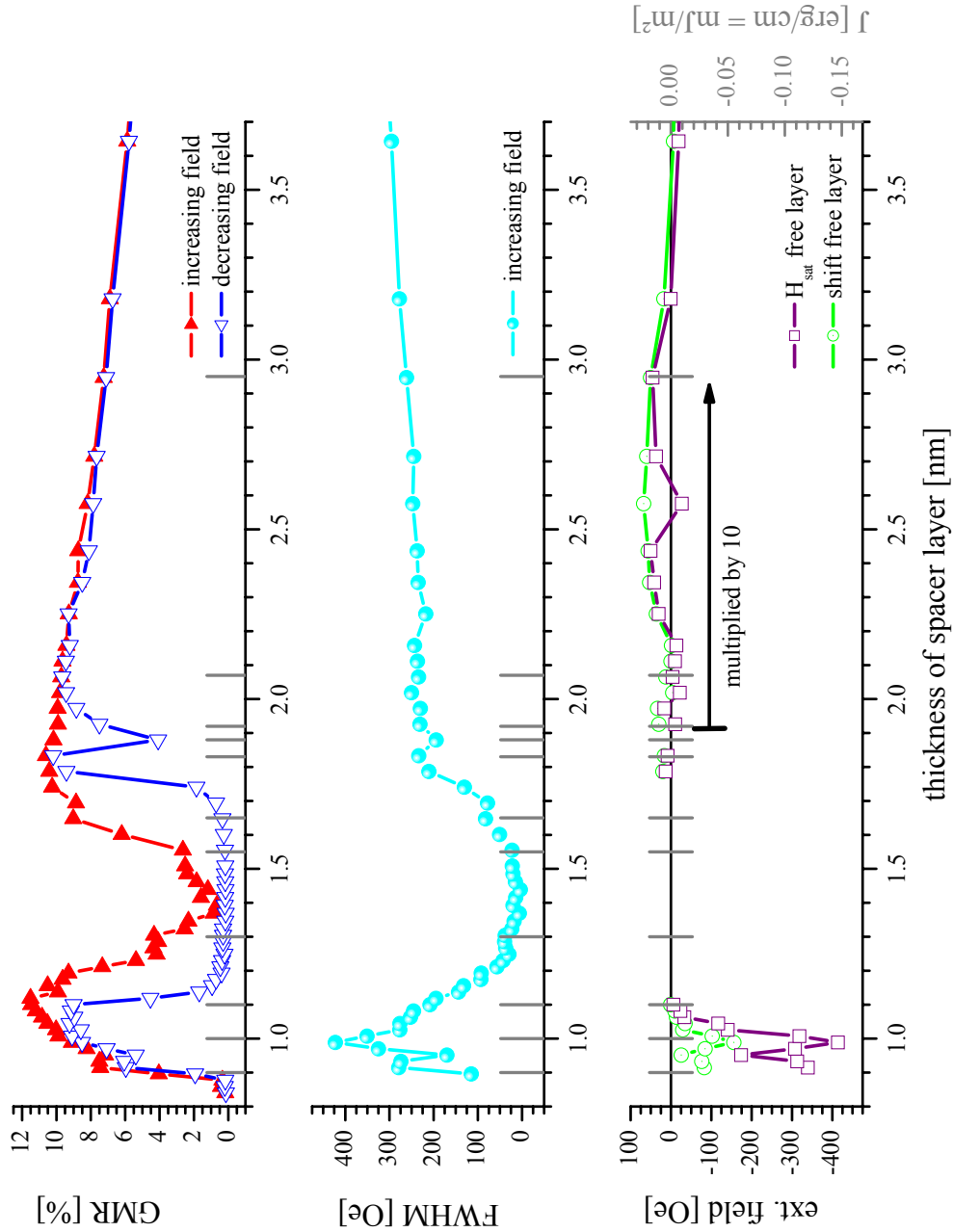


Figure 3.16: Overview to the series of pinned and interlayer coupled magnetic trilayer with varying Cu spacer thickness: $(Ni_{80}Fe_{20})_{3.9\text{ nm}} - Co_{2.7\text{ nm}}/Cu_t/Co_{2.7\text{ nm}}/IrMn_{9.0\text{ nm}}$. For samples at the marked positions you will find the Δ^R/R -characteristic and the simulated characteristic in section 4.4. The coupling constant J^* is in first approximation proportional to the saturation magnetization H_{sat} of the free layer according to Eq. 4.20.

3.8 Structural Analysis

To investigate why our systems show an extraordinary high antiferromagnetic interlayer coupling for layer thicknesses down to 1 nm structural analysis were performed. As these systems are hardly accessible for X-ray diffraction due to their small layer thickness we decided for investigate the roughness by means of AFM measurements and access grain size and layer quality by TEM measurements.

3.8.1 Investigation on Layer Roughness

The interface roughness was analyzed by measuring the RMS⁶-value for $1 \times 1 \mu\text{m}^2$ images (Fig. 3.17). Starting with a sample consisting of the $Ni_{80}Fe_{20}$ buffer layer only, a second sample with the two layers of the bottom electrode was prepared and so on, until the full stacking sequence was reached (see table 3.1). The scan was performed on air by the digital instruments Nanoscope IIIa. We accurately checked that all results were well reproducible.

The wavelength of the roughness was determined to 17.2 nm by counting the number of extrema per unit length in various line scans (see Fig. 3.18).

The standard silicon wafer with 100 nm thermal oxide was cleaned in acetone and ethyl alcohol and not further treated before mounted in the sputter chamber. The results demonstrate clearly the importance of the $Ni_{80}Fe_{20}$ -buffer layer allowing a roughness of less than 0.24 nm for the relevant spacer layer. No significant deviations was found for first ($t_{Cu} = 1.0 \text{ nm}$) and second ($t_{Cu} = 2.0 \text{ nm}$) coupling maximum.

no.	stacking sequence layer thickness in [nm]	RMS [nm]	GMR [%]
AFM01	$(Ni_{80}Fe_{20})_{3.9}$	0.19	-
AFM02	$(Ni_{80}Fe_{20})_{3.9} - Co_{2.7}$	0.21	-
AFM03	$(Ni_{80}Fe_{20})_{3.9} - Co_{2.7}/Cu_{2.0}$	0.24	-
AFM04	$(Ni_{80}Fe_{20})_{3.9} - Co_{2.7}/Cu_{2.0}/Co_{2.7}$	0.20	9.3
AFM05	$(Ni_{80}Fe_{20})_{3.9} - Co_{2.7}/Cu_{2.0}/Co_{2.7}/IrMn_{9.0}$	0.19	8.7
AFM07	$(Ni_{80}Fe_{20})_{3.9} - Co_{2.7}/Cu_{1.0}/Co_{2.7}/IrMn_{9.0}$	0.19	12.3

Table 3.1: AFM measurement of magnetic trilayers. RMS value for $1 \times 1 \mu\text{m}^2$ images, sample for GMR measurement and AFM scan were sputtered in the same process in a magnetic mask of 9.5 kA/m .

⁶Rout Mean Square

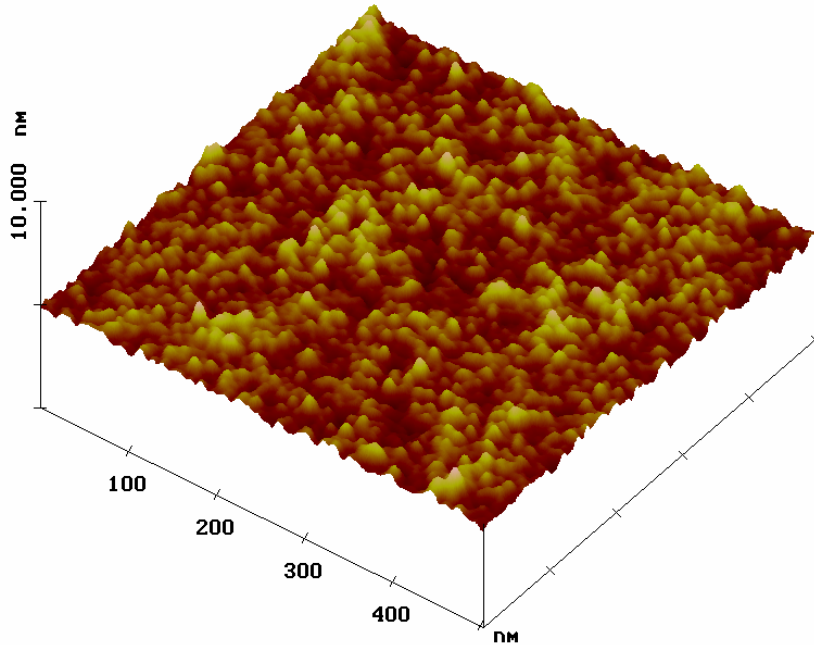


Figure 3.17: AFM-image of a trilayer. The given scan of $0.5 \times 0.5 \mu\text{m}^2$ for the sample $(\text{Ni}_{80}\text{Fe}_{20})_{3.9 \text{ nm}} - \text{Co}_{2.7 \text{ nm}} / \text{Cu}_{2.0 \text{ nm}}$ is typical for the series given in table 3.1.

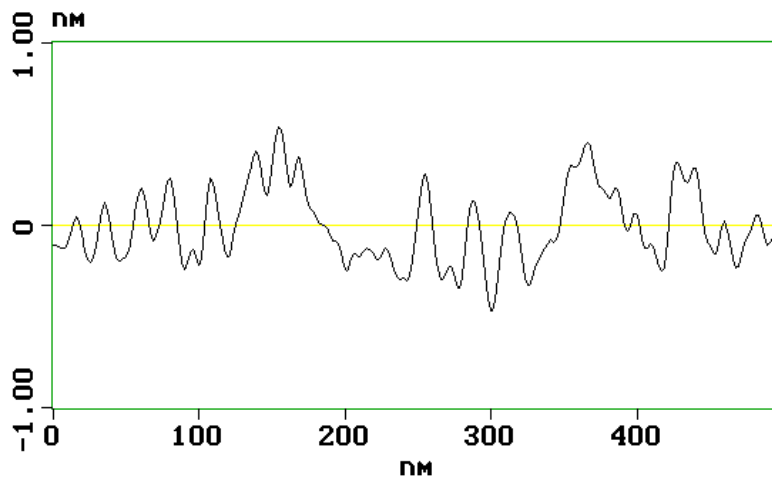


Figure 3.18: AFM-line scan of a trilayer. The given scan for the sample $(\text{Ni}_{80}\text{Fe}_{20})_{3.9 \text{ nm}} - \text{Co}_{2.7 \text{ nm}} / \text{Cu}_{2.0 \text{ nm}}$ is typical for the series given in table 3.1.

3.8.2 Investigation on Grain Size and Layer Quality

To obtain information on the grain size and layer quality we took TEM⁷ images of the system $(Ni_{80}Fe_{20})_{3.9\text{ nm}} - Co_{2.7\text{ nm}}/Cu_{2.0\text{ nm}}/Co_{2.7\text{ nm}}/IrMn_{9.0\text{ nm}}$ sputtered on a copper coated carbon grid. See Fig. 3.19 as an example. The average grain size from a series of images taken with varying tilt angles is $5.7 \pm 2.5\text{ nm}$. No in plane texture can be determined which suggests a statistical distribution of the grains in the layer plain.

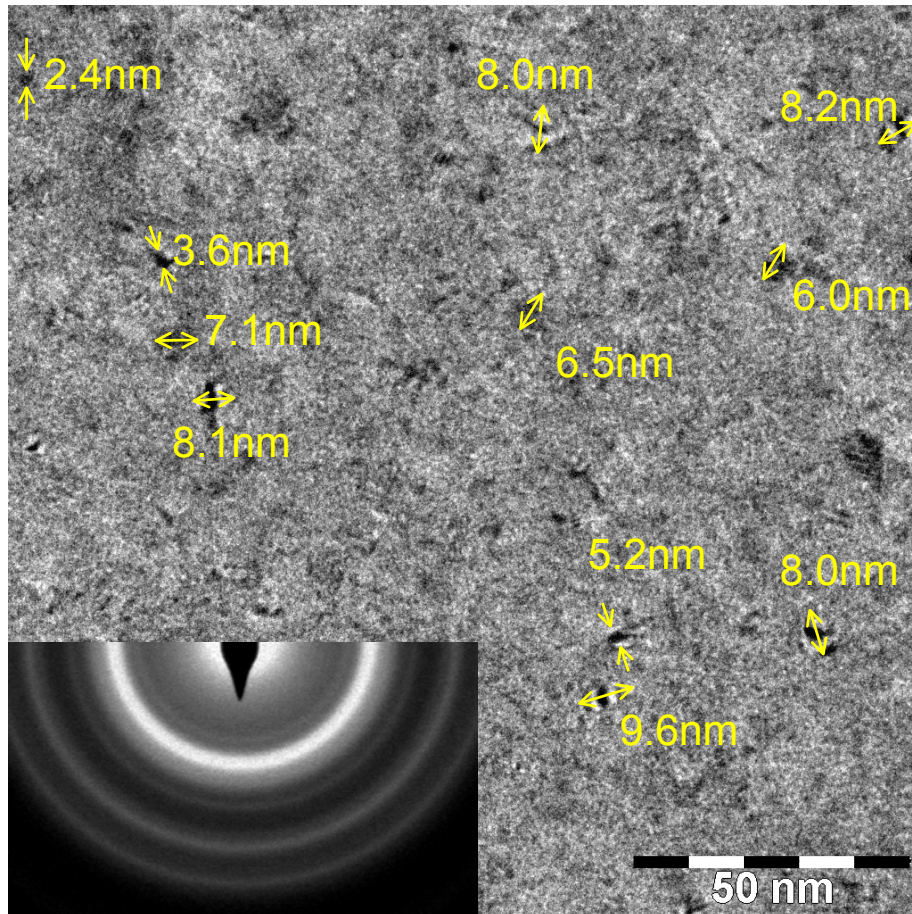


Figure 3.19: TEM-images of a trilayer. Bright-field image with a magnification of 135k, diffraction pattern with a camera length of 1.15 m. The grain size could be determined by a series of these images with different tilt angles.

⁷Philips CM 200 SuperTWIN

3.9 Magnetic Measurements

In this section we will compare magnetic measurements and GMR characteristics of samples which have been produced in the same deposition process. The magnetic measurements were performed on $4 \times 4mm^2$ samples by an alternating gradient magnetometer (AGM)⁸. The measured characteristics have been fitted by a phenomenological law as presented in section 2.8 according to Eq. (2.68).

$$M(H)_{norm} = \frac{2 A_{free}}{\pi} \operatorname{atan} \left(\frac{H - H_{shift,free}}{P_{free}} \right) + \frac{2 A_{pinned}}{\pi} \operatorname{atan} \left(\frac{H - H_{shift,pinned}}{P_{pinned}} \right)$$

The selected samples are examples for spin valves in first AFCM (Fig. 3.20), between first and second AFCM (Fig. 3.21), second AFCM (Fig. 3.22) and after the second AFCM (Fig. 3.23). For comparison two more samples of unpinned trilayers with identical stacking sequence as the second AFCM but without the *IrMn*-layer have been prepared, measured and analyzed, one sputtered within the magnetic mask with a field of $9.5 kA/m$ (Fig. 3.24) as the pinned systems, the other without the magnetic mask (Fig. 3.25).

The stacking sequence and all fitting parameters are given in table 3.2. When the shifting field for the free and pinned layers are fitted for increasing and decreasing field the coercivity fields H_C and the shift due to interlayer exchange coupling $H_{i.e.c}$ and exchange bias $H_{e.b.}$ can be calculated. See again section 2.8 for details. These data are also presented in table 3.2.

The shift of the magnetization curve for the free layer $H_{i.e.c}$ reflects very well the alternating interlayer exchange coupling. For $t_{Cu} = 1.0nm$ the coupling is strongly antiferromagnetic and $H_{i.e.c}$ becomes $-15.2 Oe$, its highest negative value. Then for $t_{Cu} = 1.6nm$ the shifting field was determined to $47.4 Oe$. The interlayer coupling is ferromagnetic. Initially it might be astonishing that the absolute value is higher than for the antiferromagnetic coupling in the first AFCM although the amplitude of the coupling oscillation decreases with increasing spacer layer thickness (see Eq. 2.43). But this is in agreement with the results presented in section 3.7 as the maximum GMR amplitude in the first AFCM is reached for already decreasing interlayer exchange coupling. In other words, the selected spacer layer thickness chosen for sample 1 does not correspond to the maximum interlayer coupling but to the highest GMR amplitude near the first AFCM.

⁸Princeton Measurements Corporation, MicroMagTM Model 2900 AGM System

sample no.	stacking sequence ($Ni_{80}Fe_{20}$) = Py layer thickness in [nm]	magn. mask	$[Oe]$				fraction	GMR [%]
			$H_{shift,pinned} \rightarrow$ $H_{shift,pinned} \leftarrow$ $H_{shift,free} \rightarrow$ $H_{shift,free} \leftarrow$	$P_{pinned} \rightarrow$ $P_{pinned} \leftarrow$ $P_{free} \rightarrow$ $P_{free} \leftarrow$	$H_{C,pinned}$ $H_{C,free}$	$H_{e,b.}$ $H_{i,e.c.}$		
1	$Py_{3.9} - Co_{2.7}/Cu_{1.0}/Co_{2.7}/IrMn_{9.0}$	yes	258.9	29.5	74.1	184.8	35%	10.7
			110.7	16.3	8.5	-15.2		
2	$Py_{3.9} - Co_{2.7}/Cu_{1.6}/Co_{2.7}/IrMn_{9.0}$	yes	-6.7	5.1	92.6	125.7	37%	9.7
			-23.7	4.5	5.7	47.4		
3	$Py_{3.9} - Co_{2.7}/Cu_{2.0}/Co_{2.7}/IrMn_{9.0}$	yes	218.3	7.7	71.9	184.4	36%	8.7
			33.1	1.3	6.9	0.7		
4	$Py_{3.9} - Co_{2.7}/Cu_{3.2}/Co_{2.7}/IrMn_{9.0}$	yes	53.0	11.4	97.5	212.2	36%	6.1
			41.7	1.3	7.8	1.5		
			256.3	9.6				
			112.5	4.7				
			7.5	0.7				
			-6.2	0.6				
			309.7	10.1				
			114.7	9.2				
			9.2	0.7				
			-6.3	0.8				

Table 3.2: Magnetization measurements: Fitting parameters and analysis.

sample no.	stacking sequence ($Ni_{80}Fe_{20}$) = Py	magn. mask	$[Oe]$				$H_{C,pinned}$	$H_{e,b.}$	fraction	GMR [%]
			$H_{shift,pinned} \rightarrow$	$H_{shift,pinned} \leftarrow$	$P_{pinned} \rightarrow$	$P_{pinned} \leftarrow$				
5	$Py_{3.9} - Co_{2.7}/Cu_{2.0}/Co_{2.7}$	yes	-45.4	45.4	6.1	6.1	45.4 ^{a)}		33%	9.3
			-11.2	11.2	1.2	1.2	11.2 ^{a)}		67%	
6	$Py_{3.9} - Co_{2.7}/Cu_{2.0}/Co_{2.7}$	no	-40.5	40.5	3.9	3.9	40.5 ^{a)}		27%	8.0
			-7.0	7.0	3.0	3.0	7.0 ^{a)}		73%	

Table 3.2: Magnetization measurements of magnetic trilayers: Stacking sequence of the samples, fitting parameters and analysis.

^{a)}These parameters have to be handled with care as the magnetization of top and bottom layer do not switch independently due to the missing pinning.

For $t_{Cu} = 2.0 \text{ nm}$ and 3.2 nm (samples 3 and 4) the shifting field is quite small. Here we have to assume as well a weak antiferromagnetic interlayer exchange coupling being an antagonist to the always present ferromagnetic coupling, e.g. due to orange peel coupling.

The coercivity field of the free layer consisting of the bottom *Co*-layer and the magnetically soft *NiFe*-layer is quite small in the pinned systems (5.7 Oe to 8.5 Oe for the measured samples) and well comparable to the bottom layer in the unpinned trilayers (samples 5 and 6).

This is different for the top *Co*-layer. The samples 1 to 4 show an average value of 84 Oe whereas the unpinned systems of sample 5 and 6 only show a coercivity field of about 43 Oe or less as here the influence of interlayer coupling and anisotropy cannot be exactly separated. This is due to the fact that the *IrMn*-layer not only cares for the exchange bias but increases the anisotropy of the top magnetic layer (see section 2.5).

Finally it is worthwhile to note that the magnetic mask during the sputtering process only adds a weak (uniaxial) anisotropy to the system (see data for samples 5 and 6). The characteristics are still symmetric to zero field and hence do not show an unidirectional alteration.

The magnetic moment per unit area A can be estimated based on data from literature for bulk magnetization and the determined layer thicknesses.

$$\begin{aligned}
 \left(\frac{m}{A}\right)_{free} &= M_{sat,NiFe} \cdot t_{NiFe} + M_{sat,Co} \cdot t_{Co,free} \\
 &= 820 \frac{kA}{m} \cdot 3.9 \text{ nm} + 1400 \frac{kA}{m} \cdot 2.7 \text{ nm} = 6978 \mu A \\
 \left(\frac{m}{A}\right)_{pinned} &= M_{sat,Co} \cdot t_{Co,pinned} \\
 &= 1400 \frac{kA}{m} \cdot 2.7 \text{ nm} = 3780 \mu A
 \end{aligned}$$

This is a relative fraction of the total magnetic moment of 65% to 35% and matches astonishingly well the corresponding fitting parameters. This result proves the validity of the simplifications for the buffer layer magnetization carried out in the simulation described in chapter 4.

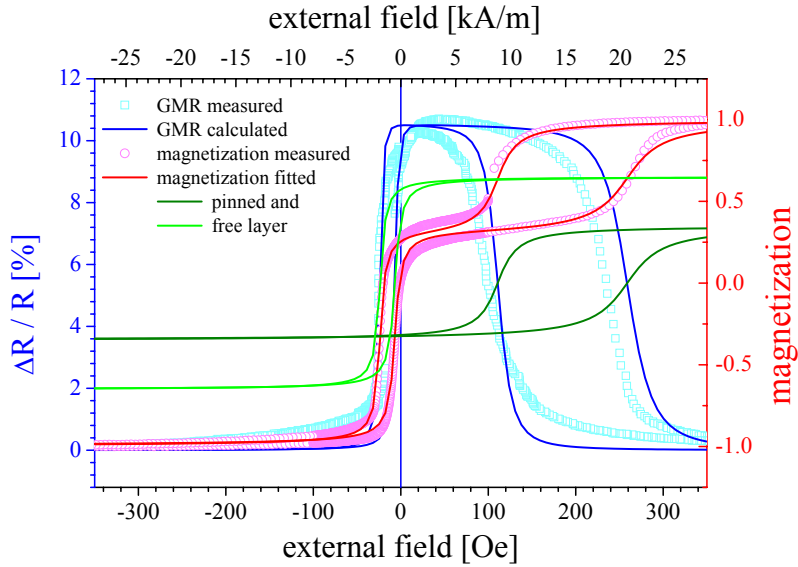


Figure 3.20: Magnetization measurement and analysis for pinned trilayer at 1st AFCM. Sample 1: $(Ni_{80}Fe_{20})_{3.9\text{ nm}} - Co_{2.7\text{ nm}}/Cu_{1.0\text{ nm}}/Co_{2.7\text{ nm}}/IrMn_{9.0\text{ nm}}$.

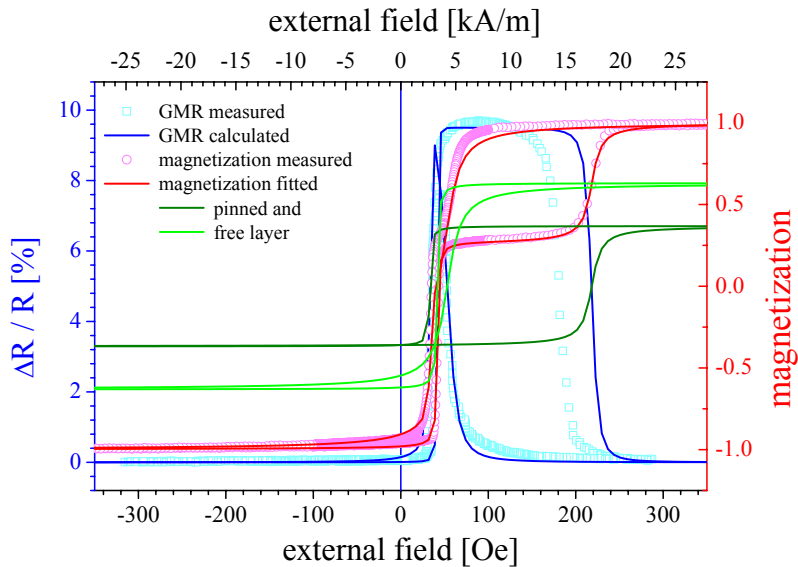


Figure 3.21: Magnetization measurement and analysis for pinned trilayer between 1st and 2nd AFCM. Sample 2: $(Ni_{80}Fe_{20})_{3.9\text{ nm}} - Co_{2.7\text{ nm}}/Cu_{1.6\text{ nm}}/Co_{2.7\text{ nm}}/IrMn_{9.0\text{ nm}}$.

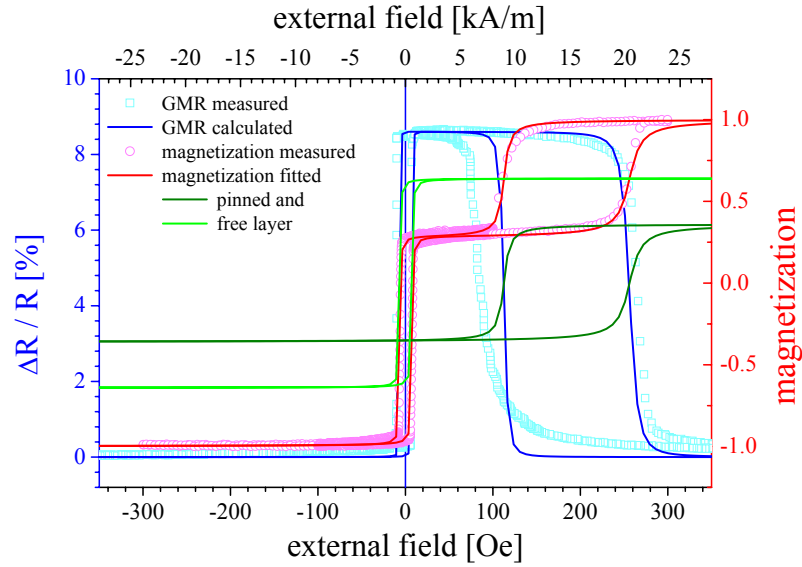


Figure 3.22: Magnetization measurement and analysis for pinned trilayer at 2nd AFCM. Sample 3: $(Ni_{80}Fe_{20})_{3.9\text{ nm}} - Co_{2.7\text{ nm}}/Cu_{2.0\text{ nm}}/Co_{2.7\text{ nm}}/IrMn_{9.0\text{ nm}}$.

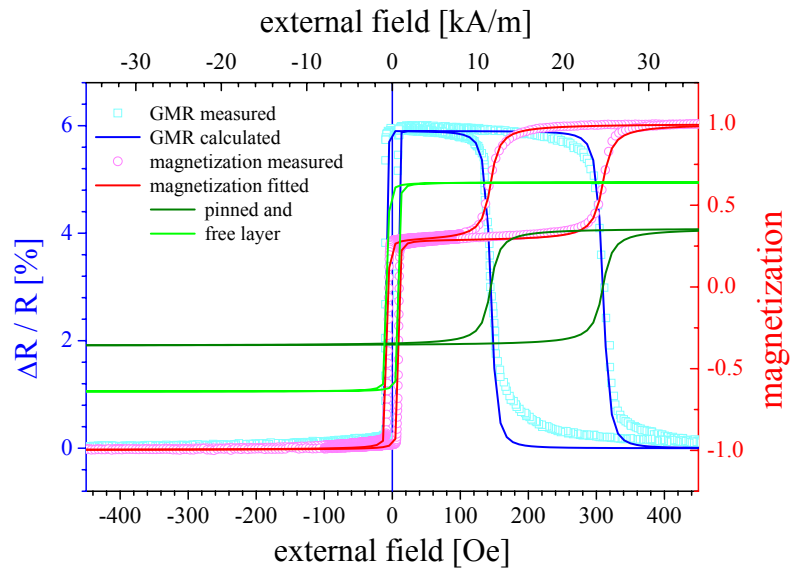


Figure 3.23: Magnetization measurement and analysis for pinned trilayer after 2nd AFCM. Sample 4: $(Ni_{80}Fe_{20})_{3.9\text{ nm}} - Co_{2.7\text{ nm}}/Cu_{3.2\text{ nm}}/Co_{2.7\text{ nm}}/IrMn_{9.0\text{ nm}}$.

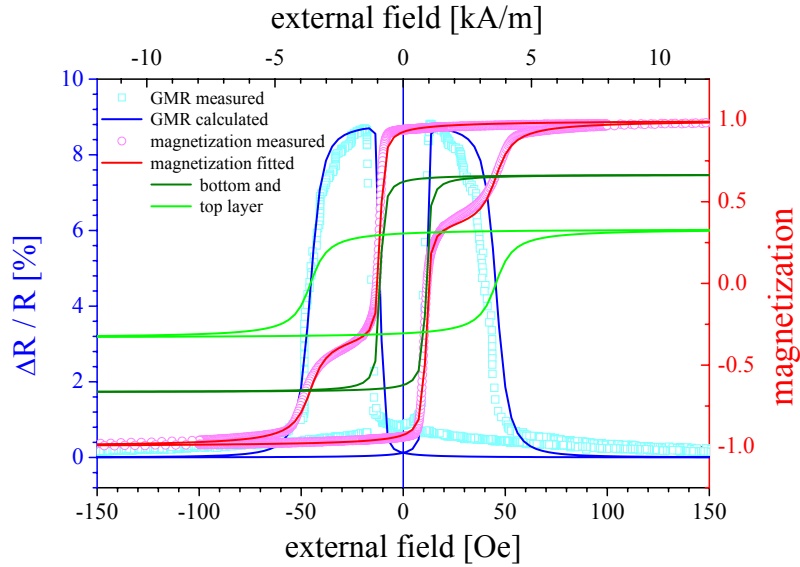


Figure 3.24: Magnetization measurement and analysis for trilayer at 2nd AFCM. Sample 5: $(Ni_{80}Fe_{20})_{3.9\text{ nm}} - Co_{2.7\text{ nm}}/Cu_{2.0\text{ nm}}/Co_{2.7\text{ nm}}$, sputtered in the magnetic mask.

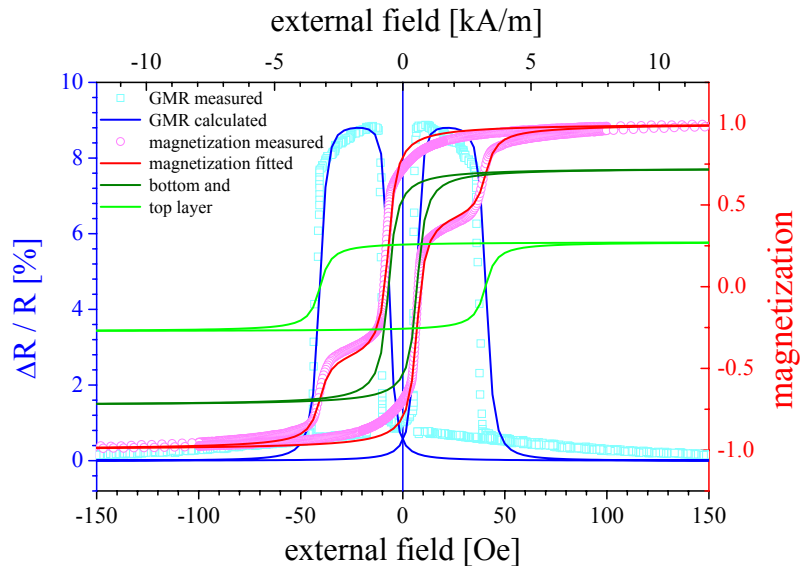


Figure 3.25: Magnetization analysis for trilayer at 2nd AFCM. Sample 6: $(Ni_{80}Fe_{20})_{3.9\text{ nm}} - Co_{2.7\text{ nm}}/Cu_{2.0\text{ nm}}/Co_{2.7\text{ nm}}$, sputtered without a magnetic mask.

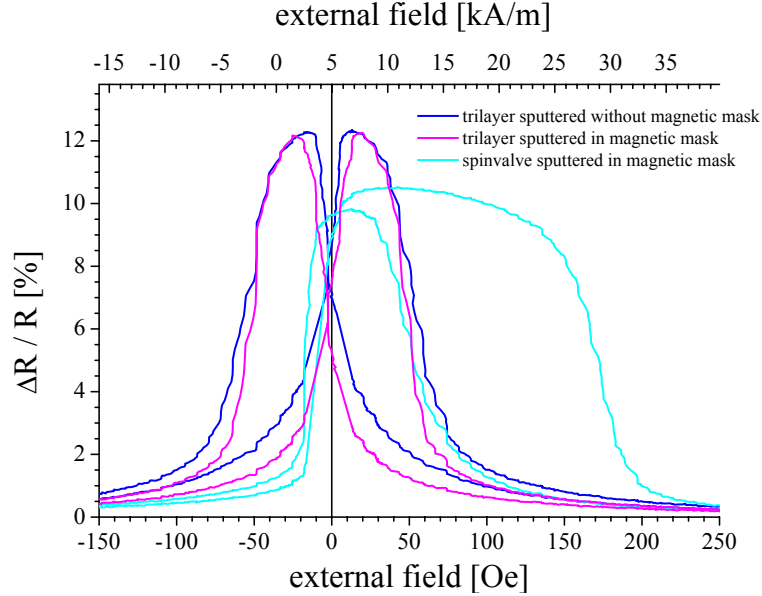


Figure 3.26: GMR characteristic for samples at the 1st AFCM. $(Ni_{80}Fe_{20})_{3.9\text{ nm}} - Co_{2.7\text{ nm}}/Cu_{1.0\text{ nm}}/Co_{2.7\text{ nm}}(/IrMn_{9.0\text{ nm}})$

3.10 Comparison of Pinned and Unpinned Trilayers

In the last section of this chapter we will again compare the pinned with the unpinned systems. In figures 3.26 and 3.27 GMR characteristics of magnetic trilayers, sputtered with or without the magnetic mask of 9.5 kA/m , and spin valves are compared near the first and second coupling maximum, respectively.

For $t_{Cu} = 1.0\text{ nm}$ the GMR amplitude for the unpinned sample is about 12% but for the pinned system only 10%. This is what is expected due to the lower resistance of the pinned system containing the *IrMn*-layer, the so called shunting effect. For $t_{Cu} = 2.0\text{ nm}$ the GMR amplitude keeps totally unchanged at 9%. Here the shunting effect is also present, of course. A detailed look at the characteristics of the unpinned samples show a crossover of more or less zero (see section 3.2 and [Hem00]) indicating a negligible interlayer exchange coupling. In combination with the fact that no plateau is developed this can be interpreted in a way that a state of fully antiparallel alignment throughout the the sample is never reached. Hence the GMR of this system is not higher as for the pinned system where we have a shunting effect but a state of fully antiparallel alignment resulting in a wide plateau.

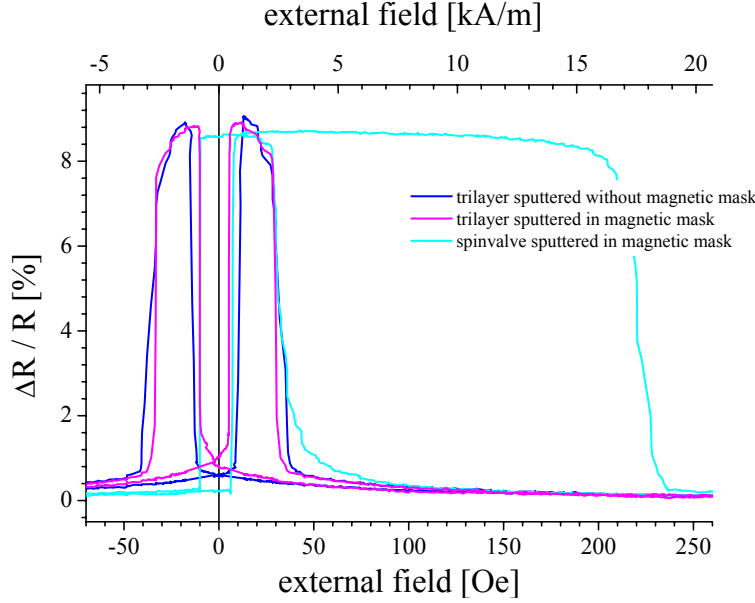


Figure 3.27: GMR characteristic for samples at the 2nd AFCM. $(Ni_{80}Fe_{20})_{3.9\text{ nm}} - Co_{2.7\text{ nm}}/Cu_{2.0\text{ nm}}/Co_{2.7\text{ nm}}(/IrMn_{9.0\text{ nm}})$

The high squareness of the magnetization curve for the pinned layer again indicates a high induced anisotropy for the upper *Co*-layer. It exceeds the anisotropy of the unpinned top *Co*-layer of identical thickness by far, again in agreement to the results reported above. The free layer behaves identically for the pinned and unpinned system resulting in identical switching points.

In Fig. 3.28 the spacer layer dependence of the GMR amplitude for the unpinned system $(Ni_{80}Fe_{20})_{2.8\text{ nm}} - Co_{2.6\text{ nm}} / Cu_t / Co_{2.9\text{ nm}}$ (Fig. 3.3) and the pinned system $(Ni_{80}Fe_{20})_{3.9\text{ nm}} - Co_{2.7\text{ nm}}/Cu_t/Co_{2.7\text{ nm}}/IrMn_{9.0\text{ nm}}$ (Fig. 3.13) are combined.

As the determination of the absolute layer thickness for the unpinned stacks was not as exact as for the new results on the pinned systems we must not draw any conclusions from the shift of the spacer layer thickness for which the GMR amplitude is at its maximum.

The unpinned system depends very much on the interlayer coupling to yield an antiferromagnetic alignment apart from remanence effects due to the differing anisotropy of top and bottom layer. Hence the GMR is completely suppressed between the first and second AFCM. Also between the second and third AFCM the now weak ferromagnetic interlayer coupling results in a vanishing GMR effect amplitude. Three maxima can be easily identified.

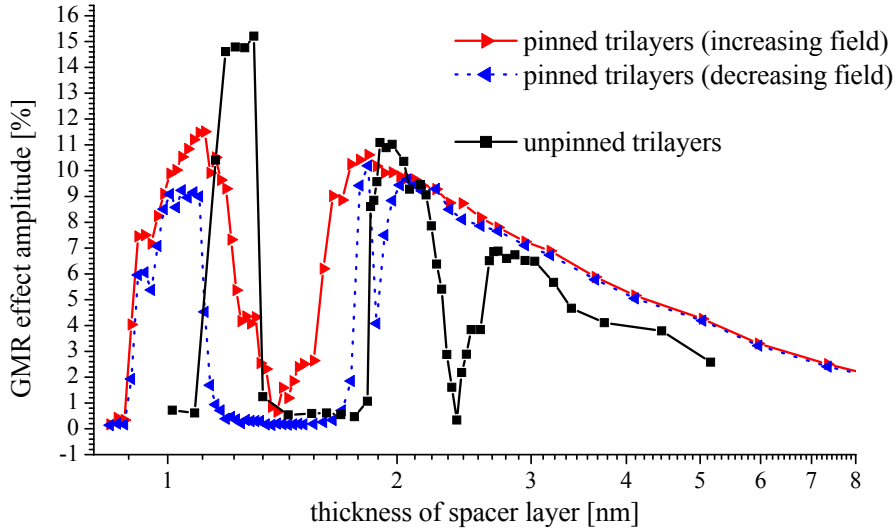


Figure 3.28: GMR amplitude as a function of the Cu layer thickness in the unpinned system $(Ni_{80}Fe_{20})_{2.8\text{ nm}} - Co_{2.6\text{ nm}} / Cu_t / Co_{2.9\text{ nm}}$ and the pinned system $(Ni_{80}Fe_{20})_{3.9\text{ nm}} - Co_{2.7\text{ nm}} / Cu_t / Co_{2.7\text{ nm}} / IrMn_{9.0\text{ nm}}$.

When the top Co -layer is pinned to the $IrMn$ -layer it does not switch its magnetization near zero field. We always yield an antiferromagnetic alignment but for very high ferromagnetic interlayer coupling. Therefore the GMR effect is only suppressed for a very small interval between first and second AFCM and drops down slightly for decreasing fields between second and third AFCM.

The maximum GMR amplitude of the unpinned system is with 15.2% evidently much higher than the 11.5% for the pinned trilayers. This again is due to the reduced shunting effect of simple magnetic trilayers.

As the maximum GMR amplitude does not necessarily coincide with the maximum in the antiferromagnetic interlayer exchange coupling the oscillation period of the GMR amplitude and of the interlayer coupling can not be deduced from each other. See section 4.4.4 for an alternative approach.

3.11 Conclusion

The simplest stacking sequence for top spin valves of the type $(Ni_{80}Fe_{20}) - Co / Cu / Co / IrMn$ was thoroughly studied. After determining the ideal thickness of the ferromagnetic layers (section 3.6) the Cu spacer layer was varied from 0.8 nm to 9.7 nm (3.7).

The evolution of the characteristics and their GMR-amplitude are an unambiguous evidence for the role the interlayer exchange coupling in this systems. It shows oscillatory behavior with a first and second antiferromagnetic coupling maximum (AFCM) for spacer layer thickness of about 1.0 nm and 2.1 nm , respectively. Considerably high GMR effect amplitudes up to 11.5% in the first and 10.6% in the second AFCM have been determined. The ferromagnetic coupling between the two AFCM suppresses the GMR effect completely for the corresponding spacer layer thickness of about 1.4 nm . The determination of the saturation magnetization allowed for a rough estimation of the interlayer exchange coupling (e.g. about $200\ \mu\text{J}/\text{m}^2$ for the first AFCM).

We could reach an antiparallel alignment for spacer layer thicknesses down to 0.9 nm . Obviously this is far below the generally observed critical spacer layer thickness of about 2 nm for copper [Die91a] [Rij94], below which the GMR effect usually rapidly drops to zero.

Structural analysis (section 3.8) showed that the samples under investigation feature an extraordinary smoothness at their interfaces with an RMS-value less than 0.24 nm . This causes the RKKY-like interlayer coupling to dominate the ferromagnetic orange peel coupling and at the same time pin holes can be avoided as a result of the surface quality of the layers.

The average grain size was determined to $5.7 \pm 2.5\text{ nm}$ with no in plane texture suggesting a statistical distribution of the grains in the layer plain.

Magnetic measurements (section 3.9) and their analysis by means of a phenomenological law as presented in section 2.8 gave an insight in the magnetization process and its implications for the $\Delta R/R$ -characteristic. It allowed for the determination of the switching points and provided a very good qualitative understanding of the GMR behavior.

The comparison of the series of unpinned and pinned trilayer (section 3.10) shows coherent results.

Two aspects can be regarded as advantageous for applications: The overall thickness of the stack is about 20 nm only, resulting in a high resistance, and only very few parameters have to be considered for a production process due to the simplicity of the system. The zero field sensitivity reaches values up to $33\%/mT$ for $t_{Cu} = 1.86\text{ nm}$ and can be easily tailored.

All results presented in this chapter are in good agreement to each other and based on a long term experience in GMR are qualitatively good understood. Still, we have only a little insight in the magnetization process, only a rough estimation of the interlayer coupling but no data for anisotropy or exchange bias.

Further experiments, especially spatial and time resolved scattering processes by x-ray, electrons or neutrons are very elaborate and hence costly and time-consuming. However, the results are not always unambiguous and need extensive analysis. As the majority of these research methods demand special preparation methods for the systems under investigation it is also quite questionable in how far the results can be transferred to the system used in later applications.

In the next chapter a totally different approach is presented. As experimental input it mainly demands the GMR characteristic and in addition some parameters available from literature. It will not only allow for a deeper insight in experimentally realized systems but also give reliable references for new designs.

Chapter 4

Simulation of the GMR-Characteristics

To get a deeper understanding of the magnetization reversal and the related GMR-characteristic in layered magnetic structures a tool to simulate GMR-characteristics and magnetization loops was developed. It will provide an approach to extract values for the interlayer coupling and anisotropy constants and for the exchange bias.

In the first section of this chapter a model for the magnetization reversal in layered GMR systems is developed. It is an extension of a model by E. C. Stoner and E. P. Wohlfarth which has been applied to layered magnetic devices for the first time by H. Holloway and D. J. Kubinski. A considerable number of further extensions and adjustments will be presented to enable the treatment of further demands.

In the main text of this thesis the model is presented for the case of the interlayer coupled and pinned trilayer in section 4.1. But this model can be adjusted to different stacking sequences. Various systems are presented in appendix A: Simple trilayers (A.1), doubled trilayers (A.2), bottom spin-valves (A.3) and a simple and an enhanced model for multilayers (A.4 and A.5).

The implementation of the model in the simulation program GMRSim is presented in the following section 4.2. As the starting point is completely different to known magnetic simulations it is quite worthwhile to compare the results to lattice calculations (section 4.3).

A substantial part of this chapter is dedicated to the application of the simulation to coupled and pinned trilayers (section 4.4) and the deduced information (section 4.5).

4.1 Model for the Magnetization Reversal in Layered GMR Systems

In 1948 E. C. Stoner and E. P. Wohlfarth introduced a model to calculate hysteresis loops [Sto48], in which they described the magnetization reversal by a coherent rotation of the spin of all electrons in a particle consisting of only one magnetic domain in an external field. The basic idea of the model is to calculate the magnetization reversal by minimizing the energy of the system. As a function of the external field the only free parameter is the direction of the magnetization.

H. Holloway and D. J. Kubinski extended this model and applied it to layered magnetic devices [Hol98]. Our research group already demonstrated the applicability of this model to hysteresis free copper/permalloy multilayers in [Hüt99], for trilayers in [Hüt01] and [Hem00].

In the course of these studies this model was further extended to fit the actual needs, especially to include all energy terms mentioned before and finally to serve as the physical model for our simulation program presented in section 4.2.

From the nice match between prediction and experiment the conclusion can be drawn, that Stoner-Wohlfarth's model can serve as an accurate tool to calculate GMR characteristics despite the fact that the original model is formulated in the single domain limit only. The reason for that is, that the experimentally determined data such as K_{eff} and J indirectly include the influence of magnetic domains which are present without any doubt.

At the beginning of this section the requirements and assumptions of the model will be pointed out. In the following subsection the extension of the model to a coupled and pinned trilayer is given, including the adjustment of equations (2.51) and (2.63) for the GMR characteristic and magnetization loop.

4.1.1 Requirements and Assumptions of the Model

To apply an extended Stoner-Wohlfarth's model to magnetic layers assumptions have to be made. All calculations included in the simulation are based on the following items:

- We assume columnar growth of the system, which can be justified by TEM-pictures of the structures (see Fig. 4.1). Within one column (= grain) the easy axis points in the same direction due to identical crystal direction.

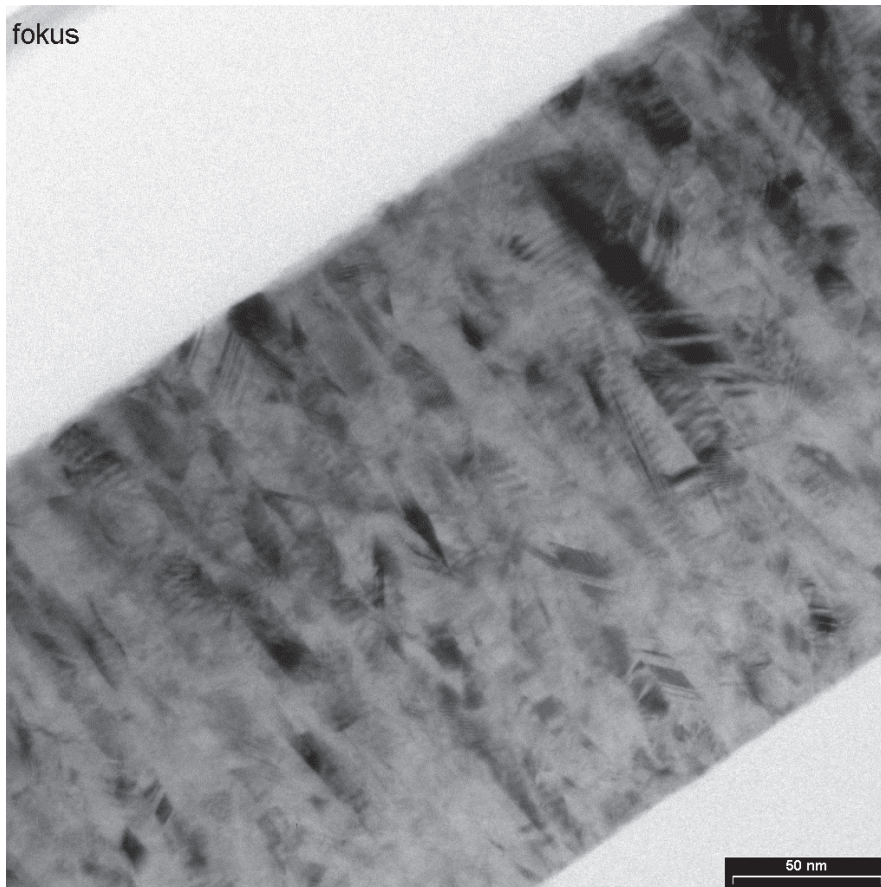


Figure 4.1: TEM micrograph of the layered system $Py_{1.9\text{ nm}}$ / $\{Cu_{1.7\text{ nm}} / Py_{1.6\text{ nm}}\}_{60}$ (TEM-preparation and micrograph: G. Haindl).

- The easy axes are always in the layer plane due to shape anisotropy.
- The magnetization of one column has no influence on adjacent columns, e.g. no domain wall propagation or stray fields are considered.
- In first approximation the saturation magnetization M_{sat} is the same as in the bulk material.
- The energy of the system is determined by the direction of the magnetization of adjacent magnetic layers. The system is not necessarily in the state of overall lowest energy but can be trapped in a local minimum.
- In the case of antiferromagnetic coupling an ideal antiparallel configuration is adopted after sample growth.

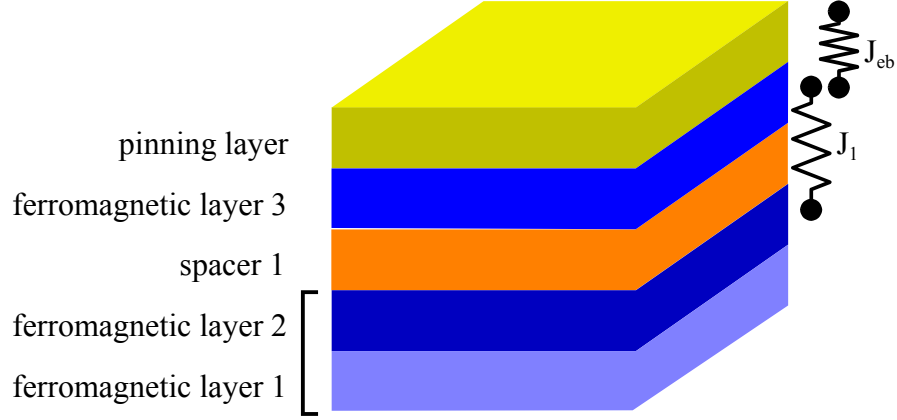


Figure 4.2: Design of a top pinned trilayer. The magnetic buffer and the bottom magnetic layer are coupled ferromagnetically and behave as one magnetic layer, the top magnetic layer is pinned by the adjacent ferromagnetic layer.

Due to these assumptions restrictions of the model have to be made. Especially the long tails in the GMR-characteristics for high external field cannot be evaluated as they are caused by the fluctuation of the layer thickness, which is not taken into consideration.

4.1.2 Model for Coupled and Pinned Trilayers

The system under investigation contains a magnetic buffer, a bottom magnetic layer, a spacer and a top magnetic layer which is pinned by an antiferromagnetic layer (Fig. 4.2). In addition to the interlayer coupling and the exchange bias the other magnetic energy contributions, e.g. the Zeeman energy and the anisotropy are taken into account.

The angles of the magnetization direction of the buffer, the bottom and the upper magnetic layer are given by θ_1 , θ_2 and θ_3 , respectively. The directions of the easy axes are given by φ_1 , φ_2 and φ_3 , γ defines the direction of the pinning. The angle between the x-axis and the long side of the shape may be defined as ξ (see Fig. 4.3).

The Zeeman energy per unit area for this system becomes:

$$\begin{aligned}
 E_{Zeeman}/A &= -\mu_0 \cdot M_{sat,1} \cdot t_1 \cdot H \cdot \cos \theta_1 \\
 &\quad -\mu_0 \cdot M_{sat,2} \cdot t_2 \cdot H \cdot \cos \theta_2 \\
 &\quad -\mu_0 \cdot M_{sat,3} \cdot t_3 \cdot H \cdot \cos \theta_3
 \end{aligned} \tag{4.1}$$

$$\begin{aligned}
E_{ani,bi}/A &= \frac{1}{4} K_{intrinsic,bi,1} \cdot t_1 \cdot \sin^2(2(\theta_b - \varphi)) \\
&+ \frac{1}{4} K_{intrinsic,bi,2} \cdot t_2 \cdot \sin^2(2(\theta_b - \varphi)) \\
&+ \frac{1}{4} K_{intrinsic,bi,3} \cdot t_3 \cdot \sin^2(2(\theta_3 - \varphi))
\end{aligned} \tag{4.4}$$

As the anisotropy does not have to be of the same nature for all magnetic layers, both energy contributions will be considered in the simulation. It is left to the user to set the anisotropy constant of the non applicable term to zero.

Induced and shape anisotropy are taken into consideration by adding the terms:

$$\begin{aligned}
E_{K,ind}/A &= K_{ind,1} \cdot t_1 \cdot \sin^2(\theta_b - \varphi_{ind}) \\
&+ K_{ind,2} \cdot t_2 \cdot \sin^2(\theta_b - \varphi_{ind}) \\
&+ K_{ind,3} \cdot t_3 \cdot \sin^2(\theta_3 - \varphi_{ind})
\end{aligned} \tag{4.5}$$

$$\begin{aligned}
E_{K,ind,bi}/A &= \frac{1}{4} K_{ind,bi,1} \cdot t_1 \cdot \sin^2(2(\theta_b - \varphi_{ind})) \\
&+ \frac{1}{4} K_{ind,bi,2} \cdot t_2 \cdot \sin^2(2(\theta_b - \varphi_{ind})) \\
&+ \frac{1}{4} K_{ind,bi,3} \cdot t_3 \cdot \sin^2(2(\theta_3 - \varphi_{ind}))
\end{aligned} \tag{4.6}$$

and

$$\begin{aligned}
E_{shape}/A &= K_{shape,1} \cdot t_1 \cdot \sin^2(\theta_b - \xi) \\
&+ K_{shape,2} \cdot t_2 \cdot \sin^2(\theta_b - \xi) \\
&+ K_{shape,3} \cdot t_3 \cdot \sin^2(\theta_3 - \xi)
\end{aligned} \tag{4.7}$$

The energy contribution due to the interlayer coupling has to be added.

$$E_{interlayer\ exchange}/A = -J_{L,total} \cos(\theta_3 - \theta_b) - J_Q (\cos^2(\theta_3 - \theta_b)) \tag{4.8}$$

The linear coupling constant $J_{L,total}$ is the sum of the interlayer coupling for the RKKY interaction J_L and the orange peel contribution J_{OP} . The last is taken from model A in section 2.6.

$$J_{L,total} = J_L + J_{OP} \quad (4.9)$$

An additional energy contribution originates from the pinning in the direction of γ . The magnitude of the exchange bias is determined by J_{eb} .

$$E_{exchange\ biasing}/A = -J_{eb} \cos(\theta_3 - \gamma) \quad (4.10)$$

The sum of Zeeman (Eq. 4.1), intrinsic anisotropy (Eq. 4.3 and Eq. 4.4), induced anisotropy (Eq. 4.5), shape anisotropy (Eq. 4.7), interlayer coupling energy (Eq. 4.8) and exchange biasing (Eq. 4.10) results in:

$$\begin{aligned}
E_{total}/A &= (E_{Zeeman} + E_{anisotropy} + E_{interlayer\ coupling} + E_{exchange\ biasing})/A \\
&= -\mu_0 \cdot M_{sat,1} \cdot t_1 \cdot H \cdot \cos \theta_b \\
&\quad -\mu_0 \cdot M_{sat,2} \cdot t_2 \cdot H \cdot \cos \theta_b \\
&\quad -\mu_0 \cdot M_{sat,3} \cdot t_3 \cdot H \cdot \cos \theta_3 \\
&\quad +K_{uni,1} \cdot t_1 \cdot \sin^2(\theta_b - \varphi) \\
&\quad +K_{uni,2} \cdot t_2 \cdot \sin^2(\theta_b - \varphi) \\
&\quad +K_{uni,3} \cdot t_3 \cdot \sin^2(\theta_3 - \varphi) \\
&\quad +\frac{1}{4} K_{bi,1} \cdot t_1 \cdot \sin^2(2(\theta_b - \varphi)) \\
&\quad +\frac{1}{4} K_{bi,2} \cdot t_2 \cdot \sin^2(2(\theta_b - \varphi)) \\
&\quad +\frac{1}{4} K_{bi,3} \cdot t_3 \cdot \sin^2(2(\theta_3 - \varphi)) \\
&\quad +K_{ind,1} \cdot t_1 \cdot \sin^2(\theta_b - \varphi_{ind}) \\
&\quad +K_{ind,2} \cdot t_2 \cdot \sin^2(\theta_b - \varphi_{ind}) \\
&\quad +K_{ind,3} \cdot t_3 \cdot \sin^2(\theta_3 - \varphi_{ind}) \\
&\quad +\frac{1}{4} K_{ind,bi,1} \cdot t_1 \cdot \sin^2(2(\theta_b - \varphi_{ind})) \\
&\quad +\frac{1}{4} K_{ind,bi,2} \cdot t_2 \cdot \sin^2(2(\theta_b - \varphi_{ind})) \\
&\quad +\frac{1}{4} K_{ind,bi,3} \cdot t_3 \cdot \sin^2(2(\theta_3 - \varphi_{ind})) \\
&\quad +K_{shape,1} \cdot t_1 \cdot \sin^2(\theta_b - \xi) \\
&\quad +K_{shape,2} \cdot t_2 \cdot \sin^2(\theta_b - \xi) \\
&\quad +K_{shape,3} \cdot t_3 \cdot \sin^2(\theta_3 - \xi) \\
&\quad -J_{L,total} \cos(\theta_3 - \theta_b) - J_Q (\cos^2(\theta_3 - \theta_b)) \\
&\quad -J_{eb} \cos(\theta_3 - \gamma)
\end{aligned} \quad (4.11)$$

4.1.3 GMR and Magnetization Characteristics

After minimizing the systems energy the angle pathes of magnetization for the different layers as a function of the external field are known. They can

be used to calculate the GMR characteristic and the magnetization loop according to Eq. (2.51) and Eq. (2.63).

Following the introduced notation θ_I becomes θ_b and θ_{II} becomes θ_3 :

$$\frac{R(H)}{R_{\uparrow\uparrow}} = g \cdot AF(H) = g \cdot \frac{1}{2} [1 - \cos(\theta_3(H) - \theta_b(H))] \quad (4.12)$$

or in terms of the enhanced model

$$\frac{R(H)}{R_{\uparrow\uparrow}} = \frac{1 + g}{1 + g \cdot \cos^2 \frac{\theta_3(H) - \theta_b(H)}{2}} - 1 = \frac{g}{2} \cdot \frac{1 - \cos(\theta_3(H) - \theta_b(H))}{1 + g \cdot \cos^2 \frac{\theta_3(H) - \theta_b(H)}{2}} \quad (4.13)$$

For the magnetization loop a term for the ferromagnetic buffer layer is added to equation (2.63).

$$M(H) = \frac{1}{t_1 + t_2 + t_3} ((M_{sat,1} \cdot t_1 + M_{sat,2} \cdot t_2) \cdot \cos \theta_b(H) + M_{sat,3} \cdot t_3 \cdot \cos \theta_3(H)). \quad (4.14)$$

4.1.4 Model for Other Stacking Sequences

Within the framework of the *Robert Bosch GmbH Leitprojekt Magneto-Elektronik*⁹ this model was extended to other stacking sequences. The results given in appendix A include simple magnetic trilayers (A.1), doubled trilayers (A.2), bottom spin valves (A.3) and a simple and an enhanced model for multilayers (A.4 and A.5).

In chapter 5 the simulation procedure based on the simple model for a multilayer is used to estimate the influence of the shape anisotropy on the GMR characteristic. A good example for the application of the simulation based on the enhanced model for multilayers is given in [Sta03].

4.1.5 Simplifications for Vanishing Anisotropy

To extract first information on the interlayer coupling from a measurement ongoing simplifications can be made. As an example this will be done for the layer system of a trilayer.

⁹Supported by the German Ministry for Education and Research, BMBF, under grant #13N73797/4

Considering the case of vanishing anisotropy in all layers, we get $K_{eff,1} = K_{eff,2} = K_{eff,3} = 0$. Vanishing anisotropy in antiferromagnetically coupled systems leads to $\theta_2 = -\theta_3 = \theta$. Then the total energy becomes:

$$\begin{aligned} E_{total}/A &= -\mu_0 \cdot (M_{sat,1} \cdot t_1 + M_{sat,2} \cdot t_2 + M_{sat,3} \cdot t_3) \cdot H \cdot \cos \theta \\ &\quad - J_L \cos(2\theta) - J_Q \cos^2(2\theta) \end{aligned} \quad (4.15)$$

The minimization $\frac{d}{d\theta} E_{total} = 0$ of the energy results in:

$$H(\theta) = -2 \cos \theta \cdot \frac{J_L + 4J_Q \cos^2 \theta - 2J_Q}{\mu_0 M^* \overline{t_{FM}}}, \quad (4.16)$$

where M^* is defined as

$$M^* = \frac{(M_{sat,buffer} \cdot t_{buffer} + M_{sat,bottom} \cdot t_{bottom} + M_{sat,top} \cdot t_{top})}{\overline{t_{FM}}} \quad (4.17)$$

and the average thickness of the ferromagnetic layers is given by

$$\overline{t_{FM}} = \frac{(t_{buffer} + t_{bottom}) + t_{top}}{2}. \quad (4.18)$$

When the system reaches saturation for $H = H_{sat}$, θ goes towards 0 and we get:

$$H_{sat} = -2 \cdot \frac{J_L + 2J_Q}{\mu_0 M^* \overline{t_{FM}}} \quad (4.19)$$

Let us now introduce a mean coupling constant $J^* = J_L + 2J_Q$, so the whole equation can be simplified to

$$H_{Sat} = -2 \cdot \frac{J^*}{\mu_0 M^* \overline{t_{FM}}}. \quad (4.20)$$

For multilayers Eq. (4.20) has to be altered because of the coupling of each ferromagnetic layer from both sides:

$$H_{Sat} = -4 \cdot \frac{J^*}{\mu_0 M^* \overline{t_{FM}}}. \quad (4.21)$$

4.2 Simulation Program GMRSim

The extended Stoner-Wohlfarth's model introduced in section 4.1 is now applied to simulate GMR-characteristics. As explained before the simulation can be used to investigate measured characteristics, e.g. to determine coupling constants etc. Furthermore it is a tool to design new systems showing requested properties.

The simulation package GMRSim¹⁰ consists of the simulation kernel and a user interface. The Fortran 90 source code of the kernel is given in appendix D.

At first the basic ideas of the simulation are given. Followed by a guide on how to extract input parameters from measured characteristics.

4.2.1 Procedure of Simulation

The procedure to be followed is depicted in Fig. 4.4. Starting from minimizing the energy the magnetization path and then the GMR-characteristic is calculated.

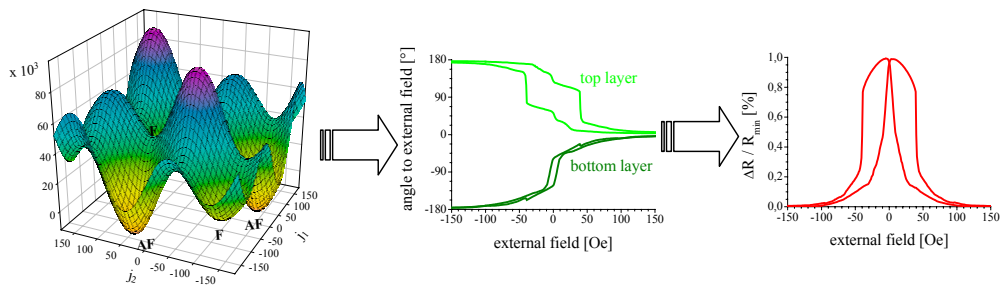


Figure 4.4: Procedure of the simulation.

In Eq. (4.11) the energy for a coupled and pinned trilayer is given. The energy terms for other stacking sequences are given in appendix A. The saturation magnetization $M_{sat,1}$, $M_{sat,2}$, $M_{sat,3}$, the anisotropy constants $K_{intrinsic,1}$, $K_{intrinsic,2}$, $K_{intrinsic,3}$ for uniaxial and/or biaxial anisotropy, the constants for induced anisotropy, $K_{ind,1}$, $K_{ind,2}$, $K_{ind,3}$ the coupling constants $J_{L,1}$, $J_{Q,1}$ have to be known as well as the layer thicknesses t_1 , t_2 , t_3 , and t_{s1} .

It is left to the user to enter the coupling constant manually or to use the fit-formula given in Eq. (2.43).

¹⁰The package is available on the authors homepage www.tobias-hempel.de

According to the presumptions for the application of the Stoner-Wohlfarth's model (section 4.1.1) the easy axes are assumed to be the same in one column and equally distributed over the sample. Therefore the energy is calculated for angles of the easy axis α from 1° to 180° in steps of 1° . For a given field value and magnetic configuration the two angles θ_I and θ_{II} are rotated until a local minimum is found. In the case of the coupled and pinned trilayer the angles are identical to θ_b and θ_3 , respectively.

Fig. 4.5 depicts the energy surface for a fixed easy axes with local and global extrema.

The GMR characteristic and magnetization loop are calculated by means of the AF-order parameter (see section 2.7.1) or the enhanced model (section 2.7.2). For output the GMR-effect and the magnetization loop are averaged for all columns (according to the easy axis). For a given field H_i with the index i and the GMR amplitude g the average over all easy axis indexed α is calculated as follows:

$$\frac{\Delta R(H_i)}{R_{\uparrow\uparrow}} = g \cdot \frac{\sum_{\alpha=1}^{180} \frac{1}{2} [1 - \cos(\theta_{II,\alpha}(H_i) - \theta_{I,\alpha}(H_i))]}{180} \quad (4.22)$$

For the enhanced GMR model this equation becomes:

$$\frac{\Delta R(H_i)}{R_{\uparrow\uparrow}} = \frac{\sum_{\alpha=1}^{180} g \cdot \frac{1 - \cos^2\left(\frac{1}{2}[\theta_{II,\alpha}(H_i) - \theta_{I,\alpha}(H_i)]\right)}{1 + g \cdot \cos^2\left(\frac{1}{2}[\theta_{II,\alpha}(H_i) - \theta_{I,\alpha}(H_i)]\right)}}{180} \quad (4.23)$$

The magnetization is given in the next equation:

$$M(H_i) = \frac{\sum_{\alpha=1}^{180} \frac{(M_{sat,1} t_1 + M_{sat,2} t_2) \cdot \cos \theta_{I,\alpha}(H_i) + M_{sat,3} t_3 \cdot \cos \theta_{II,\alpha}(H_i)}{t_1 + t_2 + t_3}}{180} \quad (4.24)$$

The averaged angle path depicts the magnetization reversal but must not be used for further calculations.

$$\overline{\theta_I}(H_i) = \frac{\sum_{\alpha=1}^{180} \arccos \cos \theta_{I,\alpha}(H_i)}{180} \quad (4.25)$$

$$\overline{\theta_{II}}(H_i) = - \frac{\sum_{\alpha=1}^{180} \arccos \cos \theta_{II,\alpha}(H_i)}{180} \quad (4.26)$$

The adjustments to the different layer systems is given in section 4.1 and in appendix A in detail.

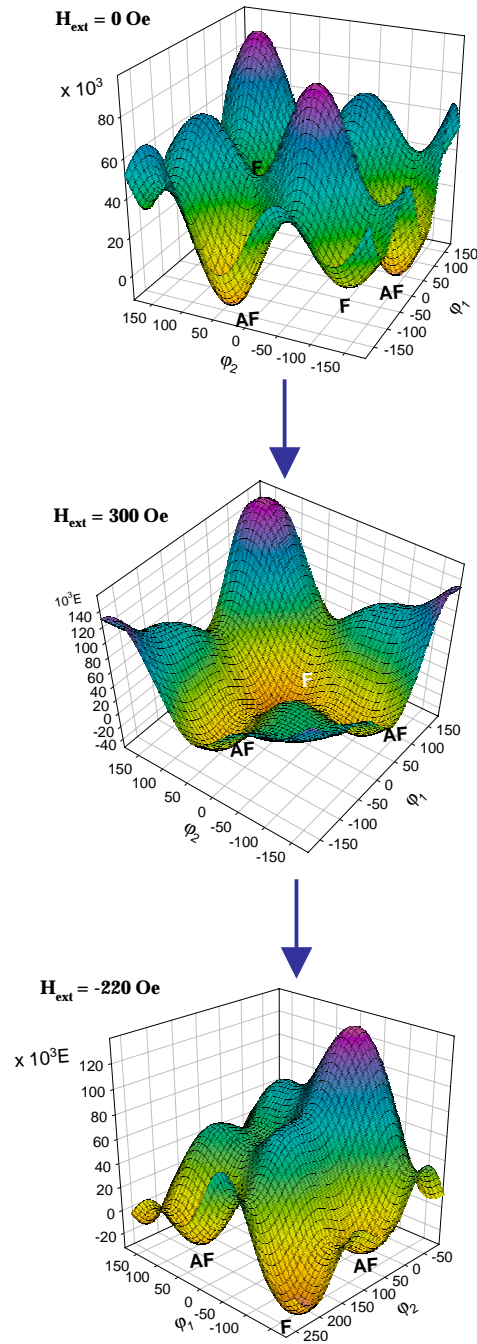


Figure 4.5: A comparison of the energy surface for different external fields with the ease-axis at 45° to the external field. The minima for ferromagnetic (F) and antiferromagnetic (AF) coupling are marked (from [Sch00a]).

4.2.2 Determination of Parameters

As there is a large set of parameters, it will always be possible to adjust the parameters ‘nicely’ to a measured characteristic. This might be of no physical meaning!

To ensure reliable data parameters, e.g. J_L , J_Q , K , have to be consistent to a whole series. This we have to remember when applying the simulation on coupled and pinned trilayers (section 4.4). For other systems this is investigated in [Hüt02].

As a starting value the coupling constants can be estimated using Eq. (4.20) or (4.21) for trilayers or multilayers, respectively. For the saturation magnetization values from appendix C can be used.

Since the AF-order parameter as defined in (2.51) or (2.62) only gives the normalized effect the amplitude has to be taken from experimental data.

Some further hints for starting parameters you will find in appendix C. A full list of all parameters for the simulation depending on the selected energy function is given in appendix B.

4.3 Comparison to Lattice Calculations

Now the question arises why not available lattice calculation programs have been used instead. Fig. 4.6 and Fig. 4.7 show the results for a simulation of a Cu/Co-multilayer with MicroMagus¹¹.

The calculations have been started with parameters which yield well acceptable results for the characteristics calculated with GMRSim compared to experimental data. The GMR characteristic adopted from lattice calculation have not much in common with the measurements. The GMR was calculated for each lattice point based on the model presented in 2.7.2. The difficulties become obvious when we look on the results for the magnetization in some detail.

In Fig. 4.8 we see a simulation for a magnetic trilayer in a lattice of 128×128 representing $500 \times 500 nm^2$. Details of the parameters are given in the figure’s caption. We see the high influence of the shape borders. Therefore the results of the calculation cannot be valid for real GMR structures of our experiments having dimensions of centimeters down to several micrometers. Scaling the lattice to a more realistic size is not suitable due to calculation time (several weeks on a double processor personal computer).

¹¹MicroMagus by D. V. Berkov and N. L. Gorn, Innovent e.V., ver. 3.25

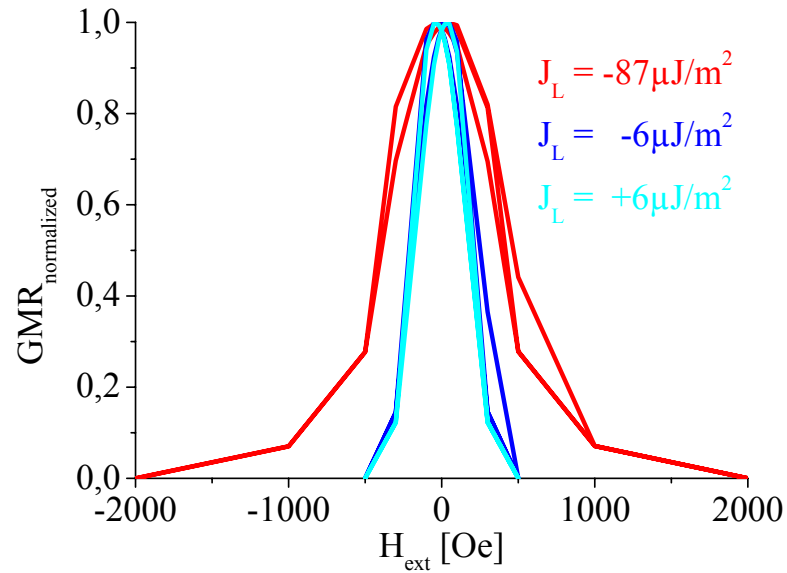


Figure 4.6: GMR characteristic calculated from lattice calculation for three different coupling constants.

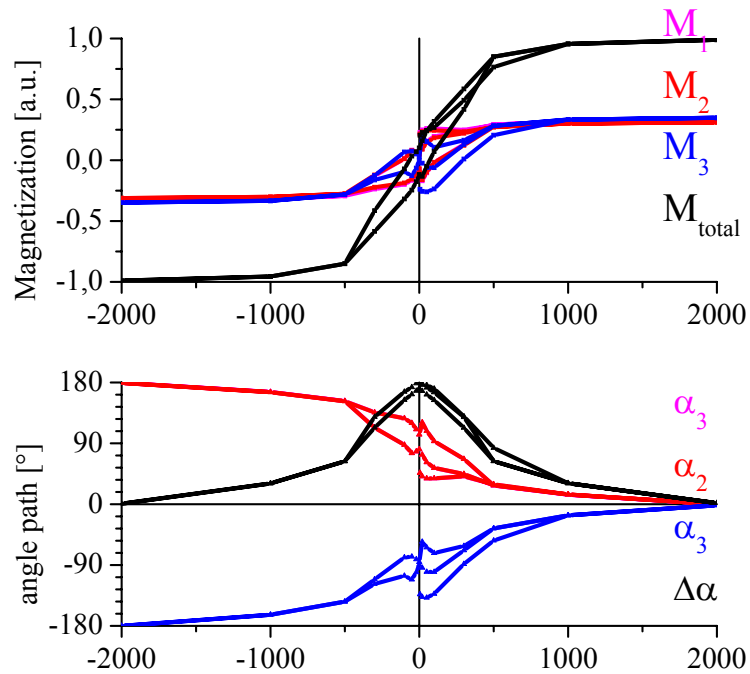


Figure 4.7: Magnetization and angle path for $J_L = -87 \mu\text{J}$ (first AFCM).

Periodic boundary conditions might show a way out of this dilemma. But the results presented in Fig. 4.9 for a lattice of 256×256 representing $1000 \times 1000 \text{ nm}^2$ shows that this does not help either. We got the behavior of a single domain of infinite size!

Anyway the simulation again depends on the input of realistic anisotropy constants, saturation magnetization and interlayer coupling, which have to be extracted from experimental values. For this data several simulations have to be performed for each characteristic of a whole series as explained in section 4.2.2. Therefore the problem of calculation time is multiplied. Also the size of the field steps is critical as the system can be trapped in local energy minima which might be skipped by too large intervals. To exploit the advantages of lattice calculations a more realistic modelation of the interfaces and including defects in the layer have to be included. On one hand this requires dividing the single metallic films in several layers which then will again increase the calculation time. On the other hand these information are usually not available from the performed experiments.

So we can conclude that the simulation GMRSim based on an extension of Stoner-Wohlfarth's Model is a more feasible tool in the hand of an experimentalist. The input from experimental results enables the determination of proper anisotropy constants and testing of newly designed stacking sequences. The results are related to the sputter system used. The calculation is fast and easy to handle.

The results in the next section (section 4.4) will confirm its validity.

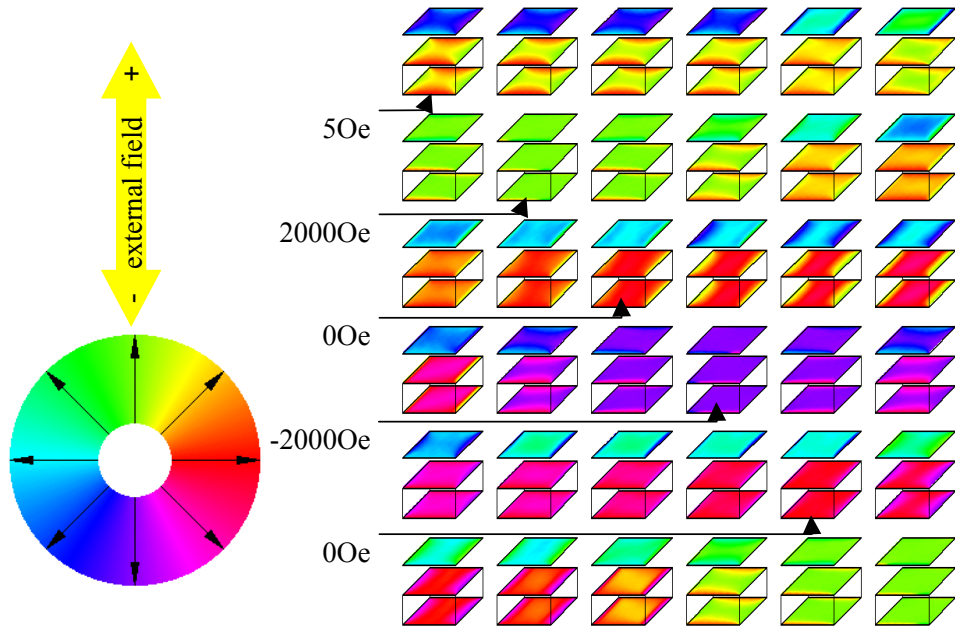


Figure 4.8: Lattice calculation with MicroMagus. The simulation refers to a magnetic trilayer of $(Ni_{80}Fe_{20})_{3.5\text{ nm}} - Co_{3.3\text{ nm}}/Cu_{2.1\text{ nm}}/Co_{3.7\text{ nm}}$, with saturation magnetizations of 820 kA/m and 1440 kA/m and crystallographic anisotropy constants of 2.7 kJ/m^3 and 4.5 kJ/m^3 for $NiFe$ and Co , respectively. The interlayer coupling constant was set to $-87\text{ }\mu\text{J/m}^2$ for the first AFCM, the exchange stiffness constant to 10^{-11} J/m . The calculation was performed in a lattice of 128×128 representing $500 \times 500\text{ nm}^2$, the metallic films have not been divided in further layers.

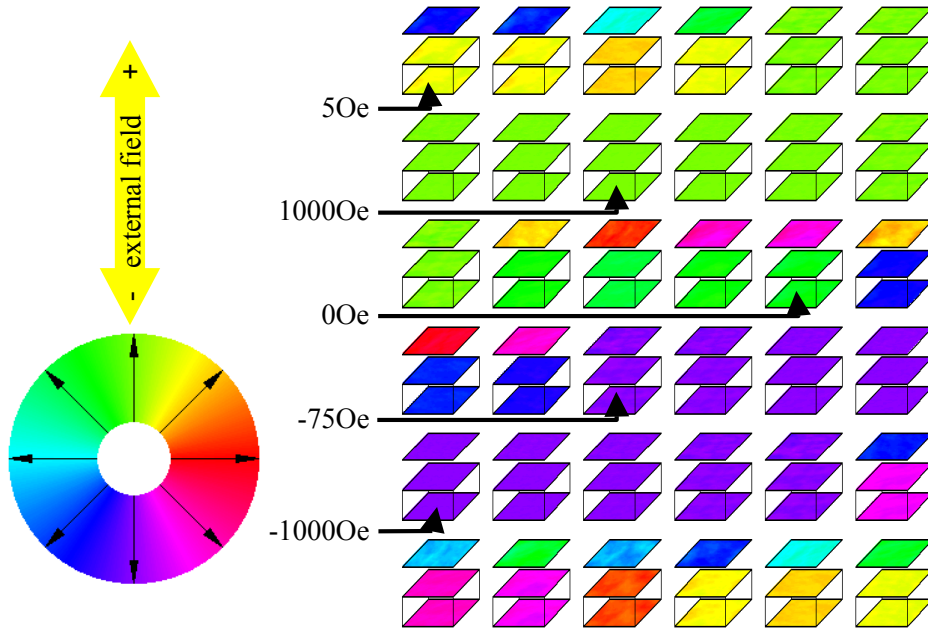


Figure 4.9: Lattice calculation with MicroMagus. The simulation again refers to a magnetic trilayer of $(Ni_{80}Fe_{20})_{3.5\text{ nm}} - Co_{3.3\text{ nm}}/Cu_{2.1\text{ nm}}/Co_{3.7\text{ nm}}$, with saturation magnetizations of 820 kA/m and 1440 kA/m and crystallographic anisotropy constants of 2.7 kJ/m^3 and 4.5 kJ/m^3 for $NiFe$ and Co , respectively. The interlayer coupling constant was set to $-18\text{ }\mu\text{J/m}^2$ for the second AFCM, the exchange stiffness constant to 10^{-11} J/m . The calculation was performed in a lattice of 256×256 representing $1000 \times 1000\text{ nm}^2$ but with periodic boundary conditions. Again the metallic films have not been divided in further layers.

4.4 Application of the Simulation to Coupled and Pinned Trilayers

To get a deeper understanding of the different factors affecting the GMR characteristics of interlayer coupled and pinned trilayers the simulation program GMRsim is now applied to selected measurements of the series $(Ni_{80}Fe_{20})_{3.9\text{ nm}} - Co_{2.7\text{ nm}}/Cu_t/Co_{2.7\text{ nm}}/IrMn_{9.0\text{ nm}}$.

4.4.1 Determination of Input Parameters

The layer thicknesses have been determined on corresponding samples by XRD (see section 3.4), the GMR amplitude were extracted from the measurements.

For the simulation the saturation magnetization for $Ni_{80}Fe_{20}$ and Co were taken from literature (e.g. [Boz51]) to 820 kA/m and 1440 kA/m , respectively.

As the anisotropy of the $Ni_{80}Fe_{20}$ buffer layer is of minor importance as it is strongly coupled to the adjacent Co layer, the referring constants for intrinsic and induced anisotropy K_1 and $K_{ind,1}$ are set to zero. In return the related constants K_2 and $K_{ind,2}$ have been reduced. The simulation of various characteristics also suggests that there is no major biquadratic anisotropy. Therefore all corresponding parameters were set to zero.

The orange peel coupling has been calculated in based on a wavelength of 17.2 nm and an amplitude of 0.68 nm . These data have been adopted from AFM measurements (section 3.8.1). For the given stacking sequence model A as presented in section 2.6 has to be applied.

4.4.2 Characteristics and Evaluated Parameters

It is worth while to have a detailed look on the presented graphs to see the nice match of measurement and simulation.

Table 4.1 shows the input parameters for the simulation as well as the extracted parameters.

t_s [nm]	A_{GMR} [%]	K_2	K_3	$K_{ind,2}$	$K_{ind,3}$	J_L	J_Q	J_{eb}	Fig.
		[kJ/m ³]				[μJ/m ²]			
0.91	7.0	1.5	4.0	0.0	0.0	-180	-45	10	4.10
1.00	9.5	1.5	4.0	0.0	0.0	-180	-36	17	4.11
1.10	11.5	1.5	2.0	0.5	9.0	-12	0	47	4.12
1.30	11.0	0.5	1.5	1.5	9.0	25	0	47	4.13
1.55	10.6	0.5	1.5	1.5	9.0	29	0	47	4.14
1.65	10.2	0.5	1.5	1.5	9.0	18	0	47	4.15
1.83	10.6	0.5	1.5	2.0	10.0	2	0	67	4.16
1.88	10.2	0.5	1.5	1.5	9.5	-2	0	47	4.17
1.92	9.9	0.5	1.5	2.0	10.0	-6	0	52	4.18
2.07	9.7	0.5	1.5	1.5	9.0	-6	0	57	4.19
2.95	7.2	0.5	1.5	1.7	10.5	0	0	66	4.20

Table 4.1: Spacer layer thickness t_s and GMR-amplitude A_{GMR} were given to the simulation. Values for the anisotropy and coupling constants were adjusted to yield meaningful results to the full series.

4.4.3 Interpretation of the Results

Now we will see if these results support the statements of section 3.7 which were only based on the pure GMR characteristics.

There the interlayer coupling in the first AFCM was estimated to $-200\mu J/m^2$. For the simulation best results were obtained for $-180\mu J/m^2$ which is in good agreement considering the fact that the estimation neglects anisotropy completely (Fig. 4.10 and 4.11). Furthermore the statement that the optimal thickness for maximal antiferromagnetic interlayer coupling and highest GMR amplitude (Fig. 4.12) do not coincident is unambiguously approved.

Also the quite unusual GMR characteristics for spacer layer thicknesses between first and second AFCM are well reproduced by the simulation (Fig. 4.13, 4.14, and 4.15). The angle paths confirm the statement that for decreasing fields the free bottom layer follows immediately the pinned layer so that no antiparallel alignment is reached and $\Delta R(H) R_{sat}$ keeps at zero.

The simulation data determine the fact that the amplitude of the interlayer coupling decreases rapidly with increasing spacer layer thickness. For J_L we yield another ferromagnetic coupling maximum at about $t_{Cu} = 1.92\text{ nm}$ (see Fig. 4.18) which is only of minor influence to the GMR characteristic which at this thickness is more and more determined by anisotropy and exchange bias, the so called spin valve behavior. The simulation for $t_{Cu} = 2.95\text{ nm}$

(Fig. 4.20) shows that the GMR effect not necessarily needs any interlayer coupling.

In addition the results demonstrate that the *IrMn* layer not only induces an exchange bias but induces a dramatic anisotropy on the adjacent ferromagnetic layer, the better the lower the interlayer coupling. A minor addition of induced anisotropy can be attributed to the magnetic mask during the sputtering process, also resulting in a small induced anisotropy for the bottom magnetic layer.

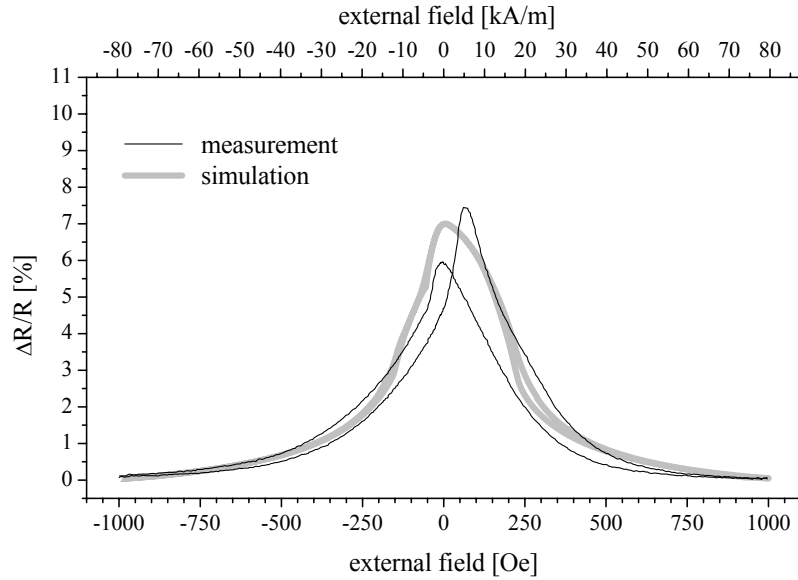


Figure 4.10: Spacer layer thickness $t_s = 0.9nm$, data for simulation: $K_2 = 1.5 kJ/m^3$, $K_3 = 4.0 kJ/m^3$, $K_{ind,2} = 0.0 kJ/m^3$, $K_{ind,3} = 0.0 kJ/m^3$, $J_L = -180 \mu J/m^2$, $J_Q = -45 \mu J/m^2$, $J_{eb} = 10 \mu J/m^2$, $A_{GMR} = 7.0\%$

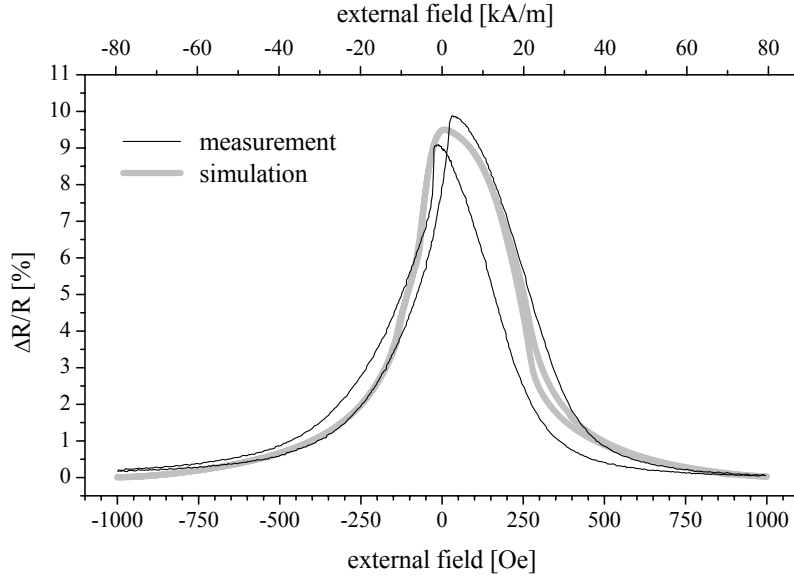


Figure 4.11: Spacer layer thickness $t_s = 1.0nm$, data for simulation: $K_2 = 1.5 kJ/m^3$, $K_3 = 4.0 kJ/m^3$, $K_{ind,2} = 0.0 kJ/m^3$, $K_{ind,3} = 0.0 kJ/m^3$, $J_L = -180 \mu J/m^2$, $J_Q = -36 \mu J/m^2$, $J_{eb} = 17 \mu J/m^2$, $A_{GMR} = 9.5\%$

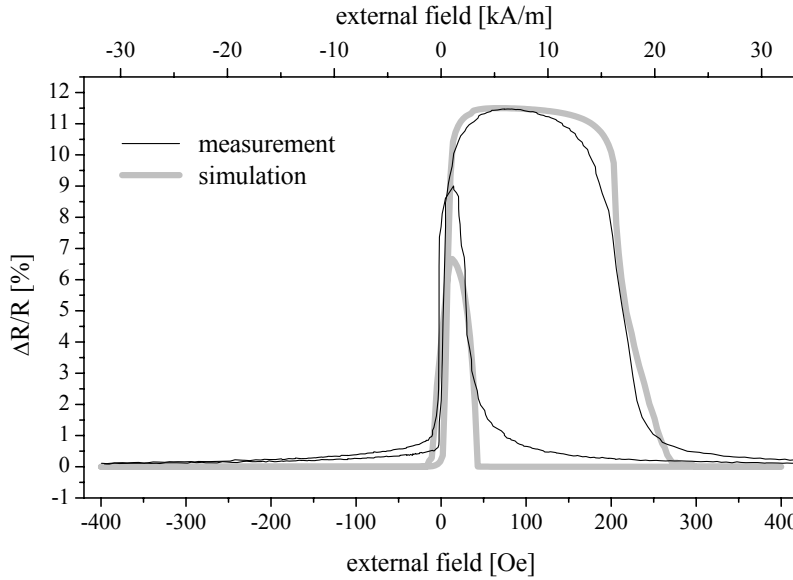


Figure 4.12: Spacer layer thickness $t_s = 1.1nm$, data for simulation: $K_2 = 1.5 kJ/m^3$, $K_3 = 2.0 kJ/m^3$, $K_{ind,2} = 0.5 kJ/m^3$, $K_{ind,3} = 9.0 kJ/m^3$, $J_L = -12 \mu J/m^2$, $J_Q = 0 \mu J/m^2$, $J_{eb} = 47 \mu J/m^2$, $A_{GMR} = 11.5\%$

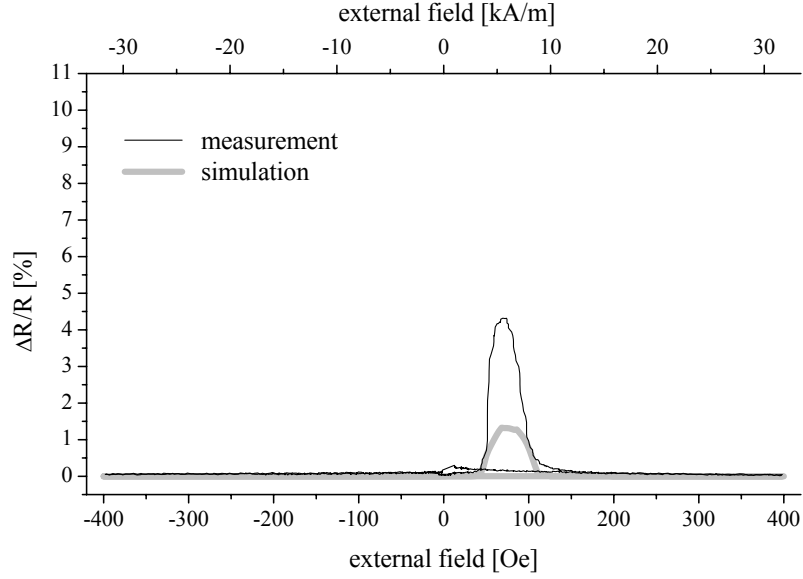


Figure 4.13: Spacer layer thickness $t_s = 1.3nm$, data for simulation: $K_2 = 0.5 kJ/m^3$, $K_3 = 1.5 kJ/m^3$, $K_{ind,2} = 1.5 kJ/m^3$, $K_{ind,3} = 9.0kJ/m^3$, $J_L = 25\mu J/m^2$, $J_Q = 0\mu J/m^2$, $J_{eb} = 47\mu J/m^2$, $A_{GMR} = 11.0\%$

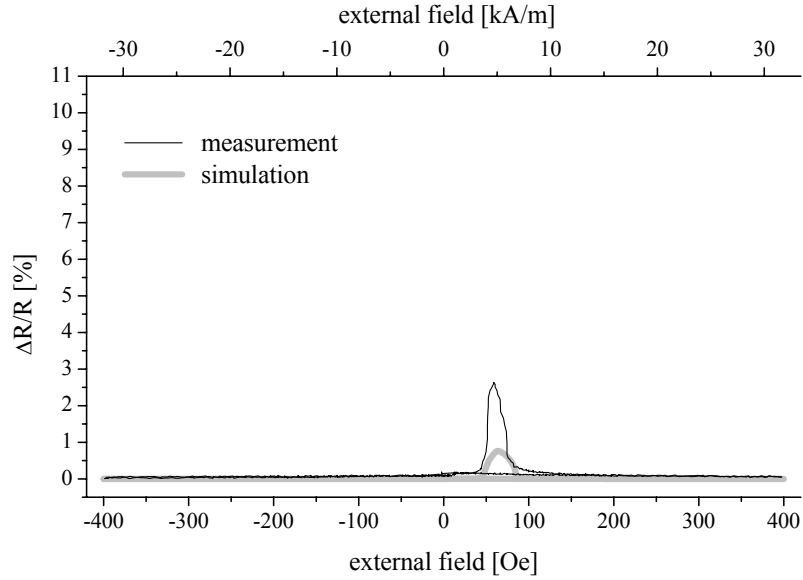


Figure 4.14: Spacer layer thickness $t_s = 1.55 nm$, data for simulation: $K_2 = 0.5 kJ/m^3$, $K_3 = 1.5 kJ/m^3$, $K_{ind,2} = 1.5 kJ/m^3$, $K_{ind,3} = 9.0kJ/m^3$, $J_L = 29\mu J/m^2$, $J_Q = 0\mu J/m^2$, $J_{eb} = 47\mu J/m^2$, $A_{GMR} = 10.6\%$

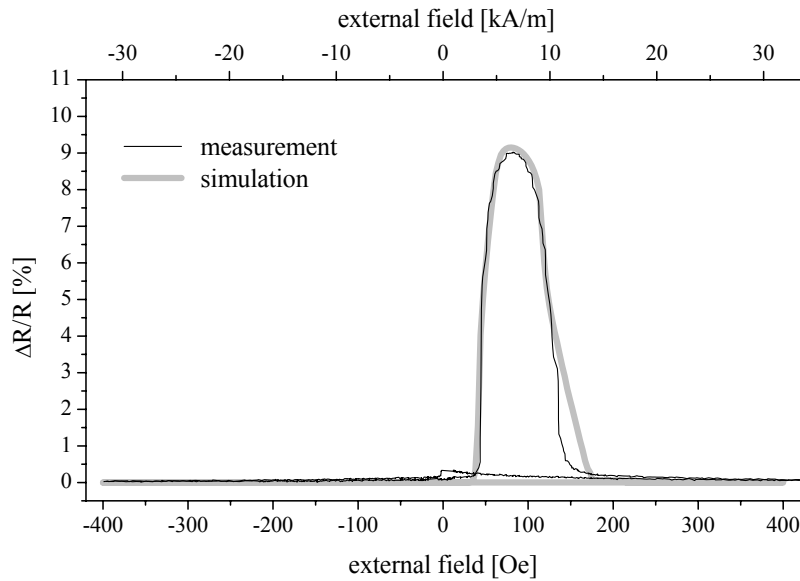


Figure 4.15: Spacer layer thickness $t_s = 1.65 \text{ nm}$, data for simulation: $K_2 = 0.5 \text{ kJ/m}^3$, $K_3 = 1.5 \text{ kJ/m}^3$, $K_{ind,2} = 1.5 \text{ kJ/m}^3$, $K_{ind,3} = 9.0 \text{ kJ/m}^3$, $J_L = 18 \mu\text{J/m}^2$, $J_Q = 0 \mu\text{J/m}^2$, $J_{eb} = 47 \mu\text{J/m}^2$, $A_{GMR} = 10.2\%$

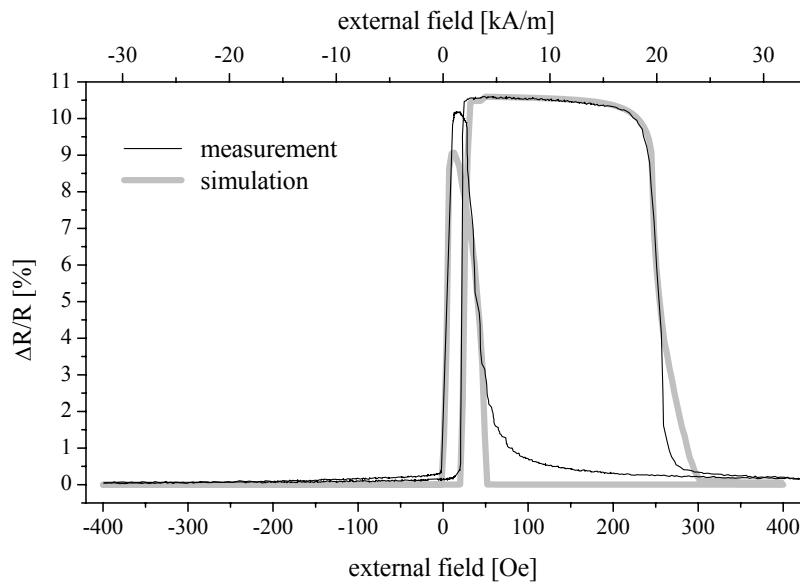


Figure 4.16: Spacer layer thickness $t_s = 1.83 \text{ nm}$, data for simulation: $K_2 = 0.5 \text{ kJ/m}^3$, $K_3 = 1.5 \text{ kJ/m}^3$, $K_{ind,2} = 2.0 \text{ kJ/m}^3$, $K_{ind,3} = 10.0 \text{ kJ/m}^3$, $J_L = 2 \mu\text{J/m}^2$, $J_Q = 0 \mu\text{J/m}^2$, $J_{eb} = 67 \mu\text{J/m}^2$, $A_{GMR} = 10.6\%$

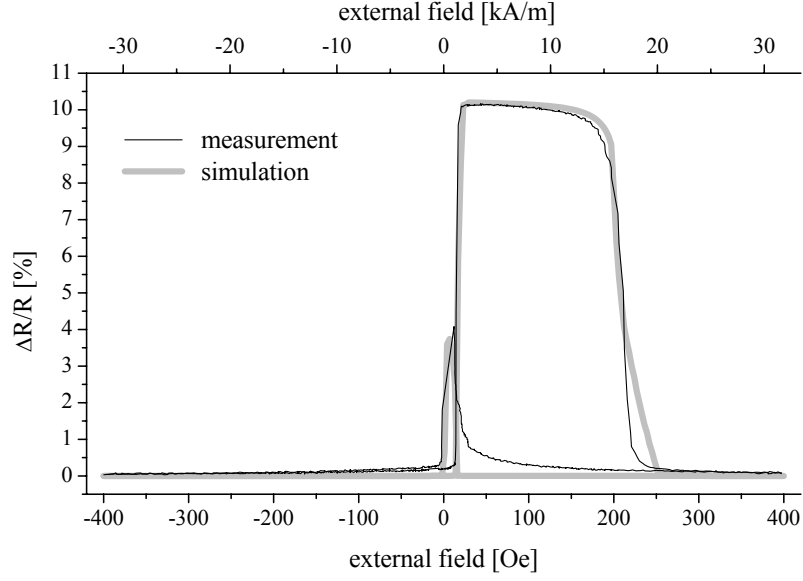


Figure 4.17: Spacer layer thickness $t_s = 1.88 \text{ nm}$, data for simulation: $K_2 = 0.5 \text{ kJ/m}^3$, $K_3 = 1.5 \text{ kJ/m}^3$, $K_{ind,2} = 1.5 \text{ kJ/m}^3$, $K_{ind,3} = 9.5 \text{ kJ/m}^3$, $J_L = -2 \text{ } \mu\text{J/m}^2$, $J_Q = 0 \text{ } \mu\text{J/m}^2$, $J_{eb} = 47 \text{ } \mu\text{J/m}^2$, $A_{GMR} = 10.2\%$

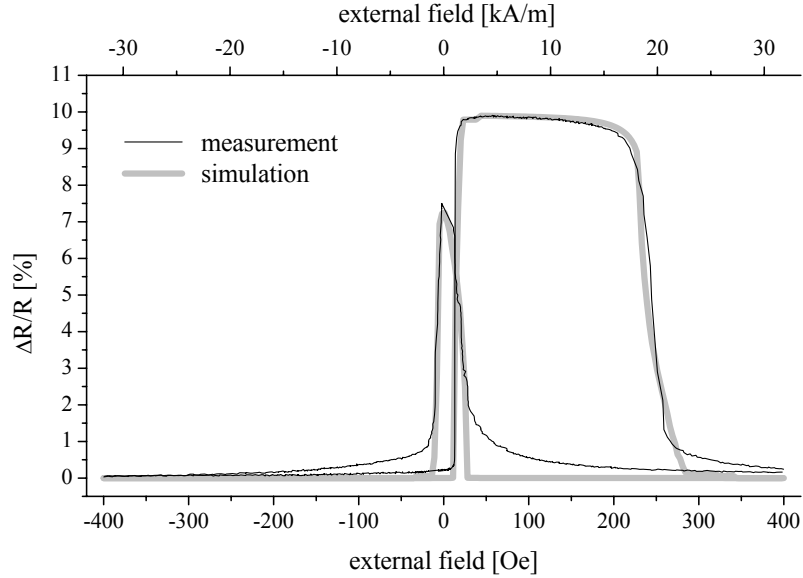


Figure 4.18: Spacer layer thickness $t_s = 1.92 \text{ nm}$, data for simulation: $K_2 = 0.5 \text{ kJ/m}^3$, $K_3 = 1.5 \text{ kJ/m}^3$, $K_{ind,2} = 2.0 \text{ kJ/m}^3$, $K_{ind,3} = 10.0 \text{ kJ/m}^3$, $J_L = -6 \text{ } \mu\text{J/m}^2$, $J_Q = 0 \text{ } \mu\text{J/m}^2$, $J_{eb} = 52 \text{ } \mu\text{J/m}^2$, $A_{GMR} = 9.9\%$

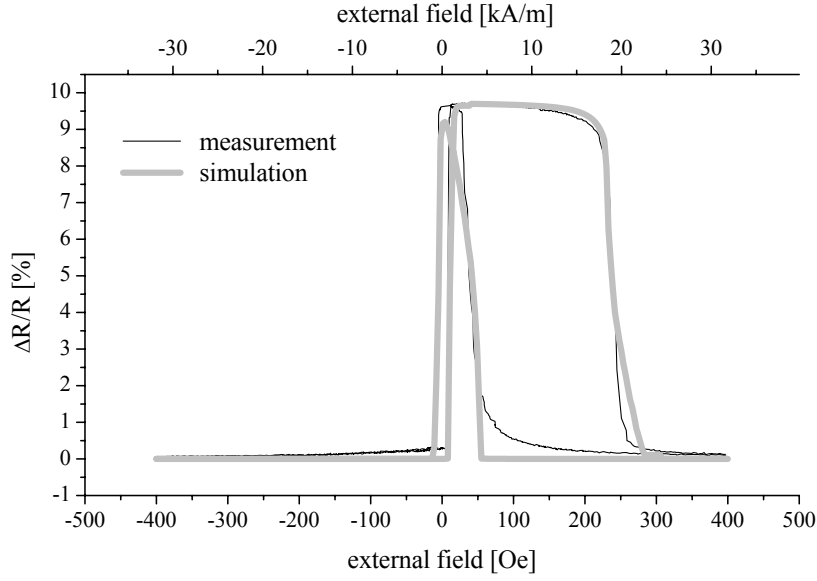


Figure 4.19: Spacer layer thickness $t_s = 2.07 \text{ nm}$, data for simulation: $K_2 = 0.5 \text{ kJ/m}^3$, $K_3 = 1.5 \text{ kJ/m}^3$, $K_{ind,2} = 1.5 \text{ kJ/m}^3$, $K_{ind,3} = 9.0 \text{ kJ/m}^3$, $J_L = -6 \text{ } \mu\text{J/m}^2$, $J_Q = 0 \text{ } \mu\text{J/m}^2$, $J_{eb} = 57 \text{ } \mu\text{J/m}^2$, $A_{GMR} = 9.7\%$

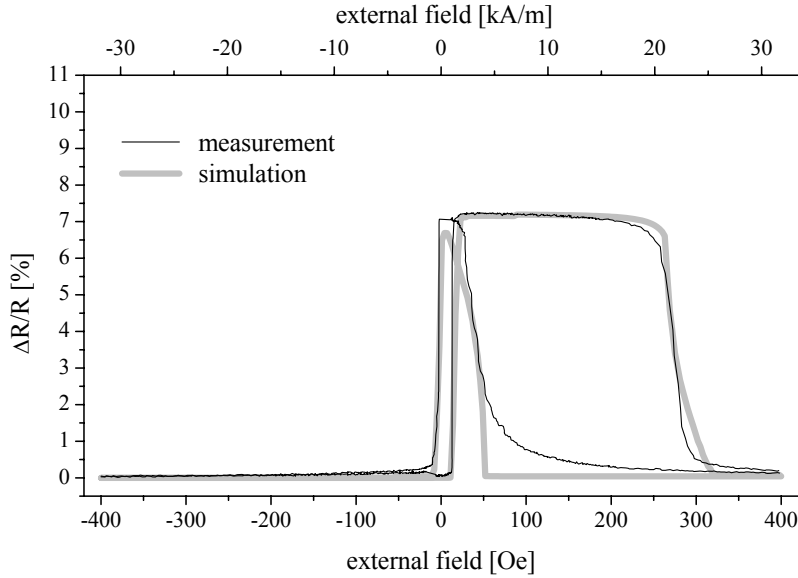


Figure 4.20: Spacer layer thickness $t_s = 2.95 \text{ nm}$, data for simulation: $K_2 = 0.5 \text{ kJ/m}^3$, $K_3 = 1.5 \text{ kJ/m}^3$, $K_{ind,2} = 1.7 \text{ kJ/m}^3$, $K_{ind,3} = 10.5 \text{ kJ/m}^3$, $J_L = 0 \text{ } \mu\text{J/m}^2$, $J_Q = 0 \text{ } \mu\text{J/m}^2$, $J_{eb} = 66 \text{ } \mu\text{J/m}^2$, $A_{GMR} = 7.2\%$

4.4.4 Comparison to RKKY-like Interaction

First data for the interlayer exchange coupling in interlayer coupled and magnetic trilayers were presented in section 3.7. These were calculated by means of Eq. 4.20 which is only valid for vanishing anisotropy. See section 4.1.5 for details. So the application for GMR characteristics beyond the first AFCM is questionable.

The simulation provided us with more reliable data for the interlayer coupling constant J_L , which will now be compared with the theoretical dependence of J_L to the spacer layer thickness t_s . Reducing Eq. 2.43 to one critical vector and adding an exponential term so as to consider possible diffuse scattering within the spacer layer (see section 2.4.5) we yield:

$$J_L(t_s) = \frac{J_0}{t_s^2} \sin\left(\frac{2\pi}{\Lambda} \cdot t_s + \phi\right) \exp\left(-\frac{t_s}{\lambda_0}\right) \quad (4.27)$$

The GMR amplitude decreases rapidly at about 0.9 nm for further decreasing spacer layer thickness although the maximum of the first AFCM is not passed. Here defects (pin holes) and orange peel coupling give rise to a strong ferromagnetic coupling which is not described by the RKKY-like interaction. Therefore we have no reliable data point for the maximum interlayer coupling (due to RKKY-like interaction) for the first AFCM.

The high ferromagnetic coupling between first and second AFCM suppresses the GMR effect from 1.3 nm to 1.6 nm . Here the highest values of the ferromagnetic coupling has to be assumed but GMR measurements are not sensitive to this effect.

In the second AFCM the amplitude has decreased already drastically. However an interval of ferromagnetic coupling at about $t_{Cu} = 1.9 \text{ nm}$ can be determined before a third AFCM is developed.

Due to this limitations a meaningful fit based on (4.27) and the data is not possible. Fig. 4.21 shows the $J_L(t_s)$ -graph for $J_0 = 400 \mu\text{J}/\text{m}^2$, $\Lambda = 1.1 \text{ nm}$, $\phi = -0.7$ and $\lambda_0 = 0.9 \text{ nm}$ with the results of the simulation. A single oscillation period of about 1.1 nm corresponds well with the theoretical prediction of for Cu (111) as discussed in section 2.4.3.

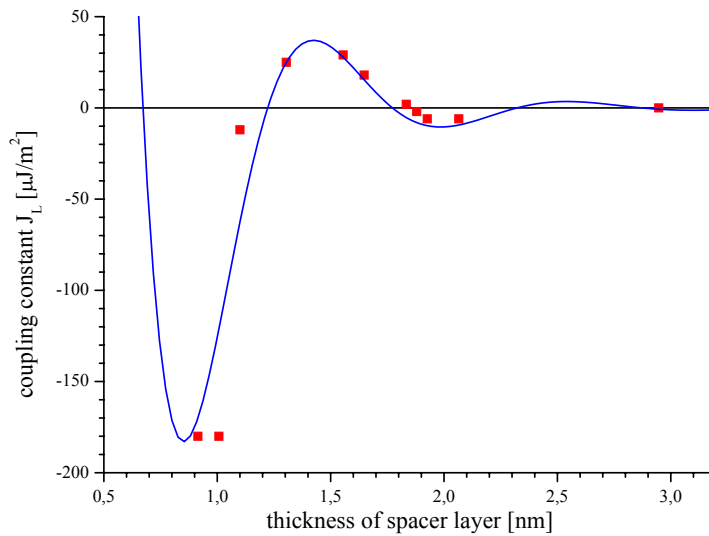


Figure 4.21: Comparison of model and simulation for $J_L(t_s)$ for the system $(Ni_{80}Fe_{20})_{3.9\text{ nm}} - Co_{2.7\text{ nm}}/Cu_t/Co_{2.7\text{ nm}}/IrMn_{9.0\text{ nm}}$. The parameters are given in the text.

4.5 Conclusion

In this chapter a new model for the magnetization reversal in layered GMR systems was presented (section 4.1). It is an extension of a model by E. C. Stoner and E. P. Wohlfarth which has been applied to layered magnetic devices for the first time by H. Holloway and D. J. Kubinski. A large number of further extensions and adjustments have been carried out to fulfill new demands.

Based on this model a new simulation procedure was proposed section 4.2 and implemented in the simulation program GRMSim. The comparison to available programs based on micro magnetic simulations (section 4.3) showed impressively that the simulation tool GRMSim is a more feasible tool in the hand of an experimentalist. The input from experimental results enables the determination of proper anisotropy constants and testing of newly designed stacking sequences within an acceptable time period.

The application of GRMSim to interlayer coupled and pinned trilayers (section 4.4) proofed the explanatory power of the new simulation tool. The results confirmed the statements concerning the GMR system under investigation presented in the previous chapter (chapter 3). It provided us with a deeper understanding of the influence of crystalline and induced anisotropy, exchange bias, and interlayer coupling (section 4.4.4) on the GMR characteristic.

Chapter 5

New Sensor Concepts – Application of the Gained Knowledge

This chapter reports on the cooperation with HL Planartechnik GmbH, Dortmund, within the framework of the *Robert Bosch GmbH Leitprojekt Magneto-Elektronik*. Aim of the project is the transfer of laboratory results to the MST¹² production of a medium sized company. Knowledge in the following areas is of special interest:

- Determination of the optimal materials and stacking sequences.
- Simulation of GMR characteristics prior to the experimental realization based on input parameters from a large set of experimental data. The simulation tool GMRSim is here especially valuable to realize customer specific characteristics.
- Experience in preparation parameters and pinning techniques.

The results of the fundamental research on interlayer coupled magnetic trilayers and the experimental and theoretical analyzing techniques as reported in the previous chapters is now used to address new concepts for sensors.

5.1 Introduction

The most common sensing circuit in electrical sensors measuring resistance is the Wheatstone bridge¹³. Its basic configuration is shown in Fig. 5.1. In

¹²Micro System Technology

¹³Proposed by Ch. Wheatstone in 1843

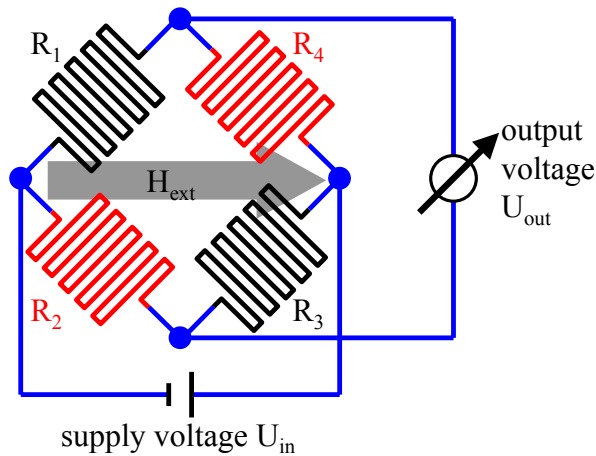


Figure 5.1: Scheme of the use of a Wheatstone bridge in a magnetic sensors. The resistance of the equally colored resistors should be identical.

an ideal system the resistance of one pair of resistors depends on an external field whereas the two other do not reply to any magnetic field. For other physical influences such as temperature, deterioration or electrical fields the answer of all resistors should be identical. This assures a sensor which is solely sensitive to the signal in question, the external magnetic field.

For sensors based on GMR different concepts have been proposed and realized beforehand:

Magnetic shielding: Two resistors placed on opposite branches of the bridge are shielded by a metal layer of high permeability, e.g. $Ni_{80}Fe_{20}$. This is the common technique for sensors based on the AMR-effect.

Alternating pinning direction: Instead of defining the pinning direction during a heat treatment in a magnetic field after the coating process, the pinning layer can be aligned during the sputtering process as demonstrated in chapter 3. So by producing every second sensor element in a second run with the magnetic field turned by 90° in the layer plane a chess board structure is realized.

Consecutive modification of the pinning direction: The alignment of the pinning layer is turned by 90° for two corresponding branches of the bridge consecutive to the sputtering process, e.g. by ion implantation [Fas03].

Here a completely different aspects has to be taken into consideration. From an economic point of view it is not reasonable for small and medium-sized

enterprises to operate their own sputtering plants, which are suitable for GMR elements. On the other hand institutes and universities do not have sufficient capacities in the structuring and housing processes as well as in the added electronics. Therefore it would be highly desirable to develop a process in which structuring, sputtering, connection to electronics (SMT), and housing are well separated.

This excludes the first two of the concepts specified above. The third concept is quite cost-intensive and has not been proven to be resistant against ageing.

In the course of the cooperation with HL Planartechnik two new concepts have been proposed and thoroughly investigated.

Exploitation of shape anisotropy: For very small GMR structures it is much easier to change the magnetization, when the field is applied parallel to the lines of the sensor element than for normal alignment (see section 5.3).

Heat treatment: When two corresponding branches are locally heated by an electric current through the sensor element, diffusion of the metallic layers makes these elements much less sensible to the magnetic field than the untreated segments (see section 5.5).

5.2 Answer of a Wheatstone Bridge

When a Wheatstone Bridge is connected to a supply voltage U_{in} as given in Fig. 5.1 the ratio of the output voltage U_{out} to U_{in} is given by

$$\frac{U_{out}}{U_{in}} = \frac{R_1}{R_1 + R_2} - \frac{R_4}{R_3 + R_4} = \frac{R_1 R_3 - R_2 R_4}{(R_1 + R_2)(R_3 + R_4)}. \quad (5.1)$$

If the resistors R_i are changed by ΔR_i and assuming that ΔR_i is much smaller than R_i Eq. (5.1) becomes

$$\frac{U_{out}}{U_{in}} = \frac{1}{4} \left(\frac{\Delta R_1}{R_1} - \frac{\Delta R_2}{R_2} + \frac{\Delta R_3}{R_3} - \frac{\Delta R_4}{R_4} \right). \quad (5.2)$$

If we further assume that the basic resistance is identical for all sensors and equal to R , that the resistance of the reference resistors R_2 and R_4 is not changed ($\Delta R_2 = \Delta R_4 = 0$) and that the change of the resistors 1 and 3 is identical ($\Delta R_1 = \Delta R_3 = \Delta R_{13}$) Eq. (5.2) can be further simplified to yield:

$$\frac{U_{out}}{U_{in}} = \frac{1}{2} \frac{\Delta R_{13}}{R} \quad (5.3)$$

This shows that the signal amplitude of a Wheatstone bridge reduces the original signal to half its amplitude but therefore eliminates disturbing noise due to temperature variation, additional electric and magnetic fields and so on depending on its layout details.

5.3 Exploitation of Shape Anisotropy

5.3.1 Initial Considerations

Before designing test structures it has to be evaluated in which range of line widths shape anisotropy might be relevant. Here two plots will be presented to demonstrate the applicability of the simulation program GMRSim (see chapter 4). The GMR characteristic of a $NiFe_{2.1\text{ nm}}/\{Cu_{0.37\text{ nm}}/NiFe_{1.6\text{ nm}}\}_{20}$ -multilayer was calculated and compared to a related measurement (Fig. 5.2). In a second step the line widths in the simulation was consecutively reduced to $0.5\ \mu\text{m}$. See Fig. 5.3 for details.

The results suggest that shape anisotropy becomes important for structure sizes below $10\ \mu\text{m}$. On the other hand a simple and therefore cost-saving mask technique can only be used for line widths of about $1\ \mu\text{m}$ and above. Therefore we decided for test structures of $100\ \mu\text{m}$ down to $1\ \mu\text{m}$.

5.3.2 Test Structures

The structures were produced from GMR trilayer systems with laser lithography in a lift-off process. One element consists of two meanders, whose lines were turned by 90° to each other. The line widths was varied from $100\ \mu\text{m}$ to $1\ \mu\text{m}$. See figures 5.4 and 5.5 for details.

The meanders produced by lift-off technique show in SEM pictures, e.g. Fig. 5.5, a well defined line structure. The effective line widths is given by the nominal line widths plus $1.9\ \mu\text{m}$ due to the photoresist. After optimizing the structuring process with reference to the line widths and edge quality using a different photoresist the offset was reduced to $0.7\ \mu\text{m}$.

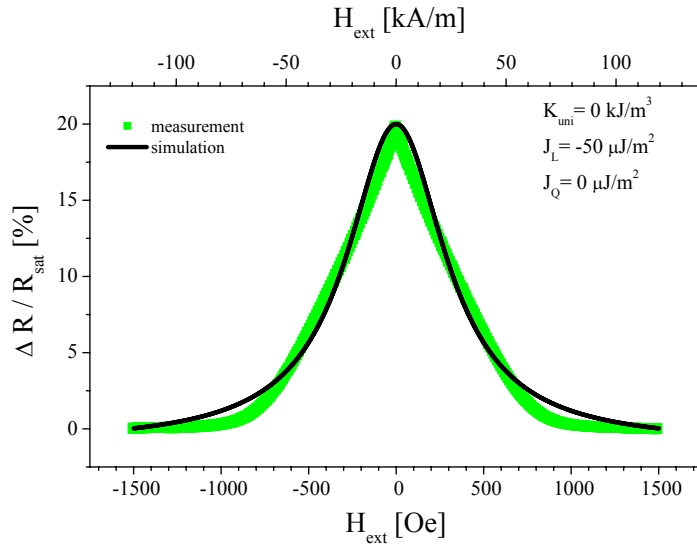


Figure 5.2: Measured and simulated GMR characteristic of a $NiFe_{2.1\text{ nm}} / \{Cu_{0.37\text{ nm}} / NiFe_{1.6\text{ nm}}\}_{20}$ -multilayer.

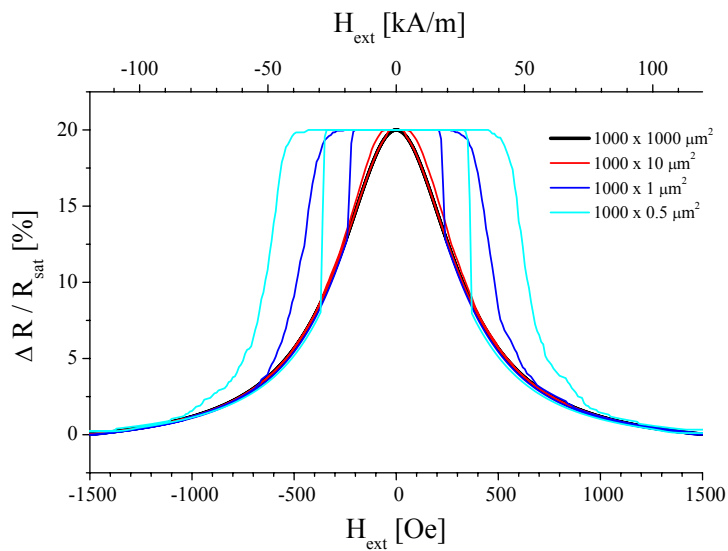


Figure 5.3: Simulation of the GMR characteristic for the $NiFe_{2.1\text{ nm}} / \{Cu_{0.37\text{ nm}} / NiFe_{1.6\text{ nm}}\}_{20}$ -multilayer with consecutively reduced line widths.

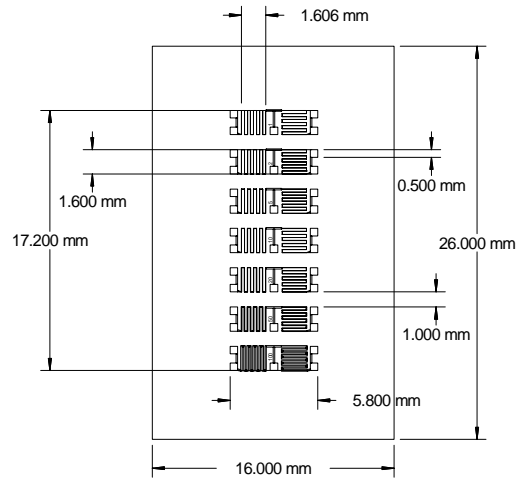


Figure 5.4: The design of the elements, each consisting of two meanders rotated by 90° to each other. At both ends two pads have been added to allow for contacting current and voltage for a four point resistance measurement, an extra voltage contact was added between the two meanders to allow for separate measurements of a single meander.

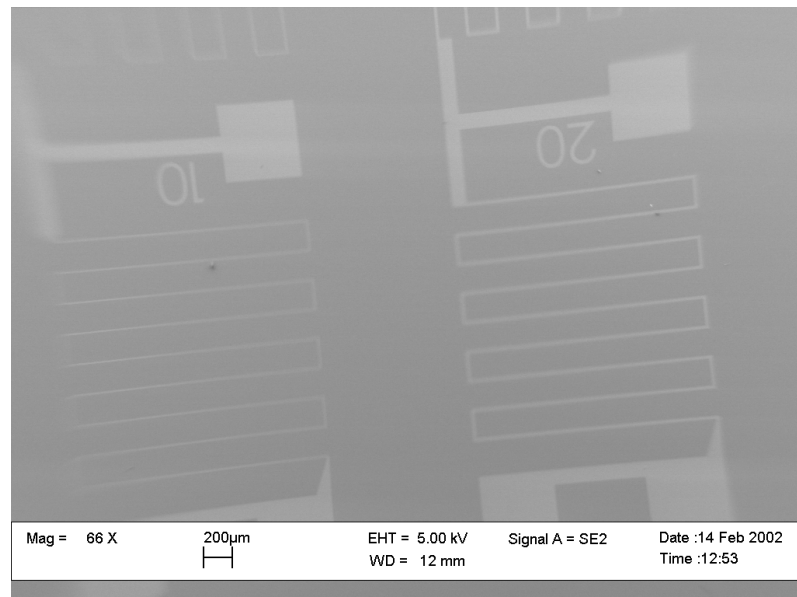


Figure 5.5: The used meander structure in the SEM picture.

nominal width [μm]	effective width [μm]	absolute resistance [$k\Omega$]	sheet resistance [$\mu\Omega m$]
1	1.7	430	0.30
2	2.7	284	0.32
5	5.7	134	0.31
10	10.7	68	0.30
20	20.7	36	0.31
50	50.7	16	0.33
100	100.7	8	0.32

Table 5.1: Absolute and sheet resistance of the meanders as function of the line width.

5.3.3 Measurement of Resistance

The absolute resistance was determined for an element length L of $33mm$. The sheet resistance was calculated for a height h of $13.6nm$ and the effective width w .

$$R_{sheet} = \frac{h \cdot b \cdot R_{abs}}{L} \quad (5.4)$$

Table 5.1 gives the measured and calculated values. The results for the sheet resistance confirm a good layer and structuring quality.

5.3.4 Measurement of GMR Characteristics

The used trilayer system was $NiFe_{3.3nm} - Co_{4.2nm} / Cu_{2.4nm} / Co_{3.7nm}$ with an original GMR-effect of about 8%. The measurements of the test elements were performed in a four point geometry for three combinations of connection (see Fig. 5.6 for details):

total: Measurement of the whole structure.

top: Measurement of the top meander.

bottom: Measurement of the bottom meander so that the two characteristics ‘top’ and ‘bottom’ belong to meander lines which are aligned normally to each other.

Each measurement was done for the external magnetic field H_{ext} applied in 0° direction with $H_{max} = 150 Oe$ and in 90° direction with $H_{max} = 250 Oe$ and

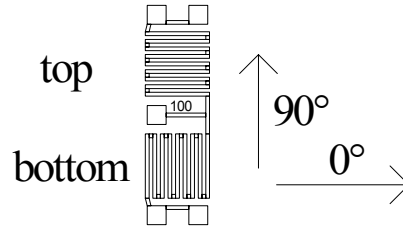


Figure 5.6: Sketch of measurement geometry.

therefore parallel to the lines of the top and bottom meander, respectively. This results in six measurements for each test element.

When regarding the characteristics for a line widths of $100\ \mu\text{m}$ (Fig. 5.7) we see that the shape depends on the direction of the external field, but not on the alignment of the meander with reference to the external field. This becomes more obvious when the same data are sorted differently as in Fig. 5.8.

The shape anisotropy becomes important for structure sizes below $10\ \mu\text{m}$. In Fig. 5.9 the results for the $5\ \mu\text{m}$ test structure are given as an example.

5.3.5 Results

For a structure size larger than $10\ \mu\text{m}$ there are no significant differences for top and bottom meander of the test structure as far as effect amplitude, sensitivity, saturation magnetization or hysteresis are concerned. On the other hand there is an obvious alteration in the characteristic when the external field is rotated by 90° for *both* meanders. This cannot be attributed to shape anisotropy, but is a clear evidence for an uniaxial in-plane anisotropy, which was induced during the sputtering process although no external field was applied on purpose.

For line widths below $10\ \mu\text{m}$ we have to state in general that GMR amplitude and sensitivity decrease, saturation field and hysteresis increase with further decreasing structure sizes. As example see Fig. 5.10 for the parameters of the top meander.

For the smallest line widths under investigation the influence of shape anisotropy becomes important. GMR amplitude, crossover and saturation field are higher for normal alignment of current (lines of meander) and external field as for parallel alignment.

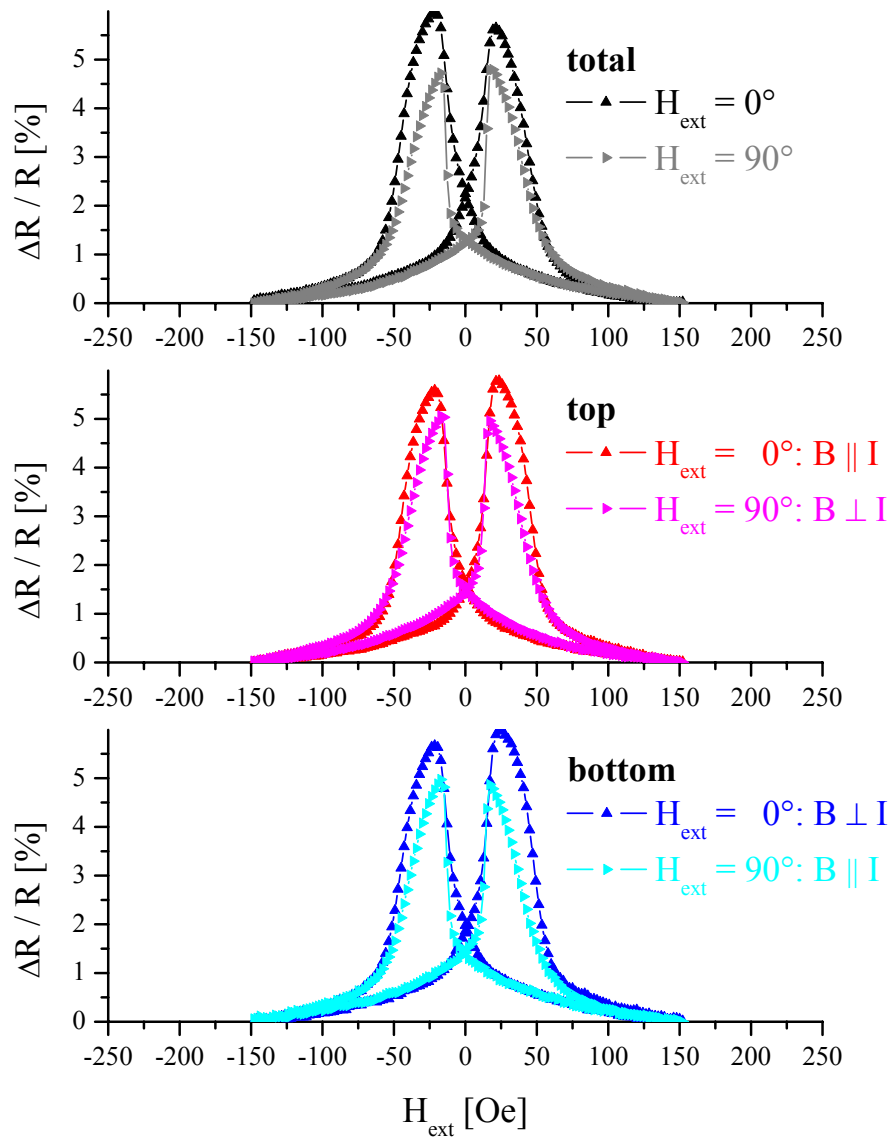


Figure 5.7: GMR characteristic of a meander with a line width of $100 \mu\text{m}$, sputtered without an external field.

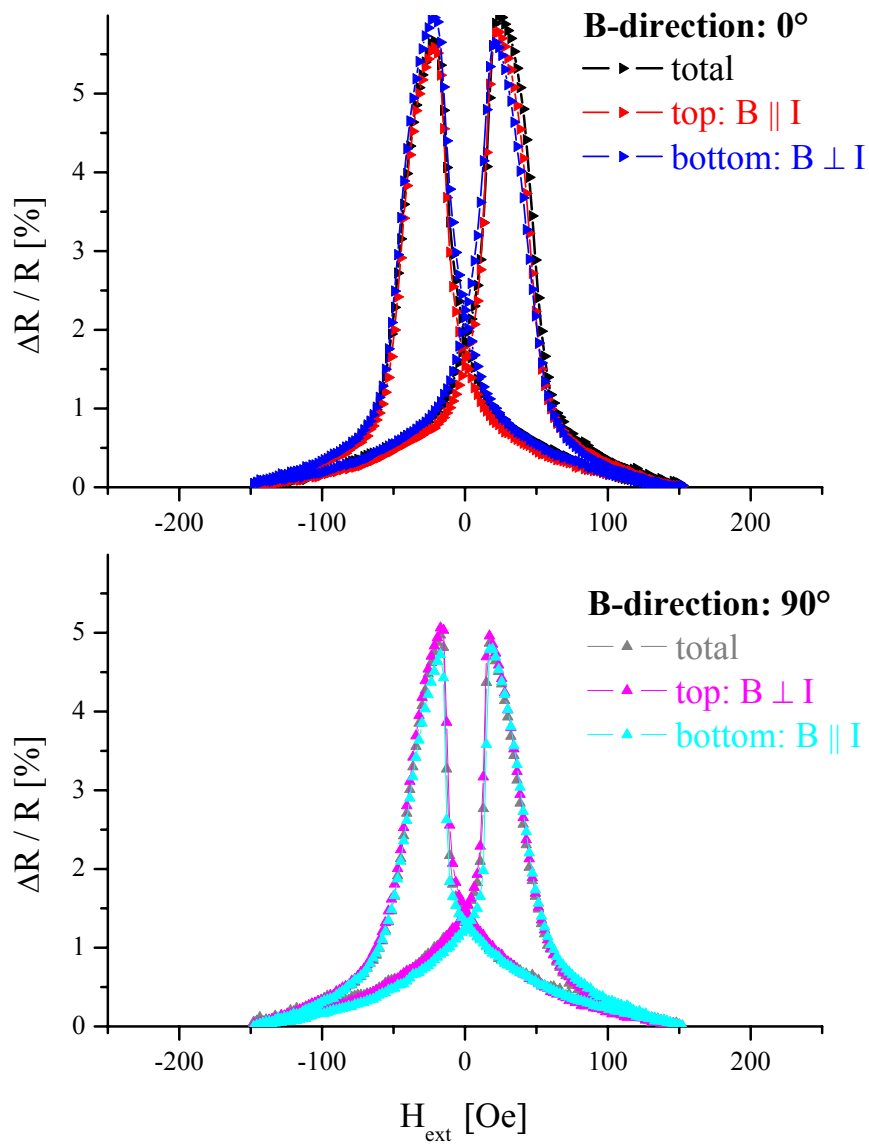


Figure 5.8: GMR characteristic of a meander with a line width of $100 \mu\text{m}$, sputtered without an external field. Alternative plot of data presented in Fig. 5.7.

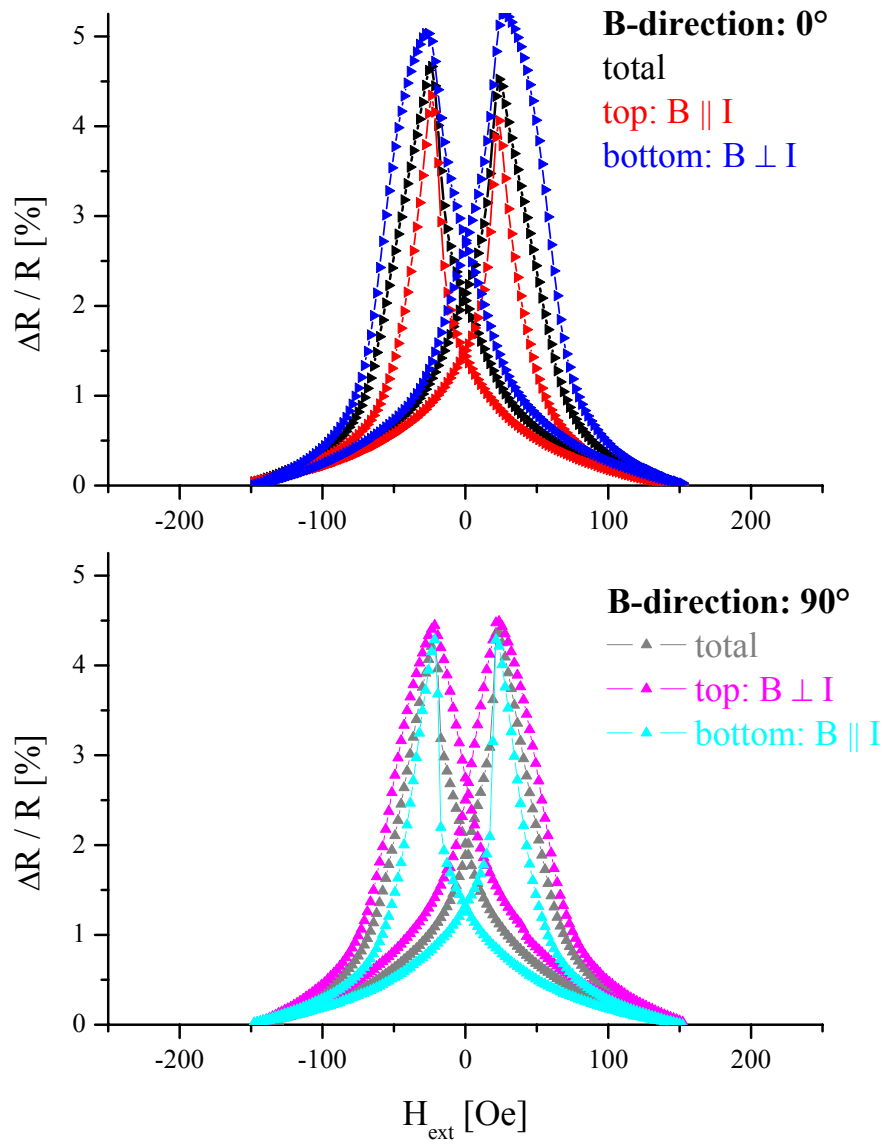


Figure 5.9: GMR characteristic of a meander with a line width of $5 \mu\text{m}$, sputtered without an external field.

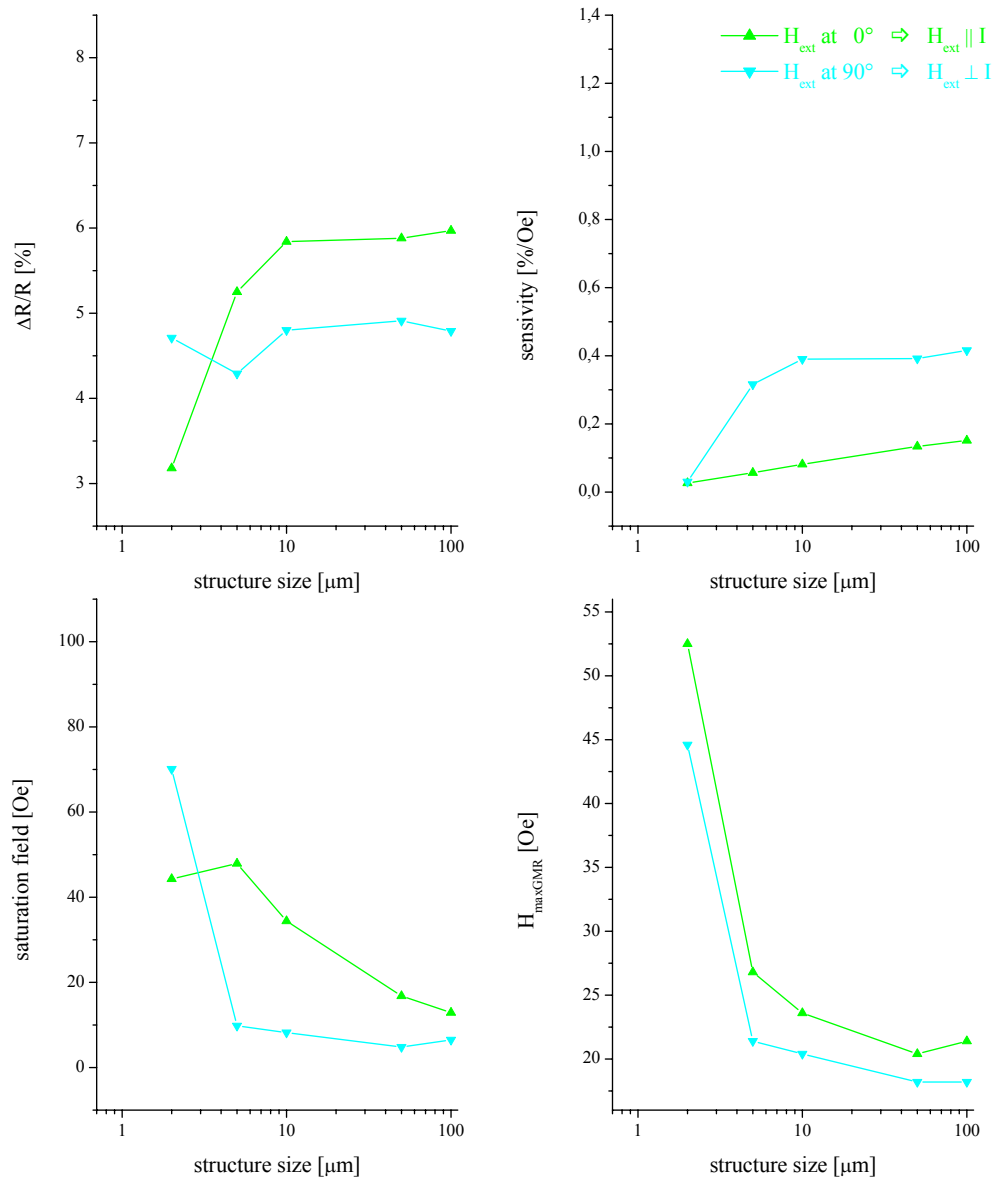


Figure 5.10: GMR amplitude, sensitivity, saturation magnetization and external field at maximum amplitude as function of the line widths for the top meander. Samples sputtered without an external field.

5.3.6 Enhancement of Sputter Anisotropy

The results presented above can be made more obvious when the anisotropy induced during the sputtering process is enhanced. An additional external field in the 0° direction is applied during the deposition process by means of a magnetic mask (see Fig. 3.5).

The characteristic parameters effect amplitude, sensitivity, saturation magnetization and hysteresis are plotted in Fig. 5.11. The general trend is identical to the results presented in 5.3.5. Significant is the higher GMR amplitude and sensitivity for these samples.

The difference for top and bottom meander is presented here exemplary for the $1\ \mu\text{m}$ test element in Fig. 5.12.

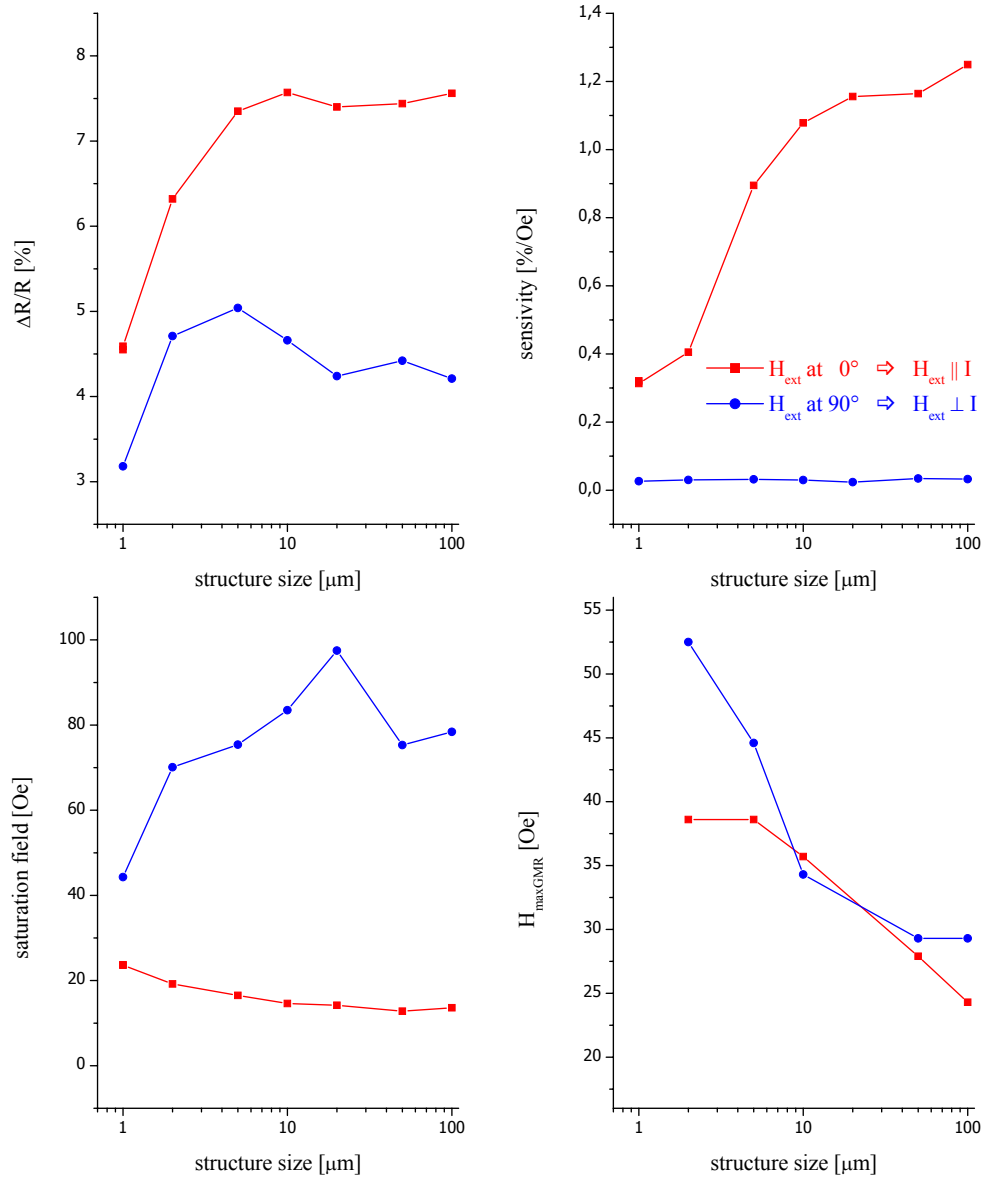


Figure 5.11: GMR amplitude, sensitivity, saturation magnetization and external field at maximum amplitude as function of the line widths for the top meander. Samples sputtered in an external field.

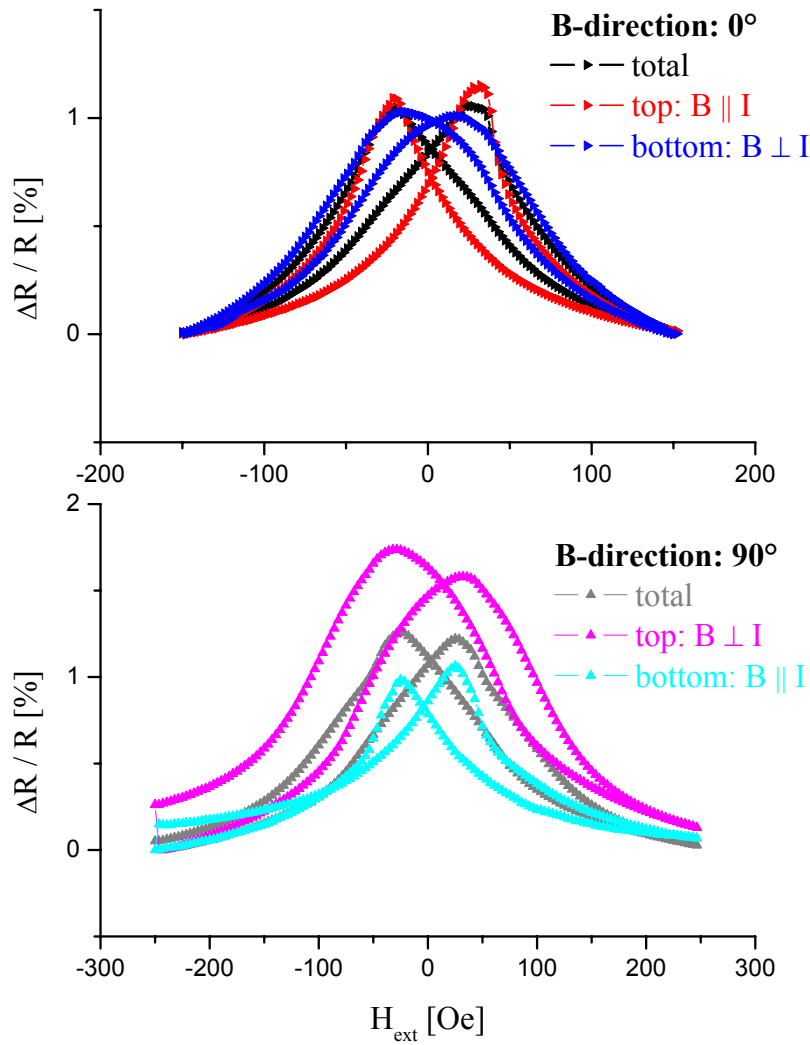


Figure 5.12: GMR characteristic of a meander with a line width of $1 \mu\text{m}$, sputtered in an external field.

5.4 Optimized Test Structures

To conclude the investigations on shape anisotropy and for further investigations reported below a wafer process for GMR test structure was developed following the AMR process which is well established at HL Planartechnik. Therefore the structuring process was done at HL Planartechnik, the GMR layers were developed and sputtered at the University of Bielefeld.

5.4.1 Processes

Sets of masks were produced for three processes, so that different realizations of Wheatstone bridges could be tested. The processes are sketched in Fig. 5.13.

Process 1: We start with the deposition and structuring of pads, immediately followed by the GMR layers. It has to be checked that the surface of the substrates is not altered during the first step, so that the GMR characteristic keeps unchanged. The structuring of the GMR layers is done by conventional dry etching. In the next step we add feed lines by lift-off technique. This conserves the GMR layers as the photo resist can be removed with acetone or a not too aggressive remover. Finally we passivate the wafer and open the pads.

Process 2: This process differs from process 1 in an additional step for a second GMR layer. That gives us the possibility to deposit two GMR layers with different reference directions.

Process 3: Here two different pinning layers can be realized.

Besides marks for adjustments the set of masks included 16 different test elements from simple test stripes to complete GMR sensors. For examples see Fig. 5.14.

By means of test samples it can be stated that the GMR amplitude is not altered during this production process.

Process section	Process 1	Process 2	Process 3
(1) Cracks Etching of cracks			
(2) Pads Deposition and structuring of pads			
(3) GMR layer system Deposition of GMR layers			
(3.1) GMR layer system 1 Deposition of GMR(1) and lift-off			
(3.2) GMR layer system 2 Deposition of GMR(2) and lift-off			
(4) GMR structures Structuring of GMR layers			
(5.1) AF 1 Deposition of AF(1) and lift-off			
(5.2) AF 2 Deposition of AF(2) and lift-off			
(6) Leads Deposition of leads			
(6.1) Leads lift off for leads			
(7) Passivation Deposition of passivation layer, opening			

Figure 5.13: Three processes for structuring test wafers.

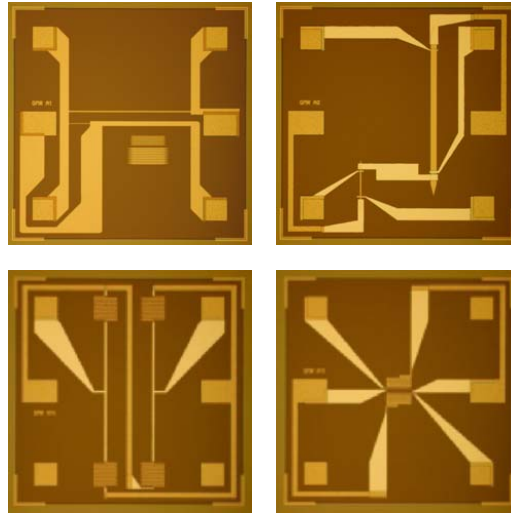


Figure 5.14: Different test structures on the mask set.

5.5 Interdiffusion by Local Heat-Treatment

To yield a bridge circuit on a completely processed wafer a local annealing treatment on two of the four branches of the bridge was considered. Aim of the investigation was to determine if it is possible to yield an irreversible change in the GMR amplitude of two of the four resistors of the bridge without altering the overall resistance.

5.5.1 Realization

A capacitor of $C = 10 \mu F$ was discharged via a stripe of $10 \times 200 \mu m^2$ on the GMR test mask (see section 5.4). The resistance of the stripe of about 60 to 70Ω and a series resistance of 33Ω result in a time constant τ of about $1 ms$. The energy released in the stripe was estimated according to $E = \frac{1}{2} C U^2$, where $\frac{1}{3}$ of the energy was released in the series resistance.

In the first series the stripe was exposed to single pulses of increasing charging voltages of the capacitor. After every pulse the GMR characteristic was measured. This process was continued until the stripe was burned out. In a second series salvos of 20 pulses with a delay of $1 s$ were given on the test structure.

As reference a second, not heated stripe of $50 \times 990 \mu m^2$ on the same test chip was measured.

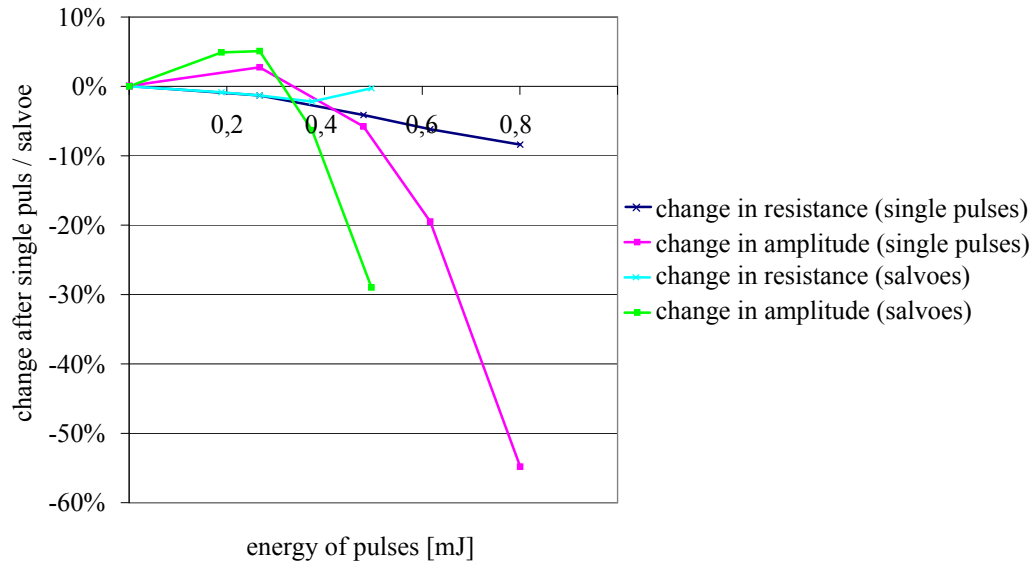


Figure 5.15: GMR amplitude and resistance as function of the pulse energy for the $NiFe - Co_{2.1\text{ nm}} / \{Cu_{1.6\text{ nm}} / Co_{2.1\text{ nm}}\}_{20}$ -multilayer.

5.5.2 Results on Cu/Co-Multilayers

For single pulses the element consisting of a $NiFe - Co_{2.1\text{ nm}} / \{Cu_{1.6\text{ nm}} / Co_{2.1\text{ nm}}\}_{20}$ -multilayer was destroyed when the energy reached about $1\ \mu J$. During the salvo with a pulse energy of $0.8\ \mu J$ the second stripe was destroyed. We yield a destroying energy density of 0.4 to $0.5\ \mu J / \mu m^2$.

The GMR amplitude of the Cu/Co-multilayer was permanently altered. Note that at the beginning the amplitude increases by 3 to 5% of the original effect amplitude (Fig. 5.15). For higher pulse energies the amplitude decreases. But before the GMR effect vanishes completely the stripes are demolished, independently of whether they were heated with single pulses or salvoes of 20 pulses (Fig. 5.16).

The destruction of the stripes occurred in very small regions. This suggests that it came to a local overheating due to a small constriction. A temperature depending increase in resistance results in an increasing power loss which again results in excessive heat. At this hotspots it came to a melting of the GMR layers, most probably accompanied by an oxidation process and therefore to a complete destruction of the test element.

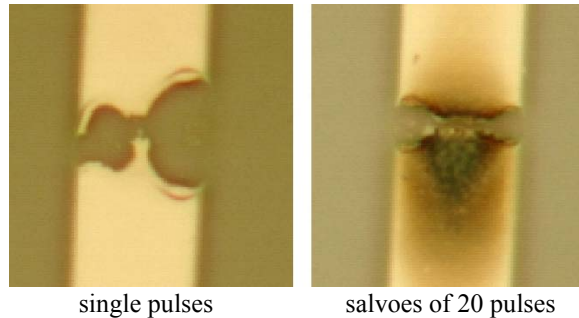


Figure 5.16: Hotspots on the Cu/Co-multilayer.

5.5.3 Results on Cu/NiFe-Multilayers

For Cu/NiFe-multilayers the time constant τ can be calculated to 2 ms for a stripe resistance of $150\ \Omega$ and a series resistance of $33\ \Omega$. As for the Cu/Co-multilayers we carried out two series, one with single pulses and a second with salvoes of 20 pulses.

An initial increase in the GMR amplitude was as well observed before it started to decrease (Fig. 5.17 and 5.18). The resistance and the GMR amplitude of the not heated reference element remained unchanged.

Note the astonishingly high stability against single pulses. For the first time the GMR amplitude could be almost completely eliminated before hotspots arose. This might be explained by the much longer time constant of the pulses due to the higher resistance of the test stripe. Heat capacity and heat conductivity of the material surrounding the stripe reduce the probability of developing hotspots.

5.5.4 Perspective for Local Annealing

The investigation demonstrate that GMR-bridges can be realized in principal by local annealing. As a conclusion and as design rules for GMR bridges processed by local annealing we can state:

- To prevent the formation of hotspots only straight, evenly wide GMR stripes connected by well conducting bridges should be used. Ends of meanders from GMR material will presumably form starting points for hotspots due to partially high current densities. To yield equally distributed current densities it is advisable to use as broad stripes as possible because of geometrical irregularities due to the patterning process.

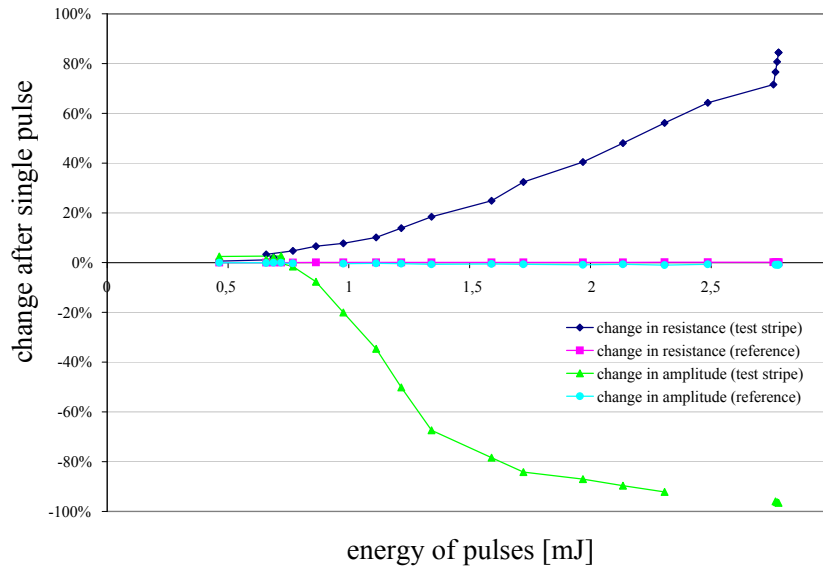


Figure 5.17: Change in GMR amplitude and resistance as function of the pulse energy for the Cu/NiFe-multilayer for single pulses.

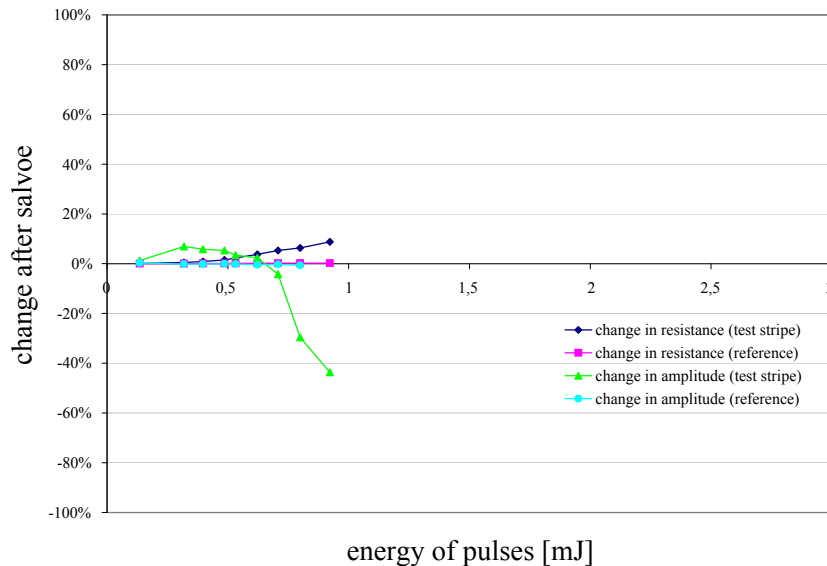


Figure 5.18: GMR amplitude and resistance as function of the pulse energy for the Cu/NiFe-multilayer for salvos of 20 pulses.

- If the distances between two stripes is small compared to their widths very short impulses and long delay times should be used. So the inner area of the meander won't reach much higher temperatures as the outer region.
- There must be a safety margin between annealed and uninfluenced structures which should be at least as wide as some normal distances of meanders.

In Fig. 5.19 the characteristic of a whole Wheatstone bridge is plotted for two different stacking sequences of the GMR system. For this simple test structure the output voltage is doubled compared to a similar bridge based on AMR technology.

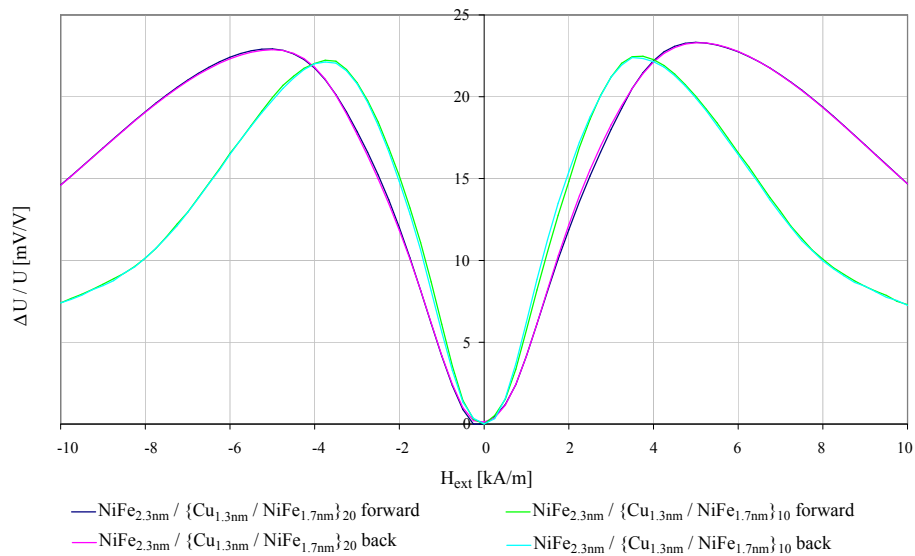


Figure 5.19: GMR characteristics of Wheatstone bridges of test stripes of $8 \times 2 \mu\text{m}^2$: (a) $NiFe/\{Cu_{1.3\text{nm}}/NiFe_{1.7\text{nm}}\}_{10}$, (b) $NiFe/\{Cu_{1.3\text{nm}}/NiFe_{1.7\text{nm}}\}_{20}$. The magnetic field was directed normal to the stripes.

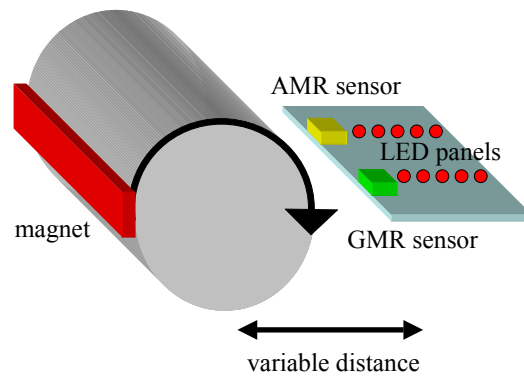


Figure 5.20: Sketch of the demonstrator device for GMR- and AMR sensor.

5.6 Demonstrator Device for GMR Sensors

To show the advantages of GMR sensors to AMR sensors used today a demonstrator device was constructed. It consists of an AMR and a GMR sensor mounted on a movable slab to vary the distance to a rotating cylinder with magnets. The output signal of the sensors is electronically processed and displayed on a diode array. See Fig. 5.20 for a sketch of the design and Fig. 5.22 for a photo of the demonstrator device.

After the wafer was fully processed the sensor elements were separated, mounted on ceramic substrate, and the pads bonded to feed lines (Fig. 5.21).

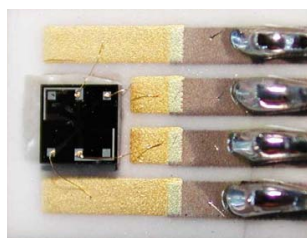


Figure 5.21: Mounted GMR sensor element.

The GMR sensor yields reliable results for distances of several centimeters between the sensor element and the rotating magnets, whereas the AMR sensor only responds for distances of less than two centimeters. The GMR sensor also provides for a simple way to measure the field strength.

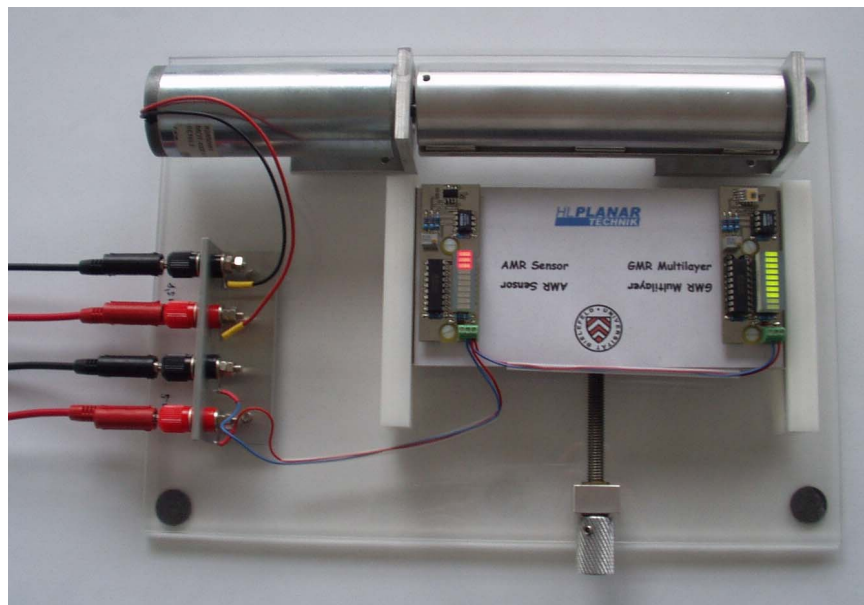


Figure 5.22: Photo of demonstrator device for GMR- and AMR sensor.

Chapter 6

Summary

Since the late 1980's there has been an enormous research on stacks of thin layers of ferro- and paramagnetic metals triggered by the discoveries of interlayer coupling [Grü86] and its oscillatory behavior regarding the spacer layer thickness ([Bai88] and [Par90]). The discovery of the giant magneto resistance (GMR) effect ([Bai88] and [Bin89]) and all related effects underlined the high application potential of these new multilayer systems. All this came along with improved deposition, especially sputtering devices, and investigation methods capable of producing, controlling and examining thin films of only a few nanometers.

Although GMR multilayers have already found their way into automotive sensor technology and into leading-edge hard disk drive products there are still many unsolved questions on both ends of the technological span:

This thesis successfully addresses on one hand the basic understanding of the oscillatory behavior in one of the simplest stacking sequences combining interlayer exchange coupling and exchange bias, the interlayer coupled and pinned magnetic trilayer (chapter 3). Here the results definitely respond to the question about the existence of a lower limit of about 2 nm below which no antiferromagnetic alignment can be realized in spin valve structures. On the other hand the transfer of laboratory results to a MST production line is investigated, especially the cost saving realization of a Wheatstone bridge (chapter 5).

A special feature of this thesis is the introduction of a new simulation tool for GMR characteristics (chapter 4). Its applicability to understand experimental results was demonstrated as well as its capability to predict characteristics of newly designed stacking sequences and other application related questions.

Theory

Of course, a theoretical chapter in a thesis to giant magneto resistance would not be complete without a review on magnetic parameters and their units (section 2.1), GMR-effect (section 2.2), magnetic anisotropy (section 2.3), interlayer exchange coupling (section 2.4), and exchange bias (section 2.5). Beyond this, important basics for the model implemented in the simulation tool have been extracted, e.g. the relevant contributions of anisotropy and fitting equations for the interlayer coupling.

Already at this point it could also be pointed out that the stacking sequence $NiFe - Co/Cu/Co/IrMn$ is an ideal test system (section 2.2.3): Bulk Co shows a high spin asymmetry. The Co/Cu -interface acts as an optimal spin filter because the good band matching for Cu and the majority-spin electrons of Co results in a high transmission, whereas a large band mismatch for Cu and the minority spins in Co implies a poor transmission. The immiscibility of Cu and Co results in a reduced intermixing at the interfaces, which is favorable for high GMR amplitudes. And finally there is an optimal lattice match of $NiFe$, $fcc - Co$ and Cu reducing spin independent scattering.

Furthermore existing models for orange peel coupling (section 2.6) and for the calculations of GMR(H) and M(H) (section 2.7) have been adjusted for the needs of the simulation and for the discussion of results. Finally a phenomenological law for M(H)-characteristics based on results of Stearns was developed (section 2.8).

Experiments and Discussion on Interlayer Coupled and Pinned Magnetic Trilayers

The simplest stacking sequence for top spin valves of the type $(Ni_{80}Fe_{20}) - Co/Cu/Co/IrMn$ was thoroughly studied. After determining the ideal thickness of the ferromagnetic layers (section 3.6) the Cu spacer layer was varied from 0.8 nm to 9.7 nm (3.7).

The evolution of the characteristics and their GMR-amplitude are an unambiguous evidence of the role the interlayer exchange coupling has in this system. It shows oscillatory behavior with a first and second antiferromagnetic coupling maximum (AFCM) for spacer layer thickness of about 1.0 nm and 2.1 nm , respectively. Considerably high GMR effect amplitudes up to 11.5% in the first and 10.6% in the second AFCM have been determined. The ferromagnetic coupling between the two AFCM suppresses the GMR effect completely for the corresponding spacer layer thickness of about 1.4 nm . The determination of the saturation magnetization allowed for a rough estimation of the interlayer exchange coupling (e.g. about $200\text{ }\mu\text{J}/\text{m}^2$ for the first AFCM).

Obviously we could definitely prove wrong the generally observed critical spacer layer thickness of about 2 nm for copper [Die91a], [Rij94] below which the GMR effect rapidly drops to zero. An antiparallel alignment was achieved for spacer layer thicknesses down to 0.9 nm .

Structural analysis (section 3.8) showed that the samples under investigation feature an extraordinary smoothness at their interfaces with an RMS-value less than 0.24 nm . This causes the RKKY-like interlayer coupling to dominate the ferromagnetic orange peel coupling and/or pin holes. The average grain size was determined to $5.7 \pm 2.5\text{ nm}$ with no in plane texture suggesting a statistical distribution of the grains in the layer plain.

Magnetic measurements (section 3.9) and their analysis by means of a phenomenological law as presented in section 2.8 gave an insight in the magnetization process and its implications for the $\Delta R/R$ -characteristic. It allowed for the determination of the switching points and provided a very good qualitative understanding of the GMR behavior.

The comparison of the former series of unpinned trilayers [Hem00] with the new measurements of pinned trilayer (section 3.10) shows coherent results.

Two aspects can be regarded as advantages for application: The overall thickness of the stack is only about 20 nm , resulting in a high resistance, and only very few parameters have to be considered for a production process due to the simplicity of the system. The zero field sensitivity reaches values up to $33\text{ \%}/mT$ for $t_{Cu} = 1.86\text{ nm}$ and can easily be tailored.

All results presented on magnetic trilayers are in good agreement and qualitatively well understood, based on a long term experience in GMR realization and interpretation. To get a deeper understanding and allow for a quantitative analysis of the interlayer coupling, anisotropy and exchange bias without excessive experimental efforts a new tool was developed.

Simulation of the GMR-Characteristics

In chapter 4 a new model for the magnetization reversal in layered GMR systems was presented (section 4.1). It is an extension of a model by E. C. Stoner and E. P. Wohlfarth which has been applied to layered magnetic devices for the first time by H. Holloway and D. J. Kubinski. A large number of further extensions and adjustments have been carried out to meet new demands.

Based on this model a new simulation procedure was proposed (section 4.2) and implemented in the simulation program GRMSim. The comparison to available programs based on micro magnetic simulations (section 4.3) showed impressively that the simulation tool GMRSim is a more feasible tool in the

hand of an experimentalist. The input from experimental results enables the determination of proper anisotropy constants and testing of newly designed stacking sequences within an acceptable time period. The results are related to the sputter system used and the simulation tool is easy to handle.

The application of GMRSim to interlayer coupled and pinned trilayers (section 4.4) proofed the explanatory power of the new simulation tool. The results confirmed the statements concerning the GMR system under investigation presented in chapter 3. The obtained data provided us with a deeper understanding of the influence of crystalline and induced anisotropy, exchange bias, and interlayer coupling (section 4.4.4) on the GMR characteristic.

New Sensor Concepts – Application of the Gained Knowledge

Chapter 5 finally reports on the cooperation with HL Planartechnik GmbH, Dortmund, within the framework of the *Robert Bosch GmbH Leitprojekt Magneto-Elektronik*. The aim of the project was the transfer of laboratory results to the MST production of a medium sized company.

The central point was to propose a cost saving realization of a Wheatstone bridge, if possible in a single photolithography and coating process. The investigation demonstrated that GMR-bridges can be realized in principal as well by taking advantage of the shape anisotropy as by local annealing.

To show reliable changes in the GMR characteristic for normal and perpendicular orientations of the meander structure with reference to the external field line widths below 2 nm should be designed. This might be a killer criteria as this is the lower limit for simple mask lithography nowadays used as standard process in sensor production.

Quite promising are the results for local annealing: For a *Cu/NiFe*-multilayer the GMR amplitude could be almost completely eliminated before hotspots arose. The resistance and the amplitude of the non-heated reference element remained unchanged. Based on these results design rules for GMR bridges were proposed (section 5.5.4).

As a special highlight a prototype was assembled as a demonstrator to show the advantages of GMR to standard AMR sensors.

This thesis definitely contributes to the understanding of GMR and the related coupling phenomena as well as providing experimentalists with a valuable tool to design GMR characteristics.

Appendix A

Enhanced Stoner-Wohlfarth's Model for Various Systems

The presented extension of Stoner-Wohlfarth's model for coupled and pinned trilayer can be easily rewritten for other systems. Here the results for simple trilayers (section A.1), doubled trilayers (section A.2), bottom spin valves (section A.3) and a simple and enhanced model for multilayers (sections A.4 and A.5) will be presented.

A.1 Model for Trilayers

A magnetic trilayer (Fig. A.1 can be treated like the coupled and pinned trilayer (see section 4.1.2 for details) but without the top antiferromagnetic layer and the energy related to exchange biasing.

The angles of the magnetization direction of the buffer, the bottom and the upper magnetic layer are given by θ_1 , θ_2 and θ_3 , respectively. The directions of the easy axes are given by φ_1 , φ_2 and φ_3 . The angle between the x-axis and the long side of the shape may be defined as ξ .

The Zeeman energy per unit area for this system becomes:

$$\begin{aligned}
 E_{Zeeman}/A = & -\mu_0 \cdot M_{sat,1} \cdot t_1 \cdot H \cdot \cos \theta_1 \\
 & -\mu_0 \cdot M_{sat,2} \cdot t_2 \cdot H \cdot \cos \theta_2 \\
 & -\mu_0 \cdot M_{sat,3} \cdot t_3 \cdot H \cdot \cos \theta_3
 \end{aligned} \tag{A.1}$$

Here M_S indicates the saturation magnetization of the material and t its thickness.

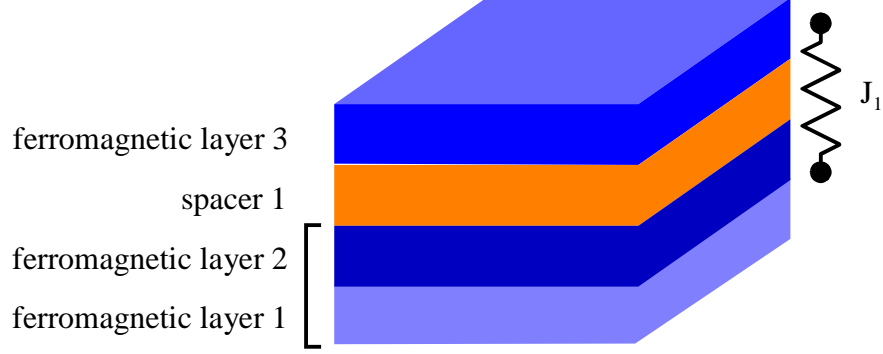


Figure A.1: Design of a magnetic trilayer. The magnetic buffer and the bottom magnetic layer are coupled ferromagnetically and behave as one magnetic layer.

The uniaxial anisotropy energy is determined for the three layers from equation (2.20):

$$\begin{aligned}
 E_{ani,uni}/A &= K_{intrinsic,uni,1} \cdot t_1 \cdot \sin^2(\theta_1 - \varphi_1) \\
 &+ K_{intrinsic,uni,2} \cdot t_2 \cdot \sin^2(\theta_2 - \varphi_2) \\
 &+ K_{intrinsic,uni,3} \cdot t_3 \cdot \sin^2(\theta_3 - \varphi_3)
 \end{aligned} \tag{A.2}$$

Before summarizing the different terms we have again to consider that the buffer and the bottom magnetic layer are coupled ferromagnetically and therefore we get $\theta_1 = \theta_2 := \theta_b$. Assuming columnar growth as explained in 4.1.1 we set $\varphi_1 = \varphi_2 = \varphi_3 := \varphi$. So equation (A.2) becomes:

$$\begin{aligned}
 E_{ani,uni}/A &= K_{intrinsic,uni,1} \cdot t_1 \cdot \sin^2(\theta_b - \varphi) \\
 &+ K_{intrinsic,uni,2} \cdot t_2 \cdot \sin^2(\theta_b - \varphi) \\
 &+ K_{intrinsic,uni,3} \cdot t_3 \cdot \sin^2(\theta_3 - \varphi)
 \end{aligned} \tag{A.3}$$

In the case of biaxial anisotropy the referring terms have to be replaced (see equation (2.21)).

$$\begin{aligned}
 E_{ani,bi}/A &= \frac{1}{4} K_{intrinsic,bi,1} \cdot t_1 \cdot \sin^2(2(\theta_b - \varphi)) \\
 &+ \frac{1}{4} K_{intrinsic,bi,2} \cdot t_2 \cdot \sin^2(2(\theta_b - \varphi)) \\
 &+ \frac{1}{4} K_{intrinsic,bi,3} \cdot t_3 \cdot \sin^2(2(\theta_3 - \varphi))
 \end{aligned} \tag{A.4}$$

As the anisotropy does not have to be of the same nature for all magnetic layers, both energy contributions will be considered in the simulation. It is left to the user to set the anisotropy constant of the non applicable term to zero.

Induced and shape anisotropy are taken into consideration by adding the terms:

$$\begin{aligned}
E_{K,ind}/A &= K_{ind,1} \cdot t_1 \cdot \sin^2(\theta_b - \varphi_{ind}) \\
&+ K_{ind,2} \cdot t_2 \cdot \sin^2(\theta_b - \varphi_{ind}) \\
&+ K_{ind,3} \cdot t_3 \cdot \sin^2(\theta_3 - \varphi_{ind})
\end{aligned} \tag{A.5}$$

$$\begin{aligned}
E_{K,ind,bi}/A &= \frac{1}{4} K_{ind,bi,1} \cdot t_1 \cdot \sin^2(2(\theta_b - \varphi_{ind})) \\
&+ \frac{1}{4} K_{ind,bi,2} \cdot t_2 \cdot \sin^2(2(\theta_b - \varphi_{ind})) \\
&+ \frac{1}{4} K_{ind,bi,3} \cdot t_3 \cdot \sin^2(2(\theta_3 - \varphi_{ind}))
\end{aligned} \tag{A.6}$$

and

$$\begin{aligned}
E_{shape}/A &= K_{shape,1} \cdot t_1 \cdot \sin^2(\theta_b - \xi) \\
&+ K_{shape,2} \cdot t_2 \cdot \sin^2(\theta_b - \xi) \\
&+ K_{shape,3} \cdot t_3 \cdot \sin^2(\theta_3 - \xi)
\end{aligned} \tag{A.7}$$

Finally the energy contribution due to the interlayer coupling has to be added.

$$E_{interlayer\ exchange}/A = -J_{L,total} \cos(\theta_3 - \theta_b) - J_Q (\cos^2(\theta_3 - \theta_b)) \tag{A.8}$$

The linear coupling constant $J_{L,total}$ is the sum of the interlayer coupling for the RKKY interaction J_L and the orange peel contribution J_{OP} . The last is taken from model A in section 2.6.

$$J_{L,total} = J_L + J_{OP} \tag{A.9}$$

The sum of Zeeman (Eq. A.1), intrinsic anisotropy (Eq. A.3 and Eq. A.4), induced anisotropy (Eq. A.5), shape anisotropy (Eq. A.7) and interlayer coupling energy (Eq. A.8) results in:

$$\begin{aligned}
E_{total}/A &= (E_{Zeeman} + E_{anisotropy} + E_{interlayer\ coupling})/A \\
&= -\mu_0 \cdot M_{sat,1} \cdot t_1 \cdot H \cdot \cos \theta_b \\
&\quad -\mu_0 \cdot M_{sat,2} \cdot t_2 \cdot H \cdot \cos \theta_b \\
&\quad -\mu_0 \cdot M_{sat,3} \cdot t_3 \cdot H \cdot \cos \theta_3 \\
&\quad +K_{uni,1} \cdot t_1 \cdot \sin^2(\theta_b - \varphi) \\
&\quad +K_{uni,2} \cdot t_2 \cdot \sin^2(\theta_b - \varphi) \\
&\quad +K_{uni,3} \cdot t_3 \cdot \sin^2(\theta_3 - \varphi) \\
&\quad +\frac{1}{4} K_{bi,1} \cdot t_1 \cdot \sin^2(2(\theta_b - \varphi)) \\
&\quad +\frac{1}{4} K_{bi,2} \cdot t_2 \cdot \sin^2(2(\theta_b - \varphi)) \\
&\quad +\frac{1}{4} K_{bi,3} \cdot t_3 \cdot \sin^2(2(\theta_3 - \varphi)) \\
&\quad +K_{ind,1} \cdot t_1 \cdot \sin^2(\theta_b - \varphi_{ind}) \\
&\quad +K_{ind,2} \cdot t_2 \cdot \sin^2(\theta_b - \varphi_{ind}) \\
&\quad +K_{ind,3} \cdot t_3 \cdot \sin^2(\theta_3 - \varphi_{ind}) \\
&\quad +\frac{1}{4} K_{ind,bi,1} \cdot t_1 \cdot \sin^2(2(\theta_b - \varphi_{ind})) \\
&\quad +\frac{1}{4} K_{ind,bi,2} \cdot t_2 \cdot \sin^2(2(\theta_b - \varphi_{ind})) \\
&\quad +\frac{1}{4} K_{ind,bi,3} \cdot t_3 \cdot \sin^2(2(\theta_3 - \varphi_{ind})) \\
&\quad +K_{shape,1} \cdot t_1 \cdot \sin^2(\theta_b - \xi) \\
&\quad +K_{shape,2} \cdot t_2 \cdot \sin^2(\theta_b - \xi) \\
&\quad +K_{shape,3} \cdot t_3 \cdot \sin^2(\theta_3 - \xi) \\
&\quad -J_{L,total} \cos(\theta_3 - \theta_b) - J_Q \cos^2(\theta_3 - \theta_b)
\end{aligned} \tag{A.10}$$

A.1.1 GMR and Magnetization for Trilayers

After minimizing the systems energy the angle paths of magnetization for the different layers as a function of the external field are known. They can be used to calculate the GMR characteristic and the magnetization loop according to equations (2.51) and (2.63).

For trilayers we set $\theta_I = \theta_b$ and $\theta_{II} = \theta_3$ to get

$$\frac{R(H)}{R_{\uparrow\uparrow}} = g \cdot AF(H) = g \cdot \frac{1}{2} [1 - \cos(\theta_3(H) - \theta_b(H))] \tag{A.11}$$

or in terms of the enhanced model

$$\frac{R(H)}{R_{\uparrow\uparrow}} = \frac{1 + g}{1 + g \cdot \cos^2 \frac{\theta_3(H) - \theta_b(H)}{2}} - 1 = \frac{g}{2} \cdot \frac{1 - \cos(\theta_3(H) - \theta_b(H))}{1 + g \cdot \cos^2 \frac{\theta_3(H) - \theta_b(H)}{2}} \tag{A.12}$$

For the magnetization loop a term for the ferromagnetic buffer layer is added to equation (2.63).

$$M(H) = \frac{1}{t_1+t_2+t_3} \left((M_{sat,1} \cdot t_1 + M_{sat,2} \cdot t_2) \cdot \cos \theta_b(H) + M_{sat,3} \cdot t_3 \cdot \cos \theta_3(H) \right). \quad (\text{A.13})$$

A.2 Model for Doubled Trilayers

When simulating a doubled trilayer only few adjustments have to be done to the energy function. The Zeeman- and the anisotropy terms of the fourth and fifth layer have to be added. As these two layers are strongly ferromagnetically coupled we will define for their angle of magnetization $\theta_4 = \theta_5 := \theta_t$. The interlayer coupling via the first and second spacer layer has to be included separately. Note that the fraction $J_{OP,1}$ of $J_{L,1}$ due to the orange peel coupling has to be calculated according to model A (Eq. 2.48). For $J_{OP,2}$ model B (Eq. 2.49) has to be used.

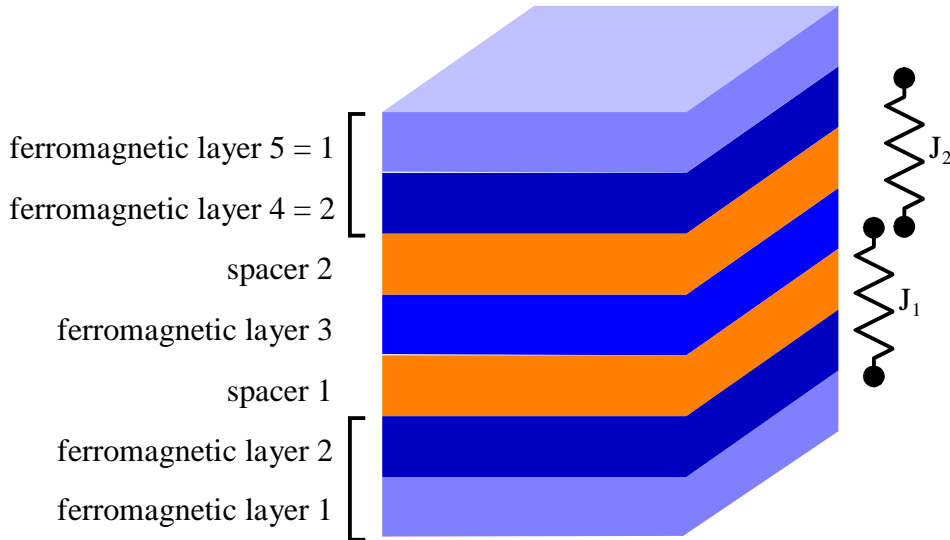


Figure A.2: Design of a doubled trilayer.

$$\begin{aligned}
E_{total}/A &= (E_{Zeeman} + E_{anisotropy} + E_{interlayer\ coupling})/A \\
&= -\mu_0 \cdot M_{sat,1} \cdot t_1 \cdot H \cdot \cos \theta_b \\
&\quad -\mu_0 \cdot M_{sat,2} \cdot t_2 \cdot H \cdot \cos \theta_b \\
&\quad -\mu_0 \cdot M_{sat,3} \cdot t_3 \cdot H \cdot \cos \theta_3 \\
&\quad -\mu_0 \cdot M_{sat,4} \cdot t_4 \cdot H \cdot \cos \theta_t \\
&\quad -\mu_0 \cdot M_{sat,5} \cdot t_5 \cdot H \cdot \cos \theta_t \\
&\quad +K_{uni,1} \cdot t_1 \cdot \sin^2(\theta_b - \varphi) \\
&\quad +K_{uni,2} \cdot t_2 \cdot \sin^2(\theta_b - \varphi) \\
&\quad +K_{uni,3} \cdot t_3 \cdot \sin^2(\theta_3 - \varphi) \\
&\quad +K_{uni,4} \cdot t_4 \cdot \sin^2(\theta_t - \varphi) \\
&\quad +K_{uni,5} \cdot t_5 \cdot \sin^2(\theta_t - \varphi) \\
&\quad +\frac{1}{4} K_{bi,1} \cdot t_1 \cdot \sin^2(2(\theta_b - \varphi)) \\
&\quad +\frac{1}{4} K_{bi,2} \cdot t_2 \cdot \sin^2(2(\theta_b - \varphi)) \\
&\quad +\frac{1}{4} K_{bi,3} \cdot t_3 \cdot \sin^2(2(\theta_3 - \varphi)) \\
&\quad +\frac{1}{4} K_{bi,4} \cdot t_4 \cdot \sin^2(2(\theta_t - \varphi)) \\
&\quad +\frac{1}{4} K_{bi,5} \cdot t_5 \cdot \sin^2(2(\theta_t - \varphi)) \\
&\quad +K_{ind,1} \cdot t_1 \cdot \sin^2(\theta_b - \varphi_{ind}) \\
&\quad +K_{ind,2} \cdot t_2 \cdot \sin^2(\theta_b - \varphi_{ind}) \\
&\quad +K_{ind,3} \cdot t_3 \cdot \sin^2(\theta_3 - \varphi_{ind}) \\
&\quad +K_{ind,4} \cdot t_4 \cdot \sin^2(\theta_t - \varphi_{ind}) \\
&\quad +K_{ind,5} \cdot t_5 \cdot \sin^2(\theta_t - \varphi_{ind}) \\
&\quad +\frac{1}{4} K_{ind,bi,1} \cdot t_1 \cdot \sin^2(2(\theta_b - \varphi_{ind})) \\
&\quad +\frac{1}{4} K_{ind,bi,2} \cdot t_2 \cdot \sin^2(2(\theta_b - \varphi_{ind})) \\
&\quad +\frac{1}{4} K_{ind,bi,3} \cdot t_3 \cdot \sin^2(2(\theta_3 - \varphi_{ind})) \\
&\quad +\frac{1}{4} K_{ind,bi,4} \cdot t_4 \cdot \sin^2(2(\theta_t - \varphi_{ind})) \\
&\quad +\frac{1}{4} K_{ind,bi,5} \cdot t_5 \cdot \sin^2(2(\theta_t - \varphi_{ind})) \\
&\quad +K_{shape,1} \cdot t_1 \cdot \sin^2(\theta_b - \xi) \\
&\quad +K_{shape,2} \cdot t_2 \cdot \sin^2(\theta_b - \xi) \\
&\quad +K_{shape,3} \cdot t_3 \cdot \sin^2(\theta_3 - \xi) \\
&\quad +K_{shape,4} \cdot t_4 \cdot \sin^2(\theta_t - \xi) \\
&\quad +K_{shape,5} \cdot t_5 \cdot \sin^2(\theta_t - \xi) \\
&\quad -J_{L,total,1} \cos(\theta_3 - \theta_b) - J_{Q,1} \cos^2(\theta_3 - \theta_b) \\
&\quad -J_{L,total,2} \cos(\theta_3 - \theta_t) - J_{Q,2} \cos^2(\theta_3 - \theta_t)
\end{aligned} \tag{A.14}$$

A.2.1 GMR and Magnetization for Doubled Trilayers

For doubled trilayers equation (2.51) for the GMR characteristic has to be extended as there are three independent ferromagnetic layers. After calculating the GMR effect for two adjacent ferromagnetic layers separately, the effect will be averaged with a weighting factor w_{gmr} ($0 < w_{gmr} < 1$).

$$\begin{aligned} \left(\frac{R(H)}{R_{\uparrow\uparrow}} \right)_{0,bottom} &= \frac{1}{2} [1 - \cos(\theta_3(H) - \theta_b(H))] \\ \left(\frac{R(H)}{R_{\uparrow\uparrow}} \right)_{0,top} &= \frac{1}{2} [1 - \cos(\theta_3(H) - \theta_t(H))] \end{aligned} \quad (\text{A.15})$$

$$\left(\frac{R(H)}{R_{\uparrow\uparrow}} \right) = g \cdot \left[w_{gmr} \cdot \left(\frac{R(H)}{R_{\uparrow\uparrow}} \right)_{0,bottom} + (1 - w_{gmr}) \cdot \left(\frac{R(H)}{R_{\uparrow\uparrow}} \right)_{0,top} \right]$$

As the parameter w_{gmr} is not accessible within the model, it has to be adjusted by the user. Similar considerations in the enhanced model lead to:

$$\left(\frac{R(H)}{R_{\uparrow\uparrow}} \right) = g \cdot \frac{1 - w_{gmr} \cos^2 \frac{\theta_3 - \theta_b}{2} - (1 - w_{gmr}) \cdot \cos^2 \frac{\theta_t - \theta_3}{2}}{1 + w_{gmr} \cdot g \cdot \cos^2 \frac{\theta_3 - \theta_b}{2} + (1 - w_{gmr}) \cdot g \cdot \cos^2 \frac{\theta_t - \theta_3}{2}} \quad (\text{A.16})$$

For the magnetization loop equation (2.63) is altered to

$$\begin{aligned} M(H) &= \frac{1}{t_1 + t_2 + t_3 + t_4 + t_5} \left(M_{sat,1} \cdot t_1 + M_{sat,2} \cdot t_2 \right) \cdot \cos \theta_b(H) \\ &\quad + M_{sat,3} \cdot t_3 \cdot \cos \theta_3(H) \\ &\quad \left(M_{sat,4} \cdot t_4 + M_{sat,5} \cdot t_5 \right) \cdot \cos \theta_t(H). \end{aligned} \quad (\text{A.17})$$

A.3 Model for Bottom Spin Valves

In a bottom spin valve only two ferromagnetic layers are involved. An additional energy contribution originates from the pinning in the direction of γ . The magnitude of the exchange bias is determined by J_{eb} .

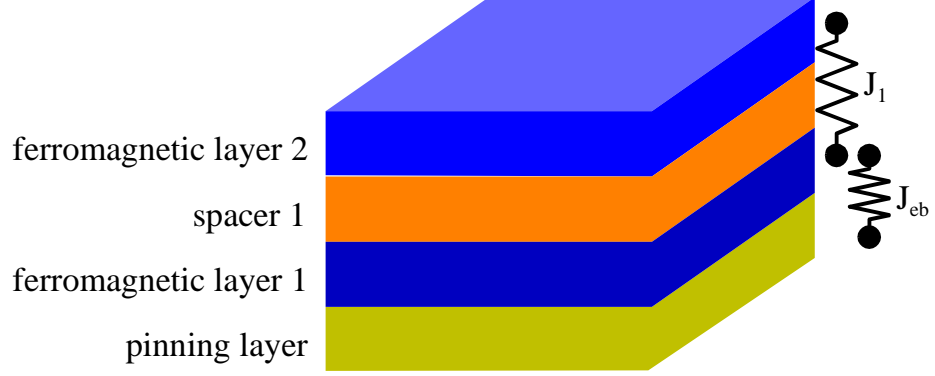


Figure A.3: Design of a bottom spin valve. The antiferromagnet pins the first magnetic layer.

$$\begin{aligned}
E_{total}/A &= (E_{Zeeman} + E_{anisotropy} + E_{interlayer\ coupling})/A \\
&= -\mu_0 \cdot M_{sat,1} \cdot t_1 \cdot H \cdot \cos \theta_1 \\
&\quad -\mu_0 \cdot M_{sat,2} \cdot t_2 \cdot H \cdot \cos \theta_2 \\
&\quad +K_{uni,1} \cdot t_1 \cdot \sin^2(\theta_1 - \varphi) \\
&\quad +K_{uni,2} \cdot t_2 \cdot \sin^2(\theta_2 - \varphi) \\
&\quad +\frac{1}{4} K_{bi,1} \cdot t_1 \cdot \sin^2(2(\theta_1 - \varphi)) \\
&\quad +\frac{1}{4} K_{bi,2} \cdot t_2 \cdot \sin^2(2(\theta_2 - \varphi)) \\
&\quad +K_{ind,1} \cdot t_1 \cdot \sin^2(\theta_1 - \varphi_{ind}) \\
&\quad +K_{ind,2} \cdot t_2 \cdot \sin^2(\theta_2 - \varphi_{ind}) \\
&\quad +\frac{1}{4} K_{ind,bi,1} \cdot t_1 \cdot \sin^2(2(\theta_1 - \varphi_{ind})) \\
&\quad +\frac{1}{4} K_{ind,bi,2} \cdot t_2 \cdot \sin^2(2(\theta_2 - \varphi_{ind})) \\
&\quad +K_{shape,1} \cdot t_1 \cdot \sin^2(\theta_1 - \xi) \\
&\quad +K_{shape,2} \cdot t_2 \cdot \sin^2(\theta_2 - \xi) \\
&\quad -J_{L,total} \cos(\theta_2 - \theta_1) - J_Q \cos^2(\theta_2 - \theta_1) \\
&\quad -J_{cb} \cos(\theta_1 - \gamma)
\end{aligned} \tag{A.18}$$

Because of the antiferromagnetic buffer layer the orange peel contribution to the coupling has to be taken from model B (section 2.6). In this aspect it differs from the model for coupled and pinned magnetic trilayers.

A.3.1 GMR and Magnetization for Bottom Spin Valves

For bottom spin valves equations (2.51), (2.62) and (2.63) can easily be adopted:

$$\frac{R(H)}{R_{\uparrow\uparrow}} = g \cdot AF(H) = g \cdot \frac{1}{2} [1 - \cos(\theta_2(H) - \theta_1(H))] \quad (\text{A.19})$$

$$\frac{R(H)}{R_{\uparrow\uparrow}} = \frac{1 + g}{1 + g \cdot \cos^2 \frac{\theta_2(H) - \theta_1(H)}{2}} - 1 = \frac{g}{2} \cdot \frac{1 - \cos(\theta_2(H) - \theta_1(H))}{1 + g \cdot \cos^2 \frac{\theta_2(H) - \theta_1(H)}{2}} \quad (\text{A.20})$$

and

$$M(H) = \frac{1}{t_1 + t_2} (M_{sat,1} \cdot t_1 \cdot \cos \theta_1(H) + M_{sat,2} \cdot t_2 \cdot \cos \theta_2(H)). \quad (\text{A.21})$$

A.4 Model for Multilayers

A multilayer can be divided into super cells as demonstrated in Fig. A.4. Note that a magnetic super cell consists of two crystallographic super cells!

The influence of the buffer layer vanishes after only very few super cells and is therefore neglected in the basic model (see next section for an enhanced model). The energy contribution due to the orange peel coupling has to be viewed with care. Apart from the first super cell model A (Eq. 2.48) will be the correct description, but the wavelength and height of the waviness is likely to vary significantly within the stack.

$$\begin{aligned} E_{total}/A &= (E_{Zeeman} + E_{anisotropy} + E_{interlayercoupling})/A \\ &= -\mu_0 \cdot M_{sat,1} \cdot t_1 \cdot H \cdot \cos(\theta_1) \\ &\quad -\mu_0 \cdot M_{sat,2} \cdot t_2 \cdot H \cdot \cos(\theta_2) \\ &\quad + K_{uni,1} \cdot t_1 \cdot \sin^2(\theta_1 - \varphi) \\ &\quad + K_{uni,2} \cdot t_2 \cdot \sin^2(\theta_2 - \varphi) \\ &\quad + \frac{1}{4} K_{bi,1} \cdot t_1 \cdot \sin^2(2(\theta_1 - \varphi)) \\ &\quad + \frac{1}{4} K_{bi,2} \cdot t_2 \cdot \sin^2(2(\theta_2 - \varphi)) \end{aligned} \quad (\text{A.22})$$

$$\begin{aligned}
& +K_{ind,1} \cdot t_1 \cdot \sin^2(\theta_1 - \varphi_{ind}) \\
& +K_{ind,2} \cdot t_2 \cdot \sin^2(\theta_2 - \varphi_{ind}) \\
& +\frac{1}{4} K_{ind,bi,1} \cdot t_1 \cdot \sin^2(2(\theta_1 - \varphi_{ind})) \\
& +\frac{1}{4} K_{ind,bi,2} \cdot t_2 \cdot \sin^2(2(\theta_2 - \varphi_{ind})) \\
& +K_{shape,1} \cdot t_1 \cdot \sin^2(\theta_1 - \xi) \\
& +K_{shape,2} \cdot t_2 \cdot \sin^2(\theta_2 - \xi) \\
& -J_{L,total,1} \cos(\theta_1 - \theta_2) - J_{Q,1} (\cos^2(\theta_1 - \theta_2)) \\
& -J_{L,total,2} \cos(\theta_1 - \theta_2) - J_{Q,2} (\cos^2(\theta_1 - \theta_2))
\end{aligned}$$

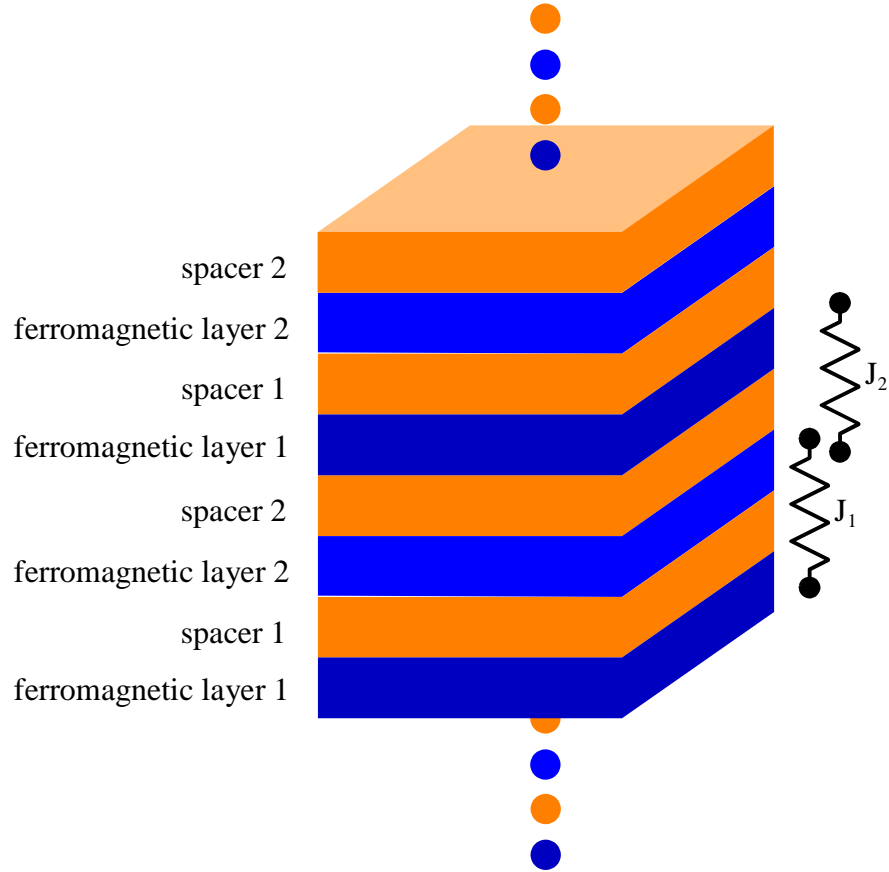


Figure A.4: Design of a multilayer. For a correct magnetic description of parallel and antiparallel magnetization a super cell containing two magnetic layers is essential in opposition to a crystallographic description.

A.4.1 GMR and Magnetization for Multilayers

For multilayers equations (2.51), (2.62) and (2.63) can easily be adopted:

$$\frac{R(H)}{R_{\uparrow\uparrow}} = g \cdot AF(H) = g \cdot \frac{1}{2} [1 - \cos(\theta_2(H) - \theta_1(H))] \quad (\text{A.23})$$

$$\frac{R(H)}{R_{\uparrow\uparrow}} = \frac{1 + g}{1 + g \cdot \cos^2 \frac{\theta_2(H) - \theta_1(H)}{2}} - 1 = \frac{g}{2} \cdot \frac{1 - \cos(\theta_2(H) - \theta_1(H))}{1 + g \cdot \cos^2 \frac{\theta_2(H) - \theta_1(H)}{2}} \quad (\text{A.24})$$

$$M(H) = \frac{1}{t_1 + t_2} (M_{sat,1} \cdot t_1 \cdot \cos \theta_1(H) + M_{sat,2} \cdot t_2 \cdot \cos \theta_2(H)) \quad (\text{A.25})$$

A.5 Enhanced Model for Multilayers

Due to crystal growth or varying substrate and target temperature the first layers deposited usually differ in their magnetic behavior from the consecutive layers. It is also very common to use a special top layer. Therefore we will now consider an enhanced model for multilayer in which the first three layers and the final layer are considered separately. In between the number of magnetic super cells N_{SC} may vary. See Fig. A.5 for details.

The energy contribution due to the orange peel coupling has to be viewed with care. Apart from the first super cell, where model B (Eq. 2.49) has to be applied, model A (Eq. 2.48) will be the correct description, but the wavelength and height of the waviness is likely to vary significantly within the stack, which is not taken into further consideration.

$$\begin{aligned} E_{total}/A &= (E_{Zeeman} + E_{anisotropy} + E_{interlayercoupling})/A \\ &= -\mu_0 \cdot M_{sat,1} \cdot t_1 \cdot H \cdot \cos(\theta_1) \\ &\quad -\mu_0 \cdot M_{sat,2} \cdot t_2 \cdot H \cdot \cos(\theta_2) \\ &\quad -\mu_0 \cdot M_{sat,3} \cdot t_3 \cdot H \cdot \cos(\theta_3) \\ &\quad -N_{SC} \cdot \mu_0 \cdot M_{sat,3} \cdot t_3 \cdot H \cdot \cos(\theta_4) \\ &\quad -N_{SC} \cdot \mu_0 \cdot M_{sat,3} \cdot t_3 \cdot H \cdot \cos(\theta_5) \\ &\quad -\mu_0 \cdot M_{sat,4} \cdot t_4 \cdot H \cdot \cos(\theta_6) \end{aligned}$$

$$\begin{aligned}
& +K_{uni,1} \cdot t_1 \cdot \sin^2(\theta_1 - \varphi) \\
& +K_{uni,2} \cdot t_2 \cdot \sin^2(\theta_2 - \varphi) \\
& +K_{uni,3} \cdot t_3 \cdot \sin^2(\theta_3 - \varphi) \\
& +N_{SC} \cdot K_{uni,3} \cdot t_3 \cdot \sin^2(\theta_4 - \varphi) \\
& +N_{SC} \cdot K_{uni,3} \cdot t_3 \cdot \sin^2(\theta_5 - \varphi) \\
& +K_{uni,4} \cdot t_4 \cdot \sin^2(\theta_6 - \varphi) \\
& +\frac{1}{4} K_{bi,1} \cdot t_1 \cdot \sin^2(2(\theta_1 - \varphi)) \\
& +\frac{1}{4} K_{bi,2} \cdot t_2 \cdot \sin^2(2(\theta_2 - \varphi)) \\
& +\frac{1}{4} K_{bi,3} \cdot t_3 \cdot \sin^2(2(\theta_3 - \varphi)) \\
& +N_{SC} \cdot \frac{1}{4} K_{bi,3} \cdot t_3 \cdot \sin^2(2(\theta_4 - \varphi)) \\
& +N_{SC} \cdot \frac{1}{4} K_{bi,3} \cdot t_3 \cdot \sin^2(2(\theta_5 - \varphi)) \\
& +\frac{1}{4} K_{bi,4} \cdot t_4 \cdot \sin^2(2(\theta_6 - \varphi)) \\
& +K_{ind,1} \cdot t_1 \cdot \sin^2(\theta_1 - \varphi_{ind}) \\
& +K_{ind,2} \cdot t_3 \cdot \sin^2(\theta_2 - \varphi_{ind}) \\
& +K_{ind,3} \cdot t_3 \cdot \sin^2(\theta_3 - \varphi_{ind}) \\
& +N_{SC} \cdot K_{ind,3} \cdot t_3 \cdot \sin^2(\theta_4 - \varphi_{ind}) \\
& +N_{SC} \cdot K_{ind,3} \cdot t_3 \cdot \sin^2(\theta_5 - \varphi_{ind}) \\
& +K_{ind,4} \cdot t_4 \cdot \sin^2(\theta_6 - \varphi_{ind}) \\
& +\frac{1}{4} K_{ind,bi,1} \cdot t_1 \cdot \sin^2(2(\theta_1 - \varphi_{ind})) \\
& +\frac{1}{4} K_{ind,bi,2} \cdot t_2 \cdot \sin^2(2(\theta_2 - \varphi_{ind})) \\
& +\frac{1}{4} K_{ind,bi,3} \cdot t_3 \cdot \sin^2(2(\theta_3 - \varphi_{ind})) \\
& +N_{SC} \cdot \frac{1}{4} K_{ind,bi,3} \cdot t_3 \cdot \sin^2(2(\theta_4 - \varphi_{ind})) \\
& +N_{SC} \cdot \frac{1}{4} K_{ind,bi,3} \cdot t_3 \cdot \sin^2(2(\theta_5 - \varphi_{ind})) \\
& +\frac{1}{4} K_{ind,bi,4} \cdot t_4 \cdot \sin^2(2(\theta_6 - \varphi_{ind})) \\
& +K_{shape,1} \cdot t_1 \cdot \sin^2(\theta_1 - \xi) \\
& +K_{shape,2} \cdot t_2 \cdot \sin^2(\theta_2 - \xi) \\
& +K_{shape,3} \cdot t_3 \cdot \sin^2(\theta_3 - \xi) \\
& +N_{SC} \cdot K_{shape,3} \cdot t_3 \cdot \sin^2(\theta_3 - \xi) \\
& +N_{SC} \cdot K_{shape,3} \cdot t_3 \cdot \sin^2(\theta_3 - \xi) \\
& +K_{shape,4} \cdot t_4 \cdot \sin^2(\theta_4 - \xi) \\
& -J_{L,total,1} \cos(\theta_2 - \theta_1) - J_{Q,1} (\cos^2(\theta_2 - \theta_1)) \\
& -J_{L,total,2} \cos(\theta_3 - \theta_2) - J_{Q,2} (\cos^2(\theta_3 - \theta_2)) \\
& -J_{L,total,3} \cos(\theta_4 - \theta_3) - J_{Q,3} (\cos^2(\theta_4 - \theta_3)) \\
& -(2N_{SC} - 1) \cdot J_{L,total,3} \cos(\theta_5 - \theta_4) - (2N_{SC} - 1) \cdot J_{Q,3} (\cos^2(\theta_5 - \theta_4)) \\
& -J_{L,total,3} \cos(\theta_6 - \theta_5) - J_{Q,3} (\cos^2(\theta_6 - \theta_5))
\end{aligned} \tag{A.26}$$

A.5.1 GMR and Magnetization for Multilayers in the Enhanced Model

$$\begin{aligned}
\frac{R(H)}{R_{\uparrow\uparrow}} &= g \cdot AF(H) \\
&= \frac{g}{2} - \frac{g}{4 \cdot N_{SC} + 6} \cdot [\cos(\theta_2 - \theta_1) + \cos(\theta_3 - \theta_2) + \\
&\quad \cos(\theta_4 - \theta_3) + (2 \cdot N_{SC} - 1) \cdot \cos(\theta_5 - \theta_4) + \cos(\theta_6 - \theta_5)] \quad (A.27)
\end{aligned}$$

$$\begin{aligned}
\frac{R(H)}{R_{\uparrow\uparrow}} &= g \cdot \left[(2 \cdot N_{SC} + 3) - \cos^2 \frac{\theta_2 - \theta_1}{2} - \cos^2 \frac{\theta_3 - \theta_2}{2} - \right. \\
&\quad \left. \cos^2 \frac{\theta_4 - \theta_3}{2} - (2 \cdot N_{SC} - 1) \cos^2 \frac{\theta_5 - \theta_4}{2} - \cos^2 \frac{\theta_6 - \theta_5}{2} \right] / \\
&\quad \left[(2 \cdot N_{SC} + 3) + g \cdot \left(\cos^2 \frac{\theta_2 - \theta_1}{2} + \cos^2 \frac{\theta_3 - \theta_2}{2} + \right. \right. \quad (A.28) \\
&\quad \left. \left. \cos^2 \frac{\theta_4 - \theta_3}{2} + (2 \cdot N_{SC} - 1) \cos^2 \frac{\theta_5 - \theta_4}{2} + \cos^2 \frac{\theta_6 - \theta_5}{2} \right) \right]
\end{aligned}$$

$$\begin{aligned}
M(H) &= (M_{sat,1} \cdot t_1 \cdot \cos \theta_1 + M_{sat,2} \cdot t_2 \cdot \cos \theta_2 + \\
&\quad M_{sat,3} \cdot t_3 \cdot (\cos \theta_3 + N_{SC} \cos \theta_4 + N_{SC} \cos \theta_5) + \\
&\quad M_{sat,4} \cdot t_4 \cdot \cos \theta_6) / \quad (A.29) \\
&\quad (t_1 + t_2 + (2 \cdot N_{SC} + 1) t_3 + t_4)
\end{aligned}$$

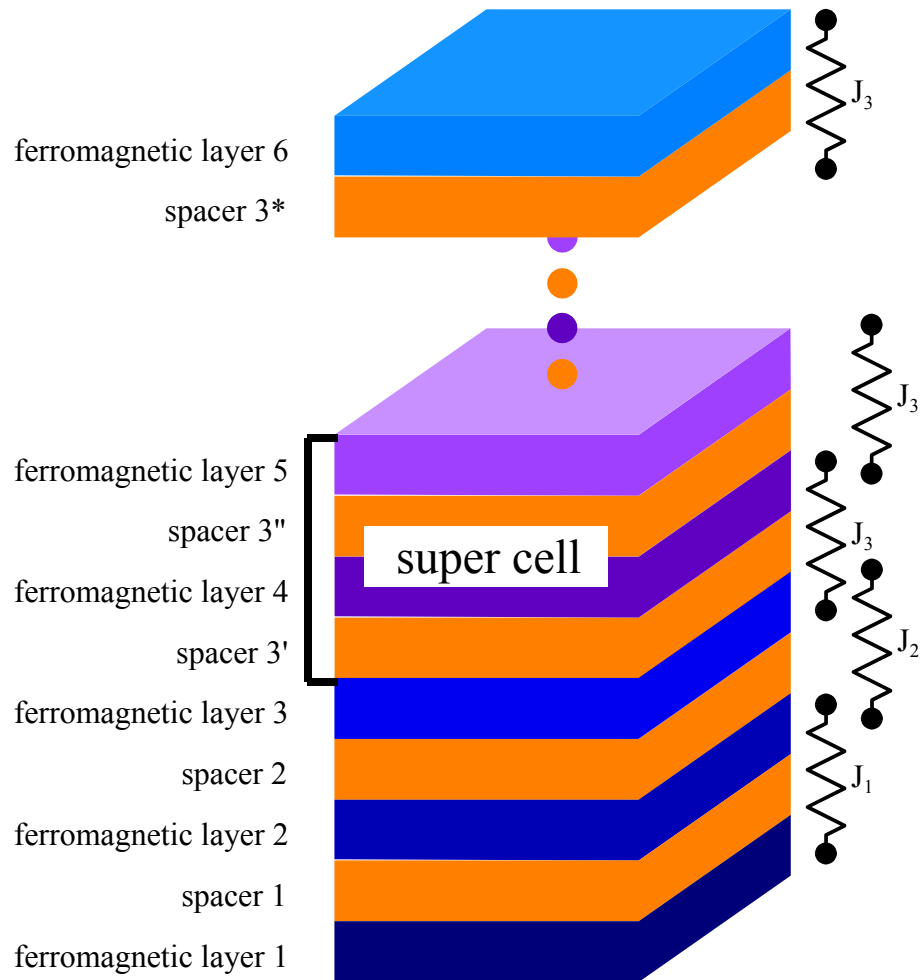


Figure A.5: Enhanced design of a multilayer. For a correct magnetic description of parallel and antiparallel magnetization a super cell containing two magnetic layers is essential in opposition to a crystallographic description. The first three layers and the top layer are considered separately.

Appendix B

Overview to Parameters for the Simulations

The table on the following pages will provide a complete list of all parameters of the simulation tool. Included are the used units and which parameters are relevant for the selected stacking sequence.

no.	description	formula	unit or range	energy function						annotations
				1	2	3	4	5	6	
1	energy function 1: trilayer 2: doubled trilayer 3: bottom spinvalve 4: top spinvalve 5: multilayer 6: multilayer (enhanced)		1, 2, 3, 4, 5, 6	x	x	x	x	x	x	
2	flag for energy plots 0: no data for energy plots 1: calculate data for energy plots		0, 1	x	x	x	x	x	x	
3	flag for virgin loop 0: no virgin loop 1: include virgin loop		0, 1	x	x	x	x	x	x	
4	flag for RKKY interaction 0: use fixed parameters for J_L 1: calculate J_L by RKKY-interaction		0, 1	x	x	x	x	x	x	
5	flag for J_Q factor 0: use fixed parameters for J_L 1: $J_Q = const \cdot J_L$		0, 1	x	x	x	x	x	x	
6	length of element	L	μm	x	x	x	x	x	x	
7	width of element	B	μm	x	x	x	x	x	x	

Table B.1: Set of parameters for each simulation.

no.	description	formula	unit or range	energy function						annotations
				1	2	3	4	5	6	
8	direction of long axis of the shape	θ	degree	x	x	x	x	x	x	
9	minimal external field	H_{min}	Oe	x	x	x	x	x	x	a maximum
10	maximal external field	H_{max}	Oe	x	x	x	x	x	x	of 100,000
11	field step		Oe	x	x	x	x	x	x	field steps
12	saturation magnetization 1	$M_{sat,1}$	$\frac{kA}{m}$	x	x	x	x	x	x	
13	saturation magnetization 2	$M_{sat,2}$	$\frac{kA}{m}$	x	x	x	x	x	x	
14	saturation magnetization 3	$M_{sat,3}$	$\frac{m}{kA}$	x	x	x	x	x	x	
15	saturation magnetization 4	$M_{sat,4}$	$\frac{m}{kA}$							
16	saturation magnetization 5	$M_{sat,5}$	$\frac{m}{kA}$							
17	thickness of ferromagnetic layer 1	t_1	nm	x	x	x	x	x	x	
18	thickness of ferromagnetic layer 2	t_2	nm	x	x	x	x	x	x	
19	thickness of ferromagnetic layer 3	t_3	nm	x	x	x	x	x	x	
20	thickness of ferromagnetic layer 4	t_4	nm							
21	thickness of ferromagnetic layer 5	t_5	nm							
22	thickness of spacer layer 1	t_{s1}	nm	x	x	x	x	x	x	
23	thickness of spacer layer 2	t_{s2}	nm							
24	thickness of spacer layer 3	t_{s3}	nm							
25	linear interlayer coupling constant 1	$J_{L,1}$	$\frac{\mu J}{m^2}$	x	x	x	x	x	x	◇
26	linear interlayer coupling constant 2	$J_{L,2}$	$\frac{\mu J}{m^2}$							◇
27	linear interlayer coupling constant 3	$J_{L,3}$	$\frac{\mu J}{m^2}$							◇
28	biquadratic interlayer coupling constant 1	$J_{Q,1}$	$\frac{\mu J}{m^2}$	x	x	x	x	x	x	★

Table B.1: Set of parameters for each simulation.

no.	description	formula	unit or range	energy function						annotations	
				1	2	3	4	5	6		
29	biquadratic interlayer coupling constant 2	$J_{Q,2}$	$\frac{\mu J}{m^2}$		x				x	x	*
30	biquadratic interlayer coupling constant 3	$J_{Q,3}$	$\frac{\mu J}{m^2}$							x	*
31	factor for biquadratic coupling constant 1	$c_{Q,1}$	0..1	x	x	x	x	x	x	x	*
32	factor for biquadratic coupling constant 2	$c_{Q,2}$	0..1		x				x	x	*
33	factor for biquadratic coupling constant 3	$c_{Q,3}$	0..1							x	*
34	antiferromagnetic coupling constant	J_{AF}	$\frac{\mu J}{m^2}$			x	x				
35	direction of pinning	γ	<i>degree</i>			x	x				
36	uniaxial anisotropy constant 1	K_1	$\frac{k_J}{m^3}$	x	x	x	x	x	x		
37	uniaxial anisotropy constant 2	K_2	$\frac{k_J}{m^3}$	x	x	x	x	x	x		
38	uniaxial anisotropy constant 3	K_3	$\frac{k_J}{m^3}$	x	x				x		
39	uniaxial anisotropy constant 4	K_4	$\frac{k_J}{m^3}$		x					x	
40	uniaxial anisotropy constant 5	K_5	$\frac{k_J}{m^3}$						x		
41	biaxial anisotropy constant 1	$K_{b,1}$	$\frac{k_J}{m^3}$	x	x	x	x	x	x		
42	biaxial anisotropy constant 2	$K_{b,2}$	$\frac{k_J}{m^3}$	x	x	x	x	x	x		
43	biaxial anisotropy constant 3	$K_{b,3}$	$\frac{k_J}{m^3}$	x	x				x		
44	biaxial anisotropy constant 4	$K_{b,4}$	$\frac{k_J}{m^3}$		x					x	
45	biaxial anisotropy constant 5	$K_{b,5}$	$\frac{k_J}{m^3}$						x		
46	uniaxial induced anisotropy constant 1	$K_{ind,1}$	$\frac{k_J}{m^3}$	x	x	x	x	x	x	x	
47	uniaxial induced anisotropy constant 2	$K_{ind,2}$	$\frac{k_J}{m^3}$	x	x	x	x	x	x	x	
48	uniaxial induced anisotropy constant 3	$K_{ind,3}$	$\frac{k_J}{m^3}$	x	x				x		
49	uniaxial induced anisotropy constant 4	$K_{ind,4}$	$\frac{k_J}{m^3}$		x					x	

Table B.1: Set of parameters for each simulation.

no.	description	formula	unit or range	energy function						annotations
				1	2	3	4	5	6	
50	uniaxial induced anisotropy constant 5	$K_{ind,5}$	$\frac{kJ}{m^3}$		x					
51	biaxial induced anisotropy constant 1	$K_{ind,b,1}$	$\frac{kJ}{m^3}$	x	x	x	x			
52	biaxial induced anisotropy constant 2	$K_{ind,b,2}$	$\frac{kJ}{m^3}$	x	x	x	x			
53	biaxial induced anisotropy constant 3	$K_{ind,b,3}$	$\frac{kJ}{m^3}$	x	x		x			
54	biaxial induced anisotropy constant 4	$K_{ind,b,4}$	$\frac{kJ}{m^3}$		x					x
55	biaxial induced anisotropy constant 5	$K_{ind,b,5}$	$\frac{kJ}{m^3}$		x					
56	angle of induced anisotropy	φ_{ind}	°	x	x	x	x	x		
57	height in orange peel coupling	H_{OP}	nm	x	x	x	x	x		
58	periodicity in orange peel coupling	L_{OP}	nm	x	x	x	x	x		
59	amplitude of RKKY interaction	A_0	%	x	x	x	x	x		◇
60	periodicity of RKKY interaction	Λ	nm	x	x	x	x	x		◇
61	decay length of RKKY interaction	L_0	nm	x	x	x	x	x		◇
62	phase of RKKY interaction	φ	degree	x	x	x	x	x		◇
63	GMR amplitude	A_{gmr}	%	x	x	x	x	x		
64	weighting factor for GMR contribution	$w_{gmr0..1}$		x	x	x	x	x		
65	number of supercells $(N-4)/2$	N_{sc}	Integer							x

Table B.1: Set of parameters for each simulation run.
 evaluation depends on RKKY-flag (◇)
 evaluation depends on jq-flag (★)

Appendix C

Starting Parameters for Simulations

Below you will find good starting parameters for the simulation as to give you an idea of the realistic order of magnitude for the different parameters.

SATURATION MAGNETIZATION

$$\text{Co: } 1400 \text{ kA/m} = 1400 \text{ emu/cm}^3$$

$$\text{Py: } 820 \text{ kA/m} = 820 \text{ emu/cm}^3$$

$$\text{Fe: } 1714 \text{ kA/m} = 1714 \text{ emu/cm}^3$$

$$\text{NiCo: } 995 \text{ kA/m} = 995 \text{ emu/cm}^3$$

$$\text{CoFe: } 1517 \text{ kA/m} = 1517 \text{ emu/cm}^3$$

LINEAR INTERLAYER COUPLING CONSTANT

$$\text{Trilayer, } 1^{\text{st}} \text{ AFCM: } -100 \mu\text{J/m}^2 = -0.1 \text{ erg/cm}^2$$

$$\text{Trilayer, } 2^{\text{nd}} \text{ AFCM: } -20 \mu\text{J/m}^2 = -0.02 \text{ erg/cm}^2$$

$$\text{Trilayer, } 3^{\text{rd}} \text{ AFCM: } -5.4 \mu\text{J/m}^2 = -0.054 \text{ erg/cm}^2$$

QUADRATIC INTERLAYER COUPLING CONSTANT

$$J_Q < 0 \text{ e.g. } J_Q = 0.4 \cdot J_L$$

ANTIFERROMAGNETIC COUPLING CONSTANT (PINNED LAYER)

$$5 \mu\text{J/m}^2 = 0.005 \text{ erg/cm}^2$$

ANISOTROPY CONSTANT

$$3.9 \text{ nm Co: } K_3 = 4.5 \text{ kJ/m}^3 = 45000 \text{ erg/cm}^3$$

GMR AMPLITUDE

$$\text{Trilayer, } 1^{\text{st}} \text{ AFCM: } 15\%$$

$$\text{Trilayer, } 2^{\text{nd}} \text{ AFCM: } 11\%$$

$$\text{Trilayer, } 3^{\text{rd}} \text{ AFCM: } 7\%$$

Appendix D

Source Code of Simulation Kernel

Here the full source code of the simulation kernel in fortran 90 is given. In addition a user interface was programmed in Visual Basic.

```

PROGRAM simkern
!   by T. Hempel and A. Huetten, University of Bielefeld, 2004

PARAMETER (version=4.0, dataformat=4.0)
PARAMETER (no_of_para=65, no_of_fieldval=100000)

IMPLICIT real (A-H,O-Z)

! energy function
EXTERNAL func

! file names and variables for parameter file, Ief = energy function
!   integer :: iterations, Iparlauf, Ief, Ipsillauf, IxaLauf
CHARACTER :: rfile *60, formlog *20, zahlstring *250
CHARACTER :: file1 *41, file2 *41, file3 *41
CHARACTER :: file4 *41, file5 *41
CHARACTER :: SDATE *8, STIME *10
LOGICAL :: logpsi, readparadat
REAL, POINTER :: x(:)
REAL, ALLOCATABLE :: para(:, :)

! psi: angle between external field and easy axis, assumed to be equal
!   for both layers, varied from 0 - 180 degrees
! theta: angle between x-axis and long side of the sample

! angle of easy axis
PARAMETER (psiStart=1, psiEnd=180, psiStep=1)
PARAMETER (Pi=3.141593)

! controls for Polak-Ribiere
PARAMETER (ftol=1.e-8)

! field variables for results
DIMENSION Rgmr(no_of_fieldval), RgmrEnh(no_of_fieldval)
DIMENSION Rfild(no_of_fieldval), Rgmag(no_of_fieldval)

! dimension for field vector
DIMENSION xAverage(no_of_fieldval,6)
DIMENSION Rangpath(no_of_fieldval,5,6)

! dimension for energies
DIMENSION RzeemanE(no_of_fieldval)
DIMENSION RcouplingLE(no_of_fieldval)
DIMENSION RcouplingQE(no_of_fieldval)
DIMENSION RanisoE(no_of_fieldval)
DIMENSION RanisobiE(no_of_fieldval)
DIMENSION RanisoindE(no_of_fieldval)

```

```

DIMENSION RanisoindbE(no_of_fieldval)
DIMENSION RshapeE(no_of_fieldval)
DIMENSION RpinningE(no_of_fieldval)
DIMENSION RtotalE(no_of_fieldval)

! several variables as explained below

COMMON /layer/ Rt1,Rt2,Rt3,Rt4,Rt5,Rt6
COMMON /msat/ Rmsat1,Rmsat2,Rmsat3,Rmsat4,Rmsat5
COMMON /coupling/ Rj11tot,Rj12tot,Rj13tot,Rj1,Rj2,Rj3
COMMON /bias/ Rjeb,Rgamma
COMMON /ani/ Rk1,Rk2,Rk3,Rk4,Rk5,Rkb1,Rkb2,Rkb3,Rkb4,Rkb5
COMMON /indani/ Rkind1,Rkind2,Rkind3,Rkind4,Rkind5,psiind
COMMON /indanibi/ Rkindb1,Rkindb2,Rkindb3,Rkindb4,Rkindb5
COMMON /kshape/ Rkshapel,Rkshape2,Rkshape3,Rkshape4,Rkshape5,Rxi
COMMON /opc/ Rhop,Rlop
COMMON /scaling/ Ragmr,Rwgmr
COMMON /state/ Ief,N,psi,Hfeld,Isc,Iparlauf
COMMON /eplot/ rfile,RmaxH,RminH,RstepH,Ivirginloop

! information on screen
write(*,*)'=====
write(*,FMT='(A25,F4.1)')
* write(*,*) ' This is SimKern version ', version
write(*,*) ' Kernel to GMRSim'
write(*,*) ' by Tobias Hempel [1,2] and Andreas Huetten [1]'
write(*,*) ' [1] University of Bielefeld, Physics, Germany'
write(*,*) ' [2] HLPanartechnik GmbH, Dortmund, Germany'
write(*,*)'=====
write(*,*)

! use input file para.dat, set .FALSE. to use data in fortran code
! readparadat=.FALSE.
readparadat=.TRUE.

!
initial parameters
rfile='a02'
iterations=1
formlog = ''
write (file3 , FMT='(A7)') 'out.log'

! read parameter matrix from parameter file
IF (readparadat) then
OPEN (unit = 1, file = 'para.dat',
* status = 'old', action = 'read')
read (1,*) df
read (1,*) ! name
read (1,*) rfile
write (formlog, FMT='(A2,I2,A4)') '(A',LEN_TRIM(rfile),',A4)'
write (file3, FMT=formlog) rfile, '.log'
if (df.eq.dataformat) then
read (1,*) ! varied parameter
read (1,*) ! min and max value of varied parameter
read (1,*) iterations
allocate (para(iterations,no_of_para))
do i=1, iterations
read (1,*) para(i,:)
end do
CLOSE(1)
else
OPEN(UNIT=22,FILE=file3 ,STATUS='replace')
write(*,*)'=====
write(*,*) 'Data format incorrect!'
write(*,*)'=====
write(22,*)'=====
write(22,*) 'Data format incorrect!'
write(22,*)'=====
close (1)
close (22)
STOP 99
end if
end if

! Logfile created or replaced
OPEN(UNIT=22,FILE=file3 ,STATUS='replace')

! B I G L O O P S T A R T S=====
do Iparlauf = 1, iterations

!#####DATA FOR DIRECT INPUT#####

if (.NOT. readparadat) then

! energy function
! 1: trilayer, 2: doubled trilayer, 3: bottom spinvalve, 4: top spinvalve,
! 5: multilayer, 6: multilayer (enh.)
Ief=6

```

```

! calculate date for energy plots      0:no      1:yes
  leplot=0

! virginloop      0:no      1:yes
  lvirginloop=0

! JL-flag      0:JL given      1:JL calculated with RKKY-interaction
  lrrkkyflag=0

! JQ-flag      0:JQ given      1:JQ calculated as factor of JL
  ljqlflag=0

! lateral dimensions of the element (cm, degree)
! External field always along x-axis!
! As the case may be, rotate the sample with regard to the x-axis and
! therefore the external field.
  Rlength=10000.0e-7
  Rwidth=10000.0e-7
  Rangles=0.0

! maximal, minimal external field, field step and field directions (Oe)
  Rminh=-15000
  Rmaxh=15000
  Rsteph=100

! saturation magnetization of bulk material (G)
  Rmsat1=1714
  Rmsat2=1715
  Rmsat3=1716
  Rmsat4=1717
  Rmsat5=1718

! layer thickness (cm)
  Rt1=3.0e-7
  Rt2=3.0e-7
  Rt3=3.0e-7
  Rt4=3.0e-7
  Rt5=3.0e-7
  Rt6=3.0e-7
!
  spacer
  Rts1=1.0e-7
  Rts2=1.0e-7
  Rts3=1.0e-7

! coupling constants (erg/cm^2) (Jl>0:ferromagnetic, Jl<0:antiferromagnetic,
! JQ<0 for biquadratic coupling)
  Rjl1=0.5 ! linear coupling 1
  Rjl2=0.1 ! linear coupling 2
  Rjl3=-1.0 ! linear coupling 3
  Rjq1=-0.5 ! biquadratic coupling 1
  Rjq2=-0.5 ! biquadratic coupling 2
  Rjq3=-0.4 ! biquadratic coupling 3
  Rjqf1=0.0 ! Factor for biquadratic coupling constant 1
  Rjqf2=0.0 ! Factor for biquadratic coupling constant 2
  Rjqf3=0.0 ! Factor for biquadratic coupling constant 3
  Rjeb=0.0 ! Antiferromagnetic coupling
  Ranglep=0 ! Direction of pinning in degree

! anisotropy constants (erg/cm^3, degree) (Ki>0)
  Rk1=10000.0
  Rk2=10000.0
  Rk3=10000.0
  Rk4=10000.0
  Rk5=10000.0

  Rkb1=45000.0
  Rkb2=45001.0
  Rkb3=45002.0
  Rkb4=45003.0
  Rkb5=45004.0

  Rkind1=0.0
  Rkind2=0.0
  Rkind3=0.0
  Rkind4=0.0
  Rkind5=0.0

  Rkindb1=0.0
  Rkindb2=0.0
  Rkindb3=0.0
  Rkindb4=0.0
  Rkindb5=0.0

  Ranglekind=0.0

! orange peel coupling (cm)
  Rhop=0.0e-7

```

```

Rlop=0.0e-7
! parameters for RKKY-coupling (% , cm , degree)
Rao=12.0
Rao=Rao/100
! periodicity of oscillation
Rlrkky=4.0e-7
! scaling factor for decay
Rlo=0.0e-7
Rphase=20

! gmr amplitude
Ragmr=15.3

! scaling top to bottom part for doubled trilayers
Rwgm=0.5

! number of supercells in enhanced ML-system  $I_{sc}=(N-4)/2$ 
Isc=3

#####DATA FOR DIRECT INPUT#####
!

else

#####READING DATA FROM PARAMETER FILE#####
! includes conversion from SI (parameter file) to cgs (internal use)

! energy function to use
Ief=para(Iparlauf,1)
! energy plots 0:do not calculate data 1:calculate data
! virginloop 0:no 1:yes
! JL-flag 0:JL given 1:JL calculated with RKKY-interaction
! JQ-flag 0:JQ given 1:JQ calculated as factor of JL
Ieplot=INT(para(Iparlauf,2))
Ivirginloop=INT(para(Iparlauf,3))
Irkkyflag=INT(para(Iparlauf,4))
Ijqflag=INT(para(Iparlauf,5))

! lateral dimensions of the element (um --> cm, degree)

Rlength=para(Iparlauf,6) * 1e-4
Rwidth=para(Iparlauf,7) * 1e-4
Rangles=para(Iparlauf,8)

! maximal, minimal external field, field step and field directions (Oe)
Rminh=para(Iparlauf,9)
Rmaxh=para(Iparlauf,10)
Rsteph=para(Iparlauf,11)

! saturation magnetization of bulk material (Gauss = kA/m)
Rmsat1=para(Iparlauf,12)
Rmsat2=para(Iparlauf,13)
Rmsat3=para(Iparlauf,14)
Rmsat4=para(Iparlauf,15)
Rmsat5=para(Iparlauf,16)

! layer thickness (nm --> cm)
Rt1=para(Iparlauf,17) * 1e-7
Rt2=para(Iparlauf,18) * 1e-7
Rt3=para(Iparlauf,19) * 1e-7
Rt4=para(Iparlauf,20) * 1e-7
Rt5=para(Iparlauf,21) * 1e-7
! spacer
Rts1=para(Iparlauf,22) * 1e-7
Rts2=para(Iparlauf,23) * 1e-7
Rts3=para(Iparlauf,24) * 1e-7

! coupling constants (uJ/m2 --> mJ/m2 = erg/cm2)
Rjl1=para(Iparlauf,25) * 1e-3
Rjl2=para(Iparlauf,26) * 1e-3
Rjl3=para(Iparlauf,27) * 1e-3
Rjq1=para(Iparlauf,28) * 1e-3
Rjq2=para(Iparlauf,29) * 1e-3
Rjq3=para(Iparlauf,30) * 1e-3
Rjqf1=para(Iparlauf,31)
Rjqf2=para(Iparlauf,32)
Rjqf3=para(Iparlauf,33)
Rjeb=para(Iparlauf,34) * 1e-3

! pinning direction
Ranglep=para(Iparlauf,35)

! anisotropy constants (kJ/m3 --> erg/cm3, degree)
Rk1=para(Iparlauf,36) * 1e4
Rk2=para(Iparlauf,37) * 1e4
Rk3=para(Iparlauf,38) * 1e4
Rk4=para(Iparlauf,39) * 1e4

```

```

Rk5=para(Iparlauf,40) * 1e4

Rkb1=para(Iparlauf,41) * 1e4
Rkb2=para(Iparlauf,42) * 1e4
Rkb3=para(Iparlauf,43) * 1e4
Rkb4=para(Iparlauf,44) * 1e4
Rkb5=para(Iparlauf,45) * 1e4

Rkind1=para(Iparlauf,46) * 1e4
Rkind2=para(Iparlauf,47) * 1e4
Rkind3=para(Iparlauf,48) * 1e4
Rkind4=para(Iparlauf,49) * 1e4
Rkind5=para(Iparlauf,50) * 1e4

Rkindb1=para(Iparlauf,51) * 1e4
Rkindb2=para(Iparlauf,52) * 1e4
Rkindb3=para(Iparlauf,53) * 1e4
Rkindb4=para(Iparlauf,54) * 1e4
Rkindb5=para(Iparlauf,55) * 1e4

Ranglekind=para(Iparlauf,56)

! orange peel coupling (nm --> cm)
Rhop=para(Iparlauf,57) * 1e-7
Rlop=para(Iparlauf,58) * 1e-7

! parameters for RKKY-coupling (% --> factor, nm --> cm, degree)
Rao=para(Iparlauf,59) * 1e-2
! periodicity of oscillation
Rlrkky=para(Iparlauf,60) * 1e-7
! scaling factor for decay
Rlo=para(Iparlauf,61) * 1e-7
Rphase=para(Iparlauf,62)

! gmr amplitude
Ragmr=para(Iparlauf,63)

! scaling top to bottom part
Rwgmr=para(Iparlauf,64)

! number of supercells Isc=(N-4)/2
Isc=para(Iparlauf,65)

END if

! writing data to logfile
write(22,*)'=====
write(22,*) 'Parameter set no.', Iparlauf
write(22,*)'=====
write(22,*) 'Input parameters'
write(22,*)'=====
write(22,*) 'File for output = ', rfile
write(22,*) ' flags (v,RKKY,JQ)', Ivirginloop, Irkkyflag, Ijqflag
write(22,*) ' selected energy function =', Ief
write(22,*)
write(22,*) ' laenge = ', Rlength, ' breite = ', Rwidth,
* ' angle = ', Rangles
write(22,*) ' minH = ', Rminh, ' maxH = ', Rmaxh,
* ' stepH = ', Rsteph
write(22,*)
write(22,*) ' Msat1 = ', Rmsat1, ' Msat2 = ', Rmsat2,
* ' Msat3 = ', Rmsat3
write(22,*) ' Msat4 = ', Rmsat4, ' Msat5 = ', Rmsat5
* ' t1 = ', Rt1, ' t2 = ', Rt2,
* ' t3 = ', Rt3,
* ' t4 = ', Rt4, ' t5 = ', Rt5,
* ' t6 = ', Rt6
write(22,*) ' ts1 = ', Rts1, ' ts2 = ', Rts2,
* ' ts3 = ', Rts3
write(22,*)
write(22,*) ' J11 = ', Rj11, ' J12 = ', Rj12,
* ' J13 = ', Rj13
write(22,*) ' Jq1 = ', Rjq1, ' Jq2 = ', Rjq2,
* ' Jq3 = ', Rjq3
write(22,*) ' Jq1fac = ', Rjqf1, ' Jq2fac = ', Rjqf2,
* ' Jq3fac = ', Rjqf3
* ' anglep = ', Ranglep
write(22,*) ' Jeb = ', Rjeb, ' K2 = ', Rk2,
* ' K1 = ', Rk1, ' K3 = ', Rk3
write(22,*) ' K4 = ', Rk4, ' K5 = ', Rk5
* ' Kb1 = ', Rkb1, ' Kb2 = ', Rkb2,
* ' Kb3 = ', Rkb3
write(22,*) ' Kb4 = ', Rkb4, ' Kb5 = ', Rkb5
* ' Kind1 = ', Rkind1, ' Kind2 = ', Rkind2,
* ' Kind3 = ', Rkind3
write(22,*) ' Kind4 = ', Rkind4, ' Kind5 = ', Rkind5
* ' Kindb1 = ', Rkindb1, ' Kindb2 = ', Rkindb2,

```

```

*
*      Kindb3 =',Rkindb3
write(22,*) 'Kindb4 =',Rkindb4, ' Kindb5 =',Rkindb5
write(22,*) 'KindAng=',Ranglekind
write(22,*)
write(22,*) 'Hop      =',Rhop,      ' Lop      =',R Lop
write(22,*) 'Ao       =',Rao,      ' Lo       =',R lo
write(22,*) 'Lrkky    =',Rlrkky,   ' phase    =',R phase
write(22,*) 'Agmr     =',Ragmr,    ' Sgmr     =',Rwgmr,
*
*      sc      =',Isc
write(22,*)

CLOSE(22)
OPEN(UNIT=22, FILE=file3 , POSITION='append' , STATUS='old')

! Setting everything to 0 before easy axis angle loop starts
MM=0
Mpsi=0
Asu=0.
Rkshape1=0.0
Rkshape2=0.0
Rkshape3=0.0
Rkshape4=0.0
Rkshape5=0.0
Rjop1=0.0
Rjop2=0.0
Rjop3=0.0
Rj11tot=0.0
Rj12tot=0.0
Rj13tot=0.0
Rzuffall=0.0
do kj=1,no_of_fieldval
Rgmr(kj)=0.
RgmrEnh(kj)=0.
Rfeld(kj)=0.
Rgmag(kj)=0.
xAverage(kj,1)=0.
xAverage(kj,2)=0.
xAverage(kj,3)=0.
xAverage(kj,4)=0.
xAverage(kj,5)=0.
xAverage(kj,6)=0.
RzeemanE(kj)=0.
RcouplingLE(kj)=0.
RcouplingQE(kj)=0.
RanisoE(kj)=0.
RanisobiE(kj)=0.
RanisoindE(kj)=0.
RanisoindbE(kj)=0.
RshapeE(kj)=0.
RpinningE(kj)=0.
RtotalE(kj)=0.
Rangpath(kj,1,1)=0.
Rangpath(kj,1,2)=0.
Rangpath(kj,1,3)=0.
Rangpath(kj,1,4)=0.
Rangpath(kj,1,5)=0.
Rangpath(kj,1,6)=0.
Rangpath(kj,2,1)=0.
Rangpath(kj,2,2)=0.
Rangpath(kj,2,3)=0.
Rangpath(kj,2,4)=0.
Rangpath(kj,2,5)=0.
Rangpath(kj,2,6)=0.
Rangpath(kj,3,1)=0.
Rangpath(kj,3,2)=0.
Rangpath(kj,3,3)=0.
Rangpath(kj,3,4)=0.
Rangpath(kj,3,5)=0.
Rangpath(kj,3,6)=0.
Rangpath(kj,4,1)=0.
Rangpath(kj,4,2)=0.
Rangpath(kj,4,3)=0.
Rangpath(kj,4,4)=0.
Rangpath(kj,4,5)=0.
Rangpath(kj,4,6)=0.
Rangpath(kj,5,1)=0.
Rangpath(kj,5,2)=0.
Rangpath(kj,5,3)=0.
Rangpath(kj,5,4)=0.
Rangpath(kj,5,5)=0.
Rangpath(kj,5,6)=0.
end do

! calculation form factors , anisotropy constants , orange peel constants , coupling constant
! setting dimension
Rxi=Rangles*Pi/180.
Rgamma=Ranglep*Pi/180.

```

```

psiind=Ranglekind*Pi/180.

if (Ijqflag.eq.1) then
  Rjq1=Rjqf1*Rj11
  Rjq2=Rjqf2*Rj12
  Rjq3=Rjqf3*Rj13
end if

Rff=(SQRT(2*Rlength/(Rwidth ** 3))-
* SQRT(2*Rwidth/(Rlength ** 3)))/Pi
Rkshape1=Rmsat1*Rmsat1*Rt1*Rff
Rkshape2=Rmsat2*Rmsat2*Rt2*Rff
Rkshape3=Rmsat3*Rmsat3*Rt3*Rff
Rkshape4=Rmsat4*Rmsat4*Rt4*Rff
Rkshape5=Rmsat5*Rmsat5*Rt5*Rff

select case (int(Ief))
! trilayer
case(1)
  Rjop1=OPmodelA(Rt1+Rt2, Rts1, Rt3,
* (Rt1*Rmsat1+Rt2*Rmsat2)/(Rt1+Rt2), Rmsat3)
  N=2
! doubled trilayer
case(2)
  Rjop1=OPmodelA(Rt1+Rt2, Rts1, Rt3,
* (Rt1*Rmsat1+Rt2*Rmsat2)/(Rt1+Rt2), Rmsat3)
  Rjop2=OPmodelB(Rt3, Rts2, Rt4+Rt5,
* Rmsat3, (Rt4*Rmsat4+Rt5*Rmsat5)/(Rt4+Rt5))
  N=3
! bottom spinvalve
case(3)
  Rjop1=OPmodelB(Rt1, Rts1, Rt2, Rmsat1, Rmsat2)
  N=2
! top spinvalve
case(4)
  Rjop1=OPmodelA(Rt1+Rt2, Rts1, Rt3,
* (Rt1*Rmsat1+Rt2*Rmsat2)/(Rt1+Rt2), Rmsat3)
  N=2
! multilayer
case(5)
  Rjop1=OPmodelB(Rt1, Rts1, Rt2, Rmsat1, Rmsat2)
  Rjop2=OPmodelB(Rt2, Rts2, Rt1, Rmsat2, Rmsat1)
  N=2
! multilayer (enh.)
case(6)
  Rjop1=OPmodelA(Rt1, Rts1, Rt2, Rmsat1, Rmsat2)
  Rjop2=OPmodelB(Rt2, Rts2, Rt3, Rmsat2, Rmsat3)
  Rjop3=OPmodelB(Rt3, Rts3, Rt3, Rmsat3, Rmsat3)
  N=6
end select

! for all energy functions
if (Irkkyflag.eq.1) then
  if (Rts1.ne.0.) then
    Rj11=Rao/Rts1/Rts1*SIN(2*Pi*Rts1/Rlrkky+Rphase*Pi/180)*
* EXP(-Rts1/Rlo)
    else
      Rj11=0.
    END if
    if (Rts2.ne.0.) then
      Rj12=Rao/Rts2/Rts2*SIN(2*Pi*Rts2/Rlrkky+Rphase*Pi/180)*
* EXP(-Rts2/Rlo)
    else
      Rj12=0.
    END if
    if (Rts3.ne.0.) then
      Rj13=Rao/Rts3/Rts3*SIN(2*Pi*Rts3/Rlrkky+Rphase*Pi/180)*
* EXP(-Rts3/Rlo)
    else
      Rj13=0.
    END if
  end if
end if

```

```

Rj11tot=Rj11+Rjop1
Rj12tot=Rj12+Rjop2
Rj13tot=Rj13+Rjop3

! In the case of all constants being identical in both layers the mimimization
! routine will not find the correct path.

      if (((Ief.eq.3) .or. (Ief.eq.5) .or. (Ief.eq.6)) .and.
*      (Rt1.eq.Rt2) .and. (Rmsat1.eq.Rmsat2) .and.
*      (Rk1.eq.Rk2) .and. (Rkb1.eq.Rkb2) .and.
*      (Rkind1.eq.Rkind2)) then
      Rt2=Rt2*1.0001
      write(22,*) 't2 changed to = ',Rt2, ' for numerical reasons.'
      write(22,*)
      end if

      if ((Ief.eq.6) .and. (Rt3.eq.Rt2) .and.
*      (Rmsat3.eq.Rmsat2) .and.
*      (Rk3.eq.Rk2) .and. (Rkb3.eq.Rkb2) .and. (Rkind3.eq.Rkind2)
*      .and. (Rj13tot.eq.Rj12tot) .and. (Rjq3.eq.Rjq2) ) then
      Rt3=Rt3*1.0001
      write(22,*) 't3 changed to = ',Rt3, ' for numerical reasons.'
      write(22,*)
      end if

      allocate (x(N))

! writing data to logfile
      write(22,*)'=====
      write(22,*) ' Calculated parameters '
      write(22,*)'=====
      write(22,*) ' Msat1 = ',Rmsat1, ' t1 = ',Rt1,
*      ' Msat1 * t1 = ',Rmsat1*Rt1
      write(22,*) ' Msat2 = ',Rmsat2, ' t2 = ',Rt2,
*      ' Msat2 * t2 = ',Rmsat2*Rt2
      write(22,*) ' Msat3 = ',Rmsat3, ' t3 = ',Rt3,
*      ' Msat3 * t3 = ',Rmsat3*Rt3
      write(22,*) ' Msat4 = ',Rmsat4, ' t4 = ',Rt4,
*      ' Msat4 * t4 = ',Rmsat4*Rt4
      write(22,*) ' Msat5 = ',Rmsat5, ' t5 = ',Rt5,
*      ' Msat5 * t5 = ',Rmsat5*Rt5
      write(22,*)
      write(22,*) ' JL1 = ',Rj11, ' Jop1 = ',Rjop1,
*      ' JL1tot = ',Rj11tot
      write(22,*) ' JL2 = ',Rj12, ' Jop2 = ',Rjop2,
*      ' JL2tot = ',Rj12tot
      write(22,*) ' JL3 = ',Rj13, ' Jop3 = ',Rjop3,
*      ' JL3tot = ',Rj13tot
      write(22,*) ' JQ1 = ',Rjq1
      write(22,*) ' JQ2 = ',Rjq2
      write(22,*) ' JQ3 = ',Rjq3
      write(22,*)
      write(22,*) ' K1 = ',Rk1, ' K1 * t1 = ',Rk1*Rt1
      write(22,*) ' Kb1 = ',Rkb1, ' Kb1 * t1 = ',Rkb1*Rt1
      write(22,*) ' Kind1 = ',Rkind1, ' Kind1 * t1 = ',Rkind1*Rt1
      write(22,*) ' Kshape1 = ',Rkshape1, ' Kshape1 * t1 = ',Rkshape1*Rt1
      write(22,*) ' K2 = ',Rk2, ' K2 * t2 = ',Rk2*Rt2
      write(22,*) ' Kb2 = ',Rkb2, ' Kb2 * t2 = ',Rkb2*Rt2
      write(22,*) ' Kind2 = ',Rkind2, ' Kind2 * t2 = ',Rkind2*Rt2
      write(22,*) ' Kindb2 = ',Rkindb2, ' Kindb2 * t2 = ',Rkindb2*Rt2
      write(22,*) ' Kshape2 = ',Rkshape2, ' Kshape2 * t2 = ',Rkshape2*Rt2
      write(22,*) ' K3 = ',Rk3, ' K3 * t3 = ',Rk3*Rt3
      write(22,*) ' Kb3 = ',Rkb3, ' Kb3 * t3 = ',Rkb3*Rt3
      write(22,*) ' Kshape3 = ',Rkshape3, ' Kshape3 * t3 = ',Rkshape3*Rt3
      write(22,*) ' Kind3 = ',Rkind3, ' Kind3 * t3 = ',Rkind3*Rt3
      write(22,*) ' Kindb3 = ',Rkindb3, ' Kindb3 * t3 = ',Rkindb3*Rt3
      write(22,*) ' K4 = ',Rk4, ' K4 * t4 = ',Rk4*Rt4
      write(22,*) ' Kb4 = ',Rkb4, ' Kb4 * t4 = ',Rkb4*Rt4
      write(22,*) ' Kind4 = ',Rkind4, ' Kind4 * t4 = ',Rkind4*Rt4
      write(22,*) ' Kindb4 = ',Rkindb4, ' Kindb4 * t4 = ',Rkindb4*Rt4
      write(22,*) ' Kshape4 = ',Rkshape4, ' Kshape4 * t4 = ',Rkshape4*Rt4
      write(22,*) ' K5 = ',Rk5, ' K5 * t5 = ',Rk5*Rt5
      write(22,*) ' Kb5 = ',Rkb5, ' Kb5 * t5 = ',Rkb5*Rt5
      write(22,*) ' Kind5 = ',Rkind5, ' Kind5 * t5 = ',Rkind5*Rt5
      write(22,*) ' Kindb5 = ',Rkindb5, ' Kindb5 * t5 = ',Rkindb5*Rt5
      write(22,*) ' Kshape5 = ',Rkshape5, ' Kshape5 * t5 = ',Rkshape5*Rt5
      write(22,*)'=====
      write(22,*)

      call DATE_AND_TIME(SDATE,STIME)
      write(22,*) ' Starting simulation! ', SDATE, ' ', STIME(1:4)
      CLOSE(22)
      OPEN(UNIT=22, FILE=file3, POSITION='append', STATUS='old')

! E A S Y A X I S L O O P S T A R T S =====
      do 200 Ipsilauf=int(psiStart),int(psiEnd),int(psiStep)

```

```

MM=MM+1
MMM=0
psi=float(Ipsilauf)*Pi/180.0

! for selected angles of the easy axis the angle path is logged seperately
logpsi=.FALSE.
IF((MOD(Ipsilauf,45).eq.0).OR.(Ipsilauf.eq.psisstart)) then
  logpsi=.TRUE.
  Mpsi=Mpsi+1
END if

write (*,FMT='(A15,I3,A13,I4,A5)') ' parameter set:',
*   Iparlauf, ' easy axis:', Ipsilauf, ' deg.'

! field loop virgin curve
! introducing a random distribution at zero field

do i=nn,N
  call RANDOMNUMBER(Rzufall)
  x(nn)=Pi*((2*Rzufall)-1)
end do

do i=0,int(Rmaxh),int(Rsteph)
  Hfeld=float(i)
  CALL frprmn(x,N,ftol,iter,fret)

  if (Ivirginloop.eq.1) then
    MMM=MMM+1
    Rgmr(MMM)=Rgmr(MMM)+RgmrContribution(x)
    RgmrEnh(MMM)=RgmrEnh(MMM)+RgmrContributionEnh(x)
    Rmag(MMM)=Rmag(MMM)+magnContribution(x)
    Rfeld(MMM)=Hfeld
    RzeemanE(MMM)=RzeemanE(MMM)+RzeemanECon(x)
    RcouplingLE(MMM)=RcouplingLE(MMM)+RcouplingLECon(x)
    RcouplingQE(MMM)=RcouplingQE(MMM)+RcouplingQECon(x)
    RanisoE(MMM)=RanisoE(MMM)+RanisoECon(x)
    RanisobiE(MMM)=RanisobiE(MMM)+RanisobiECon(x)
    RanisoindE(MMM)=RanisoindE(MMM)+RanisoindECon(x)
    RanisoindbE(MMM)=RanisoindbE(MMM)+RanisoindbECon(x)
    RshapeE(MMM)=RshapeE(MMM)+RshapeECon(x)
    RpinningE(MMM)=RpinningE(MMM)+RpinningECon(x)

    do nn=1,N
      xAverage(MMM,nn)=xAverage(MMM,nn)-
*         ((-1)**nn)*ACOS(COS(x(nn)))*180/Pi
    end do

    IF (logpsi) then
      do nn=1,N
        Rangpath(MMM,Mpsi,nn)=MODULO(x(nn),2*Pi)*180./Pi
        if (Rangpath(MMM,Mpsi,nn).gt.359.9) then
          Rangpath(MMM,Mpsi,nn)=0.
        end if
      end do
    END if

  end if

end do

! field loop
do i=int(Rmaxh),int(Rminh),int(-Rsteph)
  Hfeld=float(i)

  CALL frprmn(x,N,ftol,iter,fret)
  MMM=MMM+1
  Rgmr(MMM)=Rgmr(MMM)+RgmrContribution(x)
  RgmrEnh(MMM)=RgmrEnh(MMM)+RgmrContributionEnh(x)
  Rmag(MMM)=Rmag(MMM)+magnContribution(x)
  Rfeld(MMM)=Hfeld
  RzeemanE(MMM)=RzeemanE(MMM)+RzeemanECon(x)
  RcouplingLE(MMM)=RcouplingLE(MMM)+RcouplingLECon(x)
  RcouplingQE(MMM)=RcouplingQE(MMM)+RcouplingQECon(x)
  RanisoE(MMM)=RanisoE(MMM)+RanisoECon(x)
  RanisobiE(MMM)=RanisobiE(MMM)+RanisobiECon(x)
  RanisoindE(MMM)=RanisoindE(MMM)+RanisoindECon(x)
  RanisoindbE(MMM)=RanisoindbE(MMM)+RanisoindbECon(x)
  RshapeE(MMM)=RshapeE(MMM)+RshapeECon(x)
  RpinningE(MMM)=RpinningE(MMM)+RpinningECon(x)

  do nn=1,N
    xAverage(MMM,nn)=xAverage(MMM,nn)-
*     ((-1)**nn)*ACOS(COS(x(nn)))*180/Pi
  end do

```

```

      IF (logpsi) then
        do nn=1,N
          Rangpath(MMM,Mpsi,nn)=MODULO(x(nn),2*Pi)*180./Pi
          if (Rangpath(MMM,Mpsi,nn).gt.359.9) then
            Rangpath(MMM,Mpsi,nn)=0.
          end if
        end do
      END if

    end do

! field loop - return
  do i=int(Rminh),int(Rmaxh),int(Rsteph)
    Hfeld=float(i)

    CALL frprmn(x,N,ftol,iter,fret)
    MMM=MMM+1
    Rgmr(MMM)=Rgmr(MMM)+RgmrContribution(x)
    RgmrEnh(MMM)=RgmrEnh(MMM)+RgmrContributionEnh(x)
    Rgmag(MMM)=Rgmag(MMM)+magnContribution(x)
    Rfeld(MMM)=Hfeld
    RzeemanE(MMM)=RzeemanE(MMM)+RzeemanECon(x)
    RcouplingLE(MMM)=RcouplingLE(MMM)+RcouplingLECon(x)
    RcouplingQE(MMM)=RcouplingQE(MMM)+RcouplingQECon(x)
    RanisoE(MMM)=RanisoE(MMM)+RanisoECon(x)
    RanisobiE(MMM)=RanisobiE(MMM)+RanisobiECon(x)
    Ranisoinde(MMM)=Ranisoinde(MMM)+RanisoindeCon(x)
    RanisoindbE(MMM)=RanisoindbE(MMM)+RanisoindbECon(x)
    RshapeE(MMM)=RshapeE(MMM)+RshapeECon(x)
    RpinningE(MMM)=RpinningE(MMM)+RpinningECon(x)

    do nn=1,N
      xAverage(MMM,nn)=xAverage(MMM,nn)-
*      ((-1)**nn)*ACOS(COS(x(nn)))*180/Pi
    end do

    IF (logpsi) then
      do nn=1,N
        Rangpath(MMM,Mpsi,nn)=MODULO(x(nn),2*Pi)*180./Pi
        if (Rangpath(MMM,Mpsi,nn).gt.359.9) then
          Rangpath(MMM,Mpsi,nn)=0.
        end if
      end do
    END if

  end do

200  continue
! END OF EASY AXIS LOOP=====

! generate the output files

  call DATE_AND_TIME(SDATE,STIME)
  write(22,*) 'Writing data! ', SDATE, ' ', STIME(1:4)
  write(22,*) ; write(22,*)
  formlog = ''
*  write (formlog , FMT='(A2,I2,A9)')
  write (file1 , FMT=formlog) rfile , Iparlauf , '.gmr'
  write (file2 , FMT=formlog) rfile , Iparlauf , '.ang'
  write (file4 , FMT=formlog) rfile , Iparlauf , '.egy'
  write (file5 , FMT=formlog) rfile , Iparlauf , '.pat'

  OPEN(UNIT=20,FILE=file1 ,STATUS='replace')
  OPEN(UNIT=21,FILE=file2 ,STATUS='replace')
  OPEN(UNIT=23,FILE=file4 ,STATUS='replace')
  OPEN(UNIT=24,FILE=file5 ,STATUS='replace')

!  filling with data
  do i=1,MMM1
    write(*,FMT='(A9,F9.1,A3)') ' field = ',Rfeld(i),' Oe'

    ! number of different easy axes
    Asu=float(MM)

!    GMR(Heat):
    Rgmr(i)=Rgmr(i)/Asu
    RgmrEnh(i)=RgmrEnh(i)/Asu
    RgmrAbs=(Ragmr*Rgmr(i))

!    M(H):
    Rgmag(i)=Rgmag(i)/Asu

!    angle path:
    do nn=1,N
      xAverage(i,nn)=xAverage(i,nn)/Asu
    end do
  end do

```

```

end do

!          energies (averaging and erg/cm2 -> uJ/m2)
RzeemanE(i)=RzeemanE(i)/Asu*1000
RcouplingLE(i)=RcouplingLE(i)/Asu*1000
RcouplingQE(i)=RcouplingQE(i)/Asu*1000
RanisoE(i)=RanisoE(i)/Asu*1000
RanisobiE(i)=RanisobiE(i)/Asu*1000
RanisoindeE(i)=RanisoindeE(i)/Asu*1000
RanisoindbE(i)=RanisoindbE(i)/Asu*1000
RshapeE(i)=RshapeE(i)/Asu*1000
RpinningE(i)=RpinningE(i)/Asu*1000
RtotalE(i)=RzeemanE(i)+RcouplingLE(i)+RcouplingQE(i)+
*           RanisoE(i)+RanisobiE(i)+RanisoindeE(i)+
*           RanisoindbE(i)+RshapeE(i)+RpinningE(i)

if ((i.gt.2) .OR. (Ivirginloop.eq.0)) then
write(20,*) Rfeld(i),Rgmr(i),RgmrAbs,RgmrEnh(i),Rgmag(i)
zahlstring=''
write(zahlstring ,FMT='(I6,6F7.1)') INT(Rfeld(i)),
*           xAverage(i,1),xAverage(i,2),xAverage(i,3),
*           xAverage(i,4),xAverage(i,5),xAverage(i,6)
write(21,*) zahlstring

! RtotalE(i), RshapeE(i), RpinningE(i)
zahlstring=''
write(zahlstring ,FMT='(I6,10E12.4)') INT(Rfeld(i)),
* RtotalE(i), RzeemanE(i), RcouplingLE(i), RcouplingQE(i),
* RpinningE(i), RanisoE(i), RanisobiE(i),
* RanisoindeE(i), RanisoindbE(i), RshapeE(i)
write(23,*) zahlstring
end if

zahlstring=''
write(zahlstring ,FMT='(I6,30F7.1)')
* INT(Rfeld(i)),
* Rangpath(i,1,1),Rangpath(i,1,2),Rangpath(i,1,3),
* Rangpath(i,1,4),Rangpath(i,1,5),Rangpath(i,1,5),
* Rangpath(i,2,1),Rangpath(i,2,2),Rangpath(i,2,3),
* Rangpath(i,2,4),Rangpath(i,2,5),Rangpath(i,2,5),
* Rangpath(i,3,1),Rangpath(i,3,2),Rangpath(i,3,3),
* Rangpath(i,3,4),Rangpath(i,3,5),Rangpath(i,3,5),
* Rangpath(i,4,1),Rangpath(i,4,2),Rangpath(i,4,3),
* Rangpath(i,4,4),Rangpath(i,4,5),Rangpath(i,4,5),
* Rangpath(i,5,1),Rangpath(i,5,2),Rangpath(i,5,3),
* Rangpath(i,5,4),Rangpath(i,5,5),Rangpath(i,5,5)
write(24,*) zahlstring
END do

CLOSE(20)
CLOSE(21)
CLOSE(23)
CLOSE(24)

if (Ieplot.eq.1) then
call eplotf
end if

write(*,*) 'RUN ', Iparlauf, ' FINISHED!'

NULLIFY(x)
end do
! E N D   O F   B I G   L O O P =====

call DATE_AND_TIME(SDATE,STIME)
write(22,*) 'Simulation finished! ', SDATE, ' ', STIME(1:4)
close(22)
write(*,*) ' D O N E '

END

!----- END MAIN-----

!#####S U B R O U T I N E S#####
!#####FUNCTION CALCULATING THE ENERGY AND ITS DERIVATIONS#####
! Energy functions

function func(x)

COMMON /layer/ Rt1,Rt2,Rt3,Rt4,Rt5,Rt6
COMMON /msat/ Rmsat1,Rmsat2,Rmsat3,Rmsat4,Rmsat5
COMMON /coupling/ Rj11tot,Rj12tot,Rj13tot,Rjq1,Rjq2,Rjq3
COMMON /bias/ Rjeb,Rgamma
COMMON /ani/ Rk1,Rk2,Rk3,Rk4,Rk5,Rkb1,Rkb2,Rkb3,Rkb4,Rkb5

```

```

COMMON /indani/ Rkind1, Rkind2, Rkind3, Rkind4, Rkind5, psiind
COMMON /indanibi/ Rkindb1, Rkindb2, Rkindb3, Rkindb4, Rkindb5
COMMON /kshape/ Rkshape1, Rkshape2, Rkshape3, Rkshape4, Rkshape5, Rxi
COMMON /state/ Ief, N, psi, Hfeld, Isc, Iparlauf

REAL x(N)

select case (int(Ief))

! energy function for trilayer
case(1)

R=-(Rmsat1*Rt1+Rmsat2*Rt2)*Hfeld*COS(x(1))-
* Rmsat3*Rt3*Hfeld*COS(x(2))+
* (Rk1*Rt1+Rk2*Rt2)*(SIN(x(1)-psi)**2.)+
* Rk3*Rt3*(SIN(x(2)-psi)**2.)+
* (Rkb1*Rt1+Rkb2*Rt2)*(SIN(2*(x(1)-psi)**2.)/4+
* Rkb3*Rt3*(SIN(2*(x(2)-psi)**2.)/4+
* (Rkind1*Rt1+Rkind2*Rt2)*(SIN(x(1)-psiind)**2.)+
* Rkind3*Rt3*(SIN(x(2)-psiind)**2.)+
* (Rkindb1*Rt1+Rkindb2*Rt2)*(SIN(2*(x(1)-psiind)**2.)/4+
* Rkindb3*Rt3*(SIN(2*(x(2)-psiind)**2.)/4+
* (Rkshape1*Rt1+Rkshape2*Rt2)*(SIN(x(1)-Rxi)**2.)+
* Rkshape3*Rt3*(SIN(x(2)-Rxi)**2.)-
* Rj11tot*COS(x(2)-x(1))-
* Rjq1*(COS(x(2)-x(1))**2.)

! energy function for doubled trilayer
case(2)

R=-(Rmsat1*Rt1+Rmsat2*Rt2)*Hfeld*COS(x(1))-
* Rmsat3*Rt3*Hfeld*COS(x(2))-
* (Rmsat4*Rt4+Rmsat5*Rt5)*Hfeld*COS(x(3))+
* (Rk1*Rt1+Rk2*Rt2)*(SIN(x(1)-psi)**2.)+
* Rk3*Rt3*(SIN(x(2)-psi)**2.)+
* (Rk4*Rt4+Rk5*Rt5)*(SIN(x(3)-psi)**2.)+
* (Rkb1*Rt1+Rkb2*Rt2)*(SIN(2*(x(1)-psi)**2.)/4+
* Rkb3*Rt3*(SIN(2*(x(2)-psi)**2.)/4+
* (Rkb4*Rt4+Rkb5*Rt5)*(SIN(2*(x(3)-psi)**2.)/4+
* (Rkind1*Rt1+Rkind2*Rt2)*(SIN(x(1)-psiind)**2.)+
* Rkind3*Rt3*(SIN(x(2)-psiind)**2.)+
* (Rkind4*Rt4+Rkind5*Rt5)*(SIN(x(3)-psiind)**2.)+
* (Rkindb1*Rt1+Rkindb2*Rt2)*(SIN(2*(x(1)-psiind)**2.)/4+
* Rkindb3*Rt3*(SIN(2*(x(2)-psiind)**2.)/4+
* (Rkindb4*Rt4+Rkindb5*Rt5)*(SIN(2*(x(3)-psiind)**2.)/4+
* (Rkshape1*Rt1+Rkshape2*Rt2)*(SIN(x(1)-Rxi)**2.)+
* Rkshape3*Rt3*(SIN(x(2)-Rxi)**2.)+
* (Rkshape4*Rt4+Rkshape5*Rt5)*(SIN(x(3)-Rxi)**2.)-
* Rj11tot*COS(x(2)-x(1))-
* Rjq1*(COS(x(2)-x(1))**2.)-
* Rj12tot*COS(x(2)-x(3))-
* Rjq2*(COS(x(2)-x(3))**2.)

! energy function for bottom spinvalve
case(3)

R=-Rmsat1*Rt1*Hfeld*COS(x(1))-
* Rmsat2*Rt2*Hfeld*COS(x(2))+
* Rk1*Rt1*(SIN(x(1)-psi)**2.)+
* Rk2*Rt2*(SIN(x(2)-psi)**2.)+
* Rkb1*Rt1*(SIN(2*(x(1)-psi)**2.)/4+
* Rkb2*Rt2*(SIN(2*(x(2)-psi)**2.)/4+
* Rkind1*Rt1*(SIN(x(1)-psiind)**2.)+
* Rkind2*Rt2*(SIN(x(2)-psiind)**2.)+
* Rkindb1*Rt1*(SIN(2*(x(1)-psiind)**2.)/4+
* Rkindb2*Rt2*(SIN(2*(x(2)-psiind)**2.)/4+
* Rkshape1*Rt1*(SIN(x(1)-Rxi)**2.)+
* Rkshape2*Rt2*(SIN(x(2)-Rxi)**2.)-
* Rj11tot*COS(x(2)-x(1))-
* Rjq1*(COS(x(2)-x(1))**2.)-
* Rjeb*COS(x(1)-Rgamma)

! energy function for top spinvalve
case(4)

R=-(Rmsat1*Rt1+Rmsat2*Rt2)*Hfeld*COS(x(1))-
* Rmsat3*Rt3*Hfeld*COS(x(2))+
* (Rk1*Rt1+Rk2*Rt2)*(SIN(x(1)-psi)**2.)+
* Rk3*Rt3*(SIN(x(2)-psi)**2.)+
* (Rkb1*Rt1+Rkb2*Rt2)*(SIN(2*(x(1)-psi)**2.)/4+
* Rkb3*Rt3*(SIN(2*(x(2)-psi)**2.)/4+
* (Rkind1*Rt1+Rkind2*Rt2)*(SIN(x(1)-psiind)**2.)+
* Rkind3*Rt3*(SIN(x(2)-psiind)**2.)+
* (Rkindb1*Rt1+Rkindb2*Rt2)*(SIN(2*(x(1)-psiind)**2.)/4+
* Rkindb3*Rt3*(SIN(2*(x(2)-psiind)**2.)/4+
* (Rkshape1*Rt1+Rkshape2*Rt2)*(SIN(x(1)-Rxi)**2.)+
* Rkshape3*Rt3*(SIN(x(2)-Rxi)**2.)-
* Rj11tot*COS(x(2)-x(1))-

```

```

*      Rjq1*(COS(x(2)-x(1))**2.) -
*      Rjeb*COS(x(2)-Rgamma)

! energy function for multilayer
case(5)

R=-Rmsat1*Rt1*Hfeld*COS(x(1)) -
Rmsat2*Rt2*Hfeld*COS(x(2))+
Rk1*Rt1*(SIN(x(1)-psi)**2.)+
Rk2*Rt2*(SIN(x(2)-psi)**2.)+
Rkb1*Rt1*(SIN(2*(x(1)-psi))**2.)/4+
Rkb2*Rt2*(SIN(2*(x(2)-psi))**2.)/4+
Rkind1*Rt1*(SIN(x(1)-psiind)**2.)+
Rkind2*Rt2*(SIN(x(2)-psiind)**2.)+
Rkindb1*Rt1*(SIN(2*(x(1)-psiind))**2.)/4+
Rkindb2*Rt2*(SIN(2*(x(2)-psiind))**2.)/4+
Rkshape1*Rt1*(SIN(x(1)-Rxi)**2.)+
Rkshape2*Rt2*(SIN(x(2)-Rxi)**2.) -
Rj1tot*COS(x(2)-x(1)) -
Rjq1*(COS(x(2)-x(1))**2.) -
Rj2tot*COS(x(2)-x(1)) -
Rjq2*(COS(x(2)-x(1))**2.)

! energy function for multilayer (enh.)
case(6)

R=-Rmsat1*Rt1*Hfeld*COS(x(1)) -
Rmsat2*Rt2*Hfeld*COS(x(2)) -
Rmsat3*Rt3*Hfeld*COS(x(3)) -
Isc*Rmsat3*Rt3*Hfeld*COS(x(4)) -
Isc*Rmsat3*Rt3*Hfeld*COS(x(5)) -
Rmsat4*Rt4*Hfeld*COS(x(6))+
Rk1*Rt1*(SIN(x(1)-psi)**2.)+
Rk2*Rt2*(SIN(x(2)-psi)**2.)+
Rk3*Rt3*(SIN(x(3)-psi)**2.)+
Isc*Rk3*Rt3*(SIN(x(4)-psi)**2.)+
Isc*Rk3*Rt3*(SIN(x(5)-psi)**2.)+
Rk4*Rt4*(SIN(x(6)-psi)**2.)+
Rkb1*Rt1*(SIN(2*(x(1)-psi))**2.)/4+
Rkb2*Rt2*(SIN(2*(x(2)-psi))**2.)/4+
Rkb3*Rt3*(SIN(2*(x(3)-psi))**2.)/4+
Isc*Rkb3*Rt3*(SIN(2*(x(4)-psi))**2.)/4+
Isc*Rkb3*Rt3*(SIN(2*(x(5)-psi))**2.)/4+
Rkb4*Rt4*(SIN(2*(x(6)-psi))**2.)/4+
Rkind1*Rt1*(SIN(x(1)-psiind)**2.)+
Rkind2*Rt2*(SIN(x(2)-psiind)**2.)+
Rkind3*Rt3*(SIN(x(3)-psiind)**2.)+
Isc*Rkind3*Rt3*(SIN(x(4)-psiind)**2.)+
Isc*Rkind3*Rt3*(SIN(x(5)-psiind)**2.)+
Rkind4*Rt4*(SIN(x(6)-psiind)**2.)+
Rkindb1*Rt1*(SIN(2*(x(1)-psiind))**2.)/4+
Rkindb2*Rt2*(SIN(2*(x(2)-psiind))**2.)/4+
Rkindb3*Rt3*(SIN(2*(x(3)-psiind))**2.)/4+
Isc*Rkindb3*Rt3*(SIN(2*(x(4)-psiind))**2.)/4+
Isc*Rkindb3*Rt3*(SIN(2*(x(5)-psiind))**2.)/4+
Rkindb4*Rt4*(SIN(2*(x(6)-psiind))**2.)/4+
Rkshape1*Rt1*(SIN(x(1)-Rxi)**2.)+
Rkshape2*Rt2*(SIN(x(2)-Rxi)**2.)+
Rkshape3*Rt3*(SIN(x(3)-Rxi)**2.)+
Isc*Rkshape3*Rt3*(SIN(x(4)-Rxi)**2.)+
Isc*Rkshape3*Rt3*(SIN(x(5)-Rxi)**2.)+
Rkshape4*Rt4*(SIN(x(6)-Rxi)**2.) -
Rj1tot*COS(x(2)-x(1)) -
Rjq1*(COS(x(2)-x(1))**2.) -
Rj2tot*COS(x(3)-x(2)) -
Rjq2*(COS(x(3)-x(2))**2.) -
Rj3tot*COS(x(4)-x(3)) -
Rjq3*(COS(x(4)-x(3))**2.) -
(2*Isc-1)*Rj3tot*COS(x(5)-x(4)) -
(2*Isc-1)*Rjq3*(COS(x(5)-x(4))**2.) -
Rj3tot*COS(x(6)-x(5)) -
Rjq3*(COS(x(6)-x(5))**2.)

end select

func = R
end function func

!-----
! derivation of the energy functions

subroutine dfunc(x,df)

COMMON /layer/ Rt1,Rt2,Rt3,Rt4,Rt5,Rt6
COMMON /msat/ Rmsat1,Rmsat2,Rmsat3,Rmsat4,Rmsat5
COMMON /coupling/ Rj1tot,Rj2tot,Rj3tot,Rjq1,Rjq2,Rjq3
COMMON /bias/ Rjeb,Rgamma

```

```

COMMON / ani / Rk1 , Rk2 , Rk3 , Rk4 , Rk5 , Rkb1 , Rkb2 , Rkb3 , Rkb4 , Rkb5
COMMON / indani / Rkind1 , Rkind2 , Rkind3 , Rkind4 , Rkind5 , psiind
COMMON / indanibi / Rkindb1 , Rkindb2 , Rkindb3 , Rkindb4 , Rkindb5
COMMON / kshape / Rkshape1 , Rkshape2 , Rkshape3 , Rkshape4 , Rkshape5 , Rxi
COMMON / state / Ief , N , psi , Hfeld , Isc , Iparlauf

REAL x(N) , df(N)

select case ( int(Ief) )

! derivations of energy function for trilayer
case(1)

df(1)=(Rmsat1*Rt1+Rmsat2*Rt2)*Hfeld*SIN(x(1))+
* 2*(Rk1*Rt1+Rk2*Rt2)*SIN(x(1)-psi)*COS(x(1)-psi)+
* (Rkb1*Rt1+Rkb2*Rt2)*SIN(2*(x(1)-psi))*COS(2*(x(1)-psi))+
* 2*(Rkind1*Rt1+Rkind2*Rt2)*SIN(x(1)-psiind)*COS(x(1)-psiind)+
* (Rkindb1*Rt1+Rkindb2*Rt2)*
* SIN(2*(x(1)-psiind))*COS(2*(x(1)-psiind))+
* 2*(Rkshape1*Rt1+Rkshape2*Rt2)*SIN(x(1)-Rxi)*COS(x(1)-Rxi)-
* Rj11tot*SIN(x(2)-x(1))-
* 2*Rjq1*COS(x(2)-x(1))*SIN(x(2)-x(1))

df(2)=Rmsat3*Rt3*Hfeld*SIN(x(2))+
* 2*Rk3*Rt3*SIN(x(2)-psi)*COS(x(2)-psi)+
* Rkb3*Rt3*SIN(2*(x(2)-psi))*COS(2*(x(2)-psi))+
* 2*Rkind3*Rt3*SIN(x(2)-psiind)*COS(x(2)-psiind)+
* Rkindb3*Rt3*SIN(2*(x(2)-psiind))*COS(2*(x(2)-psiind))+
* 2*Rkshape3*Rt3*SIN(x(2)-Rxi)*COS(x(2)-Rxi)+
* Rj11tot*SIN(x(2)-x(1))+
* 2*Rjq1*COS(x(2)-x(1))*SIN(x(2)-x(1))

! derivations of energy function for doubled trilayer
case(2)

df(1)=(Rmsat1*Rt1+Rmsat2*Rt2)*Hfeld*SIN(x(1))+
* 2*(Rk1*Rt1+Rk2*Rt2)*SIN(x(1)-psi)*COS(x(1)-psi)+
* (Rkb1*Rt1+Rkb2*Rt2)*SIN(2*(x(1)-psi))*COS(2*(x(1)-psi))+
* 2*(Rkind1*Rt1+Rkind2*Rt2)*SIN(x(1)-psiind)*COS(x(1)-psiind)+
* (Rkindb1*Rt1+Rkindb2*Rt2)*
* SIN(2*(x(1)-psiind))*COS(2*(x(1)-psiind))+
* 2*(Rkshape1*Rt1+Rkshape2*Rt2)*SIN(x(1)-Rxi)*COS(x(1)-Rxi)-
* Rj11tot*SIN(x(2)-x(1))-
* 2*Rjq1*COS(x(2)-x(1))*SIN(x(2)-x(1))

df(2)=Rmsat3*Rt3*Hfeld*SIN(x(2))+
* 2*Rk3*Rt3*SIN(x(2)-psi)*COS(x(2)-psi)+
* Rkb3*Rt3*SIN(2*(x(2)-psi))*COS(2*(x(2)-psi))+
* 2*Rkind3*Rt3*SIN(x(2)-psiind)*COS(x(2)-psiind)+
* Rkindb3*Rt3*SIN(2*(x(2)-psiind))*COS(2*(x(2)-psiind))+
* 2*Rkshape3*Rt3*SIN(x(2)-Rxi)*COS(x(2)-Rxi)+
* Rj11tot*SIN(x(2)-x(1))+
* 2*Rjq1*COS(x(2)-x(1))*SIN(x(2)-x(1))

df(3)=(Rmsat4*Rt4+Rmsat5*Rt5)*Hfeld*SIN(x(3))+
* 2*(Rk4*Rt4+Rk5*Rt5)*SIN(x(3)-psi)*COS(x(3)-psi)+
* (Rkb4*Rt4+Rkb5*Rt5)*SIN(2*(x(3)-psi))*COS(2*(x(3)-psi))+
* 2*(Rkind4*Rt4+Rkind5*Rt5)*SIN(x(3)-psiind)*COS(x(3)-psiind)+
* (Rkindb4*Rt4+Rkindb5*Rt5)*
* SIN(2*(x(3)-psiind))*COS(2*(x(3)-psiind))+
* 2*(Rkshape4*Rt4+Rkshape5*Rt5)*SIN(x(3)-Rxi)*COS(x(3)-Rxi)-
* Rj12tot*SIN(x(2)-x(3))-
* 2*Rjq2*COS(x(2)-x(3))*SIN(x(2)-x(3))

! derivations of energy function for bottom spinvalve
case(3)

df(1)=Rmsat1*Rt1*Hfeld*SIN(x(1))+
* 2*Rk1*Rt1*SIN(x(1)-psi)*COS(x(1)-psi)+
* Rkb1*Rt1*SIN(2*(x(1)-psi))*COS(2*(x(1)-psi))+
* 2*Rkind1*Rt1*SIN(x(1)-psiind)*COS(x(1)-psiind)+
* Rkindb1*Rt1*SIN(2*(x(1)-psiind))*COS(2*(x(1)-psiind))+
* 2*Rkshape1*Rt1*SIN(x(1)-Rxi)*COS(x(1)-Rxi)-
* Rj11tot*SIN(x(2)-x(1))-
* 2*Rjq1*COS(x(2)-x(1))*SIN(x(2)-x(1))+
* Rjeb*SIN(x(1)-Rgamma)

df(2)=Rmsat2*Rt2*Hfeld*SIN(x(2))+
* 2*Rk2*Rt2*SIN(x(2)-psi)*COS(x(2)-psi)+
* Rkb2*Rt2*SIN(2*(x(2)-psi))*COS(2*(x(2)-psi))+
* 2*Rkind2*Rt2*SIN(x(2)-psiind)*COS(x(2)-psiind)+
* Rkindb2*Rt2*SIN(2*(x(2)-psiind))*COS(2*(x(2)-psiind))+
* 2*Rkshape2*Rt2*SIN(x(2)-Rxi)*COS(x(2)-Rxi)+
* Rj11tot*SIN(x(2)-x(1))+

```

```

*          2*Rjq1*COS(x(2)-x(1))*SIN(x(2)-x(1))

! derivations of energy function for top spinvalue
case(4)
df(1)=(Rmsat1*Rt1+Rmsat2*Rt2)*Hfeld*SIN(x(1))+
*      2*(Rk1*Rt1+Rk2*Rt2)*SIN(x(1)-psi)*COS(x(1)-psi)+
*      (Rkb1*Rt1+Rkb2*Rt2)*SIN(2*(x(1)-psi))*COS(2*(x(1)-psi))+
*      2*(Rkind1*Rt1+Rkind2*Rt2)*SIN(x(1)-psiind)*COS(x(1)-psiind)+
*      (Rkindb1*Rt1+Rkindb2*Rt2)*
*      SIN(2*(x(1)-psiind))*COS(2*(x(1)-psiind))+
*      2*(Rkshape1*Rt1+Rkshape2*Rt2)*SIN(x(1)-Rxi)*COS(x(1)-Rxi)-
*      Rj1tot*SIN(x(2)-x(1))-
*      2*Rjq1*COS(x(2)-x(1))*SIN(x(2)-x(1))

df(2)=Rmsat3*Rt3*Hfeld*SIN(x(2))+
*      2*Rk3*Rt3*SIN(x(2)-psi)*COS(x(2)-psi)+
*      Rkb3*Rt3*SIN(2*(x(2)-psi))*COS(2*(x(2)-psi))+
*      2*Rkind3*Rt3*SIN(x(2)-psiind)*COS(x(2)-psiind)+
*      Rkindb3*Rt3*SIN(2*(x(2)-psiind))*COS(2*(x(2)-psiind))+
*      2*Rkshape3*Rt3*SIN(x(2)-Rxi)*COS(x(2)-Rxi)+
*      Rj1tot*SIN(x(2)-x(1))+
*      2*Rjq1*COS(x(2)-x(1))*SIN(x(2)-x(1))+
*      Rjeb*SIN(x(2)-Rgamma)

! derivations of energy function for multilayer
case(5)
df(1)=Rmsat1*Rt1*Hfeld*SIN(x(1))+
*      2*Rk1*Rt1*SIN(x(1)-psi)*COS(x(1)-psi)+
*      Rkb1*Rt1*SIN(2*(x(1)-psi))*COS(2*(x(1)-psi))+
*      2*Rkind1*Rt1*SIN(x(1)-psiind)*COS(x(1)-psiind)+
*      Rkindb1*Rt1*SIN(2*(x(1)-psiind))*COS(2*(x(1)-psiind))+
*      2*Rkshape1*Rt1*SIN(x(1)-Rxi)*COS(x(1)-Rxi)-
*      Rj1tot*SIN(x(2)-x(1))-
*      2*Rjq1*COS(x(2)-x(1))*SIN(x(2)-x(1))-
*      Rj12tot*SIN(x(2)-x(1))-
*      2*Rjq2*COS(x(2)-x(1))*SIN(x(2)-x(1))

df(2)=Rmsat2*Rt2*Hfeld*SIN(x(2))+
*      2*Rk2*Rt2*SIN(x(2)-psi)*COS(x(2)-psi)+
*      Rkb2*Rt2*SIN(2*(x(2)-psi))*COS(2*(x(2)-psi))+
*      2*Rkind2*Rt2*SIN(x(2)-psiind)*COS(x(2)-psiind)+
*      Rkindb2*Rt2*SIN(2*(x(2)-psiind))*COS(2*(x(2)-psiind))+
*      2*Rkshape2*Rt2*SIN(x(2)-Rxi)*COS(x(2)-Rxi)+
*      Rj1tot*SIN(x(2)-x(1))+
*      2*Rjq1*COS(x(2)-x(1))*SIN(x(2)-x(1))+
*      Rj12tot*SIN(x(2)-x(1))+
*      2*Rjq2*COS(x(2)-x(1))*SIN(x(2)-x(1))

! derivations of energy function for multilayer (enh.)
case(6)
df(1)=Rmsat1*Rt1*Hfeld*SIN(x(1))+
*      2*Rk1*Rt1*SIN(x(1)-psi)*COS(x(1)-psi)+
*      Rkb1*Rt1*SIN(2*(x(1)-psi))*COS(2*(x(1)-psi))+
*      2*Rkind1*Rt1*SIN(x(1)-psiind)*COS(x(1)-psiind)+
*      Rkindb1*Rt1*SIN(2*(x(1)-psiind))*COS(2*(x(1)-psiind))+
*      2*Rkshape1*Rt1*SIN(x(1)-Rxi)*COS(x(1)-Rxi)-
*      Rj1tot*SIN(x(2)-x(1))-
*      2*Rjq1*COS(x(2)-x(1))*SIN(x(2)-x(1))

df(2)=Rmsat2*Rt2*Hfeld*SIN(x(2))+
*      2*Rk2*Rt2*SIN(x(2)-psi)*COS(x(2)-psi)+
*      Rkb2*Rt2*SIN(2*(x(2)-psi))*COS(2*(x(2)-psi))+
*      2*Rkind2*Rt2*SIN(x(2)-psiind)*COS(x(2)-psiind)+
*      Rkindb2*Rt2*SIN(2*(x(2)-psiind))*COS(2*(x(2)-psiind))+
*      2*Rkshape2*Rt2*SIN(x(2)-Rxi)*COS(x(2)-Rxi)+
*      Rj1tot*SIN(x(2)-x(1))+
*      2*Rjq1*COS(x(2)-x(1))*SIN(x(2)-x(1))-
*      Rj12tot*SIN(x(3)-x(2))-
*      2*Rjq2*COS(x(3)-x(2))*SIN(x(3)-x(2))

df(3)=Rmsat3*Rt3*Hfeld*SIN(x(3))+
*      2*Rk3*Rt3*SIN(x(3)-psi)*COS(x(3)-psi)+
*      Rkb3*Rt3*SIN(2*(x(3)-psi))*COS(2*(x(3)-psi))+
*      2*Rkind3*Rt3*SIN(x(3)-psiind)*COS(x(3)-psiind)+
*      Rkindb3*Rt3*SIN(2*(x(3)-psiind))*COS(2*(x(3)-psiind))+
*      2*Rkshape3*Rt3*SIN(x(3)-Rxi)*COS(x(3)-Rxi)+
*      Rj12tot*SIN(x(3)-x(2))+
*      2*Rjq2*COS(x(3)-x(2))*SIN(x(3)-x(2))-
*      Rj13tot*SIN(x(4)-x(3))-
*      2*Rjq3*COS(x(4)-x(3))*SIN(x(4)-x(3))

df(4)=Isc*Rmsat3*Rt3*Hfeld*SIN(x(4))+

```

```

*      Isc*2*Rk3*Rt3*SIN(x(4)-psi)*COS(x(4)-psi)+
*      Isc*Rkb3*Rt3*SIN(2*(x(4)-psi))*COS(2*(x(4)-psi))+
*      Isc*2*Rkind3*Rt3*SIN(x(4)-psiind)*COS(x(4)-psiind)+
*      Isc*Rkindb3*Rt3*SIN(2*(x(4)-psiind))*COS(2*(x(4)-psiind))+
*      Isc*2*Rkshape3*Rt3*SIN(x(4)-Rxi)*COS(x(4)-Rxi)+
*      Rj13tot*SIN(x(4)-x(3))+
*      2*Rjq3*COS(x(4)-x(3))*SIN(x(4)-x(3))-
*      (2*Isc-1)*Rj13tot*SIN(x(5)-x(4))-
*      (2*Isc-1)*2*Rjq3*COS(x(5)-x(4))*SIN(x(5)-x(4))

df(5)=Isc*Rmsat3*Rt3*Hfeld*SIN(x(5))+
*      Isc*2*Rk3*Rt3*SIN(x(5)-psi)*COS(x(5)-psi)+
*      Isc*Rkb3*Rt3*SIN(2*(x(5)-psi))*COS(2*(x(5)-psi))+
*      Isc*2*Rkind3*Rt3*SIN(x(5)-psiind)*COS(x(5)-psiind)+
*      Isc*Rkindb3*Rt3*SIN(2*(x(5)-psiind))*COS(2*(x(5)-psiind))+
*      Isc*2*Rkshape3*Rt3*SIN(x(5)-Rxi)*COS(x(5)-Rxi)+
*      (2*Isc-1)*Rj13tot*SIN(x(5)-x(4))+
*      (2*Isc-1)*2*Rjq3*COS(x(5)-x(4))*SIN(x(5)-x(4))-
*      Rj13tot*SIN(x(6)-x(5))-
*      2*Rjq3*COS(x(6)-x(5))*SIN(x(6)-x(5))

df(6)=Rmsat4*Rt4*Hfeld*SIN(x(6))+
*      2*Rk4*Rt4*SIN(x(6)-psi)*COS(x(6)-psi)+
*      Rkb4*Rt4*SIN(2*(x(6)-psi))*COS(2*(x(6)-psi))+
*      2*Rkind4*Rt4*SIN(x(6)-psiind)*COS(x(6)-psiind)+
*      Rkindb4*Rt4*SIN(2*(x(6)-psiind))*COS(2*(x(6)-psiind))+
*      2*Rkshape4*Rt4*SIN(x(6)-Rxi)*COS(x(6)-Rxi)+
*      Rj13tot*SIN(x(6)-x(5))+
*      2*Rjq3*COS(x(6)-x(5))*SIN(x(6)-x(5))

end select

return

end subroutine dfunc

!#####FUNCTIONS CALCULATING DIFFERENT ENERGY CONTRIBUTIONS#####

function RzeemanECon(x)
COMMON /layer/ Rt1,Rt2,Rt3,Rt4,Rt5,Rt6
COMMON /msat/ msat1,Rmsat2,Rmsat3,Rmsat4,Rmsat5
COMMON /state/ Ief,N,psi,Hfeld,Isc,Iparlauf
REAL x(N)

select case (int(Ief))
! energy contribution for trilayer, top spinvalve
case(1,4)
RzeemanECon=-(Rmsat1*Rt1+Rmsat2*Rt2)*Hfeld*COS(x(1))-
Rmsat3*Rt3*Hfeld*COS(x(2))
! energy contribution for doubled trilayer
case(2)
RzeemanECon=-(Rmsat1*Rt1+Rmsat2*Rt2)*Hfeld*COS(x(1))-
Rmsat3*Rt3*Hfeld*COS(x(2))-
(Rmsat4*Rt4+Rmsat5*Rt5)*Hfeld*COS(x(3))
! energy contribution for bottom spinvalve, multilayer
case(3,5)
RzeemanECon=Rmsat1*Rt1*Hfeld*COS(x(1))-
Rmsat2*Rt2*Hfeld*COS(x(2))

! energy contribution for multilayer (enh.)
case(6)
RzeemanECon=Rmsat1*Rt1*Hfeld*COS(x(1))-
Rmsat2*Rt2*Hfeld*COS(x(2))-
Rmsat3*Rt3*Hfeld*COS(x(3))-
Isc*Rmsat3*Rt3*Hfeld*COS(x(4))-
Isc*Rmsat3*Rt3*Hfeld*COS(x(5))-
Rmsat4*Rt4*Hfeld*COS(x(6))

end select
END function RzeemanECon

!-----

function RcouplingLECon(x)
COMMON /coupling/ Rj11tot,Rj12tot,Rj13tot,Rjq1,Rjq2,Rjq3
COMMON /bias/ Rjeb,Rgamma
COMMON /state/ Ief,N,psi,Hfeld,Isc,Iparlauf
REAL x(N)

select case (int(Ief))
! energy contribution for trilayer, bottom spinvalve, top spinvalve
case(1,3,4)
RcouplingLECon=Rj11tot*COS(x(2)-x(1))
! energy contribution for doubled trilayer
case(2)
RcouplingLECon=Rj11tot*COS(x(2)-x(1))-
Rj12tot*COS(x(2)-x(3))
! energy contribution for multilayer

```

```

      case(5)
        RcouplingLECon=-Rj11tot*COS(x(2)-x(1))-
        * Rj12tot*COS(x(2)-x(1))
! energy contribution for multilayer (enh.)
      case(6)
        RcouplingLECon=-Rj11tot*COS(x(2)-x(1))-
        * Rj12tot*COS(x(3)-x(2))-
        * Rj13tot*COS(x(4)-x(3))-
        * (2*Isc-1)*Rj13tot*COS(x(5)-x(4))-
        * Rj13tot*COS(x(6)-x(5))

      end select
      END function RcouplingLECon

!-----

      function RcouplingQECon(x)
      COMMON /coupling/ Rj11tot , Rj12tot , Rj13tot , Rjq1 , Rjq2 , Rjq3
      COMMON /bias/ Rjeb , Rgamma
      COMMON /state/ Ief , N , psi , Hfeld , Isc , Iparlauf
      REAL x(N)

      select case (int(Ief))
! energy contribution for trilayer , bottom spinvalve , top spinvalve
      case(1,3,4)
        RcouplingQECon=-Rjq1*(COS(x(2)-x(1))**2.)
! energy contribution for doubled trilayer
      case(2)
        RcouplingQECon=-Rjq1*(COS(x(2)-x(1))**2.)-
        * Rjq2*(COS(x(2)-x(3))**2.)
! energy contribution for multilayer
      case(5)
        RcouplingQECon=-Rjq1*(COS(x(2)-x(1))**2.)-
        * Rjq2*(COS(x(2)-x(1))**2.)
! energy contribution for multilayer (enh.)
      case(6)
        RcouplingQECon=-Rjq1*(COS(x(2)-x(1))**2.)-
        * Rjq2*(COS(x(3)-x(2))**2.)-
        * Rjq3*(COS(x(4)-x(3))**2.)-
        * (2*Isc-1)*Rjq3*(COS(x(5)-x(4))**2.)-
        * Rjq3*(COS(x(6)-x(5))**2.)

      end select
      END function RcouplingQECon

!-----

      function RanisoECon(x)
      COMMON /layer/ Rt1 , Rt2 , Rt3 , Rt4 , Rt5 , Rt6
      COMMON /ani/ Rk1 , Rk2 , Rk3 , Rk4 , Rk5 , Rkb1 , Rkb2 , Rkb3 , Rkb4 , Rkb5
      COMMON /state/ Ief , N , psi , Hfeld , Isc , Iparlauf
      REAL x(N)

      select case (int(Ief))
! energy contribution for trilayer , top spinvalve
      case(1,4)
        RanisoECon=(Rk1*Rt1+Rk2*Rt2)*(SIN(x(1)-psi)**2.)+
        * Rk3*Rt3*(SIN(x(2)-psi)**2.)
! energy contribution for doubled trilayer
      case(2)
        RanisoECon=(Rk1*Rt1+Rk2*Rt2)*(SIN(x(1)-psi)**2.)+
        * Rk3*Rt3*(SIN(x(2)-psi)**2.)+
        * (Rk4*Rt4+Rk5*Rt5)*(SIN(x(3)-psi)**2.)
! energy contribution for bottom spinvalve , multilayer
      case(3,5)
        RanisoECon=Rk1*Rt1*(SIN(x(1)-psi)**2.)+
        * Rk2*Rt2*(SIN(x(2)-psi)**2.)
! energy contribution for multilayer (enh.)
      case(6)
        RanisoECon=Rk1*Rt1*(SIN(x(1)-psi)**2.)+
        * Rk2*Rt2*(SIN(x(2)-psi)**2.)+
        * Rk3*Rt3*(SIN(x(3)-psi)**2.)+
        * Isc*Rk3*Rt3*(SIN(x(4)-psi)**2.)+
        * Isc*Rk3*Rt3*(SIN(x(5)-psi)**2.)+
        * Rk4*Rt4*(SIN(x(6)-psi)**2.)

      end select
      END function RanisoECon

!-----

      function RanisobiECon(x)
      COMMON /layer/ Rt1 , Rt2 , Rt3 , Rt4 , Rt5 , Rt6
      COMMON /ani/ Rk1 , Rk2 , Rk3 , Rk4 , Rk5 , Rkb1 , Rkb2 , Rkb3 , Rkb4 , Rkb5
      COMMON /state/ Ief , N , psi , Hfeld , Isc , Iparlauf
      REAL x(N)

```

```

        select case (int(Ief))
! energy contribution for trilayer, top spinvalve
        case(1,4)
            RanisobiECon=(Rkb1*Rt1+Rkb2*Rt2)*(SIN(2*(x(1)-psi)**2.)/4+
            * Rkb3*Rt3*(SIN(2*(x(2)-psi)**2.)/4
! energy contribution for doubled trilayer
        case(2)
            RanisobiECon=(Rkb1*Rt1+Rkb2*Rt2)*(SIN(2*(x(1)-psi)**2.)/4+
            * Rkb3*Rt3*(SIN(2*(x(2)-psi)**2.)/4+
            * (Rkb4*Rt4+Rkb5*Rt5)*(SIN(2*(x(3)-psi)**2.)/4
! energy contribution for bottom spinvalve, multilayer
        case(3,5)
            RanisobiECon=Rkb1*Rt1*(SIN(2*(x(1)-psi)**2.)/4+
            * Rkb2*Rt2*(SIN(2*(x(2)-psi)**2.)/4
! energy contribution for multilayer (enh.)
        case(6)
            RanisobiECon=Rkb1*Rt1*(SIN(2*(x(1)-psi)**2.)/4+
            * Rkb2*Rt2*(SIN(2*(x(2)-psi)**2.)/4+
            * Rkb3*Rt3*(SIN(2*(x(3)-psi)**2.)/4+
            * Isc*Rkb3*Rt3*(SIN(2*(x(4)-psi)**2.)/4+
            * Isc*Rkb3*Rt3*(SIN(2*(x(5)-psi)**2.)/4+
            * Rkb4*Rt4*(SIN(2*(x(6)-psi)**2.)/4

        end select
    END function RanisobiECon

!-----

    function RanisoindECon(x)
    COMMON /layer/ Rt1,Rt2,Rt3,Rt4,Rt5,Rt6
    COMMON /indani/ Rkind1,Rkind2,Rkind3,Rkind4,Rkind5,psiind
    COMMON /state/ Ief,N,psi,Hfeld,Isc,Iparlauf
    REAL x(N)

        select case (int(Ief))
! energy contribution for trilayer, top spinvalve
        case(1,4)
            RanisoindECon=(Rkind1*Rt1+Rkind2*Rt2)*(SIN(x(1)-psiind)**2.)+
            * Rkind3*Rt3*(SIN(x(2)-psiind)**2.)
! energy contribution for doubled trilayer
        case(2)
            RanisoindECon=(Rkind1*Rt1+Rkind2*Rt2)*(SIN(x(1)-psiind)**2.)+
            * Rkind3*Rt3*(SIN(x(2)-psiind)**2.)+
            * (Rkind4*Rt4+Rkind5*Rt5)*(SIN(x(3)-psiind)**2.)

! energy contribution for bottom spinvalve, multilayer
        case(3,5)
            RanisoindECon=Rkind1*Rt1*(SIN(x(1)-psiind)**2.)+
            * Rkind2*Rt2*(SIN(x(2)-psiind)**2.)
! energy contribution for multilayer (enh.)
        case(6)
            RanisoindECon=Rkind1*Rt1*(SIN(x(1)-psiind)**2.)+
            * Rkind2*Rt2*(SIN(x(2)-psiind)**2.)+
            * Rkind3*Rt3*(SIN(x(3)-psiind)**2.)+
            * Isc*Rkind3*Rt3*(SIN(x(4)-psiind)**2.)+
            * Isc*Rkind3*Rt3*(SIN(x(5)-psiind)**2.)+
            * Rkind4*Rt4*(SIN(x(6)-psiind)**2.)

        end select
    END function RanisoindECon

!-----

    function RanisoindbECon(x)
    COMMON /layer/ Rt1,Rt2,Rt3,Rt4,Rt5,Rt6
    COMMON /indani/ Rkind1,Rkind2,Rkind3,Rkind4,Rkind5,psiind
    COMMON /indanibi/ Rkindb1,Rkindb2,Rkindb3,Rkindb4,Rkindb5
    COMMON /state/ Ief,N,psi,Hfeld,Isc,Iparlauf
    REAL x(N)

        select case (int(Ief))
! energy contribution for trilayer, top spinvalve
        case(1,4)
            RanisoindbECon=(Rkindb1*Rt1+Rkindb2*Rt2)*
            * (SIN(2*(x(1)-psiind)**2.)/4+
            * Rkindb3*Rt3*(SIN(2*(x(2)-psiind)**2.)/4
! energy contribution for doubled trilayer
        case(2)
            RanisoindbECon=(Rkindb1*Rt1+Rkindb2*Rt2)*
            * (SIN(2*(x(1)-psiind)**2.)/4+
            * Rkindb3*Rt3*(SIN(2*(x(2)-psiind)**2.)/4+
            * (Rkindb4*Rt4+Rkindb5*Rt5)*
            * (SIN(2*(x(3)-psiind)**2.)/4
! energy contribution for bottom spinvalve, multilayer
        case(3,5)

```

```

      RansoindbECon=Rkindb1*Rt1*(SIN(2*(x(1)-psiind)**2.)/4+
*      Rkindb2*Rt2*(SIN(2*(x(2)-psiind)**2.)/4
! energy contribution for      multilayer (enh.)
      case(6)
        RansoindbECon=Rkindb1*Rt1*(SIN(2*(x(1)-psiind)**2.)/4+
*        Rkindb2*Rt2*(SIN(2*(x(2)-psiind)**2.)/4+
*        Rkindb3*Rt3*(SIN(2*(x(3)-psiind)**2.)/4+
*        Isc*Rkindb3*Rt3*(SIN(2*(x(4)-psiind)**2.)/4+
*        Isc*Rkindb3*Rt3*(SIN(2*(x(5)-psiind)**2.)/4+
*        Rkindb4*Rt4*(SIN(2*(x(6)-psiind)**2.)/4
      end select
      END function RansoindbECon

!-----

      function RshapeECon(x)
      COMMON /layer/ Rt1,Rt2,Rt3,Rt4,Rt5,Rt6
      COMMON /kshape/ Rkshape1,Rkshape2,Rkshape3,Rkshape4,Rkshape5,Rxi
      COMMON /state/ Ief,N,psi,Hfeld,Isc,Iparlauf
      REAL x(N)

      select case (int(Ief))
! energy contribution for      trilayer , top spinvalve
      case(1,4)
        RshapeECon=(Rkshape1*Rt1+Rkshape2*Rt2)*(SIN(x(1)-Rxi)**2.)+
*        Rkshape3*Rt3*(SIN(x(2)-Rxi)**2.)
! energy contribution for      doubled trilayer
      case(2)
        RshapeECon=(Rkshape1*Rt1+Rkshape2*Rt2)*(SIN(x(1)-Rxi)**2.)+
*        Rkshape3*Rt3*(SIN(x(2)-Rxi)**2.)+
*        (Rkshape4*Rt4+Rkshape5*Rt5)*(SIN(x(3)-Rxi)**2.)
! energy contribution for      bottom spinvalve , multilayer
      case(3,5)
        RshapeECon=Rkshape1*Rt1*(SIN(x(1)-Rxi)**2.)+
*        Rkshape2*Rt2*(SIN(x(2)-Rxi)**2.)
! energy contribution for      multilayer (enh.)
      case(6)
        RshapeECon=Rkshape1*Rt1*(SIN(x(1)-Rxi)**2.)+
*        Rkshape2*Rt2*(SIN(x(2)-Rxi)**2.)+
*        Rkshape3*Rt3*(SIN(x(3)-Rxi)**2.)+
*        Isc*Rkshape3*Rt3*(SIN(x(4)-Rxi)**2.)+
*        Isc*Rkshape3*Rt3*(SIN(x(5)-Rxi)**2.)+
*        Rkshape4*Rt4*(SIN(x(6)-Rxi)**2.)
      end select
      END function RshapeECon

!-----

      function RpinningECon(x)
      COMMON /coupling/ Rj11tot,Rj12tot,Rj13tot,Rjq1,Rjq2,Rjq3
      COMMON /bias/ Rjeb,Rgamma
      COMMON /state/ Ief,N,psi,Hfeld,Isc,Iparlauf
      REAL x(N)

      select case (int(Ief))
! energy contribution for trilayer , doubled trilayer , multilayer , multilayer (enh.)
      case(1,2,5,6)
        RpinningECon=0.
! energy contribution for      bottom spinvalve
      case(3)
        RpinningECon=-Rjeb*COS(x(1)-Rgamma)
! energy contribution for      top spinvalve
      case(4)
        RpinningECon=-Rjeb*COS(x(2)-Rgamma)
      END select
      END function RpinningECon

!#####Orange Peel models#####

      function OPmodelA(Rtf,Rts,Rtp,Rmsatf,Rmsatp)
      real Rtf,Rts,Rtp,Rmsatf,Rmsatp
      COMMON /opc/ Rhop,Rlop
      parameter (Pi=3.1415926535897932384626433832795)
      if (Rlop.eq.0) then
        OPmodelA = 0.0
      else
        OPmodelA = Rmsatf*Rmsatp*Pi*Pi*Rhop*Rhop/(SQRT(2.)*Rlop)*
*        (1-EXP(-2*Pi*SQRT(2.)*Rtp/Rlop))*
*        EXP(-2*Pi*SQRT(2.)*Rts/Rlop)
      END if
      end function OPmodelA

      function OPmodelB(Rtp,Rts,Rtf,Rmsatp,Rmsatf)
      real Rtp,Rts,Rtf,Rmsatp,Rmsatf

```

```

COMMON /opc/ Rhop,Rlop
PARAMETER (Pi=3.1415926535897932384626433832795)
if (Rlop.eq.0) then
  OPmodelB = 0.0
else
  OPmodelB = Rmsatf*Rmsatp*Pi*Pi*Rhop*Rhop/(SQRT(2.)*Rlop)*
*           (1-EXP(-2*Pi*SQRT(2.)*Rtf/Rlop))*
*           (1-EXP(-2*Pi*SQRT(2.)*Rtp/Rlop))*
*           EXP(-2*Pi*SQRT(2.)*Rts/Rlop)
END if
end function OPmodelB

!#####FUNCTIONS CALCULATING GMR AND MAGNETIZATION#####

function RgmrContribution(x)
COMMON /scaling/ Ragmr, Rwgmr
COMMON /state/ Ief,N,psi,Hfeld,Isc,Iparlauf
REAL x(N)

  select case (int(Ief))
! GMR contribution for trilayer, bottom spinvalve, top spinvalve, multilayer
  case(1,3,4,5)
    RgmrContribution = 0.5*(1-COS(x(2)-x(1)))
! GMR contribution for doubled trilayer
  case(2)
    RgmrContribution = 0.5*(Rwgmr)*(1-COS(x(2)-x(1)))+
*                       0.5*(1-Rwgmr)*(1-COS(x(2)-x(3)))
! GMR contribution for multilayer (enh.)
  case(6)
    RgmrContribution = 0.5-(COS(x(2)-x(1))+
*                        COS(x(3)-x(2))+
*                        COS(x(4)-x(3))+
*                        (2*Isc-1)*COS(x(5)-x(4))+
*                        COS(x(6)-x(5)))/
*                        (4*Isc+6)

  end select
end function RgmrContribution

! enhanced GMR model
function RgmrContributionEnh(x)
COMMON /scaling/ Ragmr, Rwgmr
COMMON /state/ Ief,N,psi,Hfeld,Isc,Iparlauf
REAL x(N)

  select case (int(Ief))
! GMR contribution for doubled trilayer
  case(2)
    RgmrContributionEnh = Ragmr*
* (1-Rwgmr*(COS((x(2)-x(1))/2))**2-
* (1-Rwgmr)*(COS((x(3)-x(2))/2))**2)/
* (1+Ragmr*Rwgmr*(COS((x(2)-x(1))/2))**2+
* Ragmr*(1-Rwgmr)*(COS((x(3)-x(2))/2))**2)
! GMR contribution for trilayer, bottom spinvalve, top spinvalve, multilayer
  case(1,3,4,5)
    RgmrContributionEnh = Ragmr*(1-(COS((x(2)-x(1))/2))**2)/
* (1+Ragmr*(COS((x(2)-x(1))/2))**2)
! GMR contribution for multilayer (enh.)
! identical conductance in all layers assumed
  case(6)
    RgmrContributionEnh = Ragmr*
* (1-(COS((x(2)-x(1))/2))**2+
* (COS((x(3)-x(2))/2))**2+
* (COS((x(4)-x(3))/2))**2+
* (2*Isc-1)*(COS((x(5)-x(4))/2))**2+
* (COS((x(6)-x(5))/2))**2)/(2*Isc+3))/
* (1+Ragmr*(COS((x(2)-x(1))/2))**2+
* (COS((x(3)-x(2))/2))**2+
* (COS((x(4)-x(3))/2))**2+
* (2*Isc-1)*(COS((x(5)-x(4))/2))**2+
* (COS((x(6)-x(5))/2))**2)/(2*Isc+3)

  end select
end function RgmrContributionEnh

!-----

function magnContribution(x)
COMMON /layer/ Rt1,Rt2,Rt3,Rt4,Rt5,Rt6
COMMON /msat/ Rmsat1,Rmsat2,Rmsat3,Rmsat4,Rmsat5
COMMON /state/ Ief,N,psi,Hfeld,Isc,Iparlauf
REAL x(N)

  select case(int(Ief))
! magnContribution for trilayer, top spinvalve
  case(1,4)
    magnContribution=((Rmsat1*Rt1+Rmsat2*Rt2)*COS(x(1))+

```

```

*
*           Rmsat3*Rt3*COS(x(2))/(Rt1+Rt2+Rt3)
! magnContribution for    doubled trilayer
  case(2)
    magnContribution=((Rmsat1*Rt1+Rmsat2*Rt2)*COS(x(1))+
*                    Rmsat3*Rt3*COS(x(2))+
*                    (Rmsat4*Rt4+Rmsat5*Rt5)*COS(x(3)))/
*                    (Rt1+Rt2+Rt3+Rt4+Rt5)
! magnContribution for    bottom spinvalve , multilayer
  case(3,5)
    magnContribution=(Rmsat1*Rt1*COS(x(1))+
*                    Rmsat2*Rt2*COS(x(2)))/(Rt1+Rt2)
! magnContribution for    multilayer (enh.)
  case(6)
    magnContribution=(Rmsat1*Rt1*COS(x(1))+
*                    Rmsat2*Rt2*COS(x(2))+
*                    Rmsat3*Rt3*(COS(x(3))+Isc*COS(x(4))+Isc*COS(x(5)))+
*                    Rmsat4*Rt4*COS(x(6)))/
*                    (Rt1+Rt2+(2*Isc+1)*Rt3+Rt4)
  end select
end function magnContribution

#####CALCULATING ENERGY FOR ALL ANGELS [mJ/m^2]#####

subroutine eplotf

COMMON /state/ Ief,N,psi,Hfeld,Isc,Iparlauf
COMMON /eplot/ rfile,RmaxH,RminH,RstepH,Ivirginloop

REAL x(2)
CHARACTER :: rfile *60,formlog *30,how *10
CHARACTER :: file1 *60,folder *60
CHARACTER :: fileZee *60,fileJ_l *60,fileJ_q *60
CHARACTER :: fileA_u *60,fileA_b *60,fileA_i *60,fileAib *60
CHARACTER :: fileA_s *60,fileJeb *60,filetot *60

real, allocatable :: RzeemanM(:, :)
real, allocatable :: RcouplingLEM(:, :)
real, allocatable :: RcouplingQEM(:, :)
real, allocatable :: RanisoEM(:, :)
real, allocatable :: RanisobiEM(:, :)
real, allocatable :: RanisoindbEM(:, :)
real, allocatable :: RanisoindEM(:, :)
real, allocatable :: RshapeEM(:, :)
real, allocatable :: RpinningEM(:, :)
real, allocatable :: REtotalM(:, :)

PARAMETER (Pi=3.141593)
PARAMETER (psiStart=1, psiEnd=180, psiStep=1)
! distance of lattice points in degree
PARAMETER (xstep=5)

Inox=INT(360/xstep)+1
allocate (RzeemanM(Inox,Inox))
allocate (RcouplingLEM(Inox,Inox))
allocate (RcouplingQEM(Inox,Inox))
allocate (RanisoEM(Inox,Inox))
allocate (RanisobiEM(Inox,Inox))
allocate (RanisoindEM(Inox,Inox))
allocate (RanisoindbEM(Inox,Inox))
allocate (RshapeEM(Inox,Inox))
allocate (RpinningEM(Inox,Inox))
allocate (REtotalM(Inox,Inox))

write(how,FMT='(A1,I3,A6)') '( ',Inox,'E11.3)'

write(*,*)
formlog = ''
write (formlog, FMT='(A2,I2,A6)')
* '(A',LEN_TRIM(rfile),',I3.3)'
write (folder, FMT=formlog) rfile, Iparlauf
call SYSTEM('mkdir ' // folder)
write (*,*) 'Results saved in ', folder

write (formlog, FMT='(A2,I2,A5)')
* '(A',LEN_TRIM(folder),',A10)'
write (file1, FMT=formlog) folder, '\field.dat'

OPEN(UNIT=30,FILE=file1,STATUS='replace')
write (*,*) 'Field list is saved in ', file1

write (formlog, FMT='(A2,I2,A12)')
* '(A',LEN_TRIM(folder),',A4,I4.4,A4)'

Ik=1

! virgin loop

```

```

if (Ivirginloop.eq.1) then
do k=int(2*RstepH),int(Rmaxh),int(Rsteph)
  Hfeld=float(k)
  write(30,*) Hfeld

  !opening files for different energy contributions
  write (filezee , FMP=formlog) folder , '\zee' , Ik , '.dat'
  OPEN(UNIT=31,FILE=filezee ,STATUS='replace')
  write (fileJ_l , FMP=formlog) folder , '\jli' , Ik , '.dat'
  OPEN(UNIT=32,FILE=fileJ_l ,STATUS='replace')
  write (fileJ_q , FMP=formlog) folder , '\jqu' , Ik , '.dat'
  OPEN(UNIT=33,FILE=fileJ_q ,STATUS='replace')
  write (fileA_u , FMP=formlog) folder , '\aun' , Ik , '.dat'
  OPEN(UNIT=34,FILE=fileA_u ,STATUS='replace')
  write (fileA_b , FMP=formlog) folder , '\abi' , Ik , '.dat'
  OPEN(UNIT=35,FILE=fileA_b ,STATUS='replace')
  write (fileA_i , FMP=formlog) folder , '\ain' , Ik , '.dat'
  OPEN(UNIT=36,FILE=fileA_i ,STATUS='replace')
  write (fileAib , FMP=formlog) folder , '\aib' , Ik , '.dat'
  OPEN(UNIT=37,FILE=fileAib ,STATUS='replace')
  write (fileA_s , FMP=formlog) folder , '\ash' , Ik , '.dat'
  OPEN(UNIT=38,FILE=fileA_s ,STATUS='replace')
  write (fileJeb , FMP=formlog) folder , '\jeb' , Ik , '.dat'
  OPEN(UNIT=39,FILE=fileJeb ,STATUS='replace')
  write (filetot , FMP=formlog) folder , '\tot' , Ik , '.dat'
  OPEN(UNIT=40,FILE=filetot ,STATUS='replace')

  write(*,FMT='(A25,F9.1)') ' Calculating energies for ', Hfeld

  Ii=1

  do i=-180,180,xstep
    x(1)=float(i)*Pi/180.0

    IJ=1
    do j=-180,180,xstep
      x(2)=float(j)*Pi/180.0
      RzeemanM(Ii , Ij)=RzeemanECon(x)
      RcouplingLEM(Ii , Ij)=RcouplingLECon(x)
      RcouplingQEM(Ii , Ij)=RcouplingQECon(x)
      RanisoindEM(Ii , Ij)=RanisoindECon(x)
      RanisoindbEM(Ii , Ij)=RanisoindbECon(x)
      RshapeEM(Ii , Ij)=RshapeECon(x)
      RpinningEM(Ii , Ij)=RpinningECon(x)

      !Energy depend on easy axis. Therefore it is averaged.
      MM=0
      RanisoEM(Ii , IJ)=0
      RanisobiEM(Ii , IJ)=0
      do Ipsilauf=int(psiStart) , int(psiEnd) , int(psiStep)
        MM=MM+1
        psi=float(Ipsilauf)*Pi/180.0
        RanisoEM(Ii , Ij)=RanisoEM(Ii , IJ)+RanisoECon(x)
        RanisobiEM(Ii , Ij)=RanisobiEM(Ii , Ij)+RanisobiECon(x)
      end do
      RanisoEM(Ii , IJ)=RanisoEM(Ii , IJ)/MM
      RanisobiEM(Ii , IJ)=RanisobiEM(Ii , IJ)/MM

      REtotalM(Ii , Ij)=RzeemanM(Ii , Ij)+RcouplingLEM(Ii , Ij)+
      * RcouplingQEM(Ii , Ij)+RanisoEM(Ii , Ij)+RanisobiEM(Ii , Ij)+
      * RanisoindEM(Ii , Ij)+RshapeEM(Ii , Ij)+RpinningEM(Ii , Ij)

      Ij=Ij+1
    END do

    Ii=Ii+1
  END do

  write(31,how) RzeemanM
  write(32,how) RcouplingLEM; write(33,how) RcouplingQEM
  write(34,how) RanisoEM; write(35,how) RanisobiEM
  write(36,how) RanisoindEM; write(37,how) RanisoindbEM
  write(38,how) RshapeEM; write(39,how) RpinningEM
  write(40,how) REtotalM

  CLOSE(31); CLOSE(32); CLOSE(33); CLOSE(34); CLOSE(35)
  CLOSE(31); CLOSE(36); CLOSE(37); CLOSE(38); CLOSE(39)
  CLOSE(40)
  Ik=Ik+1
END do
END if

do k=int(Rmaxh),int(Rminh),int(-Rsteph)
  Hfeld=float(k)
  write(30,*) Hfeld

  !opening files for different energy contributions
  write (filezee , FMP=formlog) folder , '\zee' , Ik , '.dat'

```

```

OPEN(UNIT=31,FILE=filezee ,STATUS='replace')
write (fileJ_l , FMT=formlog) folder , '\jli' , Ik , '.dat'
OPEN(UNIT=32,FILE=fileJ_l ,STATUS='replace')
write (fileJ_q , FMT=formlog) folder , '\jq' , Ik , '.dat'
OPEN(UNIT=33,FILE=fileJ_q ,STATUS='replace')
write (fileA_u , FMT=formlog) folder , '\aun' , Ik , '.dat'
OPEN(UNIT=34,FILE=fileA_u ,STATUS='replace')
write (fileA_b , FMT=formlog) folder , '\abi' , Ik , '.dat'
OPEN(UNIT=35,FILE=fileA_b ,STATUS='replace')
write (fileA_i , FMT=formlog) folder , '\ain' , Ik , '.dat'
OPEN(UNIT=36,FILE=fileA_i ,STATUS='replace')
write (fileAib , FMT=formlog) folder , '\aib' , Ik , '.dat'
OPEN(UNIT=37,FILE=fileAib ,STATUS='replace')
write (fileA_s , FMT=formlog) folder , '\ash' , Ik , '.dat'
OPEN(UNIT=38,FILE=fileA_s ,STATUS='replace')
write (fileJeb , FMT=formlog) folder , '\jeb' , Ik , '.dat'
OPEN(UNIT=39,FILE=fileJeb ,STATUS='replace')
write (filetot , FMT=formlog) folder , '\tot' , Ik , '.dat'
OPEN(UNIT=40,FILE=filetot ,STATUS='replace')

write(*,FMT='(A25,F9.1)') ' Calculating energies for ', Hfeld

Ii=1

do i=-180,180,xstep
  x(1)=float(i)*Pi/180.0

  IJ=1
  do j=-180,180,xstep
    x(2)=float(j)*Pi/180.0
    RzeemanM(Ii , Ij)=RzeemanECon(x)
    RcouplingLEM(Ii , Ij)=RcouplingLECon(x)
    RcouplingQEM(Ii , Ij)=RcouplingQECon(x)
    RanisoindEM(Ii , Ij)=RanisoindECon(x)
    RanisoindbEM(Ii , Ij)=RanisoindbECon(x)
    RshapeEM(Ii , Ij)=RshapeECon(x)
    RpinningEM(Ii , Ij)=RpinningECon(x)

    !Energy depend on easy axis. Therefore it is averaged.
    MM=0
    RanisoEM(Ii , IJ)=0
    RanisobiEM(Ii , IJ)=0
    do Ipsilauf=int(psiStart) , int(psiEnd) , int(psiStep)
      MM=MM+1
      psi=float(Ipsilauf)*Pi/180.0
      RanisoEM(Ii , Ij)=RanisoEM(Ii , IJ)+RanisoECon(x)
      RanisobiEM(Ii , Ij)=RanisobiEM(Ii , Ij)+RanisobiECon(x)
    end do
    RanisoEM(Ii , IJ)=RanisoEM(Ii , IJ)/MM
    RanisobiEM(Ii , IJ)=RanisobiEM(Ii , IJ)/MM

    REtotalM(Ii , Ij)=RzeemanM(Ii , Ij)+RcouplingLEM(Ii , Ij)+
    *   RcouplingQEM(Ii , Ij)+RanisoEM(Ii , Ij)+RanisobiEM(Ii , Ij)+
    *   RanisoindEM(Ii , Ij)+RshapeEM(Ii , Ij)+RpinningEM(Ii , Ij)

    Ij=Ij+1
  END do

  Ii=Ii+1
END do

write(31,how) RzeemanM
write(32,how) RcouplingLEM; write(33,how) RcouplingQEM
write(34,how) RanisoEM; write(35,how) RanisobiEM
write(36,how) RanisoindEM; write(37,how) RanisoindbEM
write(38,how) RshapeEM; write(39,how) RpinningEM
write(40,how) REtotalM

CLOSE(31); CLOSE(32); CLOSE(33); CLOSE(34); CLOSE(35)
CLOSE(31); CLOSE(36); CLOSE(37); CLOSE(38); CLOSE(39)
CLOSE(40)
Ik=Ik+1
END do

do k=int(Rminh) , int(Rmaxh) , int(Rsteph)
  Hfeld=float(k)
  write(30,*) Hfeld

  !opening files for different energy contributions
  write (filezee , FMT=formlog) folder , '\zee' , Ik , '.dat'
  OPEN(UNIT=31,FILE=filezee ,STATUS='replace')
  write (fileJ_l , FMT=formlog) folder , '\jli' , Ik , '.dat'
  OPEN(UNIT=32,FILE=fileJ_l ,STATUS='replace')
  write (fileJ_q , FMT=formlog) folder , '\jq' , Ik , '.dat'
  OPEN(UNIT=33,FILE=fileJ_q ,STATUS='replace')
  write (fileA_u , FMT=formlog) folder , '\aun' , Ik , '.dat'
  OPEN(UNIT=34,FILE=fileA_u ,STATUS='replace')
  write (fileA_b , FMT=formlog) folder , '\abi' , Ik , '.dat'

```

```

OPEN(UNIT=35,FILE=fileA_b ,STATUS='replace')
write (fileA_i ,FMT=formlog) folder , '\ain' , Ik , '.dat'
OPEN(UNIT=36,FILE=fileA_i ,STATUS='replace')
write (fileAib ,FMT=formlog) folder , '\aib' , Ik , '.dat'
OPEN(UNIT=37,FILE=fileAib ,STATUS='replace')
write (fileA_s ,FMT=formlog) folder , '\ash' , Ik , '.dat'
OPEN(UNIT=38,FILE=fileA_s ,STATUS='replace')
write (fileJeb ,FMT=formlog) folder , '\jeb' , Ik , '.dat'
OPEN(UNIT=39,FILE=fileJeb ,STATUS='replace')
write (filetot ,FMT=formlog) folder , '\tot' , Ik , '.dat'
OPEN(UNIT=40,FILE=filetot ,STATUS='replace')

write(*,FMT='(A25,F9.1)') ' Calculating energies for ', Hfeld

Ii=1
do i=-180,180,xstep
  x(1)=float(i)*Pi/180.0

  IJ=1
  do j=-180,180,xstep
    x(2)=float(j)*Pi/180.0
    RzeemanM(Ii ,Ij)=RzeemanECon(x)
    RcouplingLEM(Ii ,Ij)=RcouplingLECon(x)
    RcouplingQEM(Ii ,Ij)=RcouplingQECon(x)
    RanisoindEM(Ii ,Ij)=RanisoindECon(x)
    RanisoindbEM(Ii ,Ij)=RanisoindbECon(x)
    RshapeEM(Ii ,Ij)=RshapeECon(x)
    RpinningEM(Ii ,Ij)=RpinningECon(x)

    !Energy depend on easy axis. Therefore it is averaged.
    MM=0
    RanisoEM(Ii ,IJ)=0
    RanisobiEM(Ii ,IJ)=0
    do Ipsilauf=int(psiStart) , int(psiEnd) , int(psiStep)
      MM=MM+1
      psi=float(Ipsilauf)*Pi/180.0
      RanisoEM(Ii ,Ij)=RanisoEM(Ii ,IJ)+RanisoECon(x)
      RanisobiEM(Ii ,Ij)=RanisobiEM(Ii ,Ij)+RanisobiECon(x)
    end do
    RanisoEM(Ii ,IJ)=RanisoEM(Ii ,IJ)/MM
    RanisobiEM(Ii ,IJ)=RanisobiEM(Ii ,IJ)/MM

    REtotalM(Ii ,Ij)=RzeemanM(Ii ,Ij)+RcouplingLEM(Ii ,Ij)+
    * RcouplingQEM(Ii ,Ij)+RanisoEM(Ii ,Ij)+RanisobiEM(Ii ,Ij)+
    * RanisoindEM(Ii ,Ij)+RshapeEM(Ii ,Ij)+RpinningEM(Ii ,Ij)

    Ij=Ij+1
  END do

  Ii=Ii+1
END do

write(31,how) RzeemanM
write(32,how) RcouplingLEM; write(33,how) RcouplingQEM
write(34,how) RanisoEM; write(35,how) RanisobiEM
write(36,how) RanisoindEM; write(37,how) RanisoindbEM
write(38,how) RshapeEM; write(39,how) RpinningEM
write(40,how) REtotalM

CLOSE(31); CLOSE(32); CLOSE(33); CLOSE(34); CLOSE(35)
CLOSE(31); CLOSE(36); CLOSE(37); CLOSE(38); CLOSE(39)
CLOSE(40)
Ik=Ik+1
END do

CLOSE(30)

END subroutine eplotf

!-----
!#####ROUTINES FOR OPTIMIZATION#####

SUBROUTINE frprmn(p,nn,ftol , iter , fret)
INTEGER iter , nn,NMAX,ITMAX
REAL fret , ftol ,p(nn),EPS,func

! Iparlauf and psi used for error message
COMMON /state/ Ief,N,psi ,Hfeld ,Isc ,Iparlauf

EXTERNAL func
PARAMETER (NMAX=50,ITMAX=5000,EPS=1.e-10)
PARAMETER (Pi=3.141593)
CU USES dfunc ,func ,linmin
INTEGER its ,j
REAL dgg ,fp ,gam ,gg ,g(NMAX) ,h(NMAX) ,xi(NMAX)
fp=func(p)

```

```

    call dfunc(p, xi)
    do 11 j=1,nn
      g(j)=-xi(j)
      h(j)=g(j)
      xi(j)=h(j)
11    continue
    do 14 its=1,ITMAX
      iter=its
      call linmin(p, xi, nn, fret)
      if (2.*abs(fret-fp).le.ftol*(abs(fret)+abs(fp)+EPS)) return
      fp=func(p)
      call dfunc(p, xi)
      gg=0.
      dgg=0.
      do 12 j=1,nn
        gg=gg+g(j)**2
C        dgg=dgg+xi(j)**2
        dgg=dgg+(xi(j)+g(j))*xi(j)
12      continue
      if (gg.eq.0.) return
      gam=dgg/gg
      do 13 j=1,nn
        g(j)=-xi(j)
        h(j)=g(j)+gam*h(j)
        xi(j)=h(j)
13      continue
14    continue
    write (22,*) 'frprmn exceed maximum iterations in set ', Iparlauf,
*              ' easy axis ', psi/Pi*180
    return
  END

SUBROUTINE linmin(p, xi, n, fret)
  INTEGER n, NMAX
  REAL fret, p(n), xi(n), TOL
  PARAMETER (NMAX=50, TOL=1.e-4)
CU  USES brent, fldim, mnbrak
  INTEGER j, ncom
  REAL ax, bx, fa, fb, fx, xmin, xx, pcom(NMAX), xicom(NMAX), brent
  COMMON /flcom/ pcom, xicom, ncom
  EXTERNAL fldim
  ncom=n
  do 11 j=1, n
    pcom(j)=p(j)
    xicom(j)=xi(j)
11  continue
  ax=0.
  xx=1.
  call mnbrak(ax, xx, bx, fa, fx, fb, fldim)
  fret=brent(ax, xx, bx, fldim, TOL, xmin)
  do 12 j=1, n
    xi(j)=xmin*xi(j)
    p(j)=p(j)+xi(j)
12  continue
  return
  END

SUBROUTINE mnbrak(ax, bx, cx, fa, fb, fc, func)
  REAL ax, bx, cx, fa, fb, fc, func, GOLD, GLIMIT, TINY1
  EXTERNAL func
  PARAMETER (GOLD=1.618034, GLIMIT=100., TINY1=1.e-20)
  REAL dum, fu, q, r, u, ulim
  fa=func(ax)
  fb=func(bx)
  if (fb.gt.fa) then
    dum=ax
    ax=bx
    bx=dum
    dum=fb
    fb=fa
    fa=dum
  endif
  cx=bx+GOLD*(bx-ax)
  fc=func(cx)
1  if (fb.ge.fc) then
    r=(bx-ax)*(fb-fc)
    q=(bx-cx)*(fb-fa)
    u=bx-((bx-cx)*q-(bx-ax)*r)/(2.*sign(max(abs(q-r), TINY1), q-r))
    ulim=bx+GLIMIT*(cx-bx)
    if ((bx-u)*(u-cx).gt.0.) then
      fu=func(u)
      if (fu.lt.fc) then
        ax=bx
        fa=fb
        bx=u
        fb=fu
        return
      else if (fu.gt.fb) then

```

```

        cx=u
        fc=fu
        return
    endif
    u=cx+GOLD*(cx-bx)
    fu=func(u)
else if ((cx-u)*(u-ulim).gt.0.) then
    fu=func(u)
    if (fu.lt.fc) then
        bx=cx
        cx=u
        u=cx+GOLD*(cx-bx)
        fb=fc
        fc=fu
        fu=func(u)
    endif
else if ((u-ulim)*(ulim-cx).ge.0.) then
    u=ulim
    fu=func(u)
else
    u=cx+GOLD*(cx-bx)
    fu=func(u)
endif
ax=bx
bx=cx
cx=u
fa=fb
fb=fc
fc=fu
goto 1
endif
return
END

FUNCTION brent (ax,bx,cx,f,tol,xmin)
INTEGER ITMAX
REAL brent,ax,bx,cx,tol,xmin,f,CGOLD,ZEPS
! Iparlauf used for error message

COMMON /state/ Ief,N,psi,Hfeld,Isc,Iparlauf

EXTERNAL f
PARAMETER (ITMAX=100,CGOLD=.3819660,ZEPS=1.0e-10)
PARAMETER (Pi=3.141593)
INTEGER iter
REAL a,b,d,e,etemp,fu,fv,fw,fx,p,q,r,toll,tol2,u,v,w,x,xi
a=min(ax,cx)
b=max(ax,cx)
v=bx
w=v
x=v
e=0.
fx=f(x)
fv=fx
fw=fx
do 11 iter=1,ITMAX
    xm=0.5*(a+b)
    toll=tol*abs(x)+ZEPS
    tol2=2.*toll
    if (abs(x-xm).le.(tol2-.5*(b-a))) goto 3
    if (abs(e).gt.toll) then
        r=(x-w)*(fx-fv)
        q=(x-v)*(fx-fw)
        p=(x-v)*q-(x-w)*r
        q=2.*(q-r)
        if (q.gt.0.) p=-p
        q=abs(q)
        etemp=e
        e=d
        if (abs(p).ge.abs(.5*q*etemp).or.p.le.q*(a-x).or.p.ge.q*(b-x))
*goto 1
        d=p/q
        u=x+d
        if (u-a.lt.toll2.or.b-u.lt.toll2) d=sign(toll,xm-x)
        goto 2
    endif
1   if (x.ge.xm) then
        e=a-x
    else
        e=b-x
    endif
    d=CGOLD*e
2   if (abs(d).ge.toll) then
        u=x+d
    else
        u=x+sign(toll,d)
    endif
    fu=f(u)

```

```

    if (fu.le.fx) then
      if (u.ge.x) then
        a=x
      else
        b=x
      endif
      v=w
      fv=fw
      w=x
      fw=fx
      x=u
      fx=fu
    else
      if (u.lt.x) then
        a=u
      else
        b=u
      endif
      if (fu.le.fw .or. w.eq.x) then
        v=w
        fv=fw
        w=u
        fw=fu
      else if (fu.le.fv .or. v.eq.x .or. v.eq.w) then
        v=u
        fv=fu
      endif
    endif
11  continue
    write (22,*) 'brent exceed maximum iterations in set ', Iparlauf,
*      ' easy axis ', psi/Pi*180
3   xmin=x
    brent=fx
    return
  END

  FUNCTION f1dim(x)
  INTEGER NMAX
  REAL f1dim,func,x
  PARAMETER (NMAX=50)
! USES func
  INTEGER j,ncom
  REAL pcom(NMAX),xicom(NMAX),xt(NMAX)
  COMMON /f1com/ pcom,xicom,ncom
  do 11 j=1,ncom
    xt(j)=pcom(j)+ x * xicom(j)
11  continue
  f1dim=func(xt)
  return
  END

```

Bibliography

- [Bai88] M. N. BAIBICH, J. M. BROTO, A. FERT, F. NGUYEN VAN DAU, P. PETROFF, P. ETIENNE, G. CREUZET, A. FRIEDERICH, AND J. CHAZELAS. Giant Magnetoresistance of (001)Fe/(001)Cr Magnetic Superlattices. *Phys. Rev. Lett.*, **61**(21), 2472–2475 (1988)
- [Bar92] J. BARNA. Coupling between two ferromagnetic films through a nonmagnetic metallic layer. *J. Magn. Magn. Mater.*, **111**, L215–L219 (1992)
- [Bay99] G. BAYREUTHER. Spinvalves. In *Magnetische Schichtsysteme in Forschung und Anwendung - Vorlesungsmanuskripte*, volume 2 of *Schriften des Forschungszentrum Jülich, Matter and Materials*, pp. D4.1–17. Forschungszentrum Jülich GmbH, Institut für Festkörperforschung (1999)
- [Bin89] G. BINARSCH, P. GRÜNBERG, F. SAURENBACH, AND W. ZINN. Enhanced magnetoresistance in layered magnetic structures with antiferromagnetic interlayer exchange. *Phys. Rev. B*, **39**, 4842–4830 (1989)
- [Boz51] R. M. BOZORTH. *Ferromagnetism*. Princeton. D. van Nostrand Company, Inc., New Jersey, Toronto, Melbourne, London (1951)
- [Bru91] P. BRUNO AND C. CHAPPERT. Oscillatory Coupling between Ferromagnetic Layers Separated by a Nonmagnetic Metal Spacer. *Phys. Rev. Lett.*, **67**, 1602–1605 (1991)
- [Bru95] P. BRUNO. Theory of interlayer magnetic coupling. *Phys. Rev. B*, **52**, 411–439 (1995)
- [Bru99] P. BRUNO. Theory of interlayer exchange coupling. In *Magnetische Schichtsysteme in Forschung und Anwendung - Vorlesungsmanuskripte*, volume 2 of *Schriften des Forschungszentrum Jülich, Matter and Materials*, pp. B8.1–42. Forschungszentrum Jülich GmbH, Institut für Festkörperforschung (1999)

- [Cam82] I. A. CAMPBELL AND A. FERT. Transport Properties of Ferromagnets. *Ferromagnetic Materials*, **3**, 747–804 (1982)
- [Cam89] R. E. CAMLEY AND J. BARNAŚ. Theory of Giant Magnetoresistance Effects in Magnetic Layered Structures with Antiferromagnetic Coupling. *Phys. Rev. Lett.*, **63**, 664–667 (1989)
- [Coe91] R. COEHOORN. Period of oscillatory exchange interactions in Co/Cu and Fe/Cu multilayer systems. *Phys. Rev. B*, **44**, 9331–9337 (1991)
- [Die91a] B. DIENY, V. S. SPERIOSU, S. METIN, S. S. P. PARKIN, B. A. GURNEY, P. BAUMGART, AND D. R. WILHOIT. Magnetotransport properties of magnetically soft spin-valve structures. *J. Appl. Phys.*, **69**, 4774–4779 (1991)
- [Die91b] B. DIENY, V. S. SPERIOSU, S. S. P. PARKIN, B. A. GURNEY, D. R. WILHOIT, AND D. MAURI. Giant magnetoresistance in soft ferromagnetic multilayers. *Phys. Rev. B*, **43**, 1297–1300 (1991)
- [Die94] B. DIENY. Giant magnetoresistance in spin-valve multilayers (Review Article). *J. Magn. Magn. Mater.*, pp. 335–359 (1994)
- [Edw91] D. M. EDWARDS, J. MATHON, R. B. MUNIZ, AND M. S. PHAN. Oscillations in the exchange coupling of ferromagnetic layers separated by a nonmagnetic metallic layer. *J. Phys.: Condens. Matter* **3**, 4941–4958 (1991)
- [Eri93] R. P. ERICKSON, K. B. HATHAWAY, AND J. R. CULLEN. Mechanism for non-Heisenberg-exchange coupling between ferromagnetic layers. *Phys. Rev. B*, **47**, 2626–2635 (1993)
- [Fas03] J. FASSBENDER, S. POPPE, T. MEWES, J. JURASZEK, B. HILLEBRANDS, K.-U. BARHOLZ, R. MATTHEIS, D. ENGEL, M. JUNG, H. SCHMORANZER, AND A. EHRESMANN. Ion irradiation of exchange bias systems for magnetic sensor applications. *Applied Physics A*, **77**, 51–56 (2003)
- [Grü86] P. GRÜNBERG, R. SCHREIBER, Y. PANG, M. B. BRODSKY, AND H. SOWERS. Layered Magnetic Structures: Evidence for Antiferromagnetic Coupling of Fe Layers across Cr Interlayers. *Phys. Rev. Lett.*, **57**, 2442–2445 (1986)
- [Grü99] P. GRÜNBERG. Zwischenschichtaustauschkopplung: Phänomenologische Beschreibung, Materialabhängigkeit. In *Magnetische*

Schichtsysteme in Forschung und Anwendung - Vorlesungsmanuskripte, volume 2 of *Schriften des Forschungszentrum Jülich, Matter and Materials*, pp. B9.1–24. Forschungszentrum Jülich GmbH, Institut für Festkörperforschung (1999)

- [Gur93] B. A. GURNEY, V. S. SPERIOSU, J.-P. NOZIERES, H. LEFAKIS, D. R. WILHOIT, AND O. U. NEED. Direct measurement of spin-dependent conduction-electron mean free paths in ferromagnetic metals. *Phys. Rev. Lett.*, **71**, 4023–4026 (1993)
- [Hei00] S. HEITMANN, A. HÜTTEN, T. HEMPEL, W. SCHEPPER, AND G. REISS. Interplay of antiferromagnetic coupling in copper/permalloy combination multilayers. *J. Appl. Phys.*, **87**, 4849–4851 (2000)
- [Hei01] S. HEITMANN, A. HÜTTEN, T. HEMPEL, W. SCHEPPER, AND G. REISS. Enhanced GMR amplitude and temperature stability of copper / permalloy combination multilayers. *J. Magn. Magn. Mater.*, **226**, 1752–1754 (2001)
- [Hei04] S. HEITMANN. Cobalt / Copper Multilayers: Interplay of Microstructure and GMR and Recrystallization as the Key Toward Temperature Stability. Dissertation, Universität Bielefeld (2004)
- [Hem00] T. HEMPEL. Magnetische Dreischichtsysteme und hysteresefreie Kupfer/Kobalt-Mehrlagensysteme. Diploma thesis, Universität Bielefeld (2000)
- [Hol98] H. HOLLOWAY AND D. J. KUBINSKI. Magnetoresistive Co/Cu multilayers: Hysteresis, polycrystallinity, and irreversible changes on magnetization. *J. Appl. Phys.*, **83**, 2705–2714 (1998)
- [Hüt99] A. HÜTTEN, S. MROZEK, S. HEITMANN, T. HEMPEL, H. BRÜCKL, AND G. REISS. Evolution of the GMR-Effect Amplitude in Copper/Permalloy-Multilayered Thin Films. *Acta Materialia*, **47**, 4245–4252 (1999)
- [Hüt01] A. HÜTTEN, T. HEMPEL, W. SCHEPPER, U. KLEINEBERG, AND G. REISS. Giant magnetoresistance of hysteresis-free Cu/Co-based multilayers. *J. Magn. Magn. Mater.*, **226-230**, 1758–1760 (2001)
- [Hüt02] A. HÜTTEN, T. HEMPEL, S. HEITMANN, AND G. REISS. The Limit of the Giant Magnetoresistance Effect in Only Three Layers. *phys. stat. sol (a)*, **189**(2), 327–338 (2002)

- [Jo02] S. JO AND M. SEIGLER. Magnetoresistance and interlayer coupling in spinvalves employing very thin Cu spacer. *J. Appl. Phys.*, **91**(2), 7110–7112 (2002)
- [Koo99] J. C. S. KOOLS AND W. KULA. Effect of finite magnetic film thickness on Néel coupling in spin valves. *J. Appl. Phys.*, **85**, 4466–4468 (1999)
- [Lev95] P. M. LEVY AND S. ZHANG. Our current understanding of giant magnetoresistance in transition-metal multilayers. *J. Magn. Magn. Mater.*, **151**, 315–323 (1995)
- [Lev96] P. M. LEVY AND S. ZHANG. Current status of our understanding of magnetotransport in magnetic multilayers. *J. Magn. Magn. Mater.*, **164**, 284–292 (1996)
- [Luc03a] T. LUCIŃSKI, A. HÜTTEN, H. BRÜCKL, T. HEMPEL, S. HEITMANN, AND G. REISS. Magnetoresistive properties of $Ni_{80}Fe_{20}/Co1/CuAgAu/Co2$ pseudo-spin-valves. *phys. stat. sol (a)*, **196**(1), 97–100 (2003)
- [Luc03b] T. LUCIŃSKI, M. KOPCEWICZ, A. HÜTTEN, H. BRÜCKL, S. HEITMANN, T. HEMPEL, AND G. REISS. Magnetic and Mössbauer study of Fe/Si multilayers. *J. Appl. Phys.*, **93**, 6501–6503 (2003)
- [Luc03c] T. LUCIŃSKI, M. KOPCEWICZ, A. HÜTTEN, H. BRÜCKL, S. HEITMANN, T. HEMPEL, AND G. REISS. Magnetic properties of Fe/Si and Co/Si multilayers. *Materials Science - Poland*, **21**, 25–27 (2003)
- [Luc04] T. LUCIŃSKI, A. HÜTTEN, H. BRÜCKL, S. HEITMANN, T. HEMPEL, AND G. REISS. Magnetoresistance study of $Ni_{80}Fe_{20}/Co1/CuAgAu/Co2$ asymmetric sandwiches. *J. Magn. Magn. Mater.*, **269**, 78–88 (2004)
- [Mat91] J. MATHON. Exchange interactions and giant magnetoresistance in magnetic multilayers. *Contemporary Physics*, **32**, 143–156 (1991)
- [Mro98] S. MROZEK. Vergleich des Riesenmagnetowiderstandes und Magnetismus von granularen, kontinuierlichen und diskontinuierlichen Viellagensystemen. Diploma thesis, Universität Bielefeld (1998)
- [Née62] L. NÉEL. . *Comptes rendues de l'Académie des sciences*, **255**, 1676 (1962)

- [O'H00] R. C. O'HANDLEY. *Modern Magnetic Materials, Principles and Applications*. John Wiley & Sons, Inc., New York, Chichester, Weinheim, Brisbane, Singapore, Toronto (2000)
- [Par90] S. S. P. PARKIN, N. MORE, AND K. P. ROCHE. Oscillations in Exchange Coupling and Magnetoresistance in Metallic Superlattice Structures Co/Ru, Co/Cr, and Fe/Cr. *Phys. Rev. Lett.*, **64**, 2304–2307 (1990)
- [Pur91] S. T. PURCELL, W. FOLKERTS, M. T. JOHNSON, N. W. E. MCGEE, K. JAGER, J. AAN DE STEGGE, W. B. ZEPER, W. HOVING, AND P. GRÜNBERG. Oscillations with a period of two Cr monolayers in the antiferromagnetic exchange coupling in a (001) Fe/Cr/Fe sandwich structure. *Phys. Rev. Lett.*, **67**(7), 903–906 (1991)
- [Rei99] G. REISS, H. BRÜCKL, AND A. HÜTTEN. GMR Experimente. In *Magnetische Schichtsysteme in Forschung und Anwendung - Vorlesungsmanuskripte*, volume 2 of *Schriften des Forschungszentrum Jülich, Matter and Materials*, pp. D3.1–30. Forschungszentrum Jülich GmbH, Institut für Festkörperforschung (1999)
- [Rij94] T. G. S. M. RIJKS, R. COEHOORN, J. T. F. DAEMEN, AND W. J. M. DE JONGE. Interplay between exchange biasing and interlayer exchange coupling in $Ni_{80}Fe_{20}/Cu/Ni_{80}Fe_{20}/Fe_{50}Mn_{50}$ layered systems. *J. Appl. Phys.*, **76**, 1092–1099 (1994)
- [Sch00a] W. SCHEPPER, K. DIPLAS, T. HEMPEL, AND G. REISS. Simulation of GMR- and Magnetization Characteristics in Cu/Co-based Multilayers. In *ICM2000 in Recife, Brazil*, 4U-45 (2000)
- [Sch00b] W. SCHEPPER, A. HÜTTEN, AND G. REISS. Optimization processes for giant magnetoresistance characteristic for mixed magnetic multilayers. *J. Appl. Phys.*, **88**, 993–998 (2000)
- [Slo91] J. C. SLONCZEWSKI. Fluctuation Mechanism for Biquadratic Exchange Coupling in Magnetic Multilayers. *Phys. Rev. Lett.*, **67**(22), 3172–3175 (1991)
- [Slo93] J. C. SLONCZEWSKI. Origin of biquadratic exchange in magnetic multilayers. *J. Appl. Phys.*, **73**(10), 5957–5962 (1993)
- [Spe93] V. S. SPERIOSU, J. P. NOZIERES, B. A. GURNEY, B. DIENY, T. C. HUANG, AND H. LEFAKIS. Role of interfacial mixing in giant magnetoresistance. *Phys. Rev. B*, **47**(17), 11579–11582 (1993)

- [Sta03] K. STARKE. *Experimentelle Präparation von Eisen-Silizium-Mehrfachschichten und Untersuchung der antiferromagnetischen Kopplung benachbarter Eisenschichten*. Master's thesis, Universität Bielefeld (2003)
- [Ste94] M. B. STEARNS AND Y. CHENG. Determination of para- and ferromagnetic components of magnetization and magnetoresistance of granular Co/Ag films. *J. Appl. Phys.*, **75**, 6894–6899 (1994)
- [Sti99] M. D. STILES. Interlayer exchange coupling. *J. Magn. Magn. Mater.*, **200**, 322–337 (1999)
- [Sto48] E. C. STONER AND E. P. WOHLFARTH. A Mechanism of Magnetic Hysteresis in Heterogeneous Alloys. *Philos. Trans. Roy. Soc. London*, **A-240**, 599–642 (1948)
- [Sud00] D. SUDFELD. *Aufbau eines Messplatzes für magnetfeldabhängige Messungen der Magnetisierung und des Magnetowiderstandes d"unner Schichten*. Master's thesis, Universität Bielefeld (2000)
- [Sud02a] D. SUDFELD, A. HÜTTEN, K. ROTT, T. HEMPEL, S. KÄMMERRER, W. HACHMANN, G. REISS, K. WOJCYKOWSKI, AND P. JUTZI. Magnetic cobalt nanocrystals organized in patches and chains. *Intermag Europe 2002, Digest of Technical Papers, Magnetic Soc. IEEE*. (2002)
- [Sud02b] D. SUDFELD, K. WOJCYKOWSKI, W. HACHMANN, S. HEITMANN, T. H. K. ROTT, S. KÄMMERRER, P. JUTZI, A. HÜTTEN, AND G. REISS. Magnetic cobalt nanocrystals organized in patches and chains. *IEEE Trans. Magn.*, **38**, 2601–2603 (2002)
- [Tsy99] E. Y. TSYMBAL AND D. G. PETTIFOR. Giant magnetoresistance in spin valves: effect of interfaces and outer boundaries. *J. Magn. Magn. Mater.*, **202**, 163–173 (1999)
- [Tsy01] E. Y. TSYMBAL AND D. G. PETTIFOR. Perspectives of giant magnetoresistance. *Sol. Stat. Phys.* /, **56**, 113–237 (2001)
- [Ung91] J. UNGURIS, R. J. CELOTTA, AND D. T. PIERCE. Observation of two different oscillation periods in the exchange coupling of Fe/Cr/Fe(100). *Phys. Rev. Lett.*, **67**(1), 140–143 (1991)
- [Yaf87a] Y. YAFET. RKKY interactions across yttrium layers in Gd-Y superlattices. *J. Appl. Phys.*, **61**, 4058–4060 (1987)

-
- [Yaf87b] Y. YAFET. Ruderman-Kittel-Kasuya-Yosida range function of a one-dimensional free-electron gas. *Phys. Rev. B*, **36**, 3948–3949 (1987)
- [Zor99] R. ZORN. Magnetometrie. In *Magnetische Schichtsysteme in Forschung und Anwendung - Vorlesungsmanuskripte*, volume 2 of *Schriften des Forschungszentrum Jülich, Matter and Materials*, pp. A6.1–22. Forschungszentrum Jülich GmbH, Institut für Festkörperforschung (1999)

Publications and Conferences

Publications

A. HÜTTEN, S. MROZEK, S. HEITMANN, T. HEMPEL, H. BRÜCKL, G. REISS: Evolution of the GMR-Effect Amplitude in Copper/Permalloy-Multilayered Thin Films. *Acta Materialia*, **47**, 4245 - 4252 (1999)

S. HEITMANN, A. HÜTTEN, T. HEMPEL, W. SCHEPPER, G. REISS, AND C. ALOF: Interplay of antiferromagnetic coupling in copper/permalloy combination multilayers. *J. Appl. Phys.*, **87**, 4849 - 4851 (2000)

A. HÜTTEN, T. HEMPEL, W. SCHEPPER, U. KLEINEBERG, AND G. REISS: Giant magnetoresistance of hysteresis-free Cu/Co-based multilayers. *J. Magn. Magn. Mater.*, **226**, 1758-1760 (2001)

S. HEITMANN, A. HÜTTEN, T. HEMPEL, W. SCHEPPER, AND G. REISS: Enhanced GMR amplitude and temperature stability of copper / permalloy combination multilayers. *J. Magn. Magn. Mater.*, **226**, 1752-1754 (2001)

A. HÜTTEN, T. HEMPEL, S. HEITMANN, AND G. REISS: The Limit of the Giant Magnetoresistance Effect in Only Three Layers. *phys. stat. sol. (a)*, **189**(2), 327-338 (2002)

D. SUDFELD, K. WOJCZYKOWSKI, W. HACHMANN, S. HEITMANN, K. ROTT, T. HEMPEL, S. KÄMMERRER, P. JUTZI, A. HÜTTEN, AND G. REISS: Magnetic cobalt nanocrystals organized in patches and chains. *IEEE Trans. Magn.*, **38**, 2601 - 2603 (2002)

D. SUDFELD, A. HÜTTEN, K. ROTT, T. HEMPEL, S. KÄMMERRER, W. HACHMANN, G. REISS, K. WOJCZYKOWSKI, AND P. JUTZI: Magnetic cobalt nanocrystals organized in patches and chains. *Intermag Europe 2002, Digest of Technical Papers, Magnetic Soc. IEEE* (2002)

T. LUCIŃSKI, A. HÜTTEN, H. BRÜCKL, T. HEMPEL, S. HEITMANN, AND G. REISS: Magnetoresistive properties of $Ni_{80}Fe_{20}/Co1/CuAgAu/Co2$ pseudo-spin-valves. *phys. stat. sol. (a)*, **196**(1), 97-100 (2003)

T. LUCIŃSKI, M. KOPCEWICZ, A. HÜTTEN, H. BRÜCKL, S. HEITMANN, T. HEMPEL, AND G. REISS: Magnetic and Mössbauer study of Fe/Si multilayers. *J. Appl. Phys.*, **93**, 6501-6503 (2003)

T. LUCIŃSKI, M. KOPCEWICZ, A. HÜTTEN, H. BRÜCKL, S. HEITMANN, T. HEMPEL, AND G. REISS: Magnetic properties of Fe/Si and Co/Si multilayers. *Materials Science - Poland*, **21**, 25-27 (2003)

T. LUCIŃSKI, A. HÜTTEN, H. BRÜCKL, S. HEITMANN, T. HEMPEL, AND G. REISS: Magnetoresistance study of $Ni_{80}Fe_{20}/Co1/CuAgAu/Co2$ asymmetric sandwiches. *J. Magn. Magn. Mater.*, **269**, 78-88 (2004)

Patent

T. HEMPEL, G. REISS, H. SIEGLE, A. HÜTTEN, P. SCHMOLLNGRUBER, T. LUCIŃSKI: Integriertes Speicher- und Sensierinstrument auf Basis des GMR-Effektes.

Patent Number: DE10140606

Publication date: 2003-05-08

Applicant: Robert Bosch GmbH

Conferences

T. HEMPEL, A. HÜTTEN, AND G. REISS: Riesenmagnetowiderstand (GMR) in Dreischichtsystemen $Py_{1-x}Co_x/Cu_{1-y}Ag_y/Co$. *Frühjahrstagung des Arbeitskreises Festkörperphysik der DPG, Regensburg, Germany*, talk AM 21.2 (2000)

T. HEMPEL, A. HÜTTEN, AND G. REISS: AF-coupled tri-layers as an alternative for exchange-biased spin valves. *VDI Statusseminar, Dresden, Germany*, (2000)

T. HEMPEL, A. HÜTTEN, AND G. REISS: AF-coupled tri-layers as an alternative for exchange-biased spin valves. *Symposium on Spin-Electronics (SEE 2000), Halle, Germany* contribution PB 14 (2000)

A. HÜTTEN, T. HEMPEL, W. SCHEPPER, U. KLEINEBERG, G. REISS: Giant magnetoresistance of hysteresis-free Cu/Co-based multilayers. *International Conference on Magnetism (ICM2000), Recife, Brazil*, contribution 4U-43 (2000)

W. SCHEPPER, K. DIPLAS, T. HEMPEL, AND G. REISS: Simulation of GMR- and Magnetization Characteristics in Cu/Co-based Multilayers. *International Conference on Magnetism (ICM2000), Recife, Brazil*, contribution 4U-45 (2000)

T. HEMPEL, A. HÜTTEN, T. LUCIŃSKI, AND G. REISS: Antiferromagnetisch und ferromagnetisch gekoppelte Trilayer. *Frühjahrstagung des Arbeitskreises Festkörperphysik der DPG, Hamburg, Germany*, talk AM 3.5 (2001)

T. HEMPEL, S. HEITMANN, A. HÜTTEN, AND G. REISS: Enhancing spin dependent scattering in simple sandwich structures. *4th International Symposium on Metallic Multilayers (MML'01), Aachen, Germany* contribution SDT-I PM (2001)

T. HEMPEL, A. HÜTTEN, S. HEITMANN, W. SCHEPPER AND G. REISS: Tailoring and simulation of GMR-characteristics in advanced magnetic trilayers. *First Seeheim Conference on Magnetism (SCM2001), Seeheim, Germany* (2001)

T. HEMPEL, A. HÜTTEN, S. HEITMANN AND G. REISS: Gekoppelte magnetische Dreilager: Simulationsgestützte Untersuchung zu Sensoranwendungen. *Frühjahrstagung des Arbeitskreises Festkörperphysik der DPG, Regensburg, Germany*, talk MA 7.8 (2002)

T. HEMPEL, I. ENNEN, A. HÜTTEN, S. HEITMANN AND G. REISS: Antiferromagnetically coupled Spin Valves with Spacer Layer Thickness down to 1 nm. *Frühjahrstagung des Arbeitskreises Festkörperphysik der DPG, Dresden, Germany*, talk MA 30.1 (2003)

T. HEMPEL, I. ROHDE, I. ENNEN, A. HÜTTEN, AND G. REISS: Antiferromagnetically Coupled Spin Valves with Spacer Layer Thickness down to 1 nm. *Intermag 2003, Boston, USA* contribution FT-04 (2003)

I. ROHDE, T. HEMPEL, S. HEITMANN, AND G. REISS: Hardening and Application of FePt Buffer Layers. *Intermag 2003, Boston, USA* contribution FQ-07 (2003)

List of Figures

2.1	Illustration of the resistor network model.	9
2.2	Electronic band structures and density of states of <i>Cu</i> and <i>Co</i>	12
2.3	Illustration of the IEC.	19
2.4	Oscillation of interlayer exchange coupling.	21
2.5	Quantum well model.	22
2.6	Fermi surface of <i>Cu</i>	27
2.7	Schematic of the magnetostatic interaction.	30
2.8	Model of mixed multilayer.	32
2.9	Comparison of the two models to calculate GMR(H).	34
3.1	Coupled and pinned trilayer	38
3.2	Introduction of parameters.	40
3.3	GMR amplitude as a function of the <i>Cu</i> layer thickness in the unpinned systems.	42
3.4	Sputter device LAB560	43
3.5	Magnetic mask	44
3.6	Plot for general understanding of the GMR characteristics.	45
3.7	Variation of <i>Co</i> -pinned layer thickness, AFCM 1.	47
3.8	Variation of pinned <i>Co</i> -layer thickness, AFCM 2.	47
3.9	Variation of free <i>Co</i> -layer thickness, AFCM 1.	49
3.10	Variation of pinned <i>Co</i> -layer thickness, AFCM 2.	49
3.11	Variation of buffer layer thickness, AFCM 2.	50

3.12	Variation of pinning layer thickness, AFCM 1.	50
3.13	GMR as function of the spacer layer thickness in the pinned system.	51
3.14	GMR characteristics near the 1 st AFCM.	52
3.15	GMR characteristics near and above the 2 nd AFCM.	53
3.16	Overview to trilayer series	55
3.17	AFM-image of a trilayer	57
3.18	AFM-line scan of a trilayer	57
3.19	TEM-image of a trilayer	58
3.20	Magnetization analysis in 1 st AFCM.	63
3.21	Magnetization analysis between 1 st and 2 nd AFCM.	63
3.22	Magnetization analysis at 2 nd AFCM.	64
3.23	Magnetization analysis after 2 nd AFCM.	64
3.24	Magnetization analysis at 2 nd AFCM for trilayer.	65
3.25	Magnetization analysis at 2 nd AFCM for trilayer.	65
3.26	GMR characteristics at 1 st AFCM.	66
3.27	GMR characteristics at 2 nd AFCM.	67
3.28	GMR amplitude as a function of the <i>Cu</i> layer thickness for both systems.	68
4.1	TEM-micrograph of a layered system.	73
4.2	Design of a top pinned trilayer.	74
4.3	Magnetic configuration of a trilayer.	75
4.4	Procedure of the simulation.	80
4.5	Energy surface.	82
4.6	GMR characteristic calculated from lattice calculation.	84
4.7	84
4.8	Lattice calculation with MicroMagus.	86
4.9	Lattice calculation with MicroMagus with periodic boundary conditions.	87

4.10	$\Delta R/R$ -characteristic for $t_s = 0.91 \text{ nm}$	90
4.11	$\Delta R/R$ -characteristic for $t_s = 1.0 \text{ nm}$	91
4.12	$\Delta R/R$ -characteristic for $t_s = 1.1 \text{ nm}$	91
4.13	$\Delta R/R$ -characteristic for $t_s = 1.3 \text{ nm}$	92
4.14	$\Delta R/R$ -characteristic for $t_s = 1.55 \text{ nm}$	92
4.15	$\Delta R/R$ -characteristic for $t_s = 1.65 \text{ nm}$	93
4.16	$\Delta R/R$ -characteristic for $t_s = 1.83 \text{ nm}$	93
4.17	$\Delta R/R$ -characteristic for $t_s = 1.88 \text{ nm}$	94
4.18	$\Delta R/R$ -characteristic for $t_s = 1.92 \text{ nm}$	94
4.19	$\Delta R/R$ -characteristic for $t_s = 2.07 \text{ nm}$	95
4.20	$\Delta R/R$ -characteristic for $t_s = 2.95 \text{ nm}$	95
4.21	Comparison of model and simulation.	97
5.1	Wheatstone bridge.	100
5.2	Measured and simulated GMR characteristic of a Cu/NiFe-ML.	103
5.3	Simulation with reduces line widths.	103
5.4	Design of meanders.	104
5.5	Meanders in a SEM picture.	104
5.6	Sketch of measurement geometry.	106
5.7	GMR characteristic of meander $100 \mu\text{m}$	107
5.8	GMR characteristic of meander $100 \mu\text{m}$, alternative plot.	108
5.9	GMR characteristic of meander $5 \mu\text{m}$	109
5.10	Parameters of meanders sputtered without a magnetic field.	110
5.11	Parameters of meanders sputtered with a magnetic field.	112
5.12	GMR characteristic of meander $1 \mu\text{m}$	113
5.13	Processes for structuring test wafers.	115
5.14	Test structures on the mask set.	116
5.15	GMR amplitude and resistance as function of the pulse energy for the Cu/Co-ML.	117
5.16	Hotspots on the Cu/Co-multilayer.	118

5.17	Change in GMR amplitude and resistance as function of the pulse energy for the Cu/NiFe-ML for single pulses.	119
5.18	GMR amplitude and resistance as function of the pulse energy for the Cu/NiFe-ML for salvos.	119
5.19	GMR characteristics of Wheatstone bridges.	120
5.20	Sketch of the demonstrator device for GMR- and AMR sensor.	121
5.21	Mounted sensor element.	121
5.22	Photo of demonstrator device for GMR- and AMR sensor.	122
A.1	Design of a magnetic trilayer.	128
A.2	Design of a doubled trilayer.	131
A.3	Design of a bottom spin valve.	134
A.4	Design of a multilayer.	136
A.5	Enhanced design of a multilayer.	140

List of Tables

2.1	Comparison of SI and cgs system.	6
2.2	Demagnetizing factors for special geometries.	16
3.1	AFM measurement of magnetic trilayers	56
3.2	Magnetization measurements: Fitting parameters and analysis.	61
4.1	Parameters for GMR simulation of pinned trilayers.	89
5.1	Resistance as function of line widths	105
B.1	Set of parameters for each run.	145

Acknowledgment

Here I would like to thank all those, who contributed with their support as well as advice and experimental help to this work.

I would like to express my gratitude to my tutors Prof. Dr. G. Reiss and PD. Dr. A. Hütten who provided me with the basic ideas to this thesis as well as the experimental and financial bases. Their advice was a major contribution to the success of this investigations. Special thanks to PD Dr. H. Brückl, Dr. W. Schepper and Dr. J. Schmalhorst for multiple fruitful discussions.

I would also like to thank HL Planartechnik GmbH, Dortmund, Germany, and its employees J. Herrnsdorf, Dr. A. Bartos, Dr. H. Noetzel, A. Meisenberger, A. Özdemirel and D. Schmitz for the financial support as well as their cooperation in the investigation of sensor concepts.

I would like to thank all my colleagues in the team “Thin Films and Nanotechnology” at the University of Bielefeld, especially Dr. S. Heitmann for long nights preparing and measuring samples, long fruitful discussions and lots of encouragement.

Others who helped me by doing measurements on selected samples or during implementing and reviewing the simulation and fitting routines: Dr. S. Kämmerer (structuring, XRD measurements), I. Rohde (MOKE, device for GMR measurements), Dr. D. Sudfeld (TEM), Dr. K. Rott (structuring), I. Ennen (MOKE, AGM), D. Meyners (AFM), D. Starke and Dr. M. Justus (fitting programs) and K. Wojczykowski (GMRSim).

Moreover, I thank the mechanical and electronic workshop for the fast and reliable implementation of my plans.

This work was supported by the German Ministry for Education and Research, BMBF, under grant #13N73797/4 as part of the Robert Bosch GmbH Leitprojekt Magneto-Elektronik.